UNIVERSITY OF CALABRIA

Department of Pharmacy and Health and Nutrition Science

(DFSSN)

PhD Course

Translational Medicine

Granted by

Ministry for Universities and Research (MUR)

Cycle

XXXVII

"Methods and strategies for the synthesis of biologically active oligopeptides and small molecules for potential applications in the field of drug delivery"

Scientific disciplinary sector CHIM/06

Coordinator: Ch.mo Prof. Stefania Catalano

Signature _____ STEFANIA CATALANO 02.01.2025 13:38:11 GMT+02:00

Supervisor/Tutor: Ch.mo Prof. Antonella Leggio

Signature _____ ANTO GIO 31.12)7:03 UTC

PhD student: Dott. Palmira Alessia Cavallaro

Signature _____ PALMIRA ALESSIA CAVALLARO 06.01.2025 19:56:15 UTC

Abstract

My PhD research activity focused on the development of novel methods and strategies for synthesizing biologically active short-chain peptides and piperazine-based small molecules, as well as designing mesoporous silica-based nanocarriers capable of incorporating and transporting these compounds, with the aim of enhancing their therapeutic potential.

The main activities carried out during my PhD research were as follows:

- Development of a novel peptide synthesis method for the production of small peptides in the solution phase. This approach combines $TiCl_4$ as a condensing agent with microwave heating, enabling the rapid and efficient formation of dipeptide systems with urethane protecting groups on the N-terminal amino group.
- Design and synthesis of a new cyclic somatostatin analog, c(-FWKTE-), using microwave-assisted solid-phase peptide synthesis (SPPS) and Fmoc chemistry. This cyclic pentapeptide includes the biologically active 7-10 sequence of somatostatin and glutamic acid at the C-terminus. Preliminary in vitro tests were carried out to explore its antiproliferative activity against breast cancer cell lines.
- Design and synthesis of a novel class of piperazine-based molecules as potential inhibitors of the NS2B/NS3 protease in Flaviviridae viruses, including Zika and Dengue. These compounds, incorporating urea, sulfonamide, and acyl functional groups, were evaluated for antiviral activity through live-virus assays in human hepatoma cells. Furthermore, the anticancer potential of these piperazine derivatives was investigated in breast cancer cell lines.
- Development of mesoporous silica-based (MSN) nanodevices with a dual architecture, featuring targeting molecules on their external surface and linkers within the pores for subsequent drug anchoring via covalent and non-covalent interactions. These nanocarriers are designed to enhance the therapeutic efficacy of the synthesized compounds by improving their delivery and bioavailability. The surface properties of these systems were analyzed to assess

the impact of different modifications on the nanoparticle surface structure and their potential for novel applications.

This thesis includes published works, studies ready for submission, and ongoing research that requires further investigation before completion and publication.

Table of Contents

List of Abbreviations

ADME	Absorption, distribution, metabolism, and excretion
AFPS	Automated flow-based approach for peptide synthesis
Arg	Arginine
APTES	3-aminopropyl)triethoxysilane
Asp	Aspartic Acid
Boc	Tert-butoxycarbonyl
C	Capsid
c(-FWKTE-)	Cycle-(Phe-Trp-Lys-Thr-Glu)
CC	Cell controls
CF_3COOH	Trifluoroacetic acid
COX-2	Cyclooxygenase-2
CHIKV	Chikungunya Virus
CMC	Critical micelle concentration
CTAB	Cetyltrimethylammonium bromide
Cys	Cysteine
DCM	Dichloromethane
DDS	Drug delivery systems
DENV	Dengue Virus
DIC	*N,N′*-Diisopropylcarbodiimide
DIEA	*N*,*N*-Diisopropylethylamine
DMF	N,N-Dimethylformamide
DMSO	Dimethyl sulfoxide
DENV	Dengue Virus
E	Envelope
EDCI	1-Ethyl-3-(3-dimethylaminopropyl) carbodiimide
ELISA	Enzyme-linked immunosorbent assay
ER	Endoplasmic Reticulum
Et_3N	Triethylamine

FDA	Food and Drug Administration
FOL	Folic acid
Fmoc	Fluorenylmethoxycarbonyl
FTIR	Fourier transform infrared spectroscopy
GH	Growth hormone
Glu	Glutamic acid
HAdV	Human Adenovirus
H_2O	Water
HOBt	Hydroxybenzotriazole
HONB	*N*-hydroxy-5-norbornene-*endo*-2,3-dicarboximide
HTFSPS	High-temperature fast-stirring peptide synthesis
Huh7	Humane Hepatocellular cells
IC_{50}	Half maximal inhibitory concentration
IGF-1	Insulin-like growth factor-1
Lys	Lysine
JEV	Japanese encephalitis Virus
MCF-7	Michigan Cancer Foundation-*7*
M	Membrane
MDA-MB-231	MD Anderson-Metastatic Breast-231 Cells
MP	Melting point
MS	Mass Spectrometry
MSNs	Mesoporous silica nanoparticles
MTT	3-(4,5-Dimethylthiazol-2-yl)-2,5-diphenyltetrazolium bromide
MW	Microwave
Na_2SO_4	Sodium Sulfate
NETs	Neuroendocrine tumors
NMR	Nuclear Magnetic Resonance
NPs	Nanoparticles
NS	Non-structural proteins
NSD	NanoSilical Device

PEG	Polyethylene glycol
Phe	Phenylalanine
prM	Premembrane
RMSD	Root mean square deviation
SARS-CoV2	Severe Acute Respiratory Syndrome COronaVirus 2
SEM	Scanning electron microscopy
SI	Selectivity index
SME	Small and medium enterprise
SPOV	Spondweni Virus
SPPS	Solid-phase peptide synthesis
SOF	Sofosbuvir
STT	Somatostatin
SST-14	Somatostatin 14
SST-28	Somatostatin 28
SSTR1	Somatostatin receptor subtype 1
SSTR2	Somatostatin receptor subtype 2
SSTR3	Somatostatin receptor subtype 3
SSTR4	Somatostatin receptor subtype 4
SSTR5	Somatostatin receptor subtype 5
TBTU	2-(1H-Benzotriazole-1-yl)-1,1,3,3-tetramethylaminium tetrafluoroborate
TEM	Transmission electron microscopy
TEOS	Tetraethoxysilane
TFA	Trifluoroacetic acid
TGN	Trans-Golgi network
Thr	Threonine
$TiCl_4$	Titanium tetrachloride
TIS	Triisopropylsilane
TLC	Thin Layer Chromatography
Trp	Tryptophan
VC	Virus control

WNV	West Nile Virus
W	Watt
YFV	Yellow fever virus
Z	Benzyloxycarbonyl
ZIKV	Zika Virus
(+) ssRNA	Positive single strand Ribosomal nucleic acid

Overview of the Research Activities

My PhD project consists of three parts, with the first focusing on peptide synthesis.

Peptides are important in biology and have gained significant importance in the biomedical field due to their versatility, specificity, and therapeutic potential. They offer advantages such as high targeting precision, lower toxicity, and the ability to interact with complex molecular structures. Advances in peptide research have led to the development of peptide-based drugs, including leuprolide for prostate cancer and liraglutide for type 2 diabetes [1,2], targeted therapies, and drug delivery [3-6].

Additionally, they play key roles in cancer treatment and diagnostic imaging, such as Lutetium Lu-177 for metastatic prostate cancer and Gallium Ga-68 for imaging prostate cancer in PET scans [7,8]. Peptide synthesis has been widely studied, leading to the development of various methods for efficient peptide bond formation [9]. Solution-phase peptide synthesis is widely used for producing dipeptides and small peptides. While it is not ideal for longer peptides, this method is more scalable, cost-effective, and allows for larger quantities of high-quality peptides compared to solid-phase synthesis.

Preserving the stereochemistry of chiral amino acids during the synthesis is crucial. Therefore, developing new solution phase methods that maintain the stereochemical integrity of amino acids is important, particularly for synthesizing biologically active peptides.

In the first part of my research activity I focused on developing new and efficient synthetic strategies for producing small peptides in solution. The goal was to extend these methods to both solution and solid-phase synthesis of modified and biologically active short peptides.

The direct formation of amide bond by condensing the non-activated carboxylic component and the amine component by using metal-mediated procedures represents a valid alternative in peptide synthesis [10].

Titanium tetrachloride ($TiCl_4$) has been used as a condensing agent in the synthesis of small peptides in a pyridine-buffered medium at 40 °C. This method, although effective, requires long reaction times (approximately 5 hours) and a high ratio of $TiCl_4$ to amino acid substrates to achieve efficient condensation. These factors limit the scalability and efficiency of the process, particularly when synthesizing longer peptides [11,12].

To address these issues, I investigated the use of microwave (MW) irradiation as an alternative to conventional heating. MW heating accelerates the reaction by directly interacting with the reagents and solvents, providing faster and more uniform energy transfer. This technique is more efficient than conventional heating, as microwaves directly couple with molecules, causing rapid and uniform temperature increases. This approach also eliminates the limitations of traditional heating, such as dependence on the thermal conductivity of the reaction vessel.

By introducing microwave irradiation, we were able to achieve faster peptide synthesis with a lower $TiCl_4$-to-substrate ratio, thus improving the overall efficiency and reducing energy consumption.

Using $TiCl_4$ and microwave heating, a series of dipeptides protected on the amino function by urethane protecting groups were synthesised with high yields. The condensation reactions involved N-protected α-amino acids and α-amino acid methyl ester hydrochlorides in pyridine. The dipeptide products were efficiently recovered through filtration using a silica gel column, simplifying the work-up and minimizing product loss. The reaction conditions were compatible with various protecting groups, including (Fluorenylmethyloxycarbonyl), Z (Benzyloxycarbonyl), and Boc (*tert*-Butyloxycarbonyl), which are removable under different conditions, highlighting the versatility of the approach.

Importantly, the stereochemistry of the starting materials was preserved throughout the synthesis, with no significant racemization detected by NMR analysis.

In summary, the introduction of MW irradiation significantly reduced reaction times and improved synthesis efficiency, while the lower $TiCl_4$-to-substrate ratio enhanced overall process sustainability.

Continuing in the field of peptide synthesis, my research also expanded to the development of a novel somatostatin analogue with potential anticancer properties.

Somatostatin (SST) is a peptide hormone that regulates various physiological processes by binding to specific receptors. It inhibits hormone secretion and cell growth, making it useful for diagnosing and treating neuroendocrine tumors. The sequence 7-10 (Phe^7, Trp^8, Lys^9, and Thr^{10}) in somatostatin is critical for its biological function, with the Trp^8-Lys^9 (W-K) motif being essential for activating somatostatin receptors (SSTRs) [13, 14].

Although somatostatin plays an important role in tumor diagnosis and treatment, its clinical use is limited by a very short plasma half-life and poor selectivity. This has led to the development of synthetic analogues that aim to retain somatostatin's biological activity while improving selectivity and pharmacokinetic properties. These analogues may also help inhibit tumor growth by inducing apoptosis [15].

Small cyclic peptides based on somatostatin's active sequence (Phe-Trp-Lys-Thr) have shown promising antitumor effects and good safety profiles, making them attractive candidates for cancer therapy. A well-known example is Octreotide [16].

Based on conformational studies and structure-activity analysis of somatostatin agonists, a new somatostatin analogue, c(-FWKTE-), specific for the SST-2 receptor, was designed and synthesized. This analogue is a cyclic pentapeptide containing the biologically active sequence of somatostatin, with glutamic acid at the C-terminal. It was synthesized using microwave-assisted solid-phase synthesis combined with Fmoc-chemistry techniques. Glutamic acid, anchored to Wang resin via its side chain carboxyl group and protected at the α-carboxyl group with the orthogonal Dmab protecting

group (4-{N-[1-(4,4-dimethyl-2,6-dioxocyclohexylidene)-3-methylbutyl]amino}benzyl}), enabled head-to-tail cyclization on the resin.

The short peptide chain enhances its ability to adapt conformationally, improving its fit with the receptor. Cyclization introduces conformational constraints that help stabilize a specific peptide structure, increasing resistance to enzymatic degradation and boosting both receptor affinity and selectivity compared to the linear peptide form [17].

Early *in vitro* tests demonstrated that the compound exhibits antiproliferative effects on various breast cancer cell lines (MCF-7, T47D, ZR75, and the triple-negative MDA-MB-436), indicating its potential as an anticancer agent. However, these results are preliminary, and further *in vitro* investigations are needed to fully evaluate its efficacy.

During my doctoral course, I conducted six months of research at Universidad de Sevilla under the supervision of Professor Margarita Vega Holm. My work focused on the design, synthesis and structural characterization of new small molecules as potential viral protease inhibitors for Zika and Dengue Virus, belonged to Flaviviridae family. Currently, there are no effective drugs available to treat these infections.

The Flaviviridae family shares a common viral genome organization, with a single-stranded positive-sense RNA molecule translated into a polyprotein that is processed by host and viral proteases into mature structural and nonstructural (NS) proteins [18-20]. These NS proteins, which are involved in RNA replication, virion assembly, and immune response modulation, are key targets for antiviral therapy [21]. Among these, the NS2B/NS3 proteases play an important role in the virus life cycle, making them attractive targets for antiviral drug discovery [22].

Building on previous research conducted by Professor Margarita Vega Holm's group [23], which focused on developing effective antiviral agents based on a piperazine backbone, I successfully synthesized a novel collection of piperazine-derived small molecules as potential inhibitors of the

Flaviviridae NS3 protease. These compounds featured different urea and sulfonamide moieties at the N-1 position and various acyl groups at the N-4 position.

In collaboration with Dr. Ilaria Vicenti's team at the University of Siena, all synthesized compounds were tested for antiviral activity through live-virus assays using Huh7 human hepatoma cell lines.

A cell-based assay identified six compounds with significant activity against ZIKV, with IC50 values ranging from 1.6 to 5.1 μM, comparable to the reference compound Sofosbuvir (SOF), which has an IC50 of 3.7 μM. These compounds also demonstrated a favorable safety profile. Notably, three of them displayed potent activity against DENV, along with high selectivity indices. Among these, one compound stood out as the most promising, with an IC50 of 1.6 μM against ZIKV and a selectivity index (SI) greater than 125, as well as an IC50 of 3.8 μM against DENV and an SI of 52.7. This compound showed superior activity and selectivity compared to SOF for both viruses.

This positions the piperazine scaffold as a strong candidate for developing broad-spectrum antiviral agents targeting flaviviruses.

Piperazine rings are a critical component in several well-established anticancer drugs, including Imatinib, Dasatinib, Bosutinib, Danusertib, and VX-680. Additionally, compounds featuring 4-piperazinyl-quinoline-isatin derivatives have shown cytotoxic effects against human breast cancer cell lines, such as MDA-MB468 and MCF7 [24, 25].

Inspired by these findings, a small library of novel piperazine derivatives was designed and synthesized, with the primary objective of assessing their potential as anticancer agents, alongside their antiviral activity.

The newly synthesized piperazine derivatives, along with previously developed compounds, were tested *in vitro* on breast cancer cell lines by Professor Catia Morelli's research group at the University of Calabria. Four compounds emerged as particularly promising, demonstrating a dose-dependent antiproliferative effect against breast cancer cells (MCF-7) while sparing normal breast cells (MCF-

10A). This selective activity highlights a favorable balance between efficacy and safety, underscoring their potential as targeted anticancer agents.

These findings suggest that these compounds may serve as dual-action therapeutic agents, effective against both viruses and cancer cells. Further research will focus on optimizing these molecules through novel functionalization aiming to enhance their antiviral efficacy and improve their anticancer activity and selectivity through targeted therapeutic strategies.

The final part of my doctoral research was conducted at NanoSiliCal Devices (NSD), an innovative SME and spin-off of the University of Calabria, where I completed a 10-month industrial internship. The main objective of my research during this period was the design and development of mesoporous silica-based nanodevices with dual functionality. These nanocarriers were engineered with targeting molecules on their external surface and linkers within their pores, allowing for the anchoring of drugs via both covalent and non-covalent interactions. The goal of this work was to enhance the therapeutic efficacy of the synthesized biologically active compounds by improving their delivery, stability, and bioavailability through the use of MSN-based nanocarriers.

Advanced drug delivery systems (DDS) utilizing nanoparticles have shown considerable promise in overcoming challenges related to drug solubility, bioavailability, and targeted delivery. These systems not only improve the solubility and absorption of therapeutic molecules but also enable targeted delivery, ensuring that drugs are directed to specific sites in the body. This targeted approach helps to minimize off-target effects, increase therapeutic efficacy, and ultimately improve clinical outcomes [26].

Mesoporous silica nanoparticles (MSNs) stand out as ideal candidates for drug delivery systems (DDS) because of their unique intrinsic characteristics such as large surface area, high pore volume, and favorable properties, including biocompatibility, biodegradability, and chemical stability [27].

During my research, I focused on developing MSN-based prototypes using proprietary MSN technology of NanoSiliCal Devices. Various MSN-based nanodevices were designed, developed, and characterized in this study, with a focus on the surface properties of mesoporous silica nanoparticles and the impact of tailored functionalization.

These nanodevices were developed with folic acid (FOL) as the targeting ligand on the external surface (FOL-MSN) to ensure precise tissue recognition and efficient cellular internalization. Folic acid provides high specificity for folate receptors, which are commonly overexpressed in many types of cancer cells.

Additionally, the pores of the MSNs were functionalized with specific linkers (FOL-MSN-DIOL, FOL-MSN-COOH, FOL-MSN-HYD) designed to create versatile binding sites that can form stimuli-responsive interactions with biologically active synthesized molecules. This design enables the drugs to be loaded into the pores and released in a controlled manner, specifically targeting the microenvironment of pathological tissues.

The surface properties of mesoporous silica nanoparticles were analyzed after the various post-synthesis modifications using techniques like FTIR, Zeta potential measurements, and nitrogen adsorption porosimetry. These analyses revealed how different modifications impact the surface structure of the nanoparticles and their potential for new applications. We specifically examined how single and multi-step modifications, along with surfactant extraction protocols, influence the surface characteristics. Understanding these changes is essential for assessing the nanoparticles' suitability for drug delivery, as pore accessibility and electrostatic interactions are crucial for their effectiveness. Future research will focus on the anchoring of newly synthesized antiviral and anticancer compounds into the MSNs to enhance their delivery and therapeutic potential.

References

1. Sharifi, R., Soloway, M., Correa Jr, R. J., Glass, A. G., Guinan, P. D., Garnick, M. B. et al. Clinical study of leuprolide depot formulation in the treatment of advanced prostate cancer. *The Journal of urology* **1990**, *143*(1), 68-71.
2. Wajcberg, E., Amarah, A. Liraglutide in the management of type 2 diabetes. *Drug design, development and therapy* **2010**, 279-290.
3. Purcell, A. W., McCluskey, J., Rossjohn, J. More than one reason to rethink the use of peptides in vaccine design. *Nature reviews Drug discovery* **2007**, *6*(5), 404-414.
4. Lau, J. L., Dunn, M. K. Therapeutic peptides: Historical perspectives, current development trends, and future directions. *Bioorganic & medicinal chemistry* **2017**, *26*(10), 2700-2707.
5. Haggag, Y. A., Donia, A. A., Osman, M. A., El-Gizawy, S. A. Peptides as drug candidates: limitations and recent development perspectives. *Biomed J* **2018**, *1*(3).
6. Lee, A. C. L., Harris, J. L., Khanna, K. K., Hong, J. H. A comprehensive review on current advances in peptide drug development and design. *International journal of molecular sciences* **2019**, *20*(10), 2383.
7. Erdogan, M., Sengul, S. S., Cetin, B., Avcı, M., Yagci, S., Ozkoç, I. et al. The role of Ga68 PSMA PET/CT imaging in Lu177 PSMA treatment planning in metastatic castration-resistant prostate cancer. *Annals of Nuclear Medicine* **2022**, *36*(6), 562-569.
8. Almuradova, E., Seyyar, M., Arak, H., Tamer, F., Kefeli, U., Koca, S. et al. The real-world outcomes of Lutetium-177 PSMA-617 radioligand therapy in metastatic castration-resistant prostate cancer: Turkish Oncology Group multicenter study. *International Journal of Cancer* **2024**, *154*(4), 692-700.
9. Hollanders, K., Maes, B. U., Ballet, S. A new wave of amide bond formations for peptide synthesis. *Synthesis* **2019**, *51*(11), 2261-2277.
10. Valeur, E., Bradley, M. Amide bond formation: beyond the myth of coupling reagents. *Chemical Society Reviews* **2009**, *38*(2), 606-631; Allen, C. L., Chhatwal, A. R., & Williams, J. M. Direct amide formation from unactivated carboxylic acids and amines. *Chemical Communications* **2012**, *48*(5), 666-668.
11. Comandè, A., Greco, M., Belsito, E. L., Liguori, A., & Leggio, A. A titanium tetrachloride-based effective methodology for the synthesis of dipeptides. *RSC advances* **2019**, *9*(38), 22137-22142.
12. Leggio, A., Bagalà, J., Belsito, E. L., Comandè, A., Greco, M., Liguori, A. Formation of amides: One-pot condensation of carboxylic acids and amines mediated by TiCl 4. *Chemistry Central Journal* **2017**, *11*, 1-12.
13. Biron, E., Chatterjee, J., Ovadia, O., Langenegger, D., Brueggen, J., Hoyer, D. Improving oral bioavailability of peptides by multiple N-methylation: somatostatin analogues. *Angewandte Chemie International Edition* **2008**, 47(14), 2595-2599.
14. Janecka, A., Zubrzycka, M., Janecki, T. Somatostatin analogs. *The Journal of Peptide Research* **2001**, 58(2), 91-107.
15. Scarpignato, C., Pelosini, I. Somatostatin analogs for cancer treatment and diagnosis: an overview. *Chemotherapy* **2001**, 47(Suppl. 2), 1-29.
16. Di Bartolomeo, M., Bajetta, E., Buzzoni, R., Mariani, L., Carnaghi, C. et al. Clinical efficacy of octreotide in the treatment of metastatic neuroendocrine tumors: a study by the Italian Trials

in Medical Oncology Group. *Cancer: Interdisciplinary International Journal of the American Cancer Society* **1996**, *77*(2), 402-408.
17. Ahangarzadeh, S., Kanafi, M. M., Hosseinzadeh, S., Mokhtarzadeh, A., Barati, M., Ranjbari, J., Tayebi, L. Bicyclic peptides: types, synthesis and applications. *Drug Discovery Today* **2019**, *24*(6), 1311-1319.
18. Vasilakis, N., Weaver, S. C. Flavivirus transmission focusing on Zika. *Current opinion in virology* **2017**, *22*, 30-35.
19. Alzahrani, N., Wu, M. J., Shanmugam, S., Yi, M. Delayed by design: role of suboptimal signal peptidase processing of viral structural protein precursors in Flaviviridae virus assembly. *Viruses* **2020**, *12*(10), 1090.
20. T. C., Diamond, M. S. The continued threat of emerging flaviviruses. *Nature microbiology* **2020**, *5*(6), 796-812.
21. Zhang, S., He, Y., Wu, Z., Wang, M., Jia, R., Zhu, D. Secretory pathways and multiple functions of nonstructural protein 1 in flavivirus infection. *Frontiers in immunology* **2023**, *14*, 1205002.
22. Luo, D., Vasudevan, S. G., Lescar, J. The flavivirus NS2B–NS3 protease–helicase as a target for antiviral drug development. *Antiviral research* **2015**, *118*, 148-158.
23. del Rosario García-Lozano, M., Dragoni, F., Gallego, P., Mazzotta, S., López-Gómez, A., Boccuto, A. Piperazine-derived small molecules as potential Flaviviridae NS3 protease inhibitors. In vitro antiviral activity evaluation against Zika and Dengue viruses. *Bioorganic Chemistry* **2023**, *133*, 106408.
24. Al-Ghorbani, M., Gouda, M. A., Baashen, M., Alharbi, O., Almalki, F. A., Ranganatha, L. V. Piperazine heterocycles as potential anticancer agents: A review. *Pharmaceutical Chemistry Journal* **2022**, *56*(1), 29-37.
25. Deveshegowda, S. N., Metri, P. K., Shivakumar, R., Yang, J. R., Rangappa, S. et al. Development of 1-(4-(Substituted) piperazin-1-yl)-2-((2-((4-methoxybenzyl) thio) pyrimidin-4-yl) oxy) ethanones That Target Poly (ADP-Ribose) Polymerase in Human Breast Cancer Cells. *Molecules* **2022**, *27*(9), 2848.
26. Anselmo, A. C., Mitragotri, S. (2019). Nanoparticles in the clinic: An update. *Bioengineering & translational medicine* **2019**, *4*(3), e10143).
27. Stephen, S., Gorain, B., Choudhury, H., Chatterjee, B. Exploring the role of mesoporous silica nanoparticle in the development of novel drug delivery systems. *Drug delivery and translational research* **2022**, 1-19.

Chapter 1

Efficient solution-phase dipeptide synthesis using titanium tetrachloride and microwave heating

Palmira Alessia Cavallaro, Marzia De Santo, Rocco Marinaro, Emilia Lucia Belsito, Angelo Liguori and Antonella Leggio

Published on: *Int J Mol Sci.* **2024**, *25*(17), 9729

DOI: 10.3390/ijms25179729

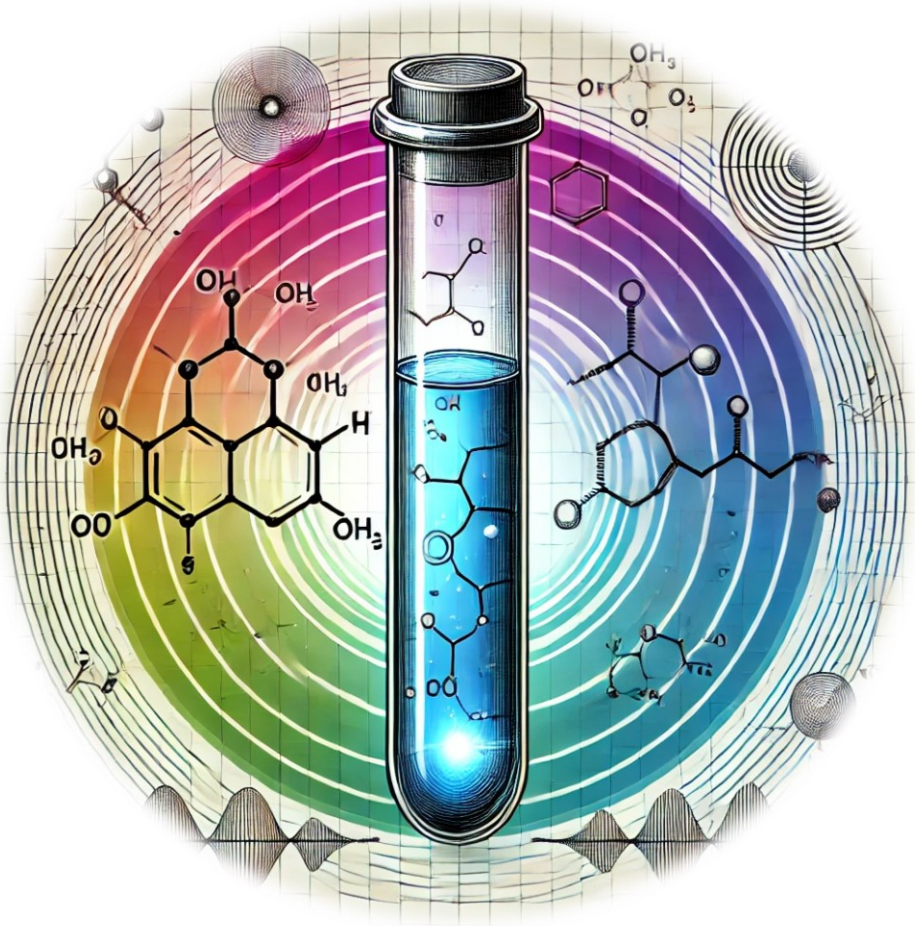

1.1 Introduction

The amide linkage is one of the most widespread chemical bonds in organic molecules, drugs and biologically active compounds including peptides and proteins [1, 2]. The amide or peptide bond is of fundamental importance for the stability and structural characteristics of all known proteins [3]. Peptides play a crucial role in biology and have gained significant importance in the biomedical field. Their growing importance in medicine is due to their versatility, specificity, and therapeutic potential, offering advantages like high specificity, lower toxicity, and the ability to target complex molecular structures [4]. Recent advancements have led to the discovery of new peptides with various therapeutic benefits [5]. Peptide-based drugs such as leuprolide for prostate cancer and liraglutide for type 2 diabetes are now available on the market [6].

Peptides are also being used in vaccine development [7] and targeted therapies to deliver drugs to specific sites, block cell surface receptors, and interfere with intracellular protein interactions [8]. Recently approved peptides include Setmelanotide, which helps manage weight in genetic obesity cases by activating the melanocortin 4 receptor [9], Trofinetide, designed to treat Rett syndrome [10] and Voclosporin, a peptide-based calcineurin inhibitor, used as an immunosuppressant for lupus nephritis [11]. Peptides are also proving to be valuable in cancer treatment and diagnostic imaging, like Lutetium Lu-177 Vipivotide Tetraxetan, a radiolabelled peptide targeting the prostate-specific membrane antigen (PSMA) for treating metastatic prostate cancer [12] and Gallium Ga-68 Gozetotide, a peptide-based imaging agent used in PET scans to visualize PSMA in prostate cancer patients [13]. The synthesis of organic molecules incorporating amide bonds, including peptides, has been extensively explored. Numerous studies have reported a variety of synthetic approaches in this regard [14-19].

Recent technological advancements have introduced a fully automated, flow-based method for solid-phase polypeptide synthesis (AFPS). This method combines the flexibility of solid-phase peptide synthesis (SPPS) with significantly faster processing times. AFPS improves peptide production by

drastically reducing the time needed for amide bond formation in standard Fmoc peptide synthesis and offers better control compared to traditional manual or automated methods [20]. In line with these advancements, Hurevich et al. developed a high-yield, cost-efficient, affordable, and fast peptide synthetic process using high-temperature fast-stirring peptide synthesis (HTFSPS). Their approach allowed them to accelerate solid-phase synthesis, proving the effective use of overhead stirring and heating without an excess of reagent, making it possible to produce a large number of peptides in a short period of time [21]. The activation of amino acid carboxylic function is a key step in peptide synthesis. It is generally performed through the conversion of N-terminal amino acids into reactive acylating intermediates (acyl chlorides, anhydrides, and activated esters) using activating reagents [22-26]. However, activation and coupling steps often face significant challenges, including the use of toxic and expensive reagents [27, 28], the generation of hard-to-isolate byproducts [29], and the risk of racemization at the activated carboxyl residues [30]. These issues underscore the ongoing need for more efficient coupling reagents and improved methods.

Recently, metal-based reagents for amide bond formation have attracted significant attention due to their efficiency and reactivity [31-34].

Titanium (IV)-based reagents have gained prominence in organic synthesis. Their ability to coordinate with the carbonyl oxygen atom and their versatility in transforming various functional groups make them valuable tools in peptide synthesis [33-40].

We investigated the use of titanium tetrachloride ($TiCl_4$) for peptide bond formation and developed a new solution-phase method for synthesizing dipeptides [41, 42]. In this method, $TiCl_4$ serves as the condensing agent in a pyridine-buffered medium at 40 ◦C. This approach produced various N-protected dipeptides within approximately 5 h. However, the 5-hour reaction time can be a limitation for synthesizing longer peptide chains. To address this, we explored the use of microwave irradiation to accelerate the process.

Microwave (MW) heating, in fact, allows us to enhance reaction yields and decrease reaction times by directly interacting with reagents and solvent, offering a faster and more efficient method of heating the reaction mixtures compared to conventional methods [43-47]. Microwave irradiation not only accelerates the reaction but also offers a more sustainable and efficient approach compared to traditional heating. However, despite these benefits, the use of microwave irradiation in solution-phase peptide synthesis remains underexplored.

Previous studies have demonstrated the potential of microwave-assisted methods. For instance, Jain et al. developed a rapid microwave-assisted protocol for dipeptide synthesis using DIC/HONB in DMF, achieving a 65% yield with no racemization [48]. Building on this, the same research group reported the first solution-phase peptide synthesis conducted in neat water using TBTU/HOBt/DIEA under microwave irradiation in 2013 [49].

In this study, we present a novel method for solution-phase peptide synthesis that combines $TiCl_4$ as a condensing agent with microwave heating, enabling the efficient formation of dipeptide systems with urethane protecting groups on the N-terminal amino function.

1.2 Results and Discussion

Titanium tetrachloride ($TiCl_4$) was employed as a condensing agent for the solution phase synthesis of aspartame, a commercially used artificial sweetener, as well as a series of dipeptides protected on the amino function with tert-butoxycarbonyl (Boc), fluorenylmethoxycarbonyl (Fmoc) and benzyloxycarbonyl (Z) groups [42]. The reactions, performed in pyridine as solvent, were completed within 5–6 h. Although the reaction conditions were mild, with a reaction temperature of 40 ◦C employed to avoid side reactions, reaction times were only acceptable (5‑6 h). Furthermore, the procedure required the use of excess $TiCl_4$ (2 eq) relative to the amino acid substrates (1 eq).

The evaluation of these aspects has led to the belief that the use of a microwave reactor could obviate these drawbacks improving the efficiency of the process and consequently enhancing further the synthetic utility of the reaction. Therefore, we decided to carry out the peptide bond formation under microwave irradiation and experimenting an equimolar ratio (1:1) between amino acid substrate and $TiCl_4$.

Preliminarily, the reaction was tested by synthesizing the dipeptide *N*-Fmoc-L-Phe-L-Ala-OMe (**1a**), chosen as model system, to evaluate the progress of the reaction and identify the best reaction conditions. Alanine methyl ester hydrochloride (1 mmol) dissolved in pyridine (3 mL) was treated with *N*-Fmoc-L-phenylalanine (1 mmol) and $TiCl_4$ (1mmol) then, the reaction mixture was stirred and subjected to microwave irradiation at 40 °C monitoring the reaction through TLC analysis (Scheme 1.1). Pyridine was chosen as the solvent based on previous studies [42], which demonstrated its effectiveness in enhancing the performance of the $TiCl_4$ reagent system.

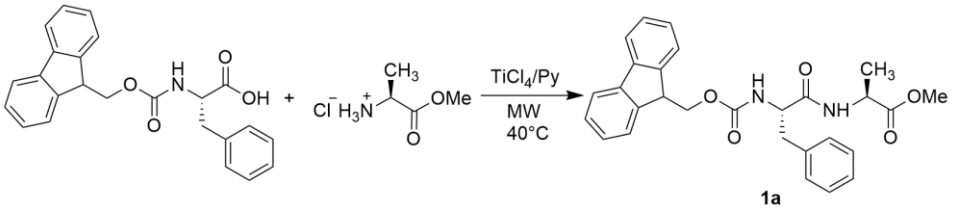

Scheme 1.1. Synthesis of *N*-Fmoc-Phe-Ala-OMe (**1a**)

To identify the best microwave power required for the reaction, we tested a range of power settings from 50 W to 250 W for synthesizing compound **1a (**Table 1.1). The results of these experiments revealed that running the reaction at 250 W resulted in high yields of product **1a** and significantly shorter reaction times compared to the lower power settings of 50 W and 100 W.

Table 1.1. Optimization of the microwave power in the synthesis of the model system **1a**

Dipeptide	Temperature °C	Power (Watt)	Time (min)	Yield[a] (%)
1a	40°C	50	60	53
1a	40°C	100	40	70
1a	40°C	250	20	90

[a]isolated yield

The reaction conducted under microwave irradiation at 250 W produced the dipeptide **1a** in just 20 minutes with a high 90% yield, using an equimolar ratio of $TiCl_4$ to the starting *N*-Fmoc-protected amino acid.

Furthermore, prolonged reaction times did not improve product yield. However, these conditions offer a notable time improvement compared to the previous conventional heating method, which demanded a reaction time of 5-6 hours. The dipeptide **1a** was recovered by co-evaporating pyridine with toluene, then filtering the crude reaction product suspended in chloroform through a silica gel column, using chloroform as the eluent. In view of these results, we performed a direct comparison with the reaction conducted under conventional heating, using the same temperature (40 °C) and the same molar ratio between $TiCl_4$ and the amino acid substrate (1:1).

Specifically, the reaction between *N*-Fmoc-phenylalanine (1 mmol) and alanine methyl ester hydrochloride (1 mmol) in the presence of $TiCl_4$ (1 mmol) was carried out in pyridine using an oil bath maintained at 40 °C. After 1 hour, the reaction mixture yielded only 33% of dipeptide **1a**. After 5 hours, a significant amount of the starting substrates (about 50%) remained in the reaction mixture.

Encouraged by the successful microwave-assisted synthesis of dipeptide **1a**, we applied the same protocol to other *N*-Fmoc protected amino acids to assess the reproducibility and effectiveness of the reaction (Scheme 1.2, Table 1.2).

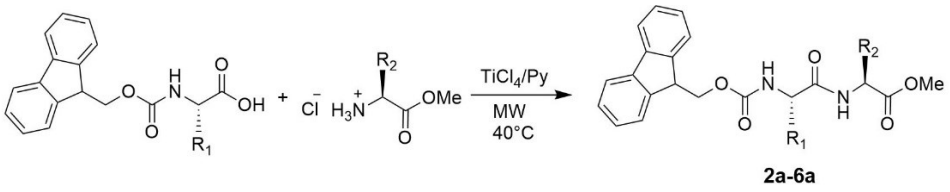

Scheme 1.2. Synthesis of *N*-Fmoc-dipeptide methyl esters **2a-6a**

Table 1.2. Results of the reaction reported in Scheme 2

Dipeptide	R_1	R_2	Time (min)	Yield[a] (%)
2a	H	CH_3	30	88
3a	$CH_2C_6H_4OtBu$	H	25	78
4a	$CH_2CH(CH_3)_2$	H	20	80
5a	$CH_2CH(CH_3)_2$	$CH(CH_3)CH_2CH_3$	40	70
6a	$CH_2SCH_2C_6H_5$	CH_3	35	70

[a]isolated yield

The $TiCl_4$-assisted reaction between *N*-Fmoc-L-Tyr(OtBu)-OH and glycine methyl ester hydrochloride efficiently produced ester **3a** in high yield, as shown in Table 2. Similarly, the coupling of *N*-Fmoc-L-Cys(Bzl)OH with L-alanine methyl ester hydrochloride yielded the dipeptide *N*-Fmoc-L-Cys(Bzl)-L-Ala-OMe (**6a**) in 35 minutes with a 70% yield (Table 1.2). These results demonstrate that the reaction conditions effectively preserve the acid-labile protecting groups on the amino acid side chains.

All the obtained *N*-Fmoc-dipeptides (**1a-6a**) were characterized by ^1H NMR and ^{13}C NMR analyses. The condensation of *N*-Fmoc-protected amino acids with amino acid methyl ester hydrochlorides was successfully achieved, with all reactions demonstrating favorable yields and significantly reduced reaction times.

The use of pyridine as a solvent effectively addresses the issue of releasing the amino function of amino acid methyl ester from its hydrochloride, as it is present in a large excess. Lastly, it is noteworthy that a 1:1 molar ratio of titanium tetrachloride to amino acid was consistently employed in each reaction.

These experiments demonstrate that microwave-driven reactions in $TiCl_4$-assisted dipeptide synthesis are significantly faster than those conducted under conventional heating at the same temperature. This suggests that microwaves might have unique effects that enhance reaction rates beyond what standard heating can achieve.

A potential issue arises from the difficulty in accurately determining the temperature inside the microwave cavity using an IR sensor. IR sensors only monitor the temperature on the external surface of the reaction vessel, which may not accurately reflect the actual internal reaction temperature. To assess potential non-thermal effects, precise temperature control is crucial. The optimal choice is an internal temperature sensor, such as an optical fiber probe, which can be directly placed into the reaction solution providing accurate measurements [46]. Moreover, maintaining a homogeneous and properly stirred reaction mixture is essential for reliable results.

When the microwave reactor was set to 40°C, temperature fluctuations were observed. The IR sensor recorded temperatures ranging from 40 to 50°C, while the fiber-optic probe detected a range of 40 to 60°C. These variations are likely due to the constant microwave power applied until the set temperature is reached, followed by a feedback loop that modulates the power to maintain the temperature. Notably, the fiber-optic sensor revealed that the actual internal reaction temperature was higher than the temperature recorded by the IR sensor.

To compare the microwave-assisted reaction at 40°C with conventional heating at 60°C, we adjusted the conventional heating temperature to match the maximum temperature measured by the fiber-optic probe during microwave irradiation.

This adjustment accounts for the approximate 10°C difference observed between the IR and fiber-optic sensors. The two experiments were conducted simultaneously to facilitate a direct comparison between the microwave-driven (40°C) and conventional heating reactions (60 °C) for synthesizing the dipeptide Fmoc-Leu-Ile-OMe (**5a**). Both reactions were performed under identical conditions, including temperature, reagent concentration, and solution volume, in identical sealed reaction vessels. The molar ratios of $TiCl_4$ (1 mmol) to the amino acid substrates, Fmoc-isoleucine (1 mmol) and leucine methyl ester hydrochloride (1 mmol), were consistent with those used for the model dipeptide Fmoc-Phe-Ala-OMe (**1a**).

Initially, the solvent (pyridine) is heated to 60°C using conventional heating with an oil bath, with the temperature inside the reaction vessel continuously monitored by a Vertex VTF digital thermoregulator. In the microwave-initiated reaction, the solvent temperature was initially set to 40°C, but it fluctuated between 40°C and 60°C, as measured by an optic fiber probe placed within the reaction mixture. Once the solvent in both reactions reached the target temperature, the reagents were simultaneously added, and the mixtures were vigorously stirred using a magnetic stirrer to ensure temperature homogeneity throughout the reaction [46, 50].

In the microwave-heated reaction, thermal conditions within the reaction mixture are uniform, with measurements taken at different points consistently showing temperature fluctuations between 40 and 60 degrees Celsius. In contrast, the temperature in the conventionally heated reaction remains stable at 60 degrees Celsius. Both reactions were monitored using TLC with a chloroform–methanol solvent system (90:10 v/v). After approximately 40 minutes, the microwave-driven reaction was complete, while the conventional heating reaction was still ongoing. At this point, both reactions were stopped and processed identically. The microwave-assisted reaction yielded the expected product, Fmoc-Leu-Ile-OMe (**5a**, Table 1.2), with a 70% yield, while the conventional heating method produced only 20% of the product.

The process began by heating the solvent to the target temperature. Once reached, reagents were added simultaneously to both systems, maintaining a nearly constant temperature throughout. This indicates that differences in heating rates cannot account for the variations in reaction progress. Additionally, no overheating was observed in the microwave-assisted reaction, as the process was conducted well below the solvent's boiling point. Therefore, the increased rate of the microwave-assisted reaction cannot be attributed to temperature effects, as described by the Arrhenius equation ($k = Ae^{-Ea/BT}$), which relates reaction rates to temperature.

Instead, microwaves may accelerate the reaction by affecting the frequency factor (A) in the Arrhenius equation, by inducing rapid rotational motion in polar reactants and intermediates and increasing the frequency of effective molecular collisions. This enhanced molecular agitation facilitates the condensation reaction, leading to a faster overall reaction rate.

To further demonstrate the protocol's versatility, it was applied to the synthesis of dipeptide systems, employing acid-labile groups like Boc and Z to protect the α-amino function.

The synthesis of *N*-Boc-dipeptides was conducted in a microwave reactor, employing the same reaction conditions used for the *N*-Fmoc-protected substrates (Scheme 1.3).

Even employing Boc-protected amino acids, the reaction proceeds rapidly, reaching completion within 20-40 minutes. After the reaction, the Boc-dipeptide systems **1b-7b** were efficiently recovered by fast filtration of the reaction mixture suspended in chloroform through a silica column, with yields ranging from 70% to 94% (Table 1.3).

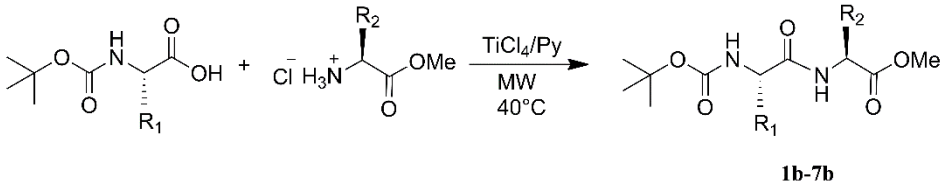

Scheme 1.3. Synthesis of *N*-Boc-protected dipeptide methyl esters **1b-7b**

Table 1.3. Results of the reaction reported in Scheme 3

Dipeptide	R_1	R_2	Time (min)	Yield[a] (%)
1b	$CH_2C_6H_5$ (L)	CH_3 (L)	20	94
2b	$CH_2C_6H_5$ (L)	CH_3 (D)	20	76
3b	$CH_2C_6H_5$ (D)	CH_3 (D)	25	71
4b	$CH(CH_3)CH_2CH_3$	$CH_2CH(CH_3)_2$	35	84
5b	$CH_2CH(CH_3)_2$	$CH(CH_3)_2$	30	70
6b	$(CH_2)_3NHCN(Z)NH(Z)$	CH_3	40	83
7b	$CH_2C_6H_5$	$CH_2CH(CH_3)_2$	25	89

[a] isolated yield

The analysis of the Boc-protected dipeptides was performed using nuclear magnetic resonance spectroscopy (^{1}H NMR and ^{13}C NMR) and gas chromatography/mass spectrometry (GC/MS (EI)). *N*-Boc-arginine, with the guanidine group's nitrogen atoms protected with the acid-labile benzyloxycarbonyl (Z) group, was reacted with alanine methyl ester hydrochloride under the previously established conditions. Following approximately 40 minutes, the dipeptide *N*-Boc-Arg(Z)$_2$-OH (**6b**) was obtained with an 83% yield (Table 1.3) and high purity, as confirmed by ^{1}H and ^{13}C NMR analyses. The spectroscopic data confirmed the stability of both the Z group on the side chain and the Boc group on the α-amino function, as no deprotection occurred under the reaction conditions.

The reaction conditions also preserved the optical purity at the chiral centers of the precursors, as evidenced by ^{1}H NMR analysis of a couple of diastereoisomeric dipeptides (**2b** and **3b**). Examination of the ^{1}H NMR spectra for both single epimers of *N*-Boc-L-Phe-D-Ala-OMe (Figure 1.1**, A**) and *N*-Boc-D-Phe-D-Ala-OMe (Figure 1.1, **B**) showed signals consistent with a single diastereomer, indicating minimal epimerization within the detection limits of the NMR technique (Figure 1.1). Distinct chemical shifts were observed for the signals originating from the amide NH protons (6.51 and 6.69 ppm) and alanine side chain CH_3 protons (1.19 and 1.30 ppm) in the two diastereoisomers. These differences were clearly resolved in the ^{1}H NMR spectrum of a mixture containing **2b** and **3b**, specifically prepared for this analytical purpose (Figure 1.1; **C**).

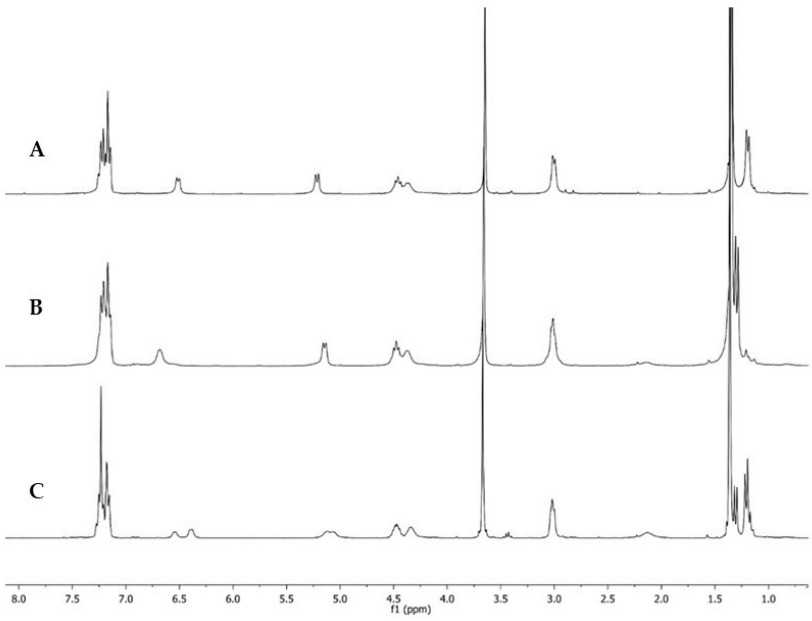

Figure 1.1. ^{1}H NMR spectra of *N*-Boc dipeptides: A) *N*-Boc-L-Phe-D-Ala-OCH_3 (**2b**); B) *N*-Boc-D-Phe-D-Ala-OCH_3 (**3b**); C) mixture consisting of 60% **2b** and 40% **3b**

Moreover, the application of microwave irradiation in the $TiCl_4$-assisted coupling reaction also produced notable results in the synthesis of dipeptides protected on the terminal amino function with the benzyloxycarbonyl (Z) protecting group (Scheme 1.4). The reactions to form the *N*-Z-protected dipeptides (Table 1.4) were completed within just 30-35 minutes, with product yields ranging from 65% to 81%.

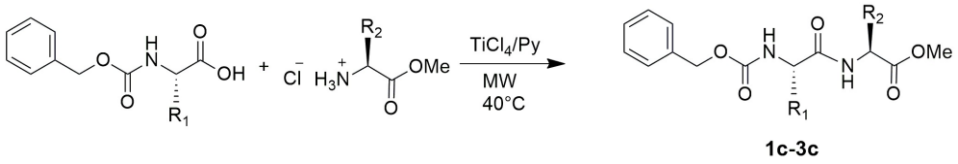

Scheme 1.4. Solution-phase synthesis of *N*-Z-protected dipeptide methyl esters **1c-3c**

Table 1.4. Results of the reaction reported in Scheme 1.4

Dipeptide	R_1	R_2	Time (min)	Yield[a] (%)
1c	$CH_2C_6H_5$	CH_3	30	81
2c	H	$CH(CH_3)_2$	30	75
3c	$CH(CH_3)_2$	$CH_2C_6H_5$	35	65

[a]isolated yield

The structures of the Z-protected dipeptides were confirmed using proton (^1H) and carbon-13 (^{13}C) nuclear magnetic resonance spectroscopy, as well as gas chromatography/mass spectrometry (GC/MS). These analyses also confirmed that the Z protecting group remained intact on the terminal amino function under the conditions of the microwave-assisted coupling procedure.

1.3 Materials and Methods

1.3.1 General Chemistry Methods

Reagents were commercially available with analytical grade and used as purchased without further purification. Solvents were purified following standard laboratory techniques and freshly distilled before use.

Reactions were conducted in a CEM Discover single-mode microwave reactor equipped with an infrared temperature sensor (IR). Additionally, a fiber-optic probe provided by the manufacturer was used to directly monitor the internal reaction temperature within a 10 mL sealed reaction vessel.

The microwave reactions were carried out at 40 °C in 10 mL glass vials (obtained from CEM) sealed with silicone/PTFE caps. The pressure release limit was set to 250 psi, and the power was set to 250 W, with the microwave instrument dynamically controlling the applied power.

The reaction mixtures were stirred magnetically and monitored by thin-layer chromatography (TLC) using silica gel 60-F254 pre-coated glass plates. The TLC spots were visualized under a UV lamp (254 nm) and by spraying with 0.2% ninhydrin in ethanol, followed by charring after elution.

^{1}H and ^{13}C NMR spectra were recorded on a Bruker Avance 300 instrument at 300 MHz and 75 MHz, respectively. Spectroscopic analysis was performed at 293 K on diluted solutions of each compound by using $CDCl_3$ as solvent. Chemical shifts (δ) are reported in ppm, while coupling constants (J) are reported in Hertz (Hz).

GC-MS analyses were performed using an Agilent GC-6890/MSD-5973 system with electronic ionization detectors and an HP-5MS capillary column (30 m x 0.25 mm, 5% diphenyl 95% dimethylpolysiloxane). The mass detector operated in electron impact ionization mode (EI/MS) with an electron energy of 70 eV. The injection port temperature was set to 250 °C. The oven temperature program started at 70 °C with a 2-minute hold, then ramped to 280 °C at a rate of 20 °C/min, and held for 10 minutes.

1.3.2 General Procedure for the synthesis of N-protected dipeptides

α-Amino acid methyl ester hydrochloride (1 mmol) is first dissolved in 3 mL of anhydrous pyridine in a 10 mL reaction vessel equipped with a magnetic stir bar. Immediately after, *N*-protected-α-amino acid (1 mmol) and $TiCl_4$ (1 mmol) are added to the solution.

The reaction mixture is stirred magnetically for 1-2 minutes while monitoring the pH, adjusting with additional pyridine to maintain near-neutral conditions if necessary. The vessel is then sealed with a PTFE cap and irradiated in the microwave reactor.

The reaction progress is monitored by TLC analysis using a chloroform-methanol (90:10, v/v) solvent system, and it completes in 20-40 minutes. Afterward, pyridine is removed by co-evaporation with toluene. The resulting crude product is suspended in chloroform and purified by column chromatography on silica gel, which also contains layers of $NaHCO_3$ and $NaHSO_4$ separated by silica gel, using chloroform as the mobile phase. Evaporation of chloroform under reduced pressure yields the corresponding *N*-protected dipeptides with yields ranging from 65% to 94%.

N-Fmoc-L-Phe-L-Ala-OMe (1a)

^{1}H NMR (300 MHz, $CDCl_3$) δ 7.78 (d, *J* = 7.5 Hz, 2H, ArH), 7.55 (t, *J* = 6.4 Hz, 2H, ArH), 7.42 (t, *J* = 7.4 Hz, 2H, ArH), 7.37 – 7.09 (m, 5H, ArH), 6.43 (s_{broad}, 1H, CONH), 5.45 (s_{broad}, 1H, OCONH), 4.66 – 4.41 (m, 3H, CH_2Fmoc, C<u>H</u>COOMe), 4.33 (m, 1H, C<u>H</u>CONH), 4.20 (t, *J* = 6.9 Hz, 1H, CHFmoc), 3.72 (s, 3H, OCH_3), 3.20-3.96 (m, 2H, C<u>H$_2$</u>Ph), 1.35 (d, *J* = 7.1 Hz, 3H, CH_3). **^{13}C-NMR** (75 MHz, $CDCl_3$) δ 172.77, 170.31, 155.89, 143.75, 141.30, 136.22, 129.39, 128.70, 127.75, 127.10, 125.03, 120.01, 67.11, 56.03, 52.48, 48.18, 47.12, 38.61, 18.31.

N-Fmoc-Gly-L-Ala-OMe (2a)

^{1}H NMR (300 MHz, $CDCl_3$) δ 7.73 (d, J = 7.5 Hz, 2H, ArH), 7.56 (d, J = 7.3 Hz, 2H, ArH), 7.47 - 7.19 (m, 4H, ArH), 6.80 (d_{broad}, J = 6.4 Hz, 1H, CONH), 5.72 (t_{broad}, J = 5.4 Hz, 1H, OCONH), 4.78 - 4.48 (m, 1H, C<u>H</u>COOCH$_3$), 4.37 (d, J = 7.0 Hz, 2H, CH_2Fmoc), 4.19 (t, J = 7.0 Hz, 1H, CHFmoc), 4.05 -3.81 (m, 2H, C<u>H$_2$</u>CONH), 3.69 (s, 3H, OCH_3), 1.37 (d, J = 7.1 Hz, 3H, C<u>H$_3$</u>CH).

^{13}C NMR (75 MHz, $CDCl_3$) δ: 173.85, 169.23, 157.23, 144.31, 141.86, 128.26, 127.64, 125.72, 120.71, 67.90, 53.06, 48.73, 47.68, 44.88, 18.82.

N-Fmoc-L-Tyr(tBu)-Gly-OMe (3a)

^{1}H NMR (300 MHz, $CDCl_3$) 7.76 (d, J = 7.4 Hz, 2H, ArH), 7.59-7.49 (m, 2H, ArH), 7.40 (t, J = 7.2 Hz, 2H, ArH), 7.32 (d, J = 7.2 Hz, 2H, ArH), 7.17-7.03 (m, 2H, ArH), 6.91 (d, J = 7.4 Hz, 2H, ArH), 6.41 (sbroad, 1H, OCONH), 5.50 (sbroad, 1H, CONH), 4.55 – 4.28 (m, 3H, CH_2Fmoc, C<u>H</u>CONH), 4.18 (t, *J* = 6.8 Hz, 1H, CHFmoc), 4.07 – 3.89 (m, 2H, C<u>H$_2$</u>COOMe), 3.71 (s, 3H, OCH_3), 3.11-2.99 (m 2H, C<u>H$_2$</u>-Tyr), 1.31 (s, 9H, $C(CH_3)_3$). **^{13}C NMR** (75 MHz, $CDCl_3$) δ: 170.75, 169.57, 154.59, 143.74, 141.31, 129.71, 127.73, 127.09, 125.02, 124.29, 119.97, 78.39, 67.09, 56.04, 52.31, 47.16, 41.17, 37.69, 28.82.

N-Fmoc-L-Leu-Gly-OMe (4a)

^{1}H NMR (300 MHz, $CDCl_3$) δ 7.76 (d, *J* = 7.5 Hz, 2H, ArH), 7.65-7.53 (m, 2H, ArH), 7.38 (d, *J* = 7.4 Hz, 2H, ArH), 7.35 – 7.27 (m, 2H, ArH), 6.89 (sbroad, 1H, CONH), 5.55 (sbroad, 1H, OCONH), 4.50-4.37 (m, 2H, CH_2Fmoc), 4.34–4.26 (m, 1H, C<u>H</u>CONH), 4.20 (t, J = 6.9 Hz, 1H, CHFmoc) 4.02 (m, 2H, C<u>H$_2$</u>$COOCH_3$), 3.71 (s, 3H, OCH_3), 1.80 – 1.46 (m, 3H, C<u>H$_2$</u>C<u>H</u>), 1.04 – 0.88 (m, 6H, $CH(C\underline{H}_3)_2$). **^{13}C NMR** (75 MHz, $CDCl_3$) δ 172.76, 170.19, 156.35, 143.79, 141.30, 127.74, 127.09, 125.07, 120.00, 67.01, 53.32, 52.38, 47.15, 41.25, 29.73, 24.65, 22.95, 21.93.

N-Fmoc-L-Leu-L-Ile-OMe (5a)

^{1}H-NMR (300 MHz, $CDCl_3$) δ 7.77 (d, J = 7.5 Hz, 2H, ArH), 7.59 (d, J = 7.5 Hz, 2H, ArH), 7.49 – 7.20 (m, 4H, ArH), 6.58 (d, J = 8.4 Hz, 1H, CONH), 5.36 (d, J = 8.4 Hz, 1H, OCONH), 4.58 (dd, J = 8.4, 5.1 Hz, 1H, C<u>H</u>COOMe), 4.50-4.35 (m, 2H, CH_2-Fmoc), 4.33-4.16 (m, 2H, CH-Fmoc, C<u>H</u>CONH), 3.73 (s, 3H, OCH_3), 1.98-1.75 (m, 2H, C<u>H</u>CH_3, C<u>H$_2$</u>$CH(CH_3)_2$), 1.74-1.59 (m, 2H, C<u>H$_2$</u>C<u>H</u>$(CH_3)_2$), 1.47 -1.33 (m, 1H, C<u>H$_2$</u>CH_3), 1.23 – 1.08 (m, 1H, C<u>H$_2$</u>CH_3), 1.07 – 0.74 (m, 12H, CHC<u>H$_3$</u>, $CH_2C\underline{H}_3$, $CH_2CH(C\underline{H}_3)_2$). **^{13}C-NMR** (75 MHz, $CDCl_3$) δ: 172.05, 171.93, 155.62, 143.80, 141.31, 127.71, 127.06, 125.02, 119.97, 67.27, 56.46, 53.62, 52.02, 47.19, 41.29, 37.86, 25.14, 24.67, 22.86, 15.40, 11.48.

N-Fmoc-L-Cys(Bzl)-L-Ala-OMe (6a)

^{1}H NMR (300 MHz, $CDCl_3$) δ 7.68 (d, 2H, J = 7.5 Hz, ArH), 7.58-7.46 (m, 2H, ArH), 7.42-7.09 (m, 9H, ArH), 6.72 (s_{broad}, 1H, CONH), 5.57 (s_{broad}, 1H, OCONH), 4.47 (m, 1H, $CHCOOCH_3$), 4.41-4.26 (m, 2H, $C\underline{H}_2$-Fmoc), 4.25-4.15 (m , 1H, CHCONH), 4.14-4.10 (m, 1H, CH-Fmoc), 3.75-3.56 (m, 5H, $SC\underline{H}_2Ph$, $OC\underline{H}_3$), 2.80 (m, 1H, $CH\underline{CH}_2S$), 2.67 (m, 1H, $CH\underline{CH}_2S$), 1.32 (d, 3H, J = 7.2 Hz, CH_3).

N-Boc-L-Phe-L-Ala-OMe (1b)

^{1}H NMR (300 MHz, $CDCl_3$) δ 7.42-7.11 (m, 5H, ArH), 6.63 (s_{broad}, 1H, CONH), 5.14 (s_{broad}, 1H, OCONH), 4.54 (m, 1H, $C\underline{H}COOMe$), 4.40 (m, 1H, $C\underline{H}CH_2Ph$), 3.72 (s, 3H, OCH_3), 3.07 (d, J = 6.2 Hz, 2H, CH_2Ph), 1.41 (s, 9H, $C(CH_3)_3$), 1.35 (d, J = 7.2 Hz, 3H, $CHC\underline{H}_3$).**^{13}C NMR** (75 MHz, $CDCl_3$) δ 173.49, 171.45, 155.98, 137.10, 129.95, 129.16, 127.50, 80.76, 56.13, 48.69, 48.59, 38.95, 28.82, 18.89. **GC-MS (EI)** m/z (% rel.): 294 (7), 263 (1), 234 (8), 131 (8), 120 (82), 91 (22), 57 (100).

N-Boc-L-Phe-D-Ala-OMe (2b)

^{1}H NMR (300 MHz, $CDCl_3$) δ 7.24 – 7.14 (m, 5H, ArH), 6.51 (d, J = 7.0 Hz, 1H, CONH), 5.22 (d, J = 8.0 Hz, 1H, OCONH), 4.45 (m, 1H, $C\underline{H}COOMe$), 4.35 (m, 1H, $C\underline{H}CH_2Ph$), 3.65 (s, 3H, OCH_3), 3.01 (d, J = 6.5 Hz, 2H, CH_2Ph), 1.34 (s, 9H, $C(CH_3)_3$), 1.19 (d, J = 6.9 Hz, 3H, $CHC\underline{H}_3$).**^{13}C NMR** (75 MHz, $CDCl_3$) δ 173.05, 170.80, 155.40, 136.68, 129.35, 128.55, 126.87, 80.07, 55.64, 52.53, 47.87, 38.77, 28.23, 17.96. **GC-MS (EI)** m/z (% rel.): 350 (3), 294 (9), 233 (15), 131 (14), 120 (100), 91 (27), 57 (67).

N-Boc-D-Phe-D-Ala-OMe (3b)

^{1}H NMR (300 MHz, $CDCl_3$) δ 7.17 (t, *J* = 9.4 Hz, 5H, ArH), 6.69 (s, 1H, CONH), 5.14 (d, *J* = 7.6 Hz, 1H, OCONH), 4.48 (t, *J* = 6.8 Hz, 1H, $C\underline{H}COOMe$), 4.36 (m, 1H, $C\underline{H}CH_2Ph$), 3.66 (s, 3H, OCH_3), 3.01 (s, 2H, CH_2Ph), 1.35 (s, 9H, $C(CH_3)_3$), 1.30 (d, *J* = 7.2 Hz, 3H, $CHC\underline{H}_3$). **^{13}C NMR** (75 MHz, $CDCl_3$) δ 172.89, 170.97, 155.41, 136.61, 129.40, 128.61, 126.88, 80.11, 55.51, 52.53, 48.10, 38.52, 28.23, 18.19. **GC-MS (EI)** m/z (% rel.): 233 (10), 131 (14), 120 (90), 91 (25), 57 (100).

N-Boc-L-Ile-L-Leu-OMe (4b)

^{1}H-NMR (300 MHz, $CDCl_3$) δ 6.35 (d, *J* = 7.6 Hz, 1H, CONH), 5.08 (d, *J* = 8.9 Hz, 1H, OCONH), 4.57 (m, 1H, C<u>H</u>COOMe), 3.89 (m, 1H, C<u>H</u>CONH), 3.68 (s, 3H, OCH_3), 1.81 (s_{broad}, 1H, C<u>H</u>CH_3), 1.66 – 1.45 (m, 4H, C<u>H</u>$_2$$CH_3$), C<u>H</u>$_2$CH), 1,38 (s, 9H, C(<u>C</u>H_3)$_3$), 1.22 – 1.08 (m, 1H, CH(CH_3)$_2$), 0.99-0.89 (m, 12H, CH(<u>C</u>H_3)$_2$, CH_2(<u>C</u>H_3)$_2$). **^{13}C NMR** (75 MHz, $CDCl_3$) δ 173.16, 171.54, 155.78, 79.86, 59.13, 52.38, 50.61, 41.37, 37.09, 28.27, 24.73, 22.80, 21.80, 15.41, 11.32. **GC-MS (EI)** m/z (% rel.): 302 (3), 285 (6), 186 (19), 172 (2), 144 (3), 130 (91), 86 (100), 57 (48).

N-Boc-L-Leu-L-Val-OMe (5b)

^{1}H NMR (300 MHz, $CDCl_3$) δ 6.57 (d_{broad}, *J* = 8.0 Hz, 1H, CONH), 4.87 (d, *J* = 8.2 Hz, 1H, OCONH), 4.51 (dd, *J* = 8.0, 4.9 Hz, 1H, C<u>H</u>COOMe), 4.09 (m, 1H, C<u>H</u>CONH), 3.70 (s, 3H, OCH_3), 2.21-2.07 (d, *J* = 4.6 Hz, 2H, C<u>H</u>$_2$CH(CH_3)$_2$, C<u>H</u>(CH_3)$_2$), 1.73-1.58 (m, 2H, C<u>H</u>$_2$C<u>H</u>(CH_3)$_2$), 1.41 (s, 9H, C(C<u>H</u>$_3$)$_3$), 0.97-0.83 (m 12H, CH(C<u>H</u>$_3$)$_2$, CH_2CH(C<u>H</u>$_3$)$_2$). **^{13}C NMR** (75 MHz, $CDCl_3$) δ 172.39, 172.19, 155.56, 80.13, 56.99, 56.91, 53.11, 40.61, 31.30, 28.29, 27.80, 24.67, 22.87, 22.09, 18.93, 17.59. **GC-MS (EI)** m/z (% rel.): 344 (1), 271 (5), 186 (15), 158 (1), 130 (100), 86 (90), 72 (14), 57 (53).

N-Boc-L-Arg(Z)$_2$-L-Ala-OMe (6b)

^{1}H NMR (300 MHz, $CDCl_3$) δ 9.56 – 9.18 (m, 2H, NHZ, NH), 7.39 – 7.23 (m, 10H, ArH), 6.91 (d, *J* = 7.0 Hz, 1H, CONH), 5.57 (d, *J* = 8.4 Hz, 1H, OCONH), 5.22 – 5.05 (m, 4H, CH_2Ph), 4.43 (m, 1H, C<u>H</u>COOMe), 4.25 (m, 1H, C<u>H</u>CONH), 4.12 – 3.75 (m, 2H, C<u>H</u>$_2$NH), 3.63 (s, 3H, OC<u>H</u>$_3$), 1.82-1.55 (m, 4H, CHC<u>H</u>$_2$C<u>H</u>$_2$$CH_2$NH), 1.39 (s, 9H, C(C<u>H</u>$_3$)$_3$), 1.16 (d, *J* = 7.2 Hz, 3H, CHC<u>H</u>$_3$). **^{13}C NMR** (75 MHz, $CDCl_3$) δ 172.90, 171.76, 163.61, 160.70, 155.85, 136.67, 134.63, 128.82, 128.47, 127.92, 127.71, 79.84, 69.00, 67.00, 53.60, 52.35, 48.02, 44.04, 28.84, 28.33, 24.59, 17.67.

N-Boc-L-Phe-L-Leu-OMe (7b)

^{1}H NMR (300 MHz, $CDCl_3$) δ 7.44 – 7.09 (m, 5H, ArH), 6.36 (d, J = 7.9 Hz, 1H, CONH), 5.08 (d, J = 8.0 Hz, 1H, OCONH), 4.57 (m, 1H, C<u>H</u>COOMe), 4.36 (m, 1H, C<u>H</u>CONH), 3.69 (s, 3H, OCH_3), 3.07 (d, J = 6.7 Hz, 2H, CHC<u>H</u>$_2$Ph), 1.66 – 1.33 (m, 12H, C<u>H</u>$_2$C<u>H</u>(CH_3)$_2$, C(C<u>H</u>$_3$)$_3$), 1.03- 0.75 (m,

6H, CH(C<u>H</u>$_3$)$_2$). **^{13}C NMR** (75 MHz, $CDCl_3$) δ 172.76, 171.08, 159.89, 136.27, 129.36, 128.59, 126.50, 82.20, 52.18, 50.73, 41.84, 37.88, 28.22, 24.66, 22.63, 21.88.

N-Z-L-Ala-L-Ala-OMe (1c)

^{1}H NMR (300 MHz, CDCl3) δ 7.40 – 7.20 (m, 5H, ArH), 6.78 (d, J = 6.2 Hz, 1H, CONH), 5.54 (d, J = 7.5 Hz, 1H, OCONH), 5.10 (s, 2H, CH_2Ph), 4.55 (m, 1H, C<u>H</u>COOMe), 4.30 (m, 1H, C<u>H</u>CH_3), 3.73 (s, 3H, OCH_3), 1.38 (d, J = 7.0 Hz, 6H, CH_3). **^{13}C NMR** (75 MHz, CDCl3) δ 173.12, 171.86, 155.88, 136.26, 128.50, 128.14, 128.01, 66.99, 52.39, 50.36, 48.07, 18.61, 18.17. **GC-MS (EI)** m/z (% rel.): 308 (2), 249 (2), 206 (3), 178 (9), 134 (16), 102 (9), 91 (100), 88 (13), 70 (6), 59 (2).

N-Z-Gly-L-Val-OMe (2c)

^{1}H NMR (300 MHz, $CDCl_3$) δ 7.42 – 7.26 (m, 5H, ArH), 6.97 (d, *J* = 8.8 Hz, 1H, CONH), 5.89 (m, 1H, OCONH), 5.12 (s, 2H, CH_2Z), 4.55 (dd, *J* = 8.8, 5.2 Hz, 1H, C<u>H</u>COOMe), 3.94 (d, *J* = 5.5 Hz, 2H, C<u>H</u>$_2$CONH), 3.71 (s, 3H, OCH_3), 2.21-2.09 (m, 1H, C<u>H</u>$(CH_3)_2$), 1.03-0.77 (m, 6H, CH(C<u>H</u>$_3$)$_2$). **^{13}C NMR** (75 MHz, $CDCl_3$) δ 172.44, 169.29, 156.73, 136.22, 128.49, 128.12, 127.99, 67.10, 57.10, 52.25, 44.41, 31.17, 18.94, 17.74. **GC-MS (EI)** m/z (% rel.): 322 (7), 290 (3), 263 (12), 215 (6), 192 (2), 130 (10), 91 (100).

N-Z-L-Val-L-Phe-OMe (3c)

^{1}H NMR (300 MHz, $CDCl_3$) δ 7.51-7.00 (m, 10H, ArH), 6.58 (d, *J* = 7.6 Hz, 1H, CONH), 5.47 (d, *J*=8.8 Hz, 1H, OCONH), 5.16-4.96 (m, 2H, CH_2Z), 4.94-4.82 (m,1H, C<u>H</u>COOMe), 4.11-3.98 (m, 1H, C<u>H</u>$CH(CH_3)_2$), 3.67 (s, 3H, OCH_3), 3.15-2.99 (m, 2H, CH_2Ph), 2.02 (m, 1H, C<u>H</u>$(CH_3)_2$), 0.97-0.73 (m, 6H, CH(C<u>H</u>$_3$)$_2$). **GC-MS (EI)** m/z (% rel.): 412 (1), 321 (3), 234 (2), 206 (15), 162 (43), 91 (100).

1.4 Conclusions

This study demonstrates an efficient solution-phase synthesis of dipeptides using titanium tetrachloride ($TiCl_4$) as a coupling agent with microwave irradiation, providing the necessary energy for the process. $TiCl_4$ effectively activates the carboxyl group, promoting its reaction with the amino group of the coupling amino acid.

The reaction conditions proved highly compatible with various protecting groups, including Fmoc, Z, and Boc, which are removable under different conditions. This highlights the method's versatility and robustness in managing the reactive functionalities of diverse amino acids.

Throughout the synthesis, the stereochemistry of the starting materials was preserved, with no significant racemization detected by NMR analysis.

The introduction of a microwave reactor marked a significant advancement in the process. Microwave irradiation drastically reduced reaction times, enabling much faster synthesis compared to conventional heating methods.

Additionally, this approach allowed for a lower molar ratio of $TiCl_4$ to the N-protected amino acid, enhancing the overall efficiency and reducing energy consumption.

This method shows promise for broader applications, particularly in the synthesis of bioactive molecules, offering a more efficient and sustainable pathway for peptide synthesis.

1.5 References

1. Greenberg, A., Breneman, C.M., Liebman, J.F. *The Amide Linkage: Structural Significance, Chemistry, Biochemistry and Material Science*, Wiley, New York, NY, USA, 2000; Kaspar, A.A.
2. Reichert, J.M. Future directions for peptide therapeutics development. *Drug Discov. Today* **2013**, *18*, 807-17.
3. Thorner, J., Emr, S.D., Abelson, J.N. Applications of chimeric genes and hybrid proteins part A: Gene expression and protein purification. In *Methods Enzymol*ogy, 1st ed.; Academic Press, Cambridge, Massachusetts, USA, 2000; 326, pp 601–617.
4. Forbes, J.; Krishnamurthy, K. Biochemistry, Peptide. In StatPearls; StatPearls Publishing: Treasure Island, FL, USA, 2023. Available online: https://www.ncbi.nlm.nih.gov/books/NBK562260).
5. Rossino, G.; Marchese, E.; Galli, G.; Verde, F.; Finizio, M. et al. Peptides as Therapeutic Agents: Challenges and Opportunities in the Green Transition Era. Molecules **2023**, *28*, 7165.
6. Wang, L., Wang, N., Zhang,W., Cheng, X., Yan, Z., Shao, G.;Wang, X., Wang, R., Fu, C. Therapeutic peptides: Current applications and future directions. *Signal Transduct. Target. Ther.* **2022**, *7*, 48.
7. Nicolás-Morales, M.L., Luisa-Sanjuan, A., Gutiérrez-Torres, M., Vences-Velázquez, A., Ortuno-Pineda, C., Espinoza-Rojo, M. et al. Peptide-Based Vaccines in Clinical Phases and New Potential Therapeutic Targets as a New Approach for Breast Cancer: A Review. *Vaccines* **2022**, *10*, 1249.
8. Vadevoo, S.M.P., Gurung, S., Lee, H.S., Gunassekaran, G.R., Lee, S.M., Yoon, J.W. et al. Peptides as multifunctional players in cancer therapy. *Exp. Mol. Med.* **2023**, *55*, 1099–1109.
9. Pressley, H.; Cornelio, C.K.; Adams, E.N. Setmelanotide: A Novel Targeted Treatment for Monogenic Obesity. *J. Pharm. Technol*. **2022**, 38, 368‑373.
10. Keam, S.J. Trofinetide: First Approval. *Drugs* **2023**, *83*, 819‑824.
11. Van Gelder, T., Lerma, E., Engelke, K., Huizinga, R.B. Voclosporin: A novel calcineurin inhibitor for the treatment of lupus nephritis. *Expert. Rev. Clin. Pharmacol.* **2022**, *15*, 515‑529.
12. Keam, S.J. Lutetium Lu 177 Vipivotide Tetraxetan: First Approval. *Mol. Diagn. Ther*. **2022**, *26*, 467‑475.
13. Sharma, K., Sharma, K.K., Sharma, A., Jain, R. Peptide-based drug discovery: Current status and recent advances. *Drug Discov. Today* **2023**, *28*, 103464.
14. Acosta-Guzmán, P., Ojeda-Porras, A., Gamba-Sánchez, D. Contemporary approaches for amide bond formation. *Adv. Synth. Catal*. **2023**, *365*, 4359.
15. de Figueiredo, R.M., Suppo, J.S., Campagne, J.M. Nonclassical Routes for Amide Bond Formation. *Chem. Rev*. **2016**,*116*, 12029‑12122.
16. De Marco, R., Spinella, M., De Lorenzo, A., Leggio, A., Liguori, A. C→NandN→C solution phase peptide synthesis using the N-acyl 4-nitrobenzenesulfonamide as protection of the carboxylic function. *Org. Biomol. Chem*. **2013**, *11*, 3786‑3796.

17. Leggio, A., Belsito, E.L., De Luca, G., Di Gioia, M.L., Leotta, V., Romio, E., Siciliano, C., Liguori, A. One-pot synthesis of amides from carboxylic acids activated using thionyl chloride. RSC Adv. **2016**, *6*, 34468‑34475.
18. Leggio, A., Comandè, A., Belsito, E.L., Greco, M., Lo Feudo, L., Liguori, A. Alternative formation of amides and β-enaminones from aroyl chlorides using the $TiCl_4$-trialkylamine reagent system. *Org. Biomol. Chem*. **2018**, *16*, 5677‑5683.
19. Li, G., Szostak, M. Non-Classical Amide Bond Formation: Transamidation and Amidation of Activated Amides and Esters by Selective N‑C/O‑C Cleavage. *Synthesis* **2020**, *52*, 2579‑2599.
20. Mijalis, A.J., Thomas, D.A., 3rd, Simon, M.D., Adamo, A., Beaumont, R. et al.A fully automated flow-based approach for accelerated peptide synthesis. *Nat. Chem. Biol*. **2017**, *13*, 464‑466.
21. Naoum, J.N., Alshanski, I., Mayer, G., Strauss, P., Hurevich, M. Stirring Peptide Synthesis to a New Level of Efficiency. *Org. Process Res. Dev*. **2022**, *26*, 129‑136.
22. Sanchez-Sancho, F., Mann, E., Herradon, B. Efficient syntheses of polyannular heterocycles featuring microwave-accelerated Bischler-Napieralski reaction, stereoselective Heck cyclization, and Claisen rearrangement. *Synlett* **2000**, *2000*, 509‑513.
23. El-Faham, A., Albericio, F. Peptide Coupling Reagents, More than a Letter Soup. *Chem. Rev.* **2011**, *111*, 6557‑6602.
24. Di Gioia, M.L., Leggio, A., Liguori, A., Perri, F., Siciliano, C., Viscomi, M.C. A preparation of N-Fmoc-N-methyl-α-amino acids and N-nosyl-N-methyl-α-amino acids. *Amino Acids* **2010**, *38*, 133‑143.
25. Chu, W., Tu, Z., McElveen, E., Xu, J., Taylor, M. et al. Synthesis and in vitro binding of N-phenyl piperazine analogs as potential dopamine D3 receptor ligands. Bioorg. *Med. Chem*. **2005**, *13*, 77‑87.
26. Gacesa, R., Tripodi, A.A.P., Cilibrizzi, A., Leggio, A., Hider, R., Abbate, V. Solid-Phase Synthesis and In-Silico Analysis of Iron-Binding Catecholato Chelators. *Int. J. Mol. Sci*. **2020**, *21*, 7498.
27. Graham, J.C., Trejo-Martin, A., Chilton, M.L., Kostal, J., Bercu, J. et al. An Evaluation of the Occupational Health Hazards of Peptide Couplers. *Chem. Res. Toxicol*. **2022**, *35*, 1011‑1022.
28. Peng, L., Xu, J.-C. 1-Ethyl 2-halopyridinium salts, highly efficient coupling reagents for hindered peptide synthesis both in solution and the solid-phase. *Tetrahedron* **2000**, *56*, 8119‑8131.
29. Isidro-Llobet, A., Kenworthy, M.N., Mukherjee, S., Kopach, M.E., Wegner, K. et al. Sustainability Challenges in Peptide Synthesis and Purification: From R&D to Production. *J. Org. Chem*. **2019**, *84*, 4615‑4628.
30. Prabhu, G., Narendra, N., Vishwanatha, T.M., Sureshbabu, V.V. Amino acid chlorides: A journey from instability and racemization toward broader utility in organic synthesis including peptides and their mimetics. *Tetrahedron* **2015**, *71*, 2785‑2832.
31. Lundberg, H., Tinnis, F., Selander, N., Adolfsson, H. Catalytic amide formation from non-activated carboxylic acids and amines. *Chem. Soc. Rev*. **2014**, *43*, 2714‑2742.

32. Lundberg, H., Tinnis, F., Adolfsson, H. Direct amide coupling of non-activated carboxylic acids and amines catalysed by zirconium(IV) chloride. *Chemistry* **2012**, *18*, 3822‑3826.
33. Muramatsu,W., Hattori, T., Yamamoto, H. Amide bond formation: Beyond the dilemma between activation and racemisation. *Chem. Commun*. **2021**, *57*, 6346‑6359.
34. Muramatsu, W., Hattori, T., Yamamoto, H.J. Substrate-directed lewis-acid catalysis for peptide synthesis. *J. Am. Chem. Soc*. **2019**, *141*, 12288‑12295.
35. Lundberg, H., Tinnis, F., Adolfsson, H. Titanium (IV) Isopropoxide as an Efficient Catalyst for Direct Amidation of Nonactivated Carboxylic Acids. *Synlett* **2012**, *23*, 2201‑2204.
36. Todorovic, M., Perrin, D.M. Recent developments in catalytic amide bond formation. *Pept. Sci.* **2020**, *112*, e24210.
37. Nordahl, A., Carlson, R. Carboxamides from Carboxylic Acids by Lewis Acid Catalysis. Use of Principal Properties for Exploring Different Reaction Conditions. *Acta Chem. Scand., Ser. B* **1988**, *42*, 28‑34.
38. Shteinberg, L.Y., Kondratov, S.A., Shein, S.M. Metal-complex catalysis under aniline acylation by substituted benzoic acids. *J. Org. Khim*. **1988**, *24*, 1968‑1972.
39. Di Gioia, M.L., Leggio, A., Guarino, I.F., Leotta, V., Romio, E., Liguori, A. A simple synthesis of anilines by LiAlH4/TiCl4 reduction of aromatic nitro compounds. *Tetrahedron Lett.* **2015**, *56*, 5341‑5344.
40. Cavallaro, P.A., De Santo, M., Greco, M., Marinaro, R., Belsito, E.L., Liguori, A., Leggio, A. Titanium Tetrachloride-Assisted Direct Esterification of Carboxylic Acids. *Molecules* **2024**, *29*, 777.
41. Leggio, A., Bagalà, J., Belsito, E.L., Comandè, A., Greco, M., Liguori, A. Formation of amides: One-pot condensation of carboxylic acids and amines mediated by TiCl4. *Chem. Cent. J.* **2017**, *11*, 87.
42. Comandè, A., Greco, M., Belsito, E.L., Liguori, A., Leggio, A. A titanium tetrachloride-based effective methodology for the synthesis of dipeptides. *RSC Adv*. **2019**, *9*, 22137‑22142.
43. De la Hoz, A., D.az-Ortiz, A., Moreno, A. Microwaves in organic synthesis. Thermal and non-thermal microwave effects. *Chem. Soc. Rev*. **2005**, *34*, 164‑178.
44. Kappe, C.O. Controlled microwave heating in modern organic synthesis. Angew. *Chem. Int. Ed. Engl.* **2004**, *43*, 6250‑6284.
45. Adam, D. Out of the kitchen. *Nature* **2003**, *421*, 571‑572; Collins, J.M., Leadbeater, N.E. Microwave energy: A versatile tool for the biosciences. *Org. Biomol. Chem*. **2007**, *5*, 1141‑1150.
46. Herrero, M.A., Kremsner, J.M., Kappe, C.O. Nonthermal Microwave Effects Revisited: On the Importance of Internal Temperature Monitoring and Agitation in Microwave Chemistry. *J. Org. Chem.* **2008**, *73*, 36‑47;
47. Loupy, *A. Microwaves in Organic Synthesis, 3rd ed*.;Wiley: Weinheim, Germany, 2012.
48. Mahindra, A., Sharma, K.K., Jain, R. Rapid microwave-assisted solution-phase peptide synthesis. *Tetrahedron Lett.* **2012**, *53*, 6931‑6935.
49. Mahindra, A., Nooney, K., Uraon, S., Sharma, K.K., Jain, R. Microwave-assisted solution phase peptide synthesis in neat water. *RSC Adv*. **2013**, *3*, 16810‑16816.

50. Priecel, P., Lopez-Sanchez, J.A. Advantages and Limitations of Microwave Reactors: From Chemical Synthesis to the Catalytic Valorization of Biobased Chemicals. *ACS Sustain. Chem. Eng.* **2019**, *7*, 3‑21).

Chapter 2

Design and synthesis of a novel cyclic somatostatin analogue peptide as a potential anticancer agent

[Ongoing work]

Abstract

Somatostatin (SST) is a peptide hormone that regulates numerous physiological processes by binding to specific receptors with high affinity and selectivity. It inhibits both hormone secretion and cell proliferation, making it useful in diagnosing and treating neuroendocrine tumors.

However, the native form of SST has a short half-life, which limits its therapeutic applications and has led to the development of more stable analogs with improved pharmacokinetic properties. These analogs, typically small cyclic peptides, include SST's active sequence (Phe-Trp-Lys-Thr), essential for receptor binding and biological activity. SST analogs have demonstrated antitumor effects in experimental models, along with favorable safety and tolerability, making them promising candidates for cancer therapy.

A new SST analog targeting the SST-2 receptor was designed and synthesized. This analog, a cyclic pentapeptide, incorporates the biologically active SST sequence along with a glutamic acid residue. It was successfully synthesized in high yields using microwave-assisted solid-phase peptide synthesis (SPPS) combined with Fmoc-based chemistry. Preliminary *in vitro* experiments revealed that the synthesized analog exhibited antiproliferative activity against various breast cancer cell lines.

2.1 Introduction

Peptides, consisting of short chains of 2 to 50 amino acids connected by amide bonds play a crucial role in nearly all fundamental cellular processes [1]. Peptides perform a diverse range of functions, including serving as structural elements, enzymatic inhibitors, cell-penetrating agents, hormones, host defense molecules, and neurotransmitters Furthermore, they function as cell surface receptors and are key components in drug delivery systems [2].

Their use in the pharmacological field offers several key advantages over traditional small-molecule drugs, such as high efficacy, selectivity, affinity and safety, good biocompatibility, along with reduced toxicity and immunogenicity and minimal tissue accumulation [3].

Therapeutic peptides represent a promising class of pharmaceutical agents, with a structural profile intermediate between small molecules and proteins, yet biochemically and therapeutically distinct from both [4,5]. The wide variety of possible amino acid combinations imparts peptides with remarkable flexibility, enabling them to serve numerous important roles in both biological processes and biomedical applications. They function as bioactive molecules that specifically recognize and bind to particular targets, making them valuable for therapeutic purposes or as biomarkers for detecting pathogens. Additionally, peptides can serve as excipients in advanced diagnostic biosensors and as carriers for targeted drug delivery, highlighting their broad potential in both diagnostics and therapeutics.

The clinical use of peptides as therapeutic agents began with the discovery of insulin in 1921, a hormone made up of 51 amino acids. Two years later, it was developed into the first commercially available peptide drug, offering diabetic patients a way to achieve tight glycemic control [6].

The field of biopharmaceuticals has achieved remarkable advancements in recent years. The global therapeutic peptide market reached a value of US$42.05 billion in 2022. This growth is largely driven by the increasing incidence of chronic conditions such as diabetes, obesity, and cancer, which has

heightened the need for more effective and personalized treatment options. Peptide drug discovery and development are projected to grow significantly in the coming years, with the market expected to reach $68.6 billion by 2030 [7-10]. Recent data report that approximately 400 peptide drugs are currently being evaluated in clinical trials with over 60 already approved worldwide [7, 11].

However, despite these achievements, peptide drugs face several challenges that limit their therapeutic potential. Key issues include physicochemical barriers such as a tendency to aggregate and poor water solubility [12]. Additionally, pharmacokinetic issues pose significant hurdles, including low permeability across cell membranes, metabolic instability, limited oral bioavailability, rapid renal clearance, and susceptibility to enzymatic degradation in plasma [13-15]. The short half-life of peptides is a major concern, as they are often cleared from the bloodstream within minutes to hours. This is primarily due to fast renal clearance and enzymatic degradation in blood, kidneys and liver, which substantially reduces their exposure time at target tissues [16, 17]. Enzymatic degradation is caused by both soluble enzymes in plasma and membrane-bound peptidases, as well as a diverse array of other proteolytic enzymes [18].

Addressing these limitations is crucial for maximizing the clinical potential of peptide-based therapies. One key approach to extending peptide half-life involves substituting natural amino acids with non-natural analogs. These substitutions reduce the recognition and binding affinity of proteolytic enzymes, thereby enhancing stability.

Over the years, numerous strategies have been devised to enhance their pharmacokinetic properties, with many relying on chemical modifications. An important strategy, to extending peptide half-life consists in replacing natural amino acids with non-natural analogues such as *N*-methylated amino acids, D-amino acids, or β-amino acids, particularly at sites susceptible to enzymatic cleavage [19]. These modifications reduce the ability of proteolytic enzymes to recognize and bind to the peptides, thereby enhancing their stability.

A particularly effective method for increasing peptide stability is the synthesis of cyclic peptides. These peptides are resistant to exonucleases due to the lack of free N-terminal and C-terminal ends. Additionally, their cyclic structure and defined conformation often exhibit a more favorable Gibbs free energy for binding to biological targets, improving binding efficiency [20]. Cyclization also promotes the formation of bioactive peptide conformations, which influence the exposure of polar atoms to solvation by water, potentially enhancing oral bioavailability [21].

Cyclic peptides offer several pharmacokinetic advantages over their linear counterparts, making them valuable candidates for drug development. They exhibit enhanced metabolic stability, increased hydrophobicity, and greater conformational rigidity. These properties contribute to improved bioavailability and prolonged activity in the body. The rigidity of cyclic peptides also makes them less prone to enzymatic degradation [22].

Moreover, cyclic peptides can bind to target molecules with higher affinity and specificity. They are particularly effective in modulating protein–protein interactions, which are typically challenging to target with conventional drugs. The high binding specificity allows cyclic peptides to precisely affect specific biological processes while minimizing interactions with other biomolecules, thus reducing the risk of adverse effects [23].

Cyclic peptides are typically formed through lactamization, lactonization, thiolactonization, or the creation of disulfide bridges between two reactive groups. Depending on the location of these reactive groups, cyclization can occur in different forms: head-to-tail, head-to-side chain, side chain-to-tail, or side chain-to-side chain [24].

Cyclization can be performed either in solution after cleavage from the resin or directly on-resin prior to cleavage. On-resin cyclization is a highly effective and straightforward method for converting linear peptides into cyclic forms. Compared to solution-phase cyclization, resin-based cyclization offers several advantages: (a) coupling reagents can be easily separated from the resin-bound peptide

through simple filtration, and (b) an excess of coupling reagents can be employed to accelerate ring closure and reduce the risk of epimerization.

Recent studies have highlighted the promising potential of peptides in cancer therapy. Despite significant advancements in cancer treatment and detection, cancer management remains a major challenge. Conventional chemotherapies are often administered systemically, but over time, they are often discontinued due to severe side effects, such as systemic toxicity or the development of drug resistance, with few alternative options available [25, 26].

Peptides offer a versatile approach to cancer therapy. They can be employed to deliver treatments directly to cancer cells, mimic natural proteins to modulate signaling pathways, or facilitate the transport of therapeutics across biological barriers [27-29]. In recent years, researchers have made substantial progress in designing anticancer peptides that effectively target key mechanisms driving uncontrolled tumor cell proliferation. These mechanisms include the regulation of apoptosis, cell cycle progression, angiogenesis, and autophagy [30-32].

Peptides show remarkable potential in addressing critical challenges in cancer therapy, including those posed by the complexities of tumor microenvironment. Addressing these challenges requires advanced delivery technologies capable of targeting tumors with high precision. In this context, targeted drug delivery systems (DDSs) have emerged as a powerful tool to improve cellular uptake, minimize off-target effects, and enhance clinical outcomes compared to non-targeted approaches [33].

Various tumor-targeting agents, including polypeptides, monoclonal antibodies, antibody fragments, small molecules have been developed to enhance treatment precision and effectiveness [34]. Targeting peptides, in particular, are employed in cancer therapeutics for their ability to selectively bind receptors that are highly expressed on cancer cells or within tumors tissue, while exhibiting minimal interaction with healthy cells. This specificity makes them ideal candidates for enhancing the precision of drug delivery [35].

Targeting peptides can be conjugated to nanoparticles loaded with therapeutic agents or directly attached to the drug molecule using specialized linkers [36, 37]. Among these, cleavable linkers are particularly advantageous as they enable the controlled release of the drug precisely at the target site, reducing systemic toxicity [36].

In modern medicine, the application of therapeutic and targeting peptides in cancer treatment is advancing the development of more effective, safer, and personalized therapeutic options. Among the many examples of therapeutic peptides, somatostatin stands out as a relevant and concrete example of the potential therapeutic value of peptides, particularly in modulating specific biological mechanisms related to tumor proliferation. As a naturally occurring hypothalamic hormone, somatostatin regulates the synthesis and secretion of several hormones, including growth hormone, glucagon, insulin, gastrin, and secretin, and is also involved in neuronal transmission. Importantly, somatostatin exhibits antiproliferative effects on tumor cells, making it not only a potential therapeutic agent but also a valuable model for developing peptide-based treatments in oncology. Its diverse biological activities are mediated through its binding to specific receptors, overexpressed in a wide range of human tumors. This overexpression has made somatostatin receptors attractive targets for therapeutic peptides, enabling the development of targeted therapies with greater precision.

Numerous studies have shown that somatostatin exhibits potent antitumor and antisecretory effects, both *in vitro* and *in vivo*, paving the way for the development of somatostatin analogues that could serve as a promising new class of antitumor drugs [38-43].

2.1.1 Structure and function of Somatostatin and its receptors

Somatostatin is a regulatory neuropeptide, first described in 1973 as a hypothalamic hormone that inhibits the release of growth hormone from the anterior pituitary. It exists in two biologically active forms, both derived from the C-terminal portion of a single pro-peptide: somatostatin 14 (SST-14), initially found in the hypothalamus and somatostatin 28 (SST-28), discovered later in the stomach. Both somatostatin isoforms share a cyclic structure of 12 amino acids, stabilized by a disulfide bridge between two cysteine residues. This cyclic structure, along with the specific sequence of four central amino acids (*Phe-Trp-Lys-Thr*), is responsible for its biological and pharmacological activity [44].

Somatostatin is predominantly produced by neurons and secretory cells in both the central and peripheral nervous systems and the gastrointestinal tract, although it is also expressed in other tissues [45]. Within the human nervous system, somatostatin is especially abundant in the deeper layers of the cortex, the limbic system, the striatum, and the hypothalamus. Its release from neurons and secretory cells is stimulated by factors such as membrane depolarization, increased cytosolic calcium levels, and secretagogue hormones, ions, growth factors, and nutrients [46].

As a key inhibitory neuropeptide, somatostatin regulates various physiological processes across multiple organs. These include the central nervous system, hypothalamus, pituitary gland, gastrointestinal tract, and both exocrine and endocrine pancreas. Its primary physiological role is the inhibition of growth hormone (GH) and thyroid-stimulating hormone (TSH) secretion. Additionally, somatostatin exerts inhibitory effects on various physiological functions, such as gastrointestinal motility, gastric acid production, pancreatic enzyme secretion, and bile secretion. It also inhibits the release of hormones like insulin, secretin, and vasoactive intestinal polypeptide (VIP) [47].

Somatostatin's extensive inhibitory effects also include antiproliferative properties, which are essential in controlling tumor growth. Because of its ability to regulate a wide range of physiological processes, somatostatin is utilized in the diagnosis and treatment of tumors, especially those associated with endocrine and neuroendocrine disorders.

In mammals, somatostatin is encoded by a single gene and synthesized as part of a larger precursor, preprosomatostatin. This precursor is 116 amino acids long and includes a 24-residue signal peptide at its N-terminal end. Preprosomatostatin is quickly processed into a shorter peptide, prosomatostatin, which consists of 92 amino acids.

The prohormone undergoes enzymatic cleavage at both its N-terminal and C-terminal ends to produce two biologically active forms of somatostatin: somatostatin-14 and somatostatin-28 [48]. The precursor protein has specific proteolytic cleavage sites where it is cut to generate these forms: a dibasic site (Arg-Lys) and a monobasic site (Arg) at the C-terminal end, producing somatostatin-14 (Figure 2.1) and somatostatin-28, respectively. Additionally, a monobasic site (Lys) at the N-terminal end gives rise to prosomatostatin [49].

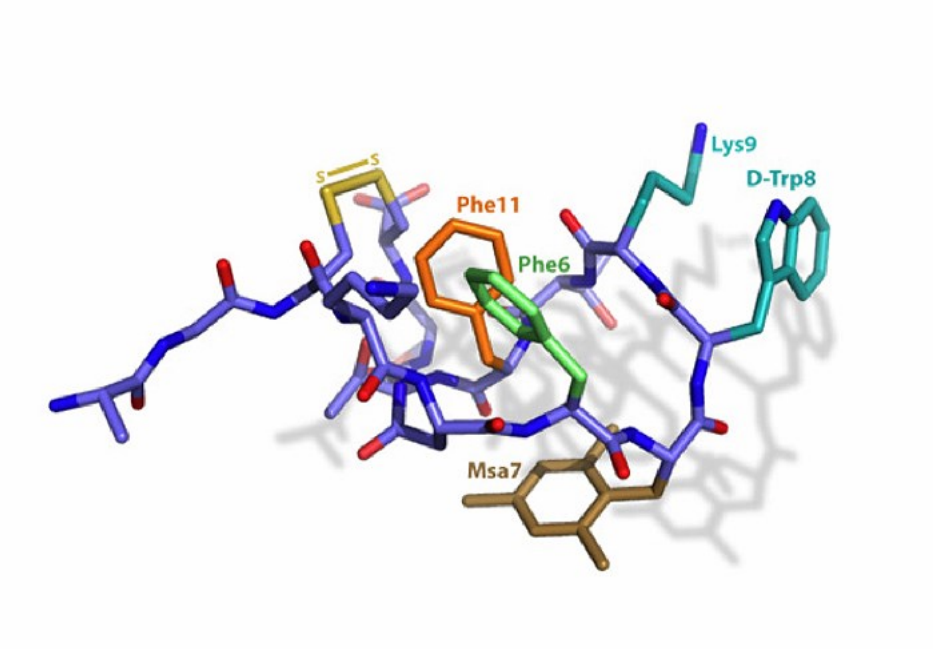

Figure 2.1. The three-dimensional structure of somatostatin-14

Somatostatin-28 is a 28-amino acid peptide that contains the full structure of somatostatin-14 at its C-terminal end. SST-14, a smaller peptide of 14 amino acids, features a disulfide bond between the third and fourteenth residues, stabilizing its structure.

The biologically active core, essential for its function, is located in residues 7 to 10 (Phe-Trp-Lys-Thr). The different molecular forms of somatostatin are not evenly distributed across tissues. SST-14 predominates in nervous tissue and is the only form present in the retina, peripheral nervous system, pancreas, and stomach neurons. In contrast, SST-28 is found at high concentrations in the brain, intestine, pancreas, and stomach [50].

Somatostatin exerts its biological effects in mammals through five high-affinity membrane receptors, SSTR-1, SSTR-2 (A and B), SSTR-3, SSTR-4, SSTR-5, that were first identified and cloned in the early 1990s [51]. These receptor subtypes are expressed widely throughout the human body, including the central nervous system, gastrointestinal tract, pancreas, kidneys, and other organs. In addition to being found in parenchymal cells, SSTR subtypes are also present in stromal cells, such as lymphocytes, fibroblasts, and endothelial cells [52].

Both somatostatin-28 and somatostatin-14 exhibit nearly equivalent affinities for all somatostatin receptor subtypes. However, somatostatin-28 shows a slightly higher affinity for the SSTR-5 receptor [53]. The receptors themselves are single glycoproteins, each containing an extracellular N-terminal domain, seven transmembrane hydrophobic segments, three extracellular loops, and an intracellular C-terminal domain [54]. These domains serve distinct functions, enabling the receptors to interact with various molecules both on the cell surface and within the cell. The localization and expression patterns of somatostatin receptors are important for understanding their role in different tissues and organs.

Research has revealed that the expression of individual SSTR subtypes varies across tissues and is influenced by both physiological and pathological conditions [55-57].

Moreover, certain receptor subtypes are associated with specific physiological functions.

For instance, SSTR2 and SSTR5 play key roles in regulating GH release, while SSTR5 is also important for controlling insulin and glucagon secretion.

SSTR1 has been implicated in angiogenesis, while the role of SSTR4 remains largely unknown. Notably, several somatostatin receptors are involved in mediating the antiproliferative effects associated with the tumor suppressor protein p53 [58]. Specifically, SSTR1, SSTR2, SSTR4, and SSTR5 contribute to these effects, while SSTR3 induces apoptosis through the activation of transcription factors that regulate the cell cycle and pro-apoptotic proteins [59]. All five receptor subtypes bind to the natural ligand somatostatin-14 with similar affinity, whereas different analogs exhibit varying affinities for each receptor. Among these subtypes, SSTR2 shows the highest affinity for somatostatin analogs and is especially effective in inducing antiproliferative effects [60].

2.1.2 Somatostatin analogues

Somatostatin's broad physiological actions make it an important tool in the diagnosis and treatment of tumors. However, its clinical use is limited by its very short plasma half-life of less than 3 minutes.

Somatostatin-14, the shorter isoform, has a plasma half-life of only 2–3 minutes, while SST-28 shows slightly greater resistance to degradation by plasma peptidases. This short half-life, coupled with its poor selectivity due to interactions with multiple organs and diverse physiological roles, has prompted the development of synthetic analogues.

These somatostatin analogues are designed to maintain the biological activity of the natural peptide while improving selectivity and pharmacokinetic properties. They have demonstrated significant antineoplastic activity in both *in vitro* and *in vivo* tumor models [61].

The antitumor effects of somatostatin and its analogues are primarily attributed to their ability to suppress the synthesis and secretion of growth factors and hormones that promote cell proliferation. Additionally, these analogues may inhibit tumor growth by inducing apoptosis [62].

Most somatostatin analogs retain the critical Phe-Trp-Lys-Thr sequence essential for receptor activation, while lacking the primary enzymatic cleavage site found in the natural peptide, which

increases their stability. These synthetic agonists not only enhance our understanding of somatostatin's structure and physiological roles but also offer significant therapeutic potential for clinical use.

Recent studies increasingly support the role of somatostatin analogues as antineoplastic agents, capable of inhibiting both tumor growth and angiogenesis [63, 64].

The first synthetic somatostatin analog approved by the FDA was octreotide (SMS 201-995), marketed as Sandostatin. Octreotide, a cyclic octapeptide, exhibits high affinity for somatostatin receptor subtype 2. By binding to SSTR2, it inhibits cellular proliferation through the activation of the tyrosine phosphatase pathway [65].

Beyond its antiproliferative effects, octreotide has demonstrated potent cytostatic activity against various malignancies, including breast cancer, primarily by inducing apoptosis in tumor cells [66, 67].

This peptide is widely used in clinical settings for the treatment of acromegaly and for managing conditions associated with neuroendocrine tumors (NETs), such as carcinoid syndrome and gastroenteropancreatic NETs (GEP-NETs) [68].

Lanreotide, another important somatostatin analog, is commonly used in the treatment of acromegaly and certain NETs. It is a synthetic cyclic peptide consisting of eight amino acids. Its structural stability and biological activity are enhanced by a disulfide bond between two cysteine residues [68]. Lanreotide primarily acts through somatostatin receptors SSTR2 and SSTR5. By binding to these receptors, it inhibits the release of GH from the pituitary, providing therapeutic benefits in conditions such as acromegaly [69]. In tumors, lanreotide activates SSTRs, leading to cell cycle arrest and apoptosis. Additionally, it reduces the production of factors that promote tumor growth and angiogenesis. Together, these effects contribute to Lanreotide' s antiproliferative activity, slowing tumor progression and alleviating associated symptoms [70].

Pasireotide, a synthetic cyclic hexapeptide, is a newer somatostatin analog with a distinct receptor binding profile compared to octreotide and lanreotide. It binds with high affinity to SSTR1, SSTR2, SSTR3, and SSTR5, in contrast to the primarily SSTR2-targeted action of first-generation analogs. Pasireotide' s strong binding to SSTR5 allows for effective inhibition of hormones like insulin and glucagon, though this may lead to elevated blood glucose levels in some patients [71]. Pasireotide is particularly indicated for the treatment of Cushing's disease, especially in patients who are not candidates for pituitary surgery [72].

Figure 2.2 illustrates the chemical structures of the three main somatostatin analogs.

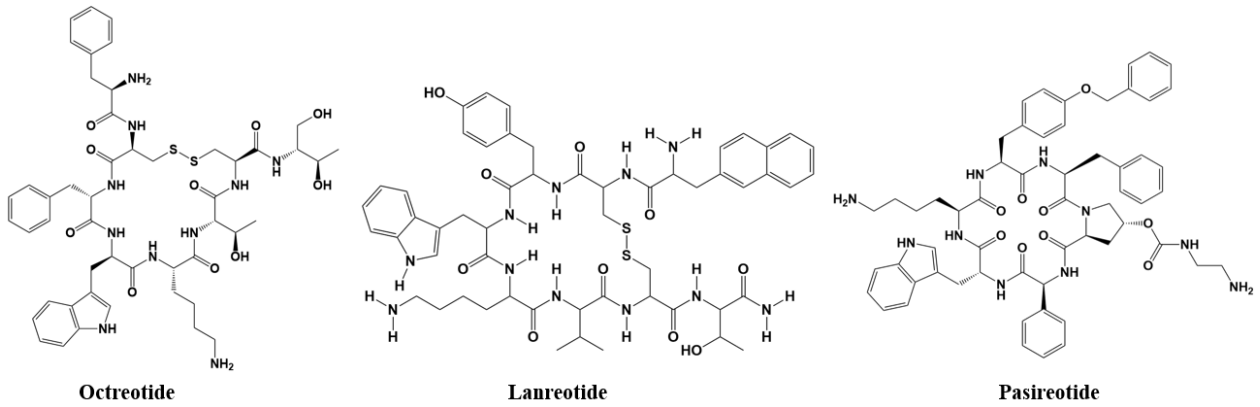

Figure 2.2. Chemical structures of Octreotide, Lanreotide and Pasireotide

2.1.3 Somatostatin receptors and breast cancer

Breast cancer is the leading cause of cancer-related mortality among women aged 40–50 worldwide and is recognized as one of the most complex and frequently diagnosed malignancies in women [73].

Research has demonstrated that somatostatin and its receptors (SSTRs) are expressed in breast cancer cells and tissues, with evidence pointing to their antiproliferative roles across various tumor types, including breast tumors [74].

The biological actions of somatostatin on breast cancer cells are believed to occur through both direct and indirect mechanisms.

Direct actions involve the binding of SST or its analogs to specific SSTR subtypes, leading to the inhibition of cell proliferation and/or the induction of apoptosis. Indirect effects may result from the suppression of growth factors such as insulin-like growth factor-1 (IGF-1), whose expression is often upregulated during tumor development (Figure 2.3) [75, 76].

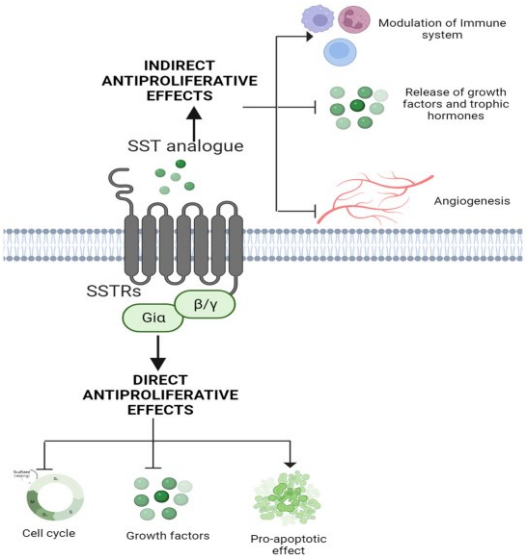

Figure 2.3. Schematic representation illustrating the direct and indirect effects of somatostatin or its analogues in inhibiting cell proliferation (created using BioRender.com)

Studies examining the expression patterns of SSTR subtypes in breast carcinoma have identified SSTR2 as the most commonly expressed subtype in breast tumor samples [77]. Furthermore, research using human breast cancer cell lines, including MCF-7 and T47D, has demonstrated that somatostatin analogs can effectively suppress tumor growth in both *in vivo* and *in vitro* models [78-81].

The therapeutic potential of somatostatin in breast cancer is significant, with its analogs representing a promising class of antitumor agents.

2.2 Results and Discussion

The somatostatin peptide consists of a sequence of 14 amino acids with a disulfide bond linking cysteine at position 3 (Cys^3) to cysteine at position 14 (Cys14). The presence of the sequence 7-10 (Phe^7, Trp^8, Lys^9, and Thr^{10}) in the structure of somatostatin is considered essential for its biological activity. Specifically, the Trp^8-Lys^9 (W-K motif) is essential for the recognition and activation of SSTRs. This motif interacts with the lower part of the SSTR binding pocket, and cleavage of this region by endopeptidases results in inactive fragments.

For this reason, efforts have been made to protect this position through specific chemical modifications, aiming to develop somatostatin analogs with improved bioavailability [82, 83].

Cyclic somatostatin analogs, such as Octreotide, have shown promising antineoplastic activity in various experimental tumor models, both *in vitro* and *in vivo*, along with good tolerability and safety profiles [84].

Building on these findings and the growing interest in the development of somatostatin analogs with antitumor properties, we designed and synthesized a novel somatostatin analog c(-FWKTE-) based on the knowledge gained from structure-activity relationships and detailed conformational studies of somatostatin agonists [85, 86].

The developed somatostatin analogue c(-FWKTE-) is a cyclic pentapeptide that incorporates the biologically active 7-10 sequence of somatostatin (Phe^7, Trp^8, Lys^9, and Thr^{10}), which is crucial for receptor binding, along with glutamic acid as the C-terminal residue. The inclusion of glutamic acid serves two purposes: it introduces a carboxyl group to potentially enhance receptor interaction and facilitates the cyclization of the peptide through head-to-tail linkage on the resin. Additionally, the short length of the peptide chain improves its conformational adaptability, allowing for better fitting to the receptor.

The introduction of conformational constraints through cyclization aims to induce or stabilize a specific conformation of the peptide, thereby increasing its resistance to enzymatic degradation and enhancing its receptor affinity and selectivity compared to the corresponding linear peptide.

The interactions of the designed peptides with SST2 receptor have been studied using computational methodologies, crucial for understanding the physicochemical mechanisms of molecular recognition. The computational studies were conducted by the PROMOCS laboratory (Prof. Marino) at the Department of Chemistry and Chemical Technologies, University of Calabria.

Molecular docking was employed to explore the binding interactions between the designed peptide ligand c(-FWKTE-) and the SST-2 receptor, highly expressed in several types of solid tumors. The docking approach utilizes efficient heuristic algorithms for ligand positioning and rapid empirical scoring functions, allowing for fast predictions of the ligand's binding mode (pose) and its affinity for the receptor. Preliminary molecular docking results (Figure 2.4) with the SST-2 receptor, obtained using AutoDock Vina revealed a good theoretical affinity between the cyclic pentapeptide and the SST-2 receptor, with a binding energy of ΔE = -7.9 kcal/mol.

The figure 2.4 displays the best docking pose, associated with a binding energy of -7.9 kcal/mol, representing the highest affinity observed.

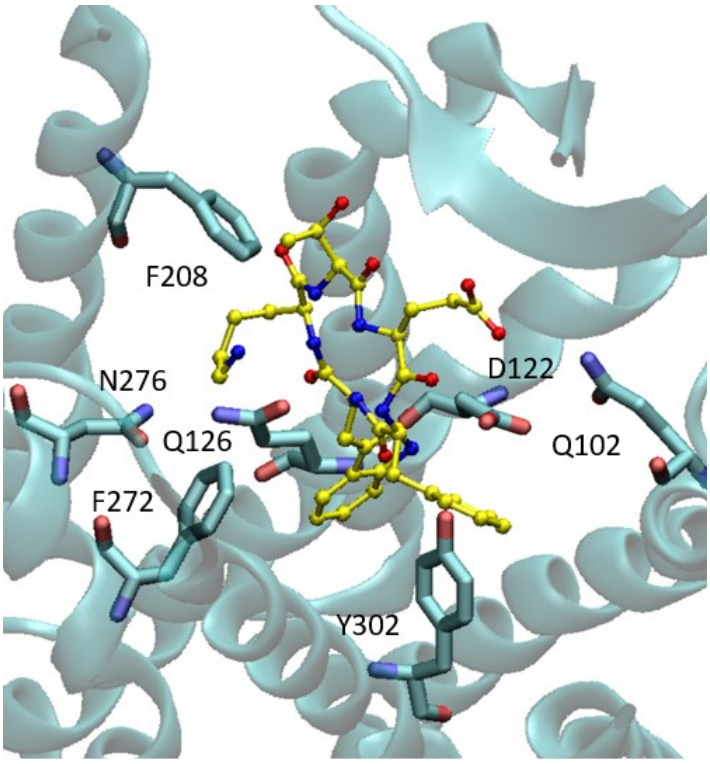

Figure 2.4. Best docking pose between the peptide c(-FWKTE-) and SST-2 receptor by molecular docking performed with AutoDock Vina

The cyclic pentapeptide was obtained by microwave-assisted solid phase peptide synthesis, using Fmoc-chemistry [87]. The strategy employed involved anchoring glutamic acid to the Wang resin via its side chain carboxyl group, while protecting the α-carboxyl function with the orthogonal Dmab (4-{N-[1-(4,4-dimethyl-2,6-dioxocyclohexylidene)-3-methylbutyl]amino}benzyl) protecting group. This approach facilitated head-to-tail cyclization on the resin, ensuring the successful formation of the desired cyclic structure.

The on-resin synthesis of head-to-tail cyclic peptides involves several key steps: (I) attaching the C-terminal glutamic acid, protected with the Dmab group, to the resin via its side chain carboxyl group, (II) sequentially building the linear peptide using solid-phase synthesis, (III) selectively removing the Dmab group from the C-terminal carboxyl group, (IV) activating the carboxyl group and coupling it with the deprotected N-terminal amino acid, and (V) finally cleaving the cyclic peptide from the resin.

The use of orthogonally protected glutamic acid is crucial for enabling efficient head-to-tail cyclization on the resin (Scheme 2.1).

The N-Fmoc-Glu(Wang resin)-ODmab (1) is first swollen in DMF for 15 minutes, then placed in the microwave synthesizer. After removing the Fmoc group from the amino function using a 20% piperidine solution in DMF, the first coupling cycle is carried out with N-Fmoc-L-O-(tBu)-Thr-OH (2), in the presence of HBTU and DIPEA. Each subsequent coupling cycle follows the same procedure, starting with the deprotection of the amino function of the last amino acid attached to the resin (Scheme 2.1).

Upon completion of the synthesis, the deprotection of the amino function of the N-terminal amino acid was carried out using 20% piperidine in DMF. Then, the Dmab group was removed from the carboxyl group of glutamic acid by treating the resin-bound linear peptide with a 5% hydrazine solution in DMF (Figure 2.5) [88].

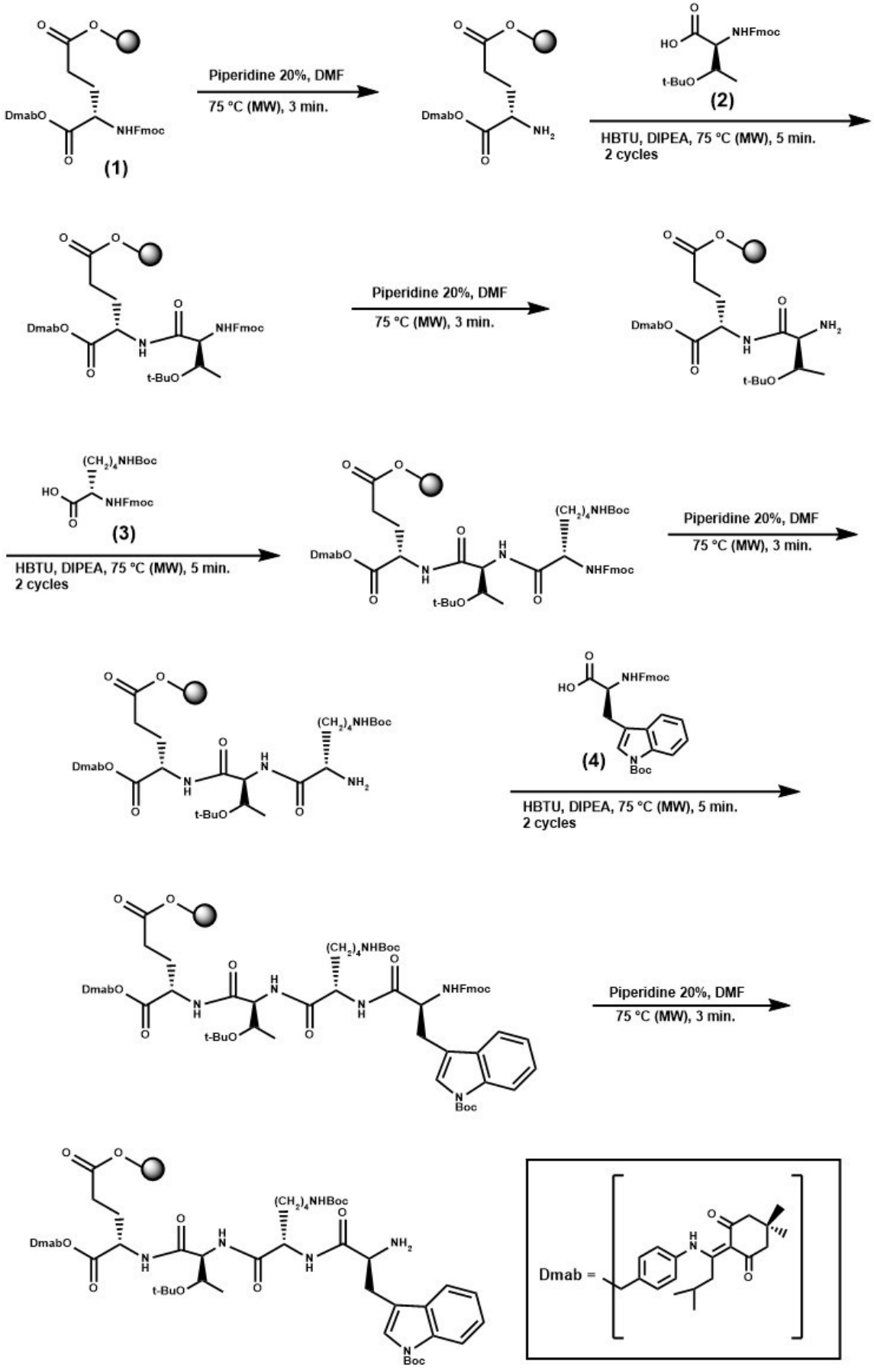
Piperidine 20%, DMF
75 °C (MW), 3 min.
(1)
(2)
HBTU, DIPEA, 75 °C (MW), 5 min.
2 cycles
(3)
(4)
Dmab =

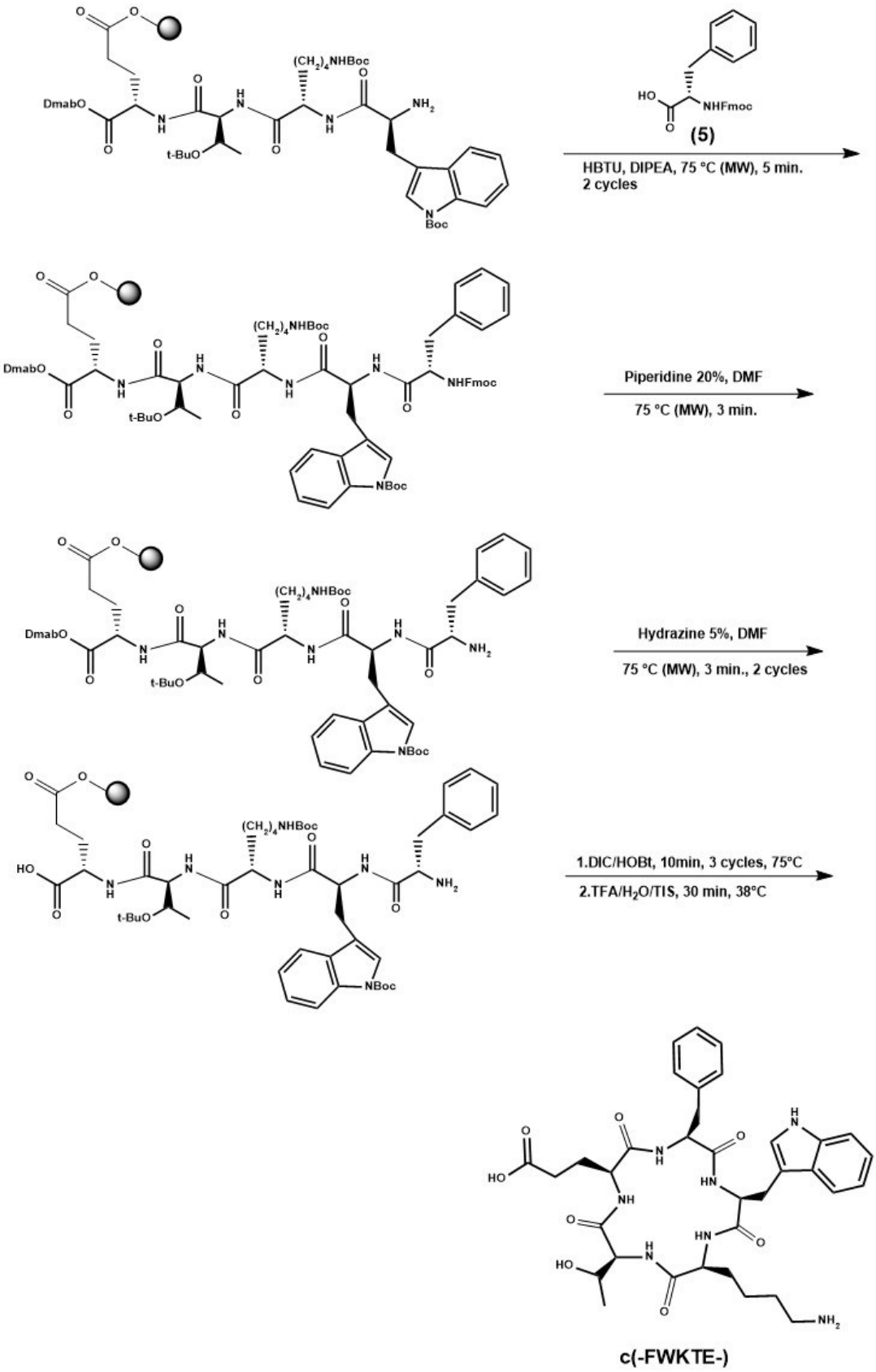

Scheme 2.1. Synthesis of the cyclic pentapeptide **c(-FWKTE-)**

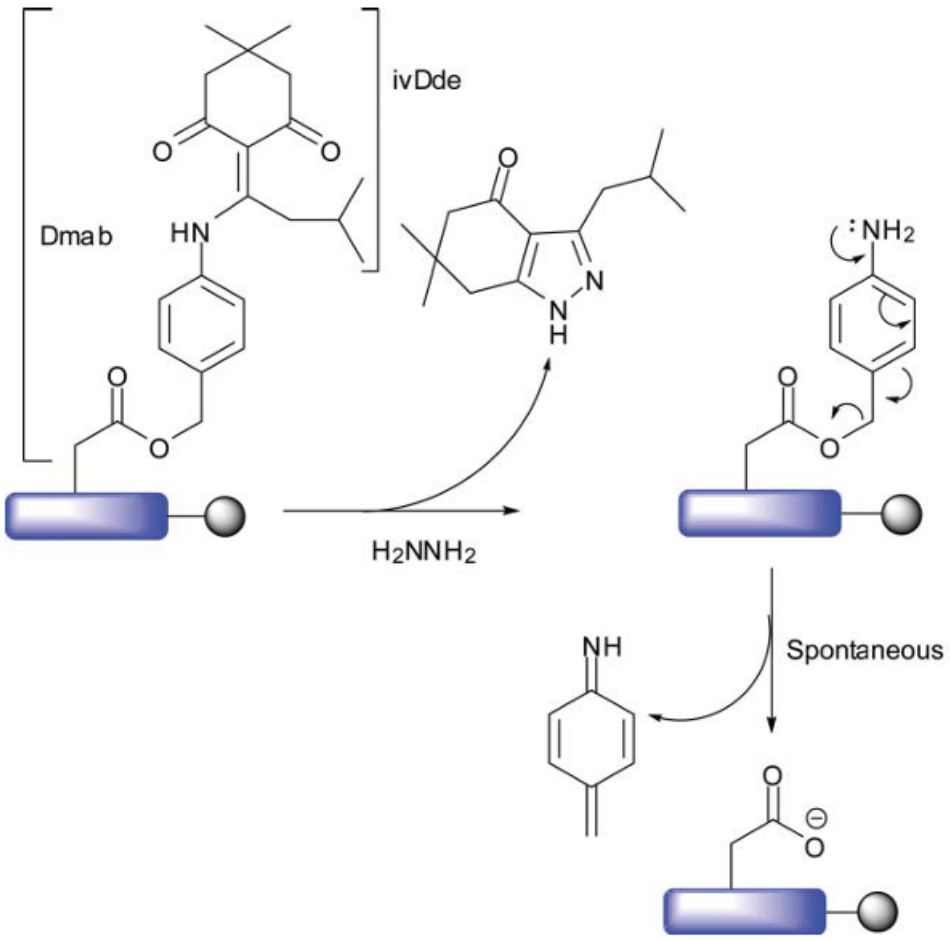

Figure 2.5. Mechanism of Dmab Group Removal Using Hydrazine

The head-to-tail cyclization of the resin-bound peptide, resulting in the formation of an amide bond between the N-terminal amino group and the free C-terminal carboxyl group, was performed using a coupling mixture consisting of a 0.25 M solution of diisopropylcarbodiimide (DIC) and a 0.5 M solution of hydroxybenzotriazole monohydrate (HOBt·H_2O) in dimethylformamide (DMF). Three coupling cycles were carried out at 75°C for 10 minutes each. After cyclization, the peptide was cleaved from the resin using a solution of trifluoroacetic acid (TFA), triisopropylsilane (TIS), and water (H_2O) in a 95/2.5/2.5 (v/v/v) ratio.

After precipitation with cold ethyl ether, followed by decantation and solvent evaporation, the cyclic peptide c(-FWKTE-) was obtained with an 85% yield.

The recovered peptide was analyzed using liquid chromatography to assess its purity and characterized by nuclear magnetic resonance (NMR) spectroscopy and mass spectrometry (MS), confirming both the structure of the peptide.

Following characterization, the peptide was tested *in vitro* on breast cancer cells to evaluate its antiproliferative activity.

To evaluate the potential antitumor efficacy of the cyclic peptide, preliminary MTT assays were carried out in Luminal A (MCF-7, T47D), Luminal B (ZR75) and in triple-negative (MDA-MB-436) breast cancer cells.

The peptide showed dose- and time-dependent antiproliferative effects, which became evident at 48 hours and were more pronounced at 72 hours. At concentrations of 40 μM and 0.4 mM, a clear reduction in cell viability was observed across all cell lines tested. In particular, the triple-negative MDA-MB-436 cells exhibited the most significant response, with a 20% reduction in cell viability at 0.4 mM, compared to the control (Figure 2.6).

These results indicate that the peptide possesses antiproliferative activity, especially in aggressive breast cancer subtypes such as triple-negative breast cancer.

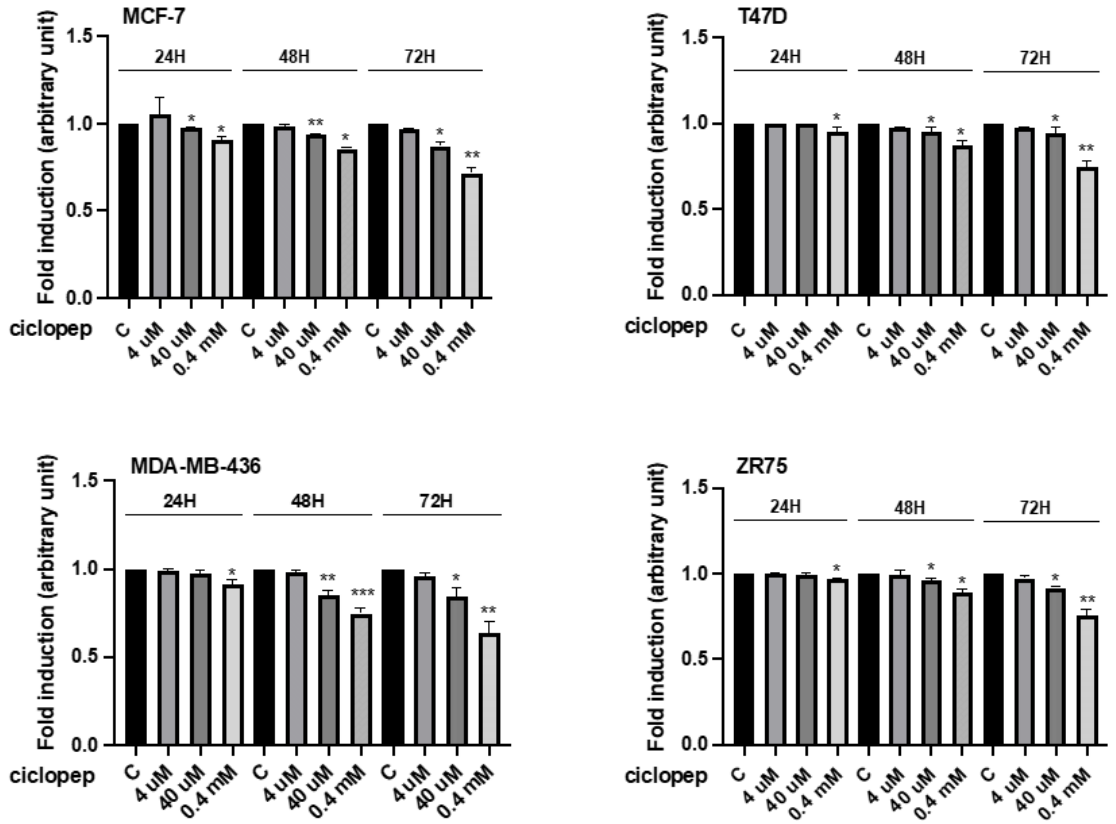

Figure 2.6. Antiproliferative activity of **c(-FWKTE-)** in breast cancer cells. Cell viability (MTT assay). Cells were treated with increasing concentrations (4μM, 40μM, 0.4mM) of ciclopep or left untreated (C = control) for 24, 48 and 72 hours, as indicated. The results are expressed as fold change respect to control cells (C). The values represent the means ± SDs of three different experiments, performed in sestuplicate. * $p < 0.05$, ** $p < 0.008$, *** $p < 0.002$

Although a 20% reduction in cell viability at 0.4 mM may seem moderate, it is a promising preliminary result, especially in early-stage *in vitro* studies. However, further biological assessments, including testing in normal cell lines and optimizing peptide dosage, are essential to fully evaluate its therapeutic potential in cancer treatment.

2.3 Experimental part

2.3.1 Chemistry

Materials and methods

Reagents were commercially available with analytical grade and used as purchased without further purification. The solvents employed in the reactions were purified following standard procedures and distilled before use. The solid phase synthesis of peptides was performed using a microwave-assisted CEM-Liberty automatic synthesizer. The peptide was synthesized using reagents and methodologies of "Fmoc-Chemistry". NMR spectra were recorded at 25 ºC on a Bruker Avance 300 spectrometer at 300 MHz. Spectroscopic analysis was performed at 293 K on diluted solutions of the sample by using DMSO-$_{d6}$ as the solvent. The chemical shifts (δ) reported are given in parts per million (ppm) on the scale relative to TMS, and the coupling constants (J) are in hertz (Hz). ^{1}H chemical shift values (δ) are referenced to the residual nondeuterated components of the NMR solvents (δ = 2.54 ppm for DMSO).

Mass spectra were recorded with a Micromass Orbitrap Elite mass spectrometer.

LC analysis was carried out using an HPLC instrument (Agilent Technologies, California, USA). Chromatographic separation was achieved using a LC C18 preparative column (Agilent 5, C18, 50 x 10.0 mm) at 25°C. The mobile phases consisted of eluent A (water) and eluent B (acetonitrile). These eluents were delivered at a flow rate of 0.4 mL/min with a linear gradient program as follows: 5% B from 0 to 3.0 min, 5–70% B from 3.0 to 7.0 min, 70–100% B from 7.0 to 10.0 min. Signal was acquired at 270 nm wavelength.

2.3.2 General procedure for microwave assisted peptide synthesis

For the synthesis, 0.2 M solutions of the required amino acids in DMF are prepared. All amino acids are Fmoc-protected on the amino group and protected on the side chain with acid-labile groups sensitive to trifluoroacetic acid. The amino acid bottles are then securely placed in their designated positions on the Liberty synthesizer.

After performing the preliminary operations, the sequence of the peptide to be synthesized is set through the PepDriver software. The instrumental parameters are checked and the Wang resin is introduced into the reactor. The swelling of the resin is carried out by adding 5 mL of DMF and bubbling for 15 minutes, subsequently the reactor containing the resin is placed in the microwave. The temperature inside the reactor is controlled by optical fiber.

Coupling reactions are performed in DMF, using approximately a 5-fold excess of Fmoc-AA-OH relative to the resin loading, along with HBTU (5 equivalents) and DIPEA (10 equivalents), for 5 minutes at 75 °C. Each coupling step includes two cycles.

The Fmoc protecting group was removed by treating the resin with a 20% piperidine solution in DMF (v/v, 7 mL), following a two-step deprotection process: an initial 30-second treatment, followed by a 3-minute incubation at 75 °C. After each cycle, the resin was thoroughly washed with DMF. Upon completion of the synthesis, the resin-bound peptide was washed with DMF and DCM.

The peptide was cleaved from the resin using a mixture of TFA, water, and TIS (9.5/0.25/0.25 by volume) for 30 min, the temperature was maintained at 38 °C via optical fiber control.

Synthesis of **c-(Phe-Trp-Lys-Thr-Glu)**

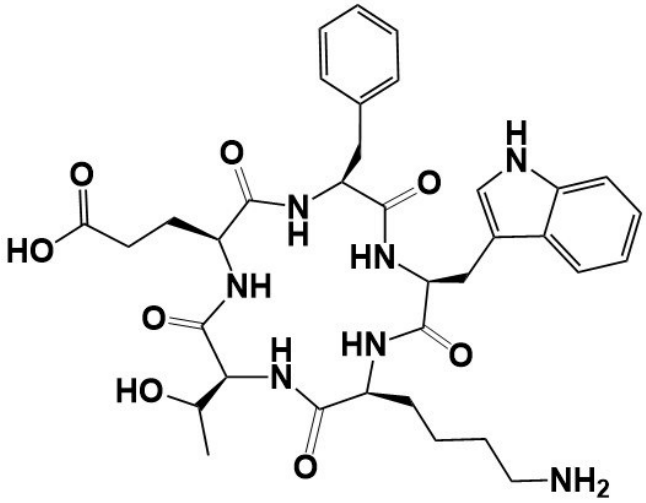

Four 100 mL containers are prepared, each containing amino acid solutions dissolved in 10 mL of N,N-Dimethylformamide (DMF). The following compounds are added to each container: N-Fmoc-Thr(tBu)-OH (0.795 g, 2 mmol), N-Fmoc-Lys(Boc)-OH (0.937 g, 2 mmol), Fmoc-Trp(Boc)-OH (1.053 g, 2 mmol), and N-Fmoc-Phe-OH (0.775 g, 2 mmol).

N-Fmoc-Glu(Wang resin)-ODmab (0.313 g, 0.32 mmol), with its side chain γ-carboxyl group anchored to the Wang resin and the α-carboxyl group protected by the orthogonal 4-{N-[1-(4,4-dimethyl-2,6-dioxocyclohexylidene)-3-methylbutyl]amino}-benzyl (Dmab) group, is suspended in 5 mL of DMF, and then transferred to the reaction vessel, where it is allowed to swell for 30 minutes. The reaction vessel is then placed in the Discovery microwave, and the temperature is controlled using an optical fiber probe. For each coupling cycle, 2.5 mL of each amino acid solution is added. The synthesis of c-(Phe-Trp-Lys-Thr-Glu) is carried out according to the general procedure.

At the end of the synthesis, after final deprotection with piperidine, the Dmab group on the α-carboxyl function was removed by treating the peptide anchored to the resin with a 5% hydrazine solution in DMF for 3 minutes at 75°C. Two cycles of deprotection with hydrazine were performed.

The head-to-tail cyclization of the resin-bound peptide was carried out using a coupling solution consisting of a 0.25 M solution of N,N-diisopropylcarbodiimide (DIC) in DMF and a 0.5 M solution of hydroxybenzotriazole monohydrate (HOBt·H2O) in DMF. Three coupling cycles were performed at 75°C for 10 minutes each.

The cyclic peptide was cleaved from the resin using a cleavage cocktail of TFA/H_2O/TIS (9.5 mL / 0.25 mL / 0.25 mL) for 30 minutes at 38°C. After cleavage, the peptide was obtained by precipitation with cold diethyl ether, achieving an 85% yield and high purity, as confirmed by HPLC analysis. The peptide was characterized using ^{1}H NMR and MS analysis.

^{1}H NMR (300 MHz, DMSO-d_6) δ 10.79 (bs, 1H, NH_{Trp}), 8.38 – 7.43 (m, 5H, NH, ArH), 7.42-6.89 (m, 10H, ArH,), 4.80 - 4.14 (m, 4H, α-CH, $\underline{CH}OH_{Thr}$), 4.12 – 3.80 (m, 2H, α-CH), 3.28 – 2.58 (m, 6H, CH_{2Phe}, CH_{2Trp}, $C\underline{H}_2NH_{2Lys}$), 2.38 – 2.06 (m, 2H, $C\underline{H}_2COOH_{Glu}$), 2.00 – 1.21 (m, 8H, $C\underline{H}_2C\underline{H}_2COOH_{Glu}$, $C\underline{H}_2C\underline{H}_2C\underline{H}_2CH_2NH_{2Lys}$), 1.10 (d, J = 7.0 Hz, 3H, CH_{3Thr}).

HRMS (m/z): calc. per $C_{35}H_{46}O_8N_7$ 692.3402 $[M+H]^+$; found 692.3378.

2.3.3 Biology: anticancer assay

Chemicals and Reagents

Dulbecco's Modified Eagle Medium/Nutrient Mixture F-12 (DMEM/F-12), RPMI 1640 (1×), and Fetal Bovine Serum (FBS) were purchased from Gibco™ (Life Technologies, Monza MB, Italy). Trypsin-EDTA solution 10×, L-Glutamine, penicillin/streptomycin (pen/strep) D-Glucose, Hepes, Sodium Pyruvate, Insulin and phosphate-buffered saline (PBS) were purchased from Sigma Aldrich (Merck Spa, Milano MI, Italy).

Cell Cultures and Treatments

Human breast cancer MCF-7, T47D, ZR75, MDA-MB-436 cell lines were purchased from ATCC, where they were authenticated. Cells were stored according to supplier's instructions and used within 6 months after frozen aliquot resuscitations. MCF-7 were cultured in DMEM/F-12 containing 5% FBS, T47D cells in RPMI containing 10% FBS, 2.5 g/ml glucose, 1% Na-Pyruvate, 10 nM Hepes, and 0.2 U/ml insulin, ZR75 in RPMI containing 10% FBS, 2.5 g/ml glucose, 1% Na-Pyruvate, 10 nM Hepes, MDA-MB-436 in DMEM/F-12 containing 10% FBS were grown in DMEM/F12 supplemented 5% HS, 20ng/ml EGF, 10 ug/ml human insulin, 0.5 mg/ml hydrocortisone, 100 ng/ml cholera toxin. All media contained 100 IU/mL pen/strep and 0.2 mM L-Glutamine. Mycoplasma negativity was tested monthly (PlasmoTest, Invivogen, Aurogene, Rome, Italy). For cell treatments, peptide was dissolved in DMSO at the stock concentration of 21.7mM. Serial dilutions were prepared, and the following concentrations were tested: 4 μM, 40 μM and 0.4 mM.

Cell proliferation assay

Cell proliferation was determined by using 3-(4,5- dimethylthiazol-2-yl)-2,5-diphenylformazan (MTT) assay. Cells (10.000 cells/well) were seeded in 96-well plates in growing medium (GM), serum starved overnight to synchronize cells in G0 phase and then treated or not with the tested cyclic peptide, as indicated, for 24, 48, and 72 hours. MTT (2mg/ml) was added to each well, and the plates

were incubated for 2 h at 37°C. The medium was then removed, and formazan crystals dissolved in 100 µl DMSO (Sigma Aldrich). Absorbance was measured at 570 nm.

2.3.4. Docking studies

Methods

Molecular docking allows to gain preliminary information on the better orientations of a ligand in the molecular target (receptor). During the docking process the molecular target, totally rigid, and ligand are treated as separated units. The ligand searches for the best location at lower energy inside the binding pocket of the receptor after a certain number of poses.

The docking procedure was carried out to obtain the complex between the SST-2 receptor and the cyclic peptide c(-FWKTE-). The crystal structure of the SST-2 receptor, retrieved from the Protein Data Bank (PDB: 7UL5) [89] excluding the NB6 region from the protein coordinates, served as the starting point for the simulations. A total of 9 distinct receptor-ligand complexes were generated by molecular docking using the Autodock Vina software [90].

For the docking simulations, a 3D grid was constructed around the receptor, with the grid center positioned near a set of key residues that participate in ligand binding. Specifically, the grid was centered on the following residues: Q102, D122, Q126, F208, F272, N276, and Y302. These residues were chosen based on their proximity to the ligand-binding site and their potential involvement in binding affinity.

The best binding pose was selected based on the most negative docking score, indicating the strongest predicted interaction between the receptor and the cyclic peptide.

2.4 Conclusions

In this study, the development of a novel somatostatin analogue, the cyclic pentapeptide c(-FWKTE), is described. The peptide was successfully synthesized using solid-phase peptide synthesis based on Fmoc-chemistry. It was designed to mimic the key amino acid sequence of somatostatin, which is critical for receptor binding and biological activity.

It includes the biologically active 7-10 sequence of somatostatin along with glutamic acid at the C-terminus, which facilitates cyclization through head-to-tail linkage on the resin. The short length of the peptide chain, combined with conformational constraints introduced by cyclization, is intended to stabilize a specific conformation, enhancing both resistance to enzymatic degradation and receptor affinity. Preliminary docking studies revealed good affinity between the peptide and the SST-2 receptor, indicating its potential as an SST-2 ligand.

Furthermore, initial *in vitro* studies demonstrated its antiproliferative activity across various breast cancer cell lines. However, given the early stage of these findings, additional *in vitro* investigations are needed to fully evaluate its efficacy. These early results establish a solid foundation for future research.

2.5 References

1. Henninot, A., Collins, J. C., Nuss, J. M. The current state of peptide drug discovery: back to the future?. *Journal of medicinal chemistry* **2018**, *61*(4), 1382-1414.
2. Wang, L., Wang, N., Zhang, W., Cheng, X., Yan, Z., Shao, G. et al. Therapeutic peptides: current applications and future directions. *Signal transduction and targeted therapy* **2022**, *7*(1), 48.
3. Thayer, A.M. Improving peptides. *Chemical & Engineering News Archive* **2011**, *89* (22), 13-20.
4. Jain, D., Mahammad, S. S., Singh, P. P., Kodipyaka, R. A review on parenteral delivery of peptides and proteins. *Drug development and industrial pharmacy* **2019**.
5. Fosgerau, K., Hoffmann, T. Peptide therapeutics: current status and future directions. *Drug discovery today* **2015**, *20*(1), 122-128.
6. Belgi, A., Akhter Hossain, M., W Tregear, G., D Wade, J. The chemical synthesis of insulin: from the past to the present. *Immunology, Endocrine & Metabolic Agents in Medicinal Chemistry (Formerly Current Medicinal Chemistry-Immunology, Endocrine and Metabolic Agents)* **2011**, *11*(1), 40-47.
7. Peptide therapeutics market analysis, 2018- 2030 – base year – 2022. Report ID: 978-1-68038-179-5, Number of pages: 110, Historical Range: 2018–2021, Industry: Healthcare.
8. Lau, J. L., Dunn, M. K. Therapeutic peptides: Historical perspectives, current development trends, and future directions. *Bioorganic & medicinal chemistry* **2018**, *26*(10), 2700-2707.
9. Vlieghe, P., Lisowski, V., Martinez, J., Khrestchatisky, M. Synthetic therapeutic peptides: science and market. *Drug discovery today* **2010**, *15*(1-2), 40-56.
10. Lee, A. C. L., Harris, J. L., Khanna, K. K., Hong, J. H. A comprehensive review on current advances in peptide drug development and design. *International journal of molecular sciences* **2019**, *20*(10), 2383.
11. Ilangala, A. B., Lechanteur, A., Fillet, M., & Piel, G. Therapeutic peptides for chemotherapy: Trends and challenges for advanced delivery systems. *European Journal of Pharmaceutics and Biopharmaceutics* **2021**, *167*, 140-158.
12. Di, L. Strategic approaches to optimizing peptide ADME properties. *The AAPS journal* **2015**, *17*, 134-143.
13. Diao, L., Meibohm, B. Pharmacokinetics and pharmacokinetic–pharmacodynamic correlations of therapeutic peptides. *Clinical pharmacokinetics* **2013**, *52*, 855-868.
14. Zhou, X. H., Po, A. L. W. Peptide and protein drugs: II. Non-parenteral routes of delivery. *International journal of pharmaceutics* **1991**, *75*(2-3), 117-130.
15. Erak, M., Bellmann-Sickert, K., Els-Heindl, S., Beck-Sickinger, A. G. Peptide chemistry toolbox–Transforming natural peptides into peptide therapeutics. *Bioorganic & medicinal chemistry* **2018**, *26*(10), 2759-2765.
16. Werle, M., Bernkop-Schnürch, A. Strategies to improve plasma half life time of peptide and protein drugs. *Amino acids* **2006**, *30*, 351-367.
17. Akizawa, H., Uehara, T., Arano, Y. Renal uptake and metabolism of radiopharmaceuticals derived from peptides and proteins. *Advanced drug delivery reviews* **2008**, *60*(12), 1319-1328.

18. Adessi, C., Soto, C. Converting a peptide into a drug: strategies to improve stability and bioavailability. *Current medicinal chemistry* **2002**, *9*(9), 963-978.
19. Davies, J. S. The cyclization of peptides and depsipeptides. *Journal of peptide science: an official publication of the European Peptide Society* **2003**, *9*(8), 471-501.
20. Ahangarzadeh, S., Kanafi, M. M., Hosseinzadeh, S., Mokhtarzadeh, A., Barati, M., Ranjbari, J. et al. Bicyclic peptides: types, synthesis and applications. *Drug Discovery Today* **2019**, *24*(6), 1311-1319.
21. Nielsen, D. S., Shepherd, N. E., Xu, W., Lucke, A. J., Stoermer, M. J. et al. Orally absorbed cyclic peptides. *Chemical reviews* **2017**, *117*(12), 8094-8128.
22. Liu, L., Yang, L., Cao, S., Gao, Z., Yang, B., Zhang, G. et al. CyclicPepedia: a knowledge base of natural and synthetic cyclic peptides. *Briefings in Bioinformatics* **2024**, *25*(3), bbae190.
23. Xiao, W., Ma, W., Wei, S., Li, Q., Liu, R., Carney, R. P. et al. High-affinity peptide ligand LXY30 for targeting α3β1 integrin in non-small cell lung cancer. *Journal of hematology & oncology* **2019**, *12*, 1-18.
24. Chow, H. Y., Zhang, Y., Matheson, E., Li, X. Ligation technologies for the synthesis of cyclic peptides. *Chemical Reviews* <**2019**, *119*(17), 9971-10001.
25. Wu, D., Gao, Y., Qi, Y., Chen, L., Ma, Y., Li, Y. Peptide-based cancer therapy: opportunity and challenge. *Cancer letters* **2014**, *351*(1), 13-22.
26. Afshar, S., Pashaki, A. S., Najafi, R., Nikzad, S., Amini, R., Shabab, N. et al. Cross-resistance of acquired radioresistant colorectal cancer cell line to gefitinib and regorafenib. *Iranian journal of medical sciences* **2020**, *45*(1), 50.
27. Hayashi, M. A., Ducancel, F., Konno, K. Natural peptides with potential applications in drug development, diagnosis, and/or biotechnology. *International journal of peptides* **2012**, *2012.*
28. Sato, A. K., Viswanathan, M., Kent, R. B., Wood, C. R. Therapeutic peptides: technological advances driving peptides into development. *Current opinion in biotechnology* **2006**, *17*(6), 638-642.
29. Tsuji, A. Small molecular drug transfer across the blood-brain barrier via carrier-mediated transport systems. *NeuroRx* **2005**, *2*, 54-62.
30. Min, K. A., Maharjan, P., Ham, S., Shin, M. C. Pro-apoptotic peptides-based cancer therapies: challenges and strategies to enhance therapeutic efficacy. *Archives of pharmacal research* **2018**, *41*, 594-616.
31. Pan, X., Xu, J., Jia, X. Research progress evaluating the function and mechanism of anti-tumor peptides. *Cancer Management and Research* **2020**, 397-409.
32. Thabault, L., Brisson, L., Brustenga, C., Martinez Gache, S. A., Prevost, J. R., Kozlova, A. et al. Interrogating the lactate dehydrogenase tetramerization site using (stapled) peptides. *Journal of medicinal chemistry* **2020**, *63*(9), 4628-4643.
33. Kristensen, M., Birch, D., Mørck Nielsen, H. Applications and challenges for use of cell-penetrating peptides as delivery vectors for peptide and protein cargos. *International journal of molecular sciences* **2016**, *17*(2), 185.
34. Payandeh, Z., Rajabibazl, M., Mortazavi, Y., Rahimpour, A., Taromchi, A. H. Ofatumumab monoclonal antibody affinity maturation through in silico modeling. *Iranian biomedical journal* **2018**, *22*(3), 180.

35. Cavallaro, P. A., De Santo, M., Belsito, E. L., Longobucco, C., Curcio, M., Morelli, C., Pasqua, L., Leggio, A. Peptides targeting HER2-positive breast cancer cells and applications in tumor imaging and delivery of chemotherapeutics. *Nanomaterials* **2023**, *13*(17), 2476.
36. Mousavizadeh, A., Jabbari, A., Akrami, M., Bardania, H. Cell targeting peptides as smart ligands for targeting of therapeutic or diagnostic agents: a systematic review. *Colloids and Surfaces B: Biointerfaces* **2017**, *158*, 507-517.
37. Shadidi, M., Sioud, M. Selective targeting of cancer cells using synthetic peptides. *Drug Resistance Updates* **2003**, *6*(6), 363-371.
38. Guillemin, R. Somatostatin. The beginnings, 1972. *Molecular and cellular endocrinology* **2008**, *286*(1-2), 3.
39. Weckbecker, G., Raulf, F., Stolz, B., & Bruns, C. Somatostatin analogs for diagnosis and treatment of cancer. *Pharmacology & therapeutics* **1993**, *60*(2), 245-264.
40. Zou, Y. I., Tan, H., Zhao, Y., Zhou, Y., Cao, L. I. N. Expression and selective activation of somatostatin receptor subtypes induces cell cycle arrest in cancer cells. *Oncology letters* **2019**, *17*(2), 1723-1731.
41. War, S. A., Kim, B., & Kumar, U. Human somatostatin receptor-3 distinctively induces apoptosis in MCF-7 and cell cycle arrest in MDA-MB-231 breast cancer cells. *Molecular and cellular endocrinology* **2015**, *413*, 129-144.
42. Staykova, S., Naydenova, E., Wesselinova, D., Kalistratova, A., Vezenkov, L. Synthesis and in vitro study of the anticancer activity of new analogs of octreotide. *Protein and Peptide Letters* **2012**, *19*(12), 1257-1262.
43. Staykova, S. T., Wesselinova, D. W., Vezenkov, L. T., Naydenova, E. D. Synthesis and in vitro antitumor activity of new octapeptide analogs of somatostatin containing unnatural amino acids. *Amino Acids* **2015**, *47*, 1007-1013.
44. Olias, G., Viollet, C., Kusserow, H., Epelbaum, J., Meyerhof, W. Regulation and function of somatostatin receptors. *Journal of neurochemistry* **2004**, *89*(5), 1057-1091.
45. De Herder, W. W., Hofland, L. J., van der Lely, A. J., Lamberts, S. W. J. Somatostatin receptors in gastroentero-pancreatic neuroendocrine tumours. *Endocrine-related cancer* **2003**, *10*(4), 451-458.
46. Gaspar, P., Berger, B., Febvret, A., Vigny, A., Krieger-Poulet, M., Borri-Voltattorni, C. Tyrosine hydroxylase-immunoreactive neurons in the human cerebral cortex: a novel catecholaminergic group?. *Neuroscience letters* **1987**, *80*(3), 257-262.
47. Guillermet-Guibert, J., Lahlou, H., Cordelier, P., Bousquet, C., Pyronnet, S., Susini, C. Physiology of somatostatin receptors. *J Endocrinol Invest* **2005**, *28*(11), 5-9.
48. Warren, T. G., Shields, D. Expression of pre pro somatostatin in heterologous cells: biosynthesis, posttranslational processing, and secretion of mature somatostatin. *Cell* **1984**, *39*(3), 547-555.
49. Gluschankof, P., Morel, A., Gomez, S., Nicolas, P., Fahy, C., Cohen, P. Enzymes processing somatostatin precursors: an Arg-Lys esteropeptidase from the rat brain cortex converting somatostatin-28 into somatostatin-14. *Proceedings of the National Academy of Sciences* **1984**, *81*(21), 6662-6666.
50. Paragliola, R. M., Prete, A., Papi, G., Torino, F., Corsello, A., Pontecorvi, A., Corsello, S. M. Clinical utility of lanreotide Autogel® in gastroenteropancreatic neuroendocrine tumors. *Drug Design, Development and Therapy* **2016**, 3459-3470.

51. Meyerhof, W., Wulfsen, I., Schönrock, C., Fehr, S., Richter, D. Molecular cloning of a somatostatin-28 receptor and comparison of its expression pattern with that of a somatostatin-14 receptor in rat brain. *Proceedings of the National Academy of Sciences* **1992**, *89*(21), 10267-10271.
52. Taniyama, Y., Suzuki, T., Mikami, Y., Moriya, T., Satomi, S., Sasano, H. Systemic distribution of somatostatin receptor subtypes in human: an immunohistochemical study. *Endocrine journal* **2005**, *52*(5), 605-611.
53. Susini, C., Buscail, L. Rationale for the use of somatostatin analogs as antitumor agents. *Annals of Oncology* **2006**, *17*(12), 1733-1742.
54. Tulipano, G., Schulz, S. Novel insights in somatostatin receptor physiology. *European Journal of Endocrinology* **2007**, *156*(Supplement_1), S3-S11.
55. Patel, Y.C. Somatostatin and its receptor family. *Front. Neuroendocrinol*. **1999**, *20*, 157–198.
56. Samim, A., Tytgat, G.A.M., Bleeker, G., Wenker, S.T.M., Chatalic, K.L.S. et al. Nuclear Medicine Imaging in Neuroblastoma: Current Status and New Developments. J. *Pers. Med.* **2021**, *11*, 270.
57. Curtis, S.B., Hewitt, J., Yakubovitz, S., Anzarut, A., Hsiang, Y.N., Buchan, A.M. Somatostatin receptor subtype expression and function in human vascular tissue. *Am. J. Physiol. Heart Circ. Physiol*. **2000**, *278*, H1815–H1822.
58. Cordelier, P., Estève, J. P., Bousquet, C., Delesque, N., O'Carroll, A. M., Schally, A. V. et al. Characterization of the antiproliferative signal mediated by the somatostatin receptor subtype sst5. *Proceedings of the National Academy of Sciences* **1997**, *94*(17), 9343-9348.
59. Lamberts, S. W., de Herder, W. W., Hofland, L. J. Somatostatin analogs in the diagnosis and treatment of cancer. *Trends in Endocrinology & Metabolism* **2002**, *13*(10), 451-457.
60. Buscail, L., Esteve, J. P., Saint-Laurent, N., Bertrand, V., Reisine, T. et al. Inhibition of cell proliferation by the somatostatin analogue RC-160 is mediated by somatostatin receptor subtypes SSTR2 and SSTR5 through different mechanisms. *Proceedings of the National Academy of Sciences* **1995**, *92*(5), 1580-1584.
61. Ricci, S., Antonuzzo, A., Galli, L., Ferdeghini, M., Bodei, L., Orlandini, C., Conte, P. F. Octreotide acetate long-acting release in patients with metastatic neuroendocrine tumors pretreated with lanreotide. *Annals of Oncology* **2000**, *11*(9), 1127-1130.
62. Bousquet, C., Puente, E., Buscail, L., Vaysse, N., Susini, C. Antiproliferative effect of somatostatin and analogs. *Chemotherapy* **2001**, *47*(Suppl. 2), 30-39.
63. Strosberg, J., Kvols, L. Antiproliferative effect of somatostatin analogs in gastroenteropancreatic neuroendocrine tumors. *World journal of gastroenterology: WJG* **2010**, *16*(24), 2963.
64. Jia, W. D., Xu, G. L., Xu, R. N., Sun, H. C., Wang, L., Yu, J. H. et al. Octreotide acts as an antitumor angiogenesis compound and suppresses tumor growth in nude mice bearing human hepatocellular carcinoma xenografts. *Journal of cancer research and clinical oncology* **2003**, *129*, 327-334.
65. Buscail, L., Delesque, N., Esteve, J. P., Saint-Laurent, N., Prats, H., Clerc, P. et al. Stimulation of tyrosine phosphatase and inhibition of cell proliferation by somatostatin analogues: mediation by human somatostatin receptor subtypes SSTR1 and SSTR2. *Proceedings of the National Academy of Sciences* **1994**, *91*(6), 2315-2319.

66. Ingle, J. N., Kardinal, C. G., Suman, V. J., Krook, J. E., Hatfield, A. K. Octreotide as first-line treatment for women with metastatic breast cancer. *Investigational new drugs* **1996**, *14*, 235-237.
67. Ajani, J. A. Role of Octreotide in Cancer and Therapy-Related Complications. *ONCOLOGY-WILLISTON PARK THEN HUNTINGTON THE MELVILLE NEW YORK* **2002**, *16*(9; SUPP/8).
68. Ben-Shlomo, A., Melmed, S. Somatostatin agonists for treatment of acromegaly. *Molecular and cellular endocrinology* **2008**, *286*(1-2), 192-198.
69. Giustina, A., Mazziotti, G., Maffezzoni, F., Amoroso, V., Berruti, A. Investigational drugs targeting somatostatin receptors for treatment of acromegaly and neuroendocrine tumors. *Expert opinion on investigational drugs* **2014**, *23*(12), 1619-1635.
70. Available online: https://go.drugbank.com/drugs/DB06791.
71. Bolanowski, M., Kałużny, M., Witek, P., Jawiarczyk-Przybyłowska, A. Pasireotide—a novel somatostatin receptor ligand after 20 years of use. *Reviews in Endocrine and Metabolic Disorders* **2022**, *23*(3), 601-620.
72. Feelders, R. A., Yasothan, U., Kirkpatrick, P. Pasireotide. *Nature Reviews Drug Discovery* **2012**, *11*(8), 597-599.
73. Dickson, R. B., Lippman, M. E. Molecular determinants of growth, angiogenesis, and metastases in breast cancer. In *Seminars in oncology* **1992***,19* (3), 286-298.
74. Chen, A., Laskar-Levy, O., Koch, Y. Selective expression of neuropeptides in the rat mammary gland: somatostatin gene is expressed during lactation. *Endocrinology* **1999**, *140*(12), 5915-5921.
75. Boccardo, F., Amoroso, D. Management of breast cancer: is there a role for somatostatin and its analogs?. *Chemotherapy* **2001**, *47*(Suppl. 2), 62-77.
76. Murray, R. D., Kim, K., Ren, S. G., Chelly, M., Umehara, Y., Melmed, S. Central and peripheral actions of somatostatin on the growth hormone–IGF-I axis. *The Journal of clinical investigation* **2004**, *114*(3), 349-356.
77. Adams, R. L., Adams, I. P., Lindow, S. W., Zhong, W., Atkin, S. L. Somatostatin receptors 2 and 5 are preferentially expressed in proliferating endothelium. *British journal of cancer* **2005**, *92*(8), 1493-1498.
78. Setyono-Han, B., Henkelman, M. S., Foekens, J. A., Klijn, J. G. Direct inhibitory effects of somatostatin (analogues) on the growth of human breast cancer cells. *Cancer research* **1987**, *47*(6), 1566-1570.
79. Nelson, J., Cremin, M., Murphy, R. F. Synthesis of somatostatin by breast cancer cells and their inhibition by exogenous somatostatin and sandostatin. *British journal of cancer* **1989**, *59*(5), 739-742.
80. Orlando, C., Raggi, C. C., Bianchi, S., Distante, V., Simi, L., Vezzosi, V. et al. Measurement of somatostatin receptor subtype 2 mRNA in breast cancer and corresponding normal tissue. *Endocrine-related cancer* **2004**, *11*(2), 323-332.
81. Hatzoglou, A., Ouafik, L. H., Bakogeorgou, E., Thermos, K., Castanas, E. Morphine cross-reacts with somatostatin receptor SSTR2 in the T47D human breast cancer cell line and decreases cell growth. *Cancer Research* **1995**, *55*(23), 5632-5636.

82. Biron, E., Chatterjee, J., Ovadia, O., Langenegger, D., Brueggen, J., Hoyer, D. Improving oral bioavailability of peptides by multiple N-methylation: somatostatin analogues. *Angewandte Chemie International Edition* **2008**, *47*(14), 2595-2599.
83. Janecka, A., Zubrzycka, M., Janecki, T. Somatostatin analogs. *The Journal of Peptide Research* **2001**, *58*(2), 91-107.
84. Han, G., Tamaki, M., Hruby, V. J. Fast, efficient and selective deprotection of the tert-butoxycarbonyl (Boc) group using HCl/dioxane (4 m). *The Journal of Peptide Research* **2001**, *58*(4), 338-341.
85. Zhang, B., Xue, L., & Wu, Z. B. Structure and Function of Somatostatin and its Receptors in Endocrinology. *Endocrine Reviews* **2024**, bnae022.
86. Martín-Gago, P., Aragón, E., Gomez-Caminals, M., Fernández-Carneado, J., Ramón, R., Martin-Malpartida, P. et al. Insights into structure-activity relationships of somatostatin analogs containing mesitylalanine. *Molecules* **2013**, *18*(12), 14564-14584.
87. Catalano, S., Leggio, A., Barone, I., De Marco, R., Gelsomino, L., Campana, A. et al. A novel leptin antagonist peptide inhibits breast cancer growth in vitro and in vivo. *Journal of cellular and molecular medicine* **2015**, *19*(5), 1122-1132.
88. Conroy, T., Jolliffe, K. A., Payne, R. J. Efficient use of the Dmab protecting group: applications for the solid-phase synthesis of N-linked glycopeptides. *Organic & Biomolecular Chemistry* **2009**, *7*(11), 2255-2258.
89. Robertson, M. J., Papasergi-Scott, M. M., He, F., Seven, A. B., Meyerowitz, J. G. et al. Structure determination of inactive-state GPCRs with a universal nanobody. *Nature Structural & Molecular Biology* **2022**, *29*(12), 1188-1195.
90. Trott, O., Olson, A. J. AutoDock Vina: improving the speed and accuracy of docking with a new scoring function, efficient optimization, and multithreading. *Journal of computational chemistry* **2010**, *31*(2), 455-461.

Chapter 3

Design, synthesis, and characterization of novel piperazine-based small molecules for antiviral and anticancer research

[work under submission]

Abstract

Piperazine is a valuable compound in drug development, known for its favorable structural properties and wide-ranging biological activities, including anti-inflammatory antibacterial, antiviral and anticancer effects. In particular, piperazine derivatives have shown promise in antiviral and breast cancer treatment. This research aimed to design, synthesize, and evaluate a series of novel piperazine derivatives as potential antiviral and anticancer agents. The compounds were designed with urea and sulphonamide groups at the N-1 position and acyl groups at the N-4 position. Their antiviral potential was tested against Zika and Dengue Virus, focusing on viral proteases due to structural similarities across the Flaviviridae family. These compounds were also tested on tumor cells to evaluate their potential as anticancer agents in addition to their antiviral properties. Among them, four compounds showed promising antiproliferative activity against breast cancer cells, selectively inhibiting cancer cell growth without significantly affecting normal cells in initial *in vitro* studies.

This study underscores the potential of piperazine-based compounds as future antiviral and anticancer therapies.

3.1 Small molecules based on piperazine core as potential Flaviviridae NS3 protease inhibitors

3.1.1. Introduction and Background

3.1.1.1 Arboviruses

Arthropod-borne viruses (arboviruses) are a major cause of human mortality globally. These viruses form a vast and diverse group that are transmitted to susceptible hosts through the bite of infected arthropod vectors, primarily mosquitoes and ticks. Asia is particularly vulnerable to arboviral diseases due to a combination of factors, including high population density, tropical climates, and environments that are ideal for the breeding of mosquito vectors. Over 500 arboviruses have been identified, with approximately 150 known to cause diseases in humans [1]. Arboviral infections can vary in severity, ranging from asymptomatic cases to fulminant, life-threatening disease. Clinically, symptoms are typically classified into three main categories: systemic febrile illness, haemorrhagic fever, and invasive neurological disease [2].

The majority of arboviruses responsible for human disease belong to four main families: *Flaviviridae* (genus Flavivirus), *Togaviridae* (genus Alphavirus), *Peribunyaviridae* (genus Orthobunyavirus) and *Phenuiviridae* (genus Phlebovirus). Additionally, members of four other families: *Nairoviridae* (genus Orthonairovirus), *Orthomyxoviridae* (genus Thogotovirus), *Rhabdoviridae* (genus Vesiculovirus) and *Reoviridae* (genus Orbivirus) also play a significant role [3,4].

3.1.1.2 Flaviviruses

Flaviviridae family is subdivided into four genera namely: Flavivirus, Hepacivirus, Pegivirus and Pestivirus. Flavivirus genus includes prevalently arboviruses transmitted by infected arthropod, such as Dengue Virus (DENV), Japanese Encephalitis Virus (JEV), Yellow Fever Virus (YFV),

Chikungunya Virus (CHIKV), Spondweni Virus (SPOV or SPONV), West Nile Virus (WNV) and Zika Virus (ZIKV) [5] (Figure 3.1).

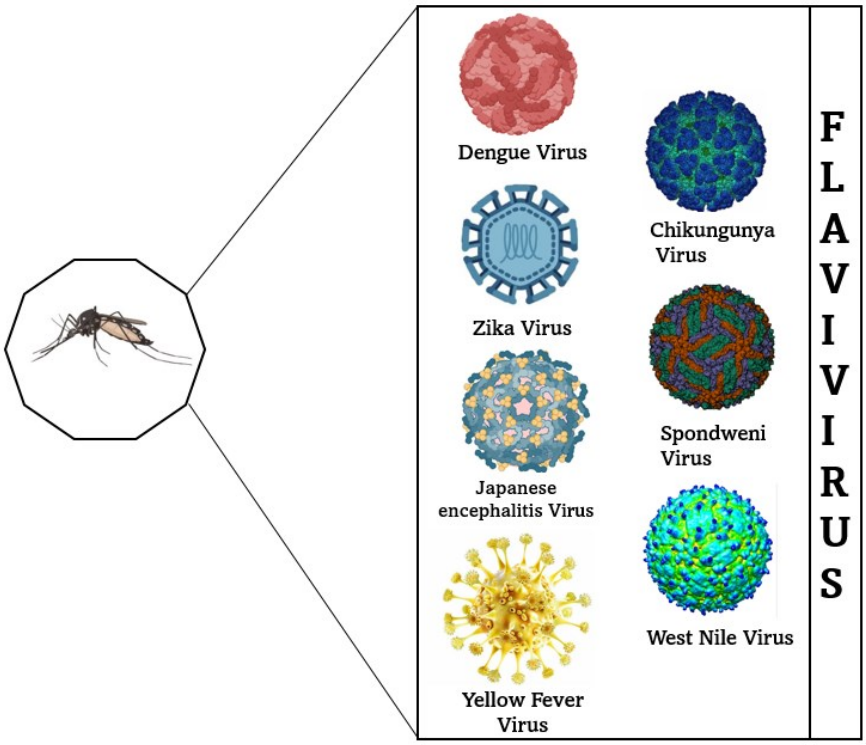

Figure 3.1. Flavivirus family

The genus Flavivirus, part of the Flaviviridae family, includes around 73 viruses that share common features such as size, structure, and nucleic acid properties. In particular, Flaviviruses are enveloped viruses containing a single-stranded positive-sense RNA genome of approximately 11 kb in length, enclosed in a spherical nucleocapsid core and surrounded by an icosahedral membrane. The amino terminus of the viral genome encodes three structural proteins: capsid [C], membrane [M]—which is expressed as the precursor prM and envelope [E] proteins, all of which are essential for forming the virus particle, and seven non- structural proteins (NS1, NS2A, NS2B, NS3, NS4A, NS4B, and NS5) crucial for viral replication (Figure 3.2) [6].

The non-structural proteins [NS] play key roles in RNA genome replication, virion assembly, and modulation of the host's innate immune response. Due to their critical functions, these viral proteins are promising targets for the development of novel antiviral therapies [7].

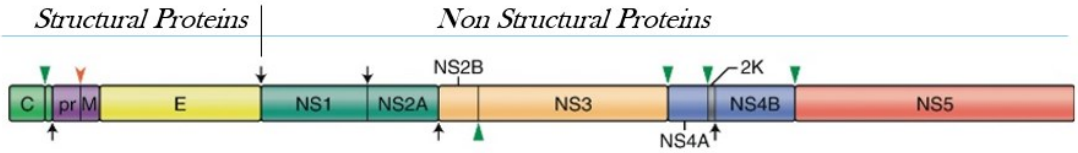

Figure 3.2. Schematic representation of the Flavivirus genome

3.1.1.3 Flavivirus life cycle

The viral life cycle begins when the viral [E] protein binds to its specific receptor on the host cell surface, initiating viral entry through clathrin-mediated endocytosis. This interaction facilitates the internalization of the virus, marking the first crucial step in infection [8,9].

Once inside the endosome, the acidic environment induces conformational changes in the E protein, promoting fusion between the viral envelope and the endosomal membrane. This fusion releases the viral nucleocapsid into the cytoplasm advancing the infection process [10-12].

Once the viral genome is released into the cytoplasm, translation and RNA replication occur. The positive-sense RNA is translated into a single polyprotein, which is cleaved into mature functional proteins by both viral and host proteases.

Viral genome replication takes place on intracellular membranes, while virus assembly occurs at the endoplasmic reticulum (ER). Newly synthesized RNA and structural proteins bud into the ER lumen, forming immature, non-infectious virions.

These immature virions, along with subviral particles, are transported through the trans-Golgi network (TGN), where they undergo maturation. The host protease furin cleaves the prM protein on

the immature particles, resulting in the formation of fully infectious virions. Both mature virions and subviral particles are then released from the host cell through exocytosis, completing the viral life cycle (Figure 3.3) [13].

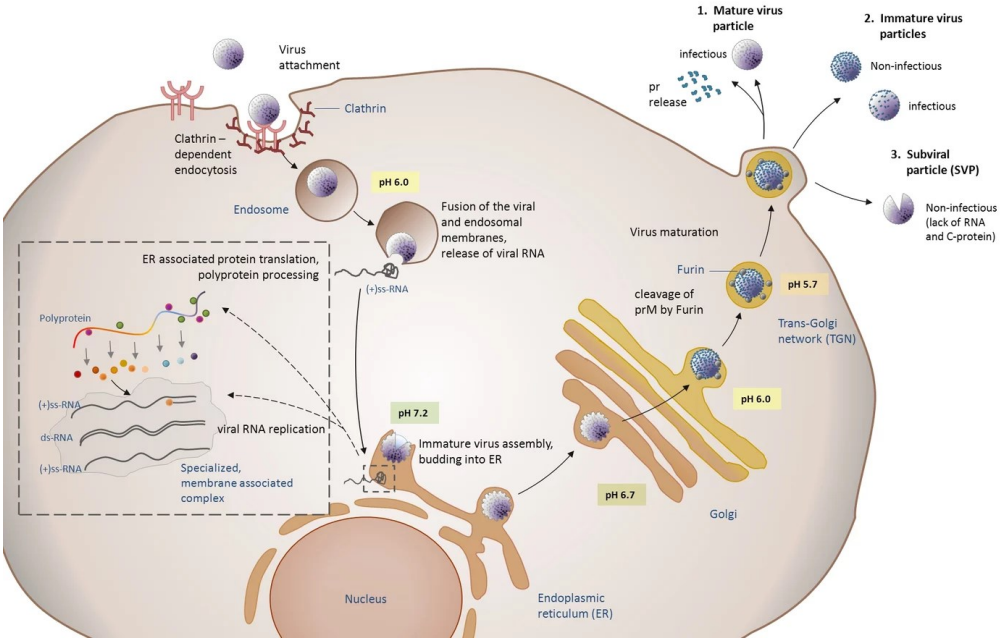

Figure 3.3. Virus replication cycle [14].

3.1.1.4 Zika and Dengue infections

Both ZIKV and DENV are common in tropical countries and are still a threat in low and middle-income countries, such as Brazil and India, and in some regions of Africa and Asia [15, 16].

Vector-borne diseases, responsible for over 700,000 deaths annually, make up more than 17% of all infectious diseases and can be caused by parasites, bacteria, or viruses. Their distribution is influenced by demographic, environmental, and social factors. Key contributors to the spread of these diseases include global travel and trade, unplanned urbanization, climate change, and the silent adaptation and spread of vectors. Despite significant vector control efforts, there are no licensed vaccines or specific treatments, and these diseases continue to spread rapidly worldwide.

It is estimated that 400 million DENV infections occur each year and that over half of the world's population live in countries with active DENV or ZIKV transmission. Among the Flaviviruses, Dengue is the most widespread virus. It causes a spectrum of diseases, ranging from a mild febrile illness to a life-threatening dengue haemorrhagic fever. Equally lethal is the spread of Zika virus with the following complications of infection that are congenital microcephaly and Guillan Barrè syndrome. The primary vectors for both dengue and Zika viruses are *Aedes albopictus* and *Aedes aegypti* mosquitoes. However, additional transmission modes have been identified for both viruses, including vertical transmission from mother to child, blood transfusions and organ transplants. Notably, Zika virus can also be transmitted through sexual contact [17].

NS2B/NS3 Zika and Dengue Protease: Structures and Functions

ZIKV and DENV, members of the Flaviviridae family, are RNA virus with a genome consisting of single-stranded positive-sense RNA (+ssRNA). Both shares the typical structural features of flavivirus genomes [18].

The viral genome, formed by three structural proteins and by seven non-structural ones is translated into a single large precursor polyprotein, which is subsequently cleaved by the viral NS2B/NS3 serine protease and host proteases into functional proteins. The Zika virus NS3 protein is multifunctional, featuring two distinct domains: a 176-residue N-terminal domain with protease activity and a 444-residue C-terminal domain responsible for helicase, nucleoside 5′-transferase (NTPase), and 5′-terminal RNA triphosphatase RNA triphosphatase (RTPase) functions. The Zika virus NS3 protein functions as a serine protease, containing a catalytic triad of serine, histidine, and aspartate (His51, Asp75, Ser135) at its active site. It requires NS2B as a cofactor for full activity. Studies have shown that the NS3 protease adopts two conformational states: "open" and "closed." In the catalytically active "closed" state, NS2B is fully bound around the NS3 active site. In contrast, in the "open"

inactive conformation, NS2B is only partially bound, with its chain turning away and binding behind the active site, leading to inactivation of the protease [19-21].

The DENV NS2B/NS3 complex is a trypsin-like serine protease with dual roles in viral replication and modulation of innate immunity. The NS3 protease contains a catalytic triad of residues—His51, Asp75, and Ser135—positioned in a cleft between two β-barrels [18].

The NS2B protein serves as a cofactor for the NS3 protease, undergoing a conformational change upon binding to NS3, which is essential for activating the protease. NS2B, a membrane-associated protein composed of 130 amino acids, features three hydrophobic domains and a central hydrophilic region, with its C-terminal region responsible for substrate recognition. In addition to its role in viral replication, the NS2B/NS3 protease is involved in immune evasion by cleaving the human interferon regulatory factor-3 activator (IRF-3), a key mediator of the antiviral response [22-24].

The cleavage mechanism of the NS3 protease begins with the nucleophilic attack of Ser135, activated by His51, on the carbonyl group at the P1 position, forming a stabilized tetrahedral intermediate through hydrogen bonding with Gly153. The intermediate then decomposes, releasing the C-terminal amine fragment. The N-terminal fragment remains covalently bound to the protease via an ester bond, which is hydrolysed by a water molecule. His51 acts as a base, enhancing the nucleophilicity of the water, leading to the release of the N-terminal fragment and the initiation of a new catalytic cycle [18].

The ZIKV NS2B/NS3 sequence shares high homology with DENV NS2B/NS3, with the primary difference being two key residues: Glu/Ala 153 and Lys/Asp 139 in DENV and ZIKV proteases, respectively [25].

Due to its essential role in viral replication and immune evasion, the NS2B/NS3 serine protease is a highly promising target for developing new therapies against ZIKV and DENV infections. Extensive research is focused on designing inhibitors of this protease as potential therapeutic candidates.

Currently no effective drugs [23] or vaccines against these diseases, ZIKV and DENV are available, the only vaccine approved against DENV, Dengvaxia is restricted to patients with preexisting DENV immunity and for this reason its distribution is limited to endemic area [26]. Therefore, at present the therapy for the treatment of ZIKV and DENV infections, includes only symptomatic treatment or supportive care in a hospital setting.

Therefore, the risk of worldwide spread of ZIKV and DENV still exists, more effort of affording prophylactic or therapeutic agents to block ZIKV transmission is in need.

Several classes of inhibitors targeting the NS2B/NS3 protease have been identified, exhibiting significant promise *in vitro* and, in some cases, *in vivo*. A diverse range of molecular scaffolds has been developed as potential inhibitors of the NS2B/NS3 protease in ZIKV and DENV, with several categories displaying notable activity. These include peptide-based inhibitors, small molecules, natural products and their derivatives, as well as allosteric modulators.

Several alkaloids have been reported to act as inhibitors of the ZIKV NS2B-NS3 protease, including bromocriptine (a derivative of the alkaloid ergoline) [27], hydroxychloroquine (a semisynthetic derivative of quinine) [28] and the bis-indole alkaloids flinderol A and flinderol B (Figure 3.4) [29, 30].

Seven novel berberine derivatives were tested as possible inhibitors of the ZIKV NS2B-NS3 protein, and one presented a high value of binding energy [31]. Additionally, the isoquinoline alkaloid cassiarin D, along with the flavonoids 3′-*O*-methyldiplacone and exiguaflavanone A, in addition to the sesquiterpene lactucopicrin, showed strong anchoring properties with the NS3 helicase of ZIKV [32].

A total of 38 flavonoids was subjected to molecular docking and molecular dynamics simulation studies against the ZIKV NS2B-NS3 protease. According to the authors, epigallocatechin gallate, epigallocatechin gallate-7-O-glucopyranoside, epigallocatechin gallate-4’-O-α-glucopyranoside,

isoquercetin, rutin, and sanggenon O were capable of interacting with the catalytic triad (His51, Asp75 and Ser135) from the active site of the ZIKV NS2B-NS3 protease. These compounds showed stability in the active site of the protein ligand complex [33].

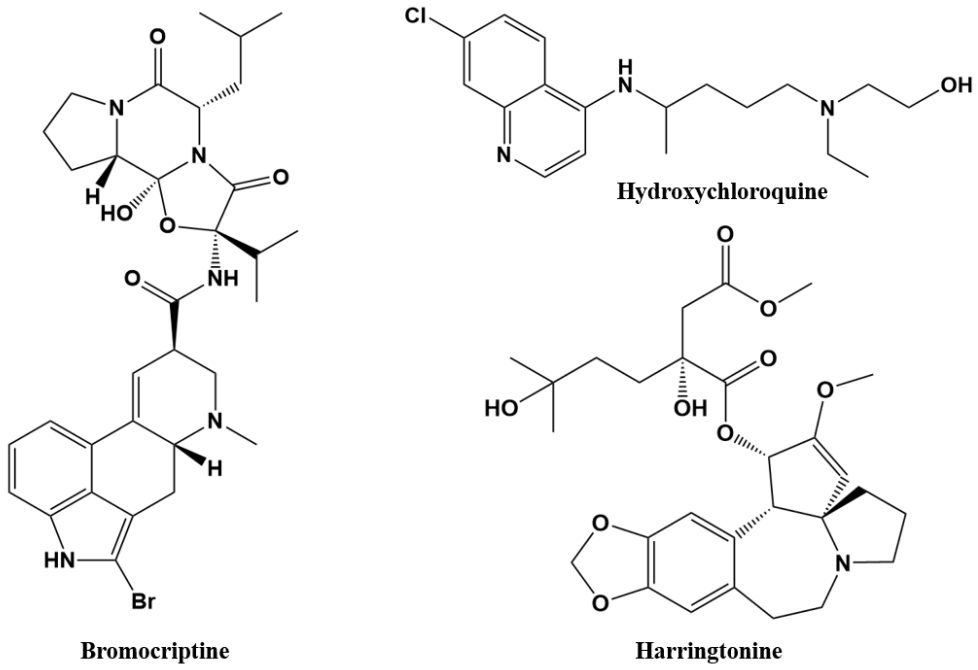

Figure 3.4. Structure of **Bromocriptine**, **Hydroxychloroquine** and **Harringtonine**: natural alkaloids targeting NS2B-NS3 protease inhibition.

Another class of inhibitors against viral protease NS2B/NS3 is represented by peptide boronates [34]. Among which the most active inhibitor is Bz-Nle-Lys-Arg-Arg-B(OH)$_2$ (Figure 3.5, a) that shows a K_i value of 0.043 μM against the viral protease. The introduction of this new electrophilic warhead led to an increase in inhibitory potency, being responsible of a 1000-fold enhancement in affinity. Another dipeptide endowed with the boronic acid moiety is Bz-(4-CH_2NH_2)Phe-Arg-B(OH)$_2$ (Figure 3.5, b), which showed K_i values of 0.051 and 0.04 ± 0.06 μM against DENV and ZIKV proteases, respectively.

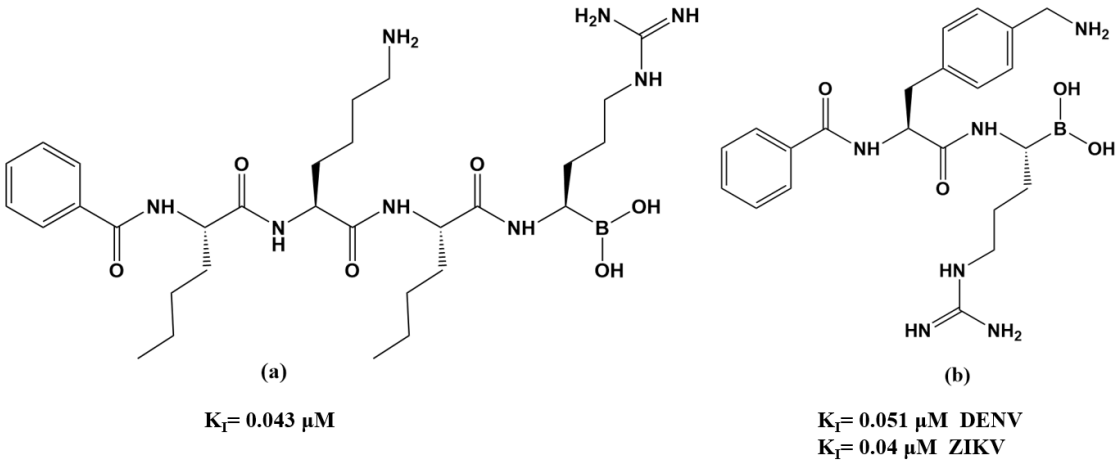

Figure 3.5. Peptidomimetics (**a**) and (**b**) containing a boronic acid as a warhead.

Concerning the development of ZIKA and DENGUE NS2B/NS3 protease inhibitors, in this study, we present the design and synthesis of a small library of piperazine-derived small molecules as potential inhibitors of the Flaviviridae NS3 protease, a well-established therapeutic target for antiviral development. By employing a privileged structure-based approach, these compounds were carefully designed, and their antiviral properties were evaluated using a live-virus cell-based phenotypic assay against ZIKV and DENV, leading to the identification of promising lead candidates. These compounds demonstrated significant antiviral activity, highlighting their potential as broad-spectrum inhibitors for flavivirus infections.

3.1.2 Results and Discussion

3.1.2.1 Design

The design of the new antiviral compounds was inspired by the previous experience of our collaborator's research group in synthesizing piperazine-based scaffolds, which had proven effective in anti-adenovirus activity [35, 36].

Building on this expertise, we utilized piperazine as a key structural element to develop novel inhibitors targeting the Flaviviridae NS3 protease.

Piperazines are six-membered cyclic structures featuring two nitrogen atoms at the 1st and 4th positions, while the remaining positions are occupied by carbon atoms.

This structure provides a large polar surface area, relative structural rigidity, and both hydrogen bond donors and acceptors.

These features often contribute to enhanced water solubility, improved oral bioavailability, and favorable ADME (absorption, distribution, metabolism, and excretion) properties. Additionally, they can lead to greater target affinity and specificity, making piperazine a valuable scaffold in drug design [37, 38]. The nitrogen atoms impart basicity to the piperazine core, making it a versatile building block for medicinal chemists. This unique structural property facilitates the development of novel bioactive molecules with a wide range of pharmacological potential [39].

Nowadays, various piperazine derivatives are discovered and have been used for several biological activities like antidepressant [40], antipsychotic [41], anticancer [42] antibacterial [43] and anti-inflammatory [44] (Figure 3.6)

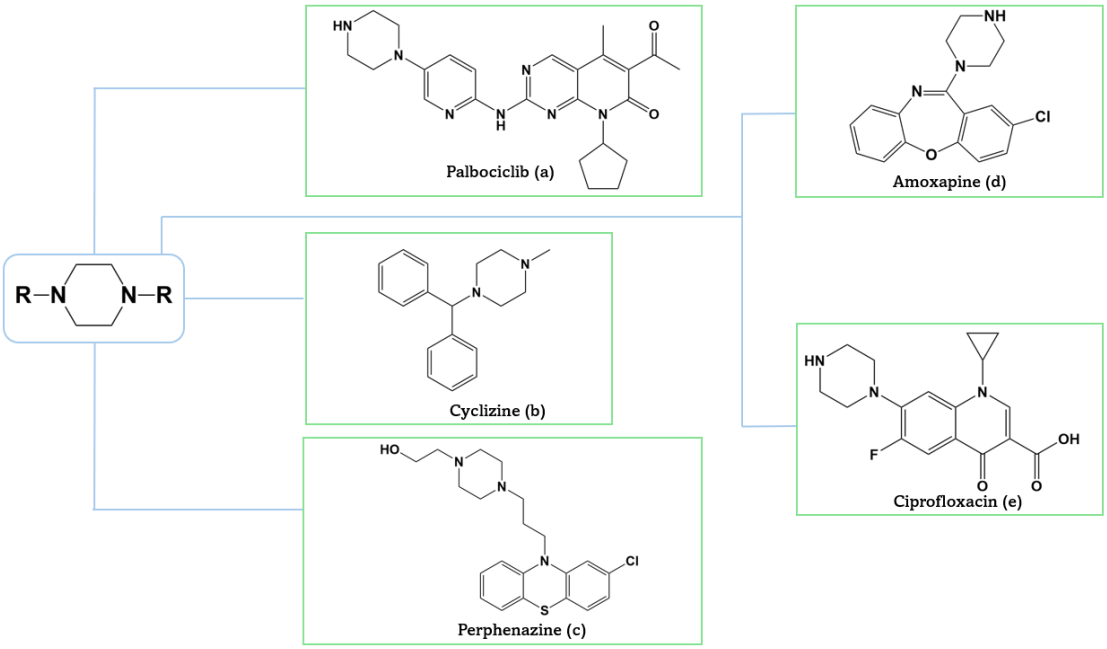

Figure 3.6. Piperazine derivatives used as anticancer (**a**), anti-inflammatory (**b**), antipsicotic (**c**), antidepressant (**d**) and anti-bacterial (**e**).

Due to the relevance of the piperazine ring in the biological activity of compounds [45], we chose to retain it as the central core.

Building on previous research by our collaborators at the University of Seville, which focused on the development of potent antiviral agents with a piperazine scaffold, two new piperazine-derived compounds were identified (Figure 3.7).

Building on their expertise in developing potent antiviral agents with a piperazine scaffold, our collaborators at the University of Seville have identified two novel piperazine-derived compounds.

These compounds, designed through a strategic, privileged structure-based approach, demonstrated significant promise as broad-spectrum antiviral agents against Flaviviruses, including ZIKV and DENV, while exhibiting minimal cytotoxicity. Their antiviral efficacy was assessed using a live-virus, cell-based phenotypic assay [46].

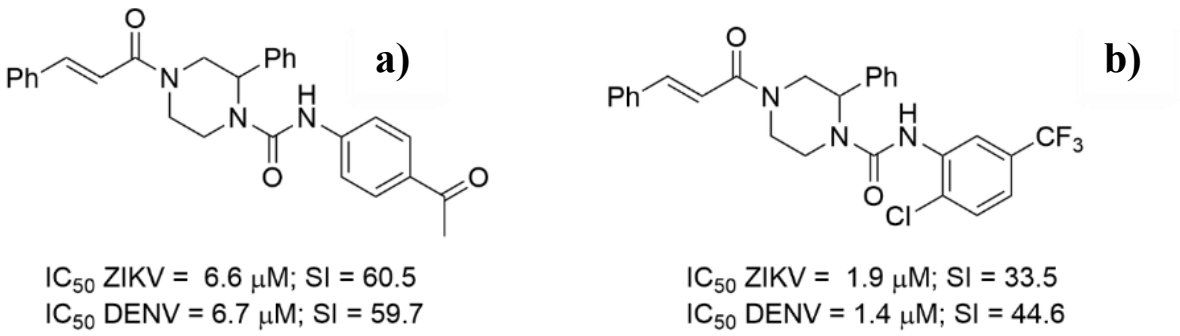

Figure 3.7. Two piperazine-derived compounds identified as the most promising lead compounds

Following these promising results, we have initiated an optimization process to preserve the molecular complexity of these compounds while designing new analogues aimed at enhancing antiviral efficacy and maintaining a low toxicity profile.

We have successfully synthetized novel small molecules with potential antiviral activity. The common structural feature is the unsubstituted piperazine ring, which serves as the main backbone, functionalized at the N-1 position with various urea or sulphonamide groups and at the N-4 position with different acyl groups. (Figure 3.8)

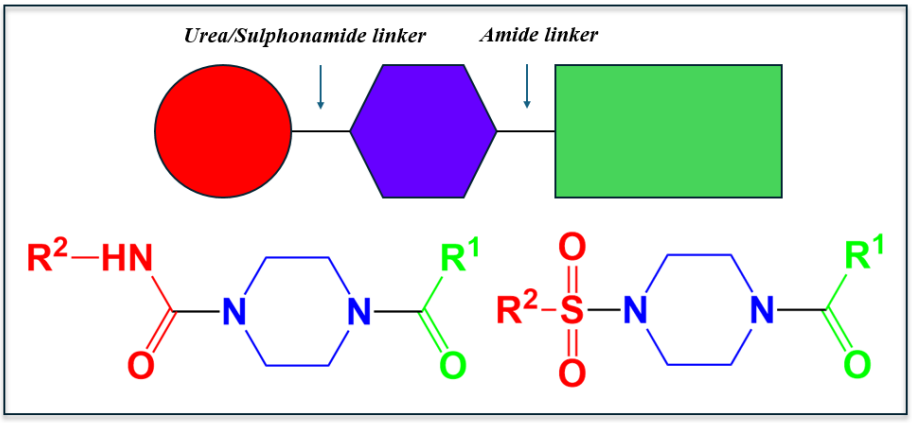

Figure 3.8. General structure of 4-acyl-1-substituted piperazine urea derivatives.for the development of potential piperazine-derived antiflavivirus agents

3.1.2.2 Synthesis

On the amine function at the N-4 position, four different acyl residues were introduced: 1,4-benzodioxane-5-carbonyl (**A**), 1,1'-biphenyl-4-carbonyl (**B**), 5-chloro-2-hydroxybenzoyl (**C**) and 3-phenoxybenzoyl (**D**) (Figure 3.9).

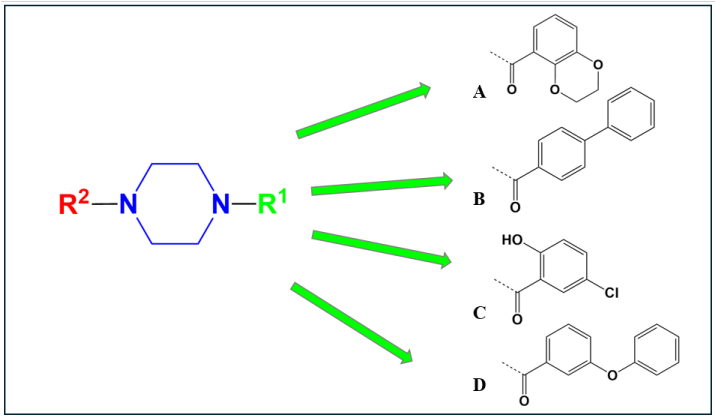

Figure 3.9. Structures of the acyl group at the N-4 position

Concerning the urea function in the N-1 position, the following groups were chosen: 2,4-dimethoxyphenylcarbamoyl (**E**), 2-chloro-5-(trifluoromethyl)phenylcarbamoyl (**F**), 3,5-dichlorophenylcarbamoyl (**G**), 4-chlorophenyl carbamoyl (**H**) and 2-chloro-4-nitrophenylcarbamoyl (**I**) (Figure 3.10).

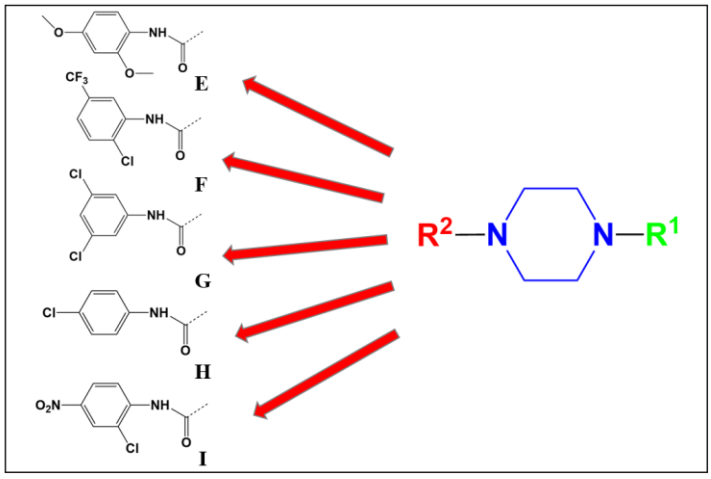

Figure 3.10. Structures of the carbamoyl group at the N-1 position

The 2-chloro-5-(trifluoromethyl)phenylcarbamoyl group was successfully employed in a study to identify piperazine derivatives against human adenovirus (HAdV) infection [35].

This group is also present in the structure of compound (**b**) (Figure 3.7, compound **b**) active against both Zika virus (ZKV) and Dengue virus (DENV).

Furthermore, the 2-chloro-4-nitrophenyl ring is present in Niclosamide, a well-known inhibitor of ZIKV infection which acts after viral entry, probably during the viral RNA replication phase [47].

To enhance chemical diversity, we replaced the urea group with a sulphonamide by introducing sulfonyl chloride groups. Several prototypes were synthesized, incorporating a variety of functional groups, including 4-chloro-2-nitrophenylsulfonyl (**L**), 4-chlorophenylsulfonyl (**M**), 4-methoxyphenylsulfonyl (**N**), 2,4-dimethoxyphenylsulfonyl (**O**), and 4-nitrophenylsulfonyl (**P**) (Figure 3.11).

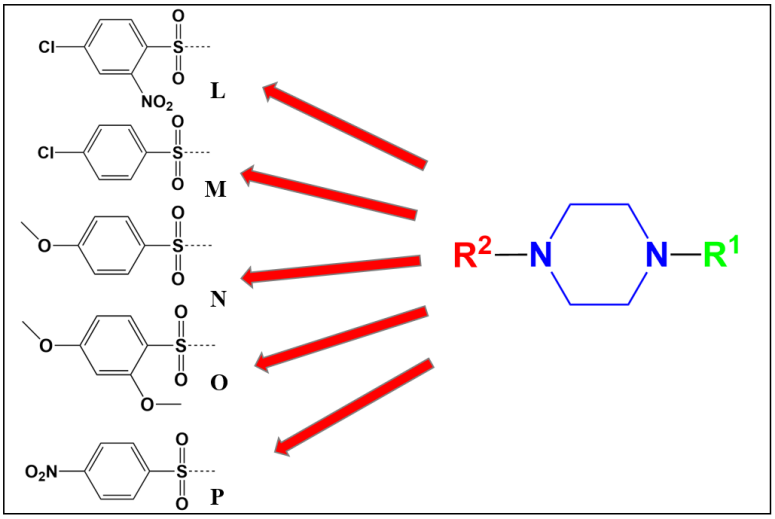

Figure 3.11. Structure of sulfonyl groups at the N-1 position

A) Urea and sulphonamide derivatives

The preparation of the new family of small molecules starts from the commercial compound 1-Boc-piperazine (**1**). The reaction of compound **1** with different carboxylic acid, in the presence of EDCI/HOBt introduced the acyl group to the other nitrogen, producing the N-acylated derivatives (**2-5**).

For the introduction of the urea or sulphonamide function at the N-1 position , compounds **2-5** were treated with CF_3COOH to remove the Boc protective group. The resulting deprotected products **6-9** were characterized by Mass Spectrometry and used directly in the next reaction without purification. The reaction of the acylated derivatives (**6-9**) with the appropriate isocyanate or sulphonyl chloride gave compounds **10-28**. All reactions were performed at room temperature. The synthetic pathway is illustrated in Scheme 3.1, and the final compounds are summarised in the Table 3.1.

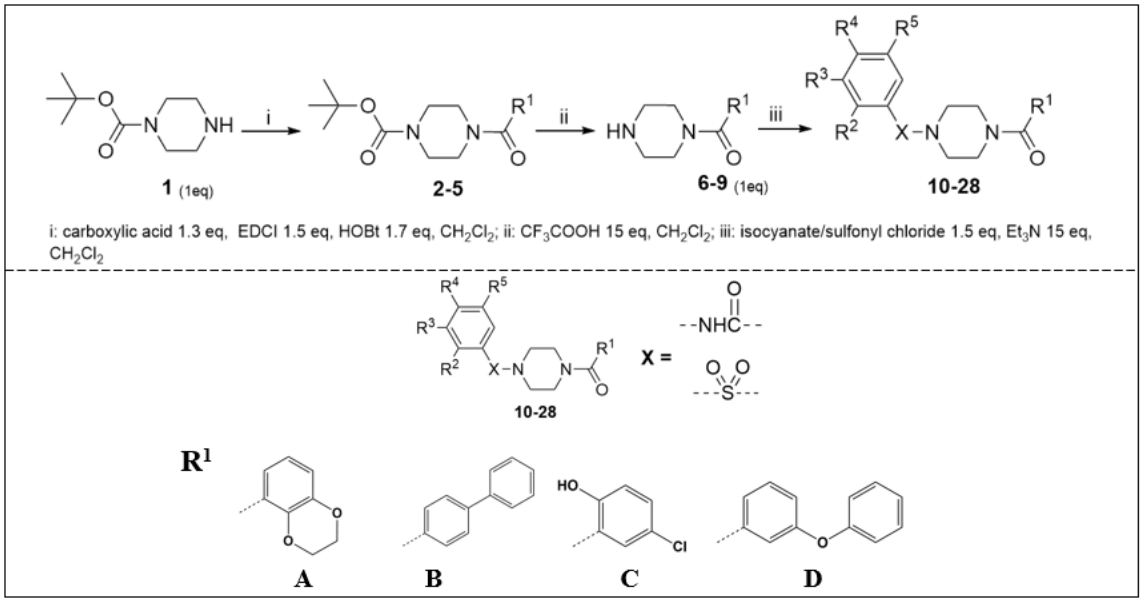

Scheme 3.1. Synthesis of urea and sulphonamide derivatives (**10-28**).

Compounds **10–28** were purified by column chromatography and characterized using nuclear magnetic resonance (NMR) spectroscopy and high-resolution mass spectrometry (HRMS).

Table 3.1. Final compounds **10-28**

Comp.	R^1	R^2	R^3	R^4	R^5	X	Yield%
10	A	Cl	H	NO_2	H	-NHCO-	68
11	A	Cl	H	H	CF_3	-NHCO-	70
12	A	OCH_3	H	OCH_3	H	-NHCO-	73
13	A	H	Cl	H	Cl	-NHCO-	88
14	B	Cl	H	NO_2	H	-NHCO-	65
15	B	Cl	H	H	CF_3	-NHCO-	74
16	B	OCH_3	H	OCH_3	H	-NHCO-	66
17	C	Cl	H	NO_2	H	-NHCO-	68
18	C	Cl	H	H	CF_3	-NHCO-	58
19	D	Cl	H	H	CF_3	-NHCO-	60
20	A	NO_2	H	Cl	H	-SO_2-	83
21	A	H	H	Cl	H	-SO_2-	74
22	A	H	H	OCH_3	H	--SO_2-	83
23	A	OCH_3	H	OCH_3	H	-SO_2-	65
24	B	NO_2	H	Cl	H	-SO_2-	72
25	B	H	H	Cl	H	-SO_2-	77
26	B	OCH_3	H	OCH_3	H	-SO_2-	69
27	B	H	H	NO_2	H	-SO_2-	85
28	D	NO_2	H	Cl	H	-SO_2-	78

The compounds **10-28** were purified by column chromatography and obtained with high purity and yields.

B) Adamantyl urea derivatives

Adamantane, a highly symmetrical polycyclic hydrocarbon, has proven to be a valuable scaffold in drug design due to its unique structural features. Its rigid cage-like structure and lipophilic properties make it an ideal candidate for developing a variety of therapeutic agents.

Adamantane moiety is widely employed in medicinal chemistry to enhance lipophilicity, and metabolic stability of the drugs, thereby improving their pharmacokinetics.

Additionally, the rigid structure of adamantane helps to protect functional groups from metabolic degradation, extending the drug's half-life [48-51].

Drugs incorporating adamantane, such as amantadine, rimantadine, tromantadine, and memantine, were among the first to be introduced to clinical practice. These compounds have been used in the treatment of viral infections, including Influenza A and herpes, as well as neurological disorders like Parkinson's disease and Alzheimer's disease.

Based on these features, we chose to incorporate the adamantylcarbamoyl group at the N-1 position of our compounds to evaluate their antiviral activity. (Scheme 3.2; Table 3.2).

Scheme 3.2 illustrates the synthetic pathway for the preparation of the adamantyl urea derivatives. Boc-piperazine is acylated using four different carboxylic acids (A-D) to produce compounds **2-5**. Selective deprotection with trifluoroacetic acid yielded amine derivatives **6-9**. These derivatives (**6-9)** were then reacted with adamantyl isocyanate to afford compounds **29-32,** which were obtained in high yields following purification by column chromatography.

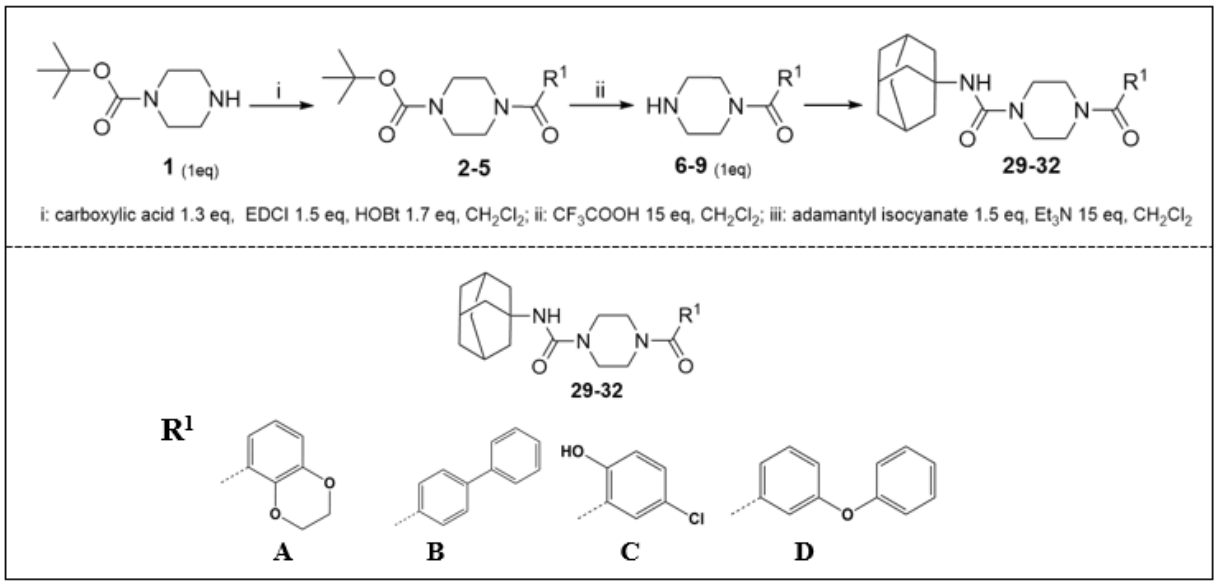

Scheme 3.2. Synthesis of adamantyl urea derivatives **29-32**

The final compounds are summarised in the Table 3.2.

Table 3.2 Final compounds **29-32**.

Comp.	R^1	Yield %
29	A	75
30	B	78
31	C	83
32	D	69

The compounds **29-32** were purified by column chromatography and obtained with high purity and yields.

C) Proline derivatives

Proline derivatives have been extensively studied in antiviral research, with some studies showing that modifications to proline structure can improve biological activity. For example, proline-based peptidomimetics have shown inhibitory effects on viral replication, particularly by targeting protease enzymes critical to viral life cycles. Recent research has also focused on proline analogues as potential

inhibitors of the SARS-CoV-2 main protease (Mpro), a critical target in the context of the COVID-19 pandemic.

The unique cyclic structure of proline can contribute to the development of potent antiviral agents when incorporated into larger, bioactive molecules [52].

Several studies have highlighted the antiviral potential of proline and its derivatives. Notably, gem-dimethyl bicyclic proline serves as a crucial structural component in antiviral drugs like Nirmatrelvir, Boceprevir, and Narlaprevir (Figure 3.12).

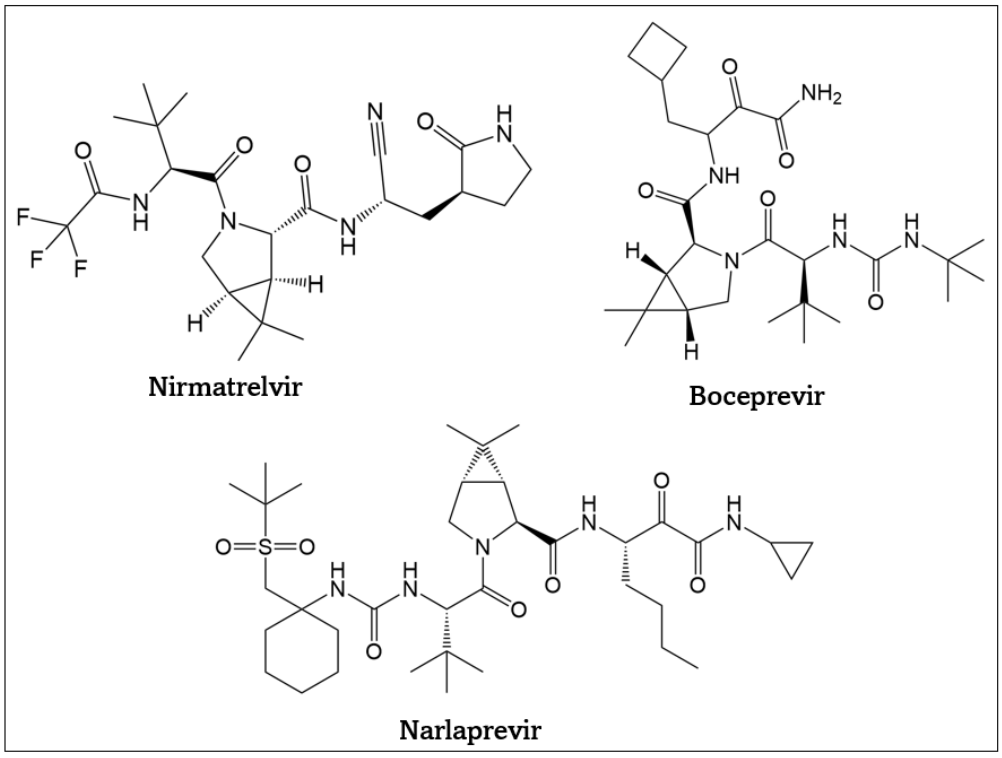

Figure 3.12. Structure of Nirmatrelvir, Boceprevir and Narlaprevir

These compounds play a key role as intermediates in antiviral therapies, particularly by inhibiting viral proteases critical to the replication of viruses such as Hepatitis C and SARS-CoV-2 [53].

In particular, proline-based compounds have demonstrated also allosteric inhibition of Zika and Dengue virus NS2B/NS3 proteases . Millies et al. synthesized a novel inhibitor scaffold that targets

a shared allosteric site in flavivirus NS2B/NS3 proteases, showing efficacy in *in vitro* studies [54] (Figure 3.13).

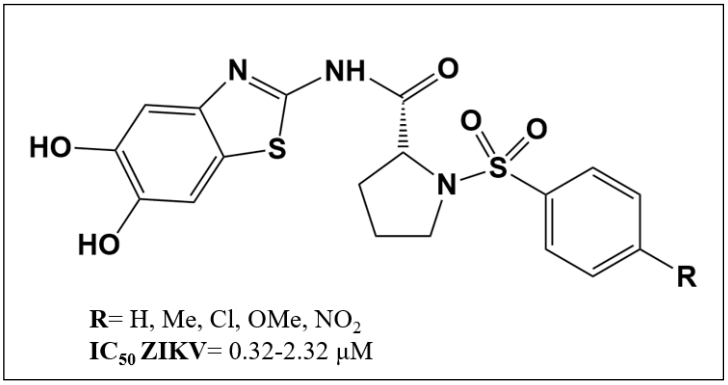

Figure 3.13. Structure of novel proline derivative inhibitor against ZIKV

Zhou and coauthors [55], developed a series of linear dipeptides that was screened against NS2B-NS3pro from DENV2. Among these, one compound comprising Met-Pro sequence exhibited an excellent activity anti-DENV2, with IC_{50} and Ki values of 1.2 ± 0.4 and 4.9 μM, respectively (Figure 3.14).

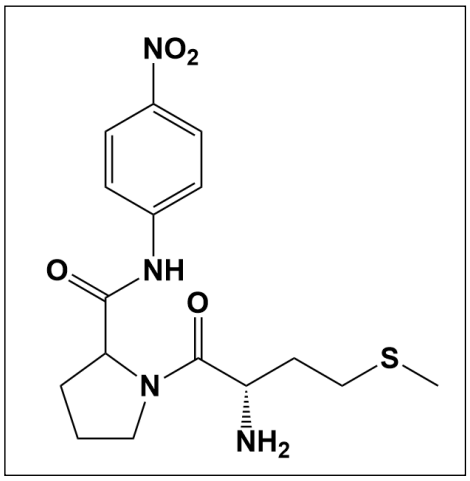

Figure 3.14. Structure of Methionine-proline dipeptide

Given the importance of this ring structure, an additional round of optimization was undertaken to design a second series of inhibitors. The goal was to increase molecular complexity by integrating an amino acid and an acyl group, both connected through amide bonds, within a single molecule.

The synthetic strategy centered on incorporating two biologically relevant motifs onto the nitrogen atoms of the piperazine ring, aiming to enhance antiviral potency while maintaining low cytotoxicity. To synthesize the piperazine derivatives substituted at the N-1 position with proline (**34-36**) in substitution of the urea or sulphonamide function, the route outlined in Scheme 3 was followed. The Boc protecting group on the N-acylated intermediates (**2**,**4**,**5**) was removed using trifluoroacetic acid (CF_3COOH), exposing the free nitrogen atom. This nitrogen was then functionalized by coupling the N-acylated derivatives (**6**, **8**, **9**) with N-Boc-L-proline as shown in Scheme 3. The coupling reaction was facilitated by EDCI and HOBt, which activated the carboxyl group of the proline. After purification by column chromatography, the final compounds **33-35** were successfully obtained. (Scheme 3.3, Table 3.3).

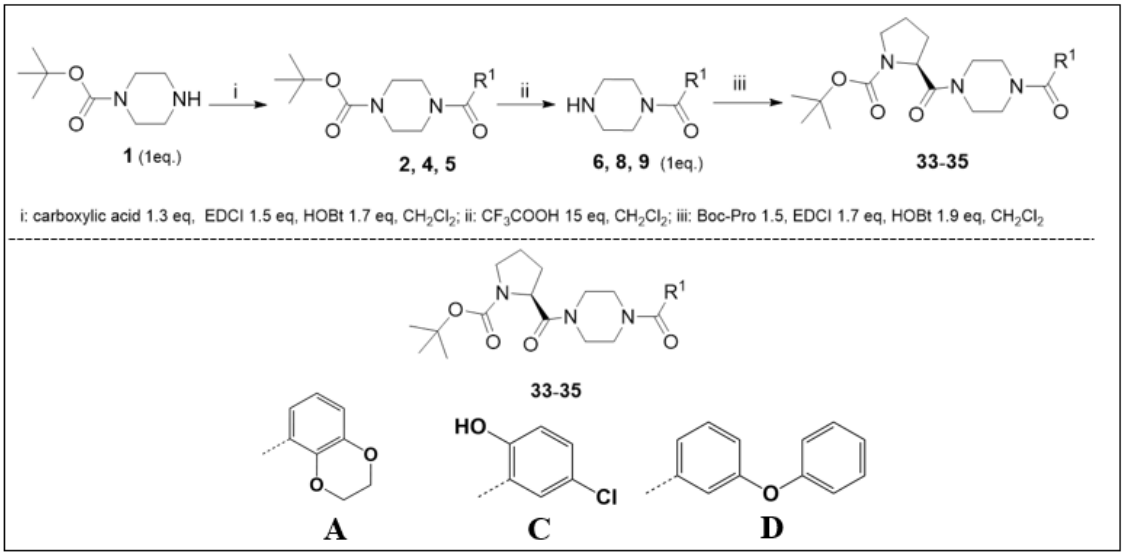

Scheme 3.3. Synthesis of Proline-based compounds

The final compounds are summarised in the Table 3.3.

Table 3.3. Final compounds **33-35**

Comp.	R^1	Yield %
33	A	82
34	C	75
35	D	70

Subsequently, the Boc protecting group was removed from the compounds **33**–**35** using trifluoroacetic acid, affording the corresponding deprotected proline-based derivatives **36**–**38** (Scheme 3.4). The nitrogen atom of proline in compounds **36–38** was then functionalized by reacting these derivatives with 2-chloro-5-trifluoromethylphenyl isocyanate, to introduce the carbamoyl group. This reaction resulted in the formation of the final products **39–41**. All reactions were carried out at room temperature (Scheme 3.4; Table 3.4).

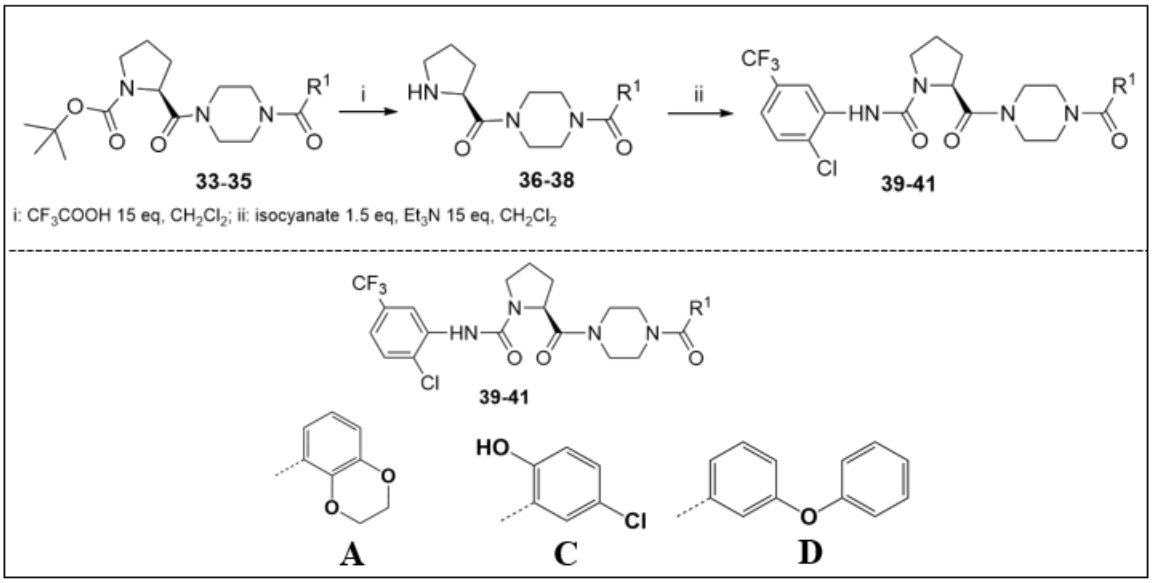

Scheme 3.4. Synthesis of Proline-based derivatives

The final compounds are summarised in the Table 3.4.

Table 3.4. Final compounds **39-41**

Comp.	R^1	Yield %
39	A	55
40	C	58
41	D	49

Compounds **39–41** were purified by column chromatography and characterized by nuclear magnetic resonance (NMR) and mass spectrometry (MS), with the spectral data confirming their proposed structures.

3.1.2.3 *In vitro* essay

The antiviral screening of the synthesized compounds was conducted at the Department of Medical Biotechnology at the University of Siena under the supervision of Dr. Ilaria Vicenti and her research team. This initial evaluation was critical in determining the antiviral potential of the compounds against viruses from the Flaviviridae family, laying the foundation for further investigation and optimization of these promising molecules.

First, the cytotoxicity of the compounds was assessed using the hepatoma cell line (Huh7), which is also employed to evaluate their antiviral activity against Zika (ZIKV) and Dengue (DENV) viruses. For each compound, 4-fold serial dilutions were performed, and after three days, cell viability was measured using a cell titer assay that quantifies luminescence emission. The results were normalized against a vitality control and a death control to determine the concentration inhibiting 50% of cell viability (CC_{50}).

Subsequently, starting from the first non-cytotoxic dose (approximately CC_{90}), 4-fold serial dilutions were conducted for each compound, followed by infection of the cells with ZIKV and DENV. Antiviral activity was evaluated after 72 hours using an immunodetection assay (ELISA) to quantify the viral envelope protein. The results were expressed as half-maximal inhibitory concentrations (IC_{50}), normalized against cell controls (CC) and virus controls (VC). Sofosbuvir (SOF) was used as a reference compound to validate the antiviral assay (Figure 3.15).

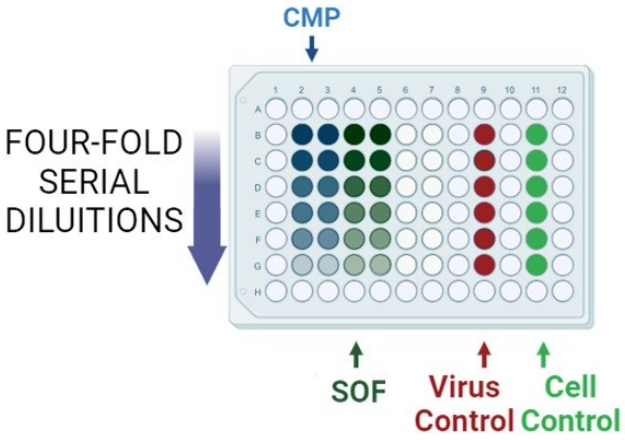

Figure 3.15. Illustration of dilution assay to evaluate *in vitro* antiviral activity of CMPs Against ZIKV and DENV.

Table 3.5 presents the most active compounds against both Zika and Dengue viruses, as well as those specifically effective against Zika.

Table 3.5. Cytotoxic profile and antiviral activity of compounds (**2-5** and **10-32**) *in vitro*. Sofosbuvir, tested in each assay was used as reference control. Experiments were performed in Huh-7 cell line.

Comp	CC_{50}[a] (μM)	IC_{50}[b] (μM) ZIKV	SI[c] ZIKV	IC_{50} (μM) DENV	SI[c] DENV
2	> 200	NA	-	NA	-
3	> 200	NA	-	NT	-
4	> 200	43.7±3.6	>4.6	NA	-
5	52	NA	-	NT	-
10	32	NA	-	NT	-
11	>200	27.9±5.3	>7.2	NA	-
12	>200	38.7±0.7	>5.2	NA	-
13	53	5.1±0.0	10.4	NA	-
14	>200	4.6±0.7	>43.8	11.7±2.2	>17.1
15	>200	1.6±0.0	>125.0	3.8±0.7	>52.7
16	>100	NA	-	NT	-
17	39.1	NA	-	NT	-
18	32.4	NA	-	NT	-
19	50	NT	-	NT	-
20	156	13.2±0.4	11.8	33.8±3.3	4.6
21	>100	NA	-	NT	-
22	>100	NA	-	NT	-
23	>100	NA	-	NT	-
24	>200	3.2±0.9	>62.5	NA	-
25	>100	NA	-	NT	-
26	>200	2.7±0.7	>74.1	NA	-
27	Tox	NT	-	NT	-
28	>100	NA	-	NT	-
29	182	48.1±0.3	3.8	67.9±5.4	2.7
30	133	NA	-	NT	-
31	>100	2.7±0.1	>37.0	8.9±0.8	>11.2
32	31.5	NT	-	NT	-
SOF	>200	3.7±5.5	>54.1	4.3±1.4	>46.5

[a] Half-maximal cytotoxic concentration (CC_{50}). The results represent means of triplicate experiments.
[b] Half-maximal inhibitory concentration (IC_{50}). The results represent means ± Standard deviation of two independent experiments performed in triplicate
[c] The selectivity index value was determined as the ratio of CC_{50} to IC_{50} for each compound.
NA: Not active
NT: Not tested

Anti-ZIKV activity was observed in the micromolar range in 11 out 27 compounds that compose the library that has been tested with a median [IQR] IC_{50} of 23 [1.6–43.7] µM and a mean SI of 64 [3.8–125.0]. Five of them were phenylurea derivatives with different groups at the aromatic ring (**11**-**15**) and two were adamantyl urea derivatives (**29** and **31**). Three sulphonamide derivatives were active (**20**, **24** and **26**). Related to the acyl group at N-4, 1,4-benzodioxane-5-carbonyl and 1,1'-biphenyl-4-carbonyl groups showed activity, being more active those with the biphenyl moiety, such as 2-chloro-5-trifluromethylphenyl urea derivatives, **15** IC_{50} 1.6 µM vs **11** 27.9 µM; 2-chloro-4-nitro phenyl urea derivatives, **14** IC_{50} 4.6 µM vs **10** not active and 4-chloro-2-nitrophenyl sulphonamide derivatives **24** IC_{50} 3.2 µM vs **20** 13.2 µM.

Anti-DENV activity was also observed in the micromolar range in 5 of the tested compounds with a median [IQR] IC_{50} of 36 [3.8–67.9] µM and a mean SI of 28 [2.7–52.7]. Four urea derivatives, **14** (2-chloro-4-nitro phenyl) and **15** (2-chloro-5-trifluromethylphenyl) both with the biphenyl moiety at N-4, and adamantyl urea derivatives **29** (1,4-benzodioxane-5-carbonyl at N-4) and **31** (5-chloro-2-hydroxybenzoyl at N-4). Compound **20** presented 4-chloro-2-nitrophenyl sulphonamide at N-1.

The activity and the security profile were better (lower IC_{50} and higher CC_{50}) against ZIKV than those against DENV. This can be observed in Figure 3.16, that presents a comparison of compounds **14**, **15**, and **31** which exhibit activity against both Zika and Dengue viruses. Sofosbuvir was used as a reference to validate the antiviral activity.

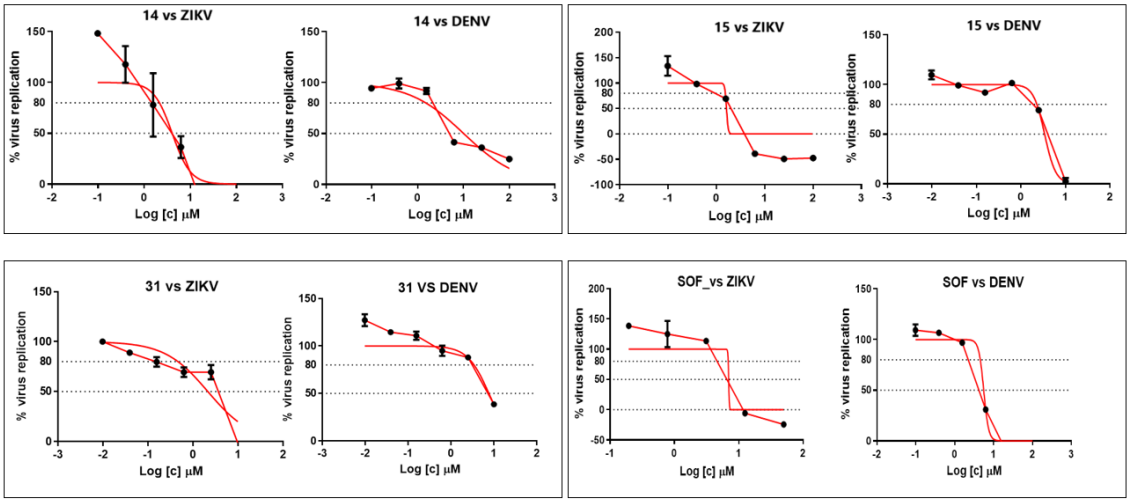

Figure 3.16. Inhibitory activity of compound **14, 15, 31** and Sofosbuvir used as reference compound against ZIKV and DENV in cell culture. The micromolar compound concentration is expressed as logarithm on x-axis, the viral replication is expressed on y-axis as percentage. The normalized curve for each compound derives from 2 independent experiments performed in triplicate.

3.1.2.4. Docking studies

To confirm whether the inhibitors target the viral protease and support our hypothesis that this protein could serve as a potential target for our compounds (based on our design and prior research findings), molecular docking analyses were conducted on the most promising compounds for both viruses.

These studies were conducted by the Structural Bioinformatics and High-Performance Computing (BIO-HPC) Research Group from the Universidad Católica de Murcia under the supervision of Dr. Horacio Pérez-Sánchez and his research team

They performed docking calculations using AutoDock Vina [56] and LeadFinder [57] algorithms to study and establish the most promising compounds in the Zika and Dengue target proteins.

Docking scores and interactions were studied to check the compounds' binding affinity in the Zika and Dengue NS2B/NS3 Protease active sites.

For the docking score, they considered the scores obtained by each docking algorithm separately and the mean value between both. It was also calculated the ESSENCE Docking score, which considers the RMSD between both poses and gives a more accurate interaction value.

A) Zika Virus NS2B/NS3 Protease Molecular Modeling

The results obtained by docking show that the compounds with lower IC_{50} against ZKV are correlated with those molecules with higher binding affinity values (Mean affinity and ESSENCE scores) and interactions with critical residues in the active site detected (Table 3.6)

Table 3.6. Docking results and interactions for the compounds and Zika NS2B/NS3 protease residues by AutoDock Vina and LeadFinder and consensus between both methods.

				LeadFinder					AutoDock Vina		
				Interactions (Å)					Interactions (Å)		
7	**Mean Score**	**ESSENCE-Docking Score**	**Docking Score**	**Hydrophobic**	**Hydrogen Bonds**	**pi-Cation**	**pi-Stacking**	**Docking Score**	**Hydrophobic**	**Hydrogen Bonds**	**pi-Cation**
13	-7.305	**-7.393**	-6.692	**His77 (3.38)**	**Gly159 (2.88), Ser161 (3.78)**	**His77 (5.63, 4.52)**	–	-7.379	Tyr176 (3.77), **Tyr187 (3.38)**	Ser161 (3.08), Asn178 (3.08)	–
14	-7.242	**-5.642**	-7.040	**His77 (3.49)**, Val98 (3.84)	Ala158 (3.62), **Ser161 (4.02)**	**His77 (4.91)**	**Tyr176 (3.88)**	-7.445	Thr1034 (3.55), Pro1102 (3.74), Ala1132 (3.48)	Ser1135 (161) (3.13), Gly1151 (2.96)	Tyr161 (4.1)
15	-7.640	**-7.546**	-7.045	**His77 (3.32)**, Val98 (3.70)			**His77 (4.90)**	-7.640	Asp83 (3.66), Val181 (3.58), **Tyr187 (3.66)**	–	Pro157 (3.19), **Tyr176 (3.11)**, Gly159 (3.64)
20	-7.038	**-6.700**	-7.063	**His77 (3.91)**	Lys80 (3.21), Gly159 (3.64)	**His77 (3.41)**	–	-7.014	Val181 (3.92), **Tyr161 (3.33)**	**His77 (2.72)**, **Gly159 (3.11)**, **Ser161 (2.96)**	–
24	-7.503	**-13.003**	-7.716	**His77 (3.63)**, Val98 (3.64)	Gly159 (3.84), **Ser161 (2.82)**	–	**Tyr187 (5.14)**	-7.383	**His77 (3.8)**, **Tyr 187 (3.65, 3.82)**	Ser161 (3.73)	
26	-7.522	**-13.378**	-7.623	His77 (3.71), Val98 (3.75)	Ala158 (3.37), **Ser161 (3.17)**, Gly179 (4.00)	–	**His77 (4.55)**	-7.329	**His77(3.66)**, Tyr187 (3.72, 3.74)	Ser161 (3.08)	
31	-7.896	**-14.906**	-7.728	**His77 (3.63)**, Ala158 (3.62), **Tyr176 (3.84)**, **Tyr187 (3.31, 3.81, 3.37, 3.56)**	**Ser161 (2.43)**, **Asn178 (2.84, 1.87)**	**His77 (4.82)**	–	-8.063	**Tyr187 (3.49)**	Asp101 (4.75)	**His77 (4.75)**

Compounds with lower IC_{50} values, such as **15**, **26**, and **31**, achieved the highest ESSENCE scores. Additionally, these compounds demonstrated interactions with key residues in the active site, including His77 and Ser161 [34]. Compound **20**, detected as a more inactive compound, was ranked last in Mean Binding Affinity scores.

Figures 3.17 and 3.18 show the interactions and poses obtained for most active compound in the active site of the protease.

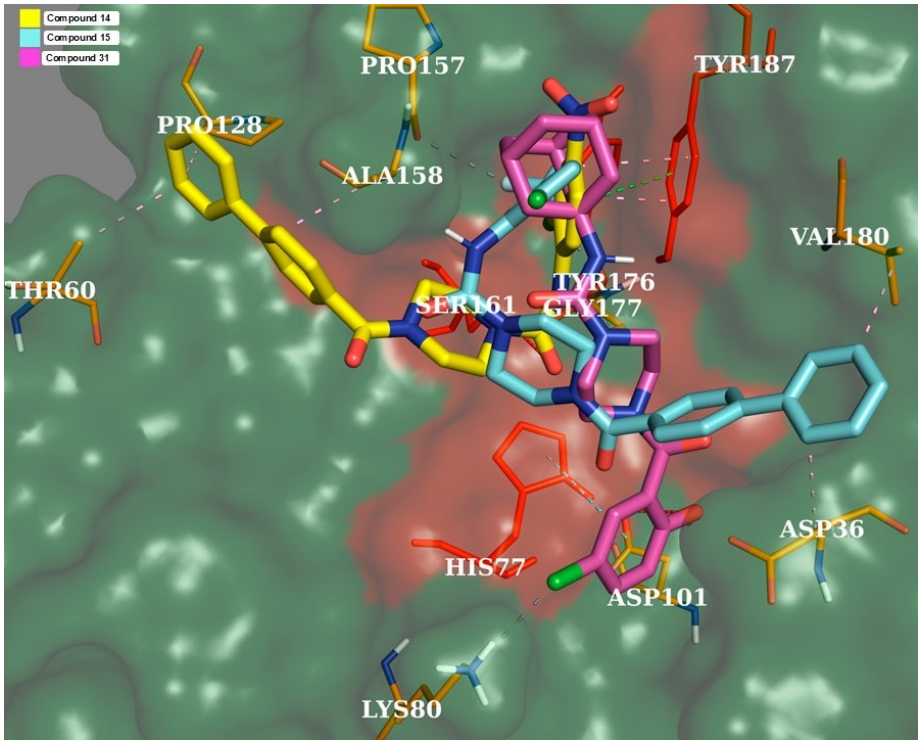

Figure 3.17. Results obtained from the docking calculation performed by AutoDock Vina software for Zika NS2B/NS3 protein against the active compounds **14** (yellow), **15** (green) and **31** (purple). The figure also shows the interactions between the compounds and the active site: hydrophobic interactions (pink), hydrogen bonds (red), π-stacking (green), and halogen bonds (grey).

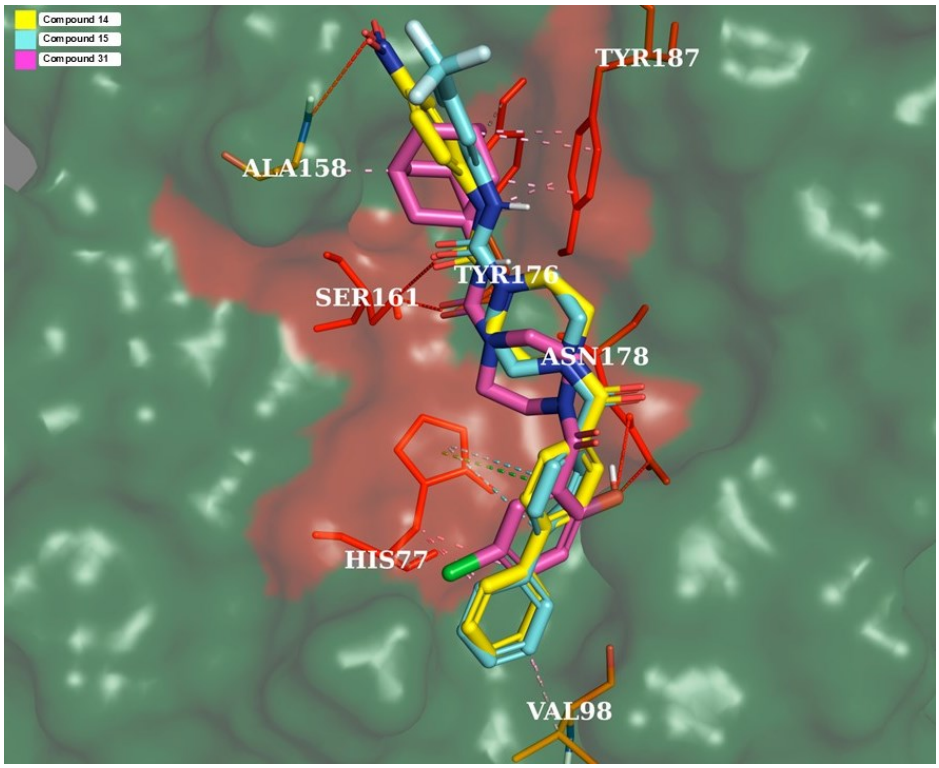

Figure 3.18: Results obtained from the docking calculation performed by LeadFinder software for Zika NS2B/NS3 protein against the active compounds **14** (yellow), **15** (green) and **31** (purple). The figure also shows the interactions between the compounds and the active site: hydrophobic interactions (pink), hydrogen bonds (red), π-stacking (green), and halogen bonds (grey).

B) Dengue Virus NS2B/NS3 Protease Molecular Modeling

Corresponding to Dengue NS2B/NS3, the ESSENCE score exhibits a strong correlation with the experimental IC_{50} values. Compounds **15** and **31**, with ESSENCE scores of -8.150 and -8.417 respectively, demonstrated more stability and stronger interactions with the NS2B/NS3 active site compared to compounds **14** and **20**, which showed lower antiviral inhibition.

Furthermore, compound **31** interacts with some crucial residues, such as a hydrophobic interaction with Asp75 and forming a hydrogen bond interaction with Asn152 [58].

Also, **20** compound's lowest activity can be justified by its lack of critical residue interactions and the lowest Mean Docking and ESSENCE energy scores.

Table 3.7 shows the docking values calculated and the interactions detected in each case.

Table 3.7. Docking results and interactions for the compounds and Dengue NS2B/NS3 protease residues by AutoDock Vina and LeadFinder and consensus between both methods.

				LeadFinder				AutoDock Vina		
				Interactions (Å)				Interactions (Å)		
Compound	**Mean Score**	**ESSENCE-Docking Score**	**Docking Score**	**Hydrophobic**	**Hydrogen Bonds**	**Halogen Bonds**	**Docking Score**	**Hydrophobic**	**Hydrogen Bonds**	**Halogen Bond**
14	-8.166	**-6.356**	-8.013	Lys73 (3.39), Leu76 (3.75, 3.32), Val154 (3.16)	Trp83 (2.92), Thr120 (3.05)	**Asn152 (3.09)**	-8.319	Lys74(3.98, 3.57, 3.69), Ile123 (3.53), Val154 (3.52), Ala164 (3.28), Asn167 (3.82)	Thr118 (2.92), Val155 (3.92)	
15	-8.150	**-8.348**	-7.712	Lys74 (3.85, 3.71), Leu76 (3.41), Val154 (3.94), Ala164 (3.47)	Lys73 (3.6)	Val72 (3.73)	-8.588	Lys74 (4.00), Val154 (3.71), Ala164 (3.63), Asn167 (3.76)		Lys73 (3.15)
20	-7.194	**-5.043**	-6.671	Leu128 (3.18), Pro132 (3.25)	Gly153 (2.85)	Phe130 (3.47)	-7.717	Val72 (3.93), Lys73 (3.84), Ile123 (3.68), Val154 (3.55), Ala164 (3.53), Asn167 (3.80)	Lys73 (3.19), Thr118 (3.21), Thr120 (2.83)	
31	-8.063	**-8.417**	-8.108	**Asp75 (3.24),** Ile123 (3.96), Asn167 (3.45)	Lys73(3.82), Thr120 (3.58), **Asn152 (3.37),** Asn167 (3.31)		-8.019	Lys74 (3.68), Leu76 (3.77), Thr120 (3.29), Val155 (3.54)	Thr120 (3.33, 2.92), Asn167 (3.00)	

Figures 3.19 and 3.20 show the interactions and poses obtained for most active compounds in the active site of the protease.

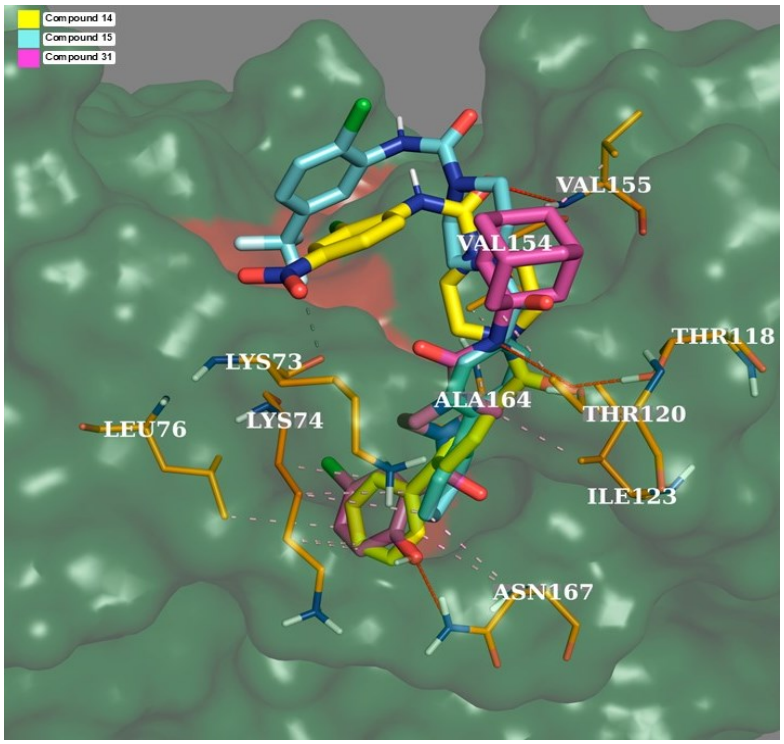

Figure 3.19. Results obtained from the docking calculation performed by AutoDock Vina software for Dengue NS2B/NS3 protein against the active compounds **14** (yellow), **15** (green) and **31** (purple). The figure also shows the interactions between the compounds and the active site: hydrophobic interactions (pink), hydrogen bonds (red), π-stacking (green), and halogen bonds (grey)

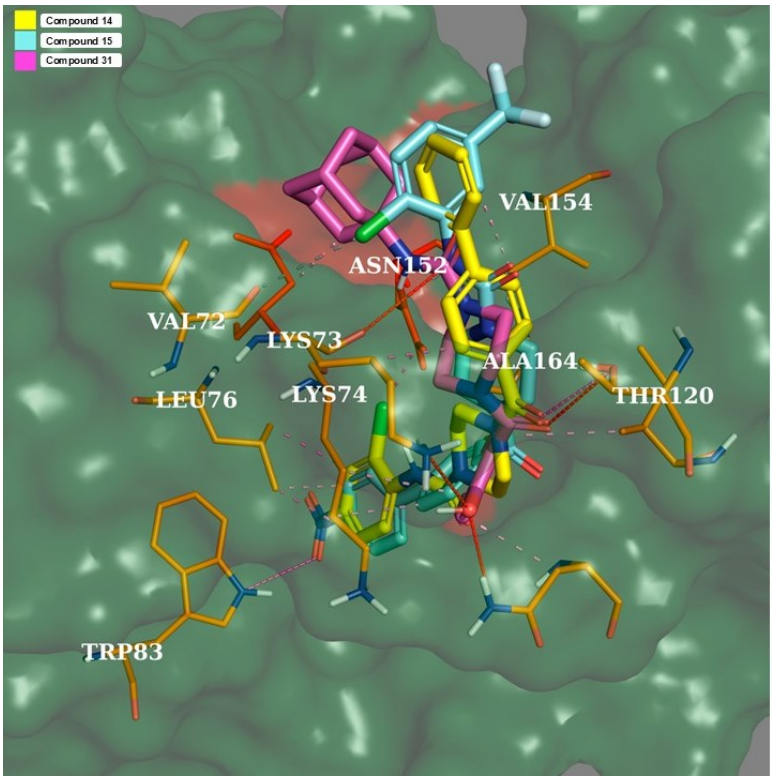

Figure 3.20. Results obtained from the docking calculation performed by LeadFinder software for Dengue NS2B/NS3 protein against the active compounds **14** (yellow), **15** (green) and **31** (purple). The figure also shows the interactions between the compounds and the active site: hydrophobic interactions (pink), hydrogen bonds (red), π-stacking (green), and halogen bonds (grey).

3.2 Piperazine derivatives as potential anticancer agents

3.2.1 Background

Cancer, characterized by the uncontrolled proliferation of abnormal cells, poses a major global public health concern, emphasizing the need for new and effective treatments [42].

Heterocyclic compounds play a central role in numerous scientific fields, including medicinal and pharmaceutical chemistry, due to their structural diversity and biological relevance. Representative examples such as purines, pyridines, and piperazines have demonstrated wide-ranging applications in drug development, agrochemistry, and industrial processes [59–62].

The FDA reports that approximately 60% of small molecule drugs are nitrogen-containing heterocycles. In 2014, the top 25 nitrogen-containing medications alone generated over $50 billion in annual sales [63, 64].

Among these heterocycles, piperazine stands out as a crucial structural component in numerous pharmaceutical agents, recognized for its remarkable therapeutic versatility. It is one of the most prevalent chemotypes in modern drug discovery, ranking third in importance among nitrogen-containing molecules, following piperidine and pyridine [65, 66]. Novel piperazine derivatives and piperazine-containing frameworks have been widely studied for their antiproliferative activity against breast cancer (Figure 3.21)[67-69]. Hybrid compounds containing pharmacophores with 4-piperazinyl-quinoline-isatin derivatives (Figure 3.21, **a**) exhibited cytotoxicity against two human breast cancer cell lines (MDA-MB468 and MCF7), with IC_{50} values in the range of 10.34–66.78 μM [67].

Three of the compounds tested showed two- to four-fold lower cytotoxic effects in noncancerous breast cell lines (184B5 and MCF 10A). Thiouracil amide derivatives bearing a piperazine ring (Figure 3.21, **b**) were synthesized and screened for cytotoxic activity in MCF7 cells, with IC_{50} values in the range of 18.23 to 100 μM [68].

The most active compounds, characterized by tolyl or halophenyl groups attached to the piperazine ring, demonstrated two- to three-fold lower cytotoxicity in normal MCF 10A cells compared to cancer cells. Also, small molecules such as 1-(4-substitutedbenzoyl)-4-(4-chlorobenzhydryl) piperazine derivatives (Figure 3.21, **c**) with different groups at the aryl amide function showed cytotoxic activity against breast cancer cells (MCF7, BT20, T47D, and CAMA-1) and other types of cancer cell lines [69]. These compounds were also evaluated in normal breast epithelial cells (MCF-12A). The IC_{50} values were in the range of 0.31–120.52 μM against breast cancer cell lines and 6.6–299.66 μM against normal breast cells (Figure 3.21).

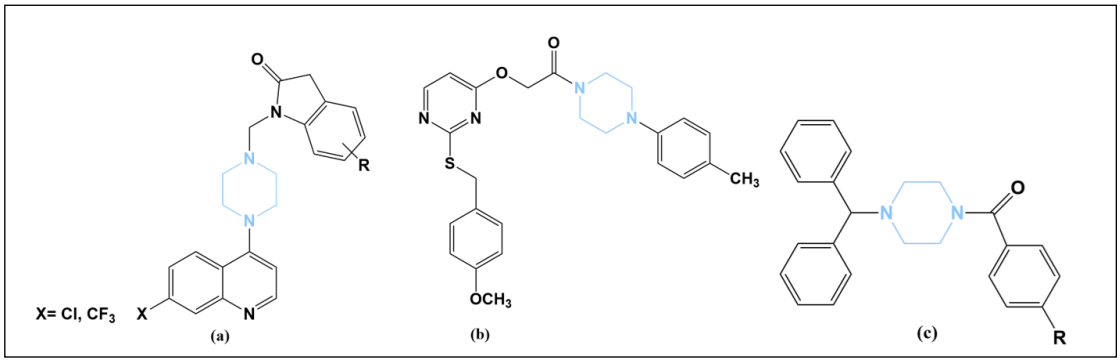

Figure 3.21. General structures of piperazine-derived compounds **a**–**c** showing piperazine moiety in blue.

The urea function also constitutes a relevant moiety in anticancer agents. Biaryl-urea-based kinase inhibitors have been approved in anticancer therapy, for example, sorafenib (**d**) and its analogue, regorafenib (**e**). The development of novel biaryl-urea-based small molecules as potential kinase inhibitors has been increasingly highlighted with the clinical success of these compounds [70], such as compound **(f)**, a multikinase inhibitor that showed significant anticancer activity against diverse cancer cells [71] (Figure 3.22).

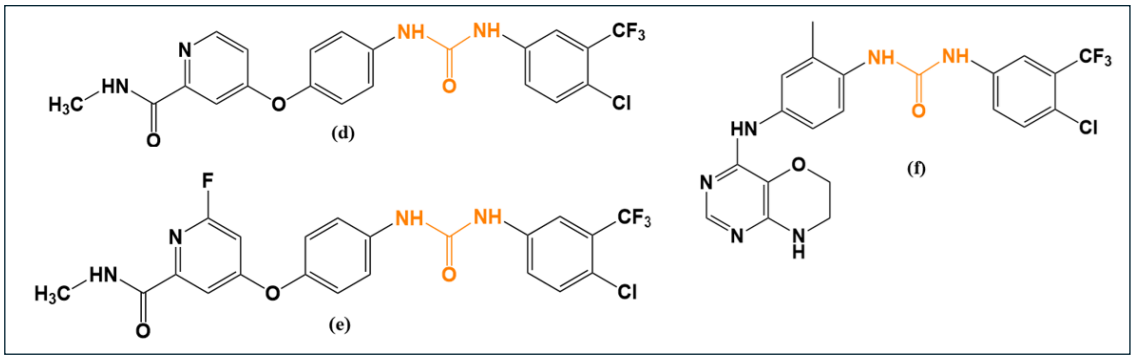

Figure 3.22. Structures of biaryl-urea kinase inhibitors (**d-f**) with the urea function highlighted in orange.

The piperazine moiety has proven to be a crucial element in the development of various anticancer compounds, with several FDA-approved piperazine derivatives demonstrating its efficacy in cancer treatment like Dasatinib, Olaparib, Imatinib [72] (Figure 3.23).

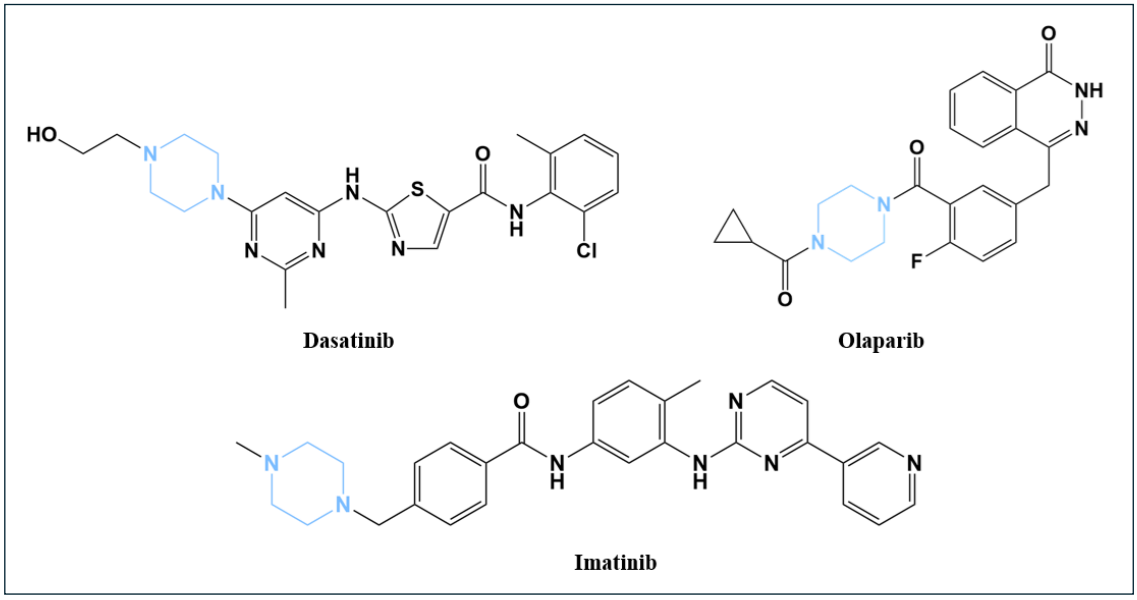

Figure 3.23 Structures of FDA-approved anticancer drugs based on piperazine rings

Piperazine-based compounds can exert anticancer effects through multiple mechanisms. These derivatives interact with DNA, inhibiting key enzymes such as telomerase and topoisomerase-1, thereby maximizing cytotoxicity. Notably, piperazine derivatives are recognized for activating the mitochondrial pathway to induce apoptosis in cancer cells, demonstrating strong in-vivo anticancer activity. Furthermore, they reduce the risk of thrombosis by acting as plasminogen activator inhibitor-1 (PAI-1) inhibitors, limiting thrombin generation and enhancing activated protein C (APC) function.

These compounds also inhibit cell survival via the Akt hyperphosphorylation pathway and induce cell cycle arrest by activating the p53 protein. They exhibit a 50% inhibition of cell proliferation and have chemo preventive properties by blocking the prostaglandin cascade and suppressing COX-2 overexpression, both of which are linked to carcinogenesis [72-75] (Figure 3.24).

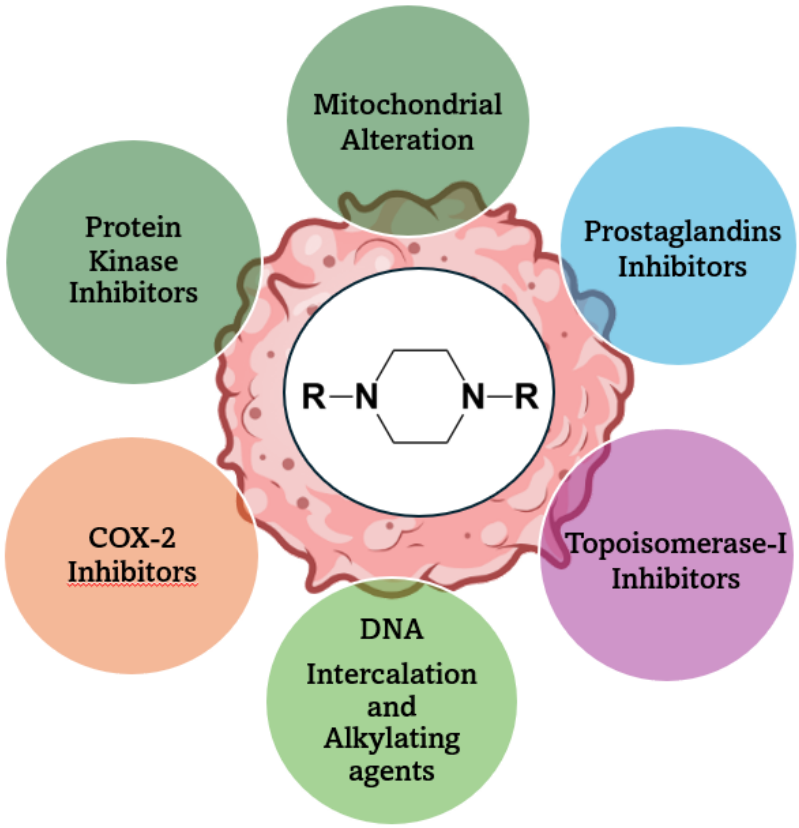

Figure 3.24. Potential molecular targets for piperazine derivatives in anticancer therapy

Recognizing the potential of piperazine-based drugs in cancer therapy, we synthesized a small library of novel piperazine derivatives to evaluate their anticancer properties. In a preliminary study, both the newly synthesized compounds and previously developed piperazine-based molecules, originally designed as antiviral agents, were tested on breast cancer cell lines. This evaluation aimed to explore their dual potential as anticancer and antiviral agents, leveraging the therapeutic significance of the piperazine ring and aryl urea functionalities—key structural motifs frequently associated with anticancer drugs.

3.2.2 Results and Discussion

In this study, we synthesized and characterized a small library of eight molecules, with the aim of investigating their anti-proliferative activity against breast cancer cell lines.

The piperazine ring is retained as the central core, attached to three previously used carboxylic acids (1,1'-biphenyl-4-carbonyl (**B**), 5-chloro-2-hydroxybenzoyl (**C**) and 3-phenoxybenzoyl (**D**)), and further functionalized with a limited selection of aromatic isocyanates and sulfonyl chlorides (Scheme 3.5). Specifically, we opted to incorporate two distinct substituents on the phenyl ring: a chlorine (Cl) group and a methoxy group.

Akkoc et al. [76] demonstrated that introducing a 3,4-dichlorophenyl group onto the piperazine moiety significantly enhanced potency compared to the standard drug 5-fluorouracil (5-FU), with IC_{50} values of 2.92, 3.42, and 9.33 μM against HUH7, MCF7, and HCT116 cell lines, respectively. The compound exhibited IC_{50} values of 2.92, 3.42, and 9.33 μM against these cell lines. Meanwhile Zhang *et al.* [77] reported that the presence of a methoxy group on the benzene ring resulted in promising inhibition across various cancer cell lines, highlighting its potential as a key substituent for anticancer activity.

The synthetic pathway began with the acylation of Boc-protected piperazine using three distinct carboxylic acids (**B**-**D**), yielding intermediates **2**-**5**. Subsequent selective deprotection with trifluoroacetic acid generated the amine derivatives **6-9,** whose structures were confirmed via mass spectrometry. These amine intermediates were then used directly, without purification, in the next step, where they were reacted with aromatic isocyanates and sulfonyl chlorides to afford the final compounds **42**-**49**.

The synthesis of these derivatives is reported in Scheme 3.5 and results are displayed in Table 3.8.

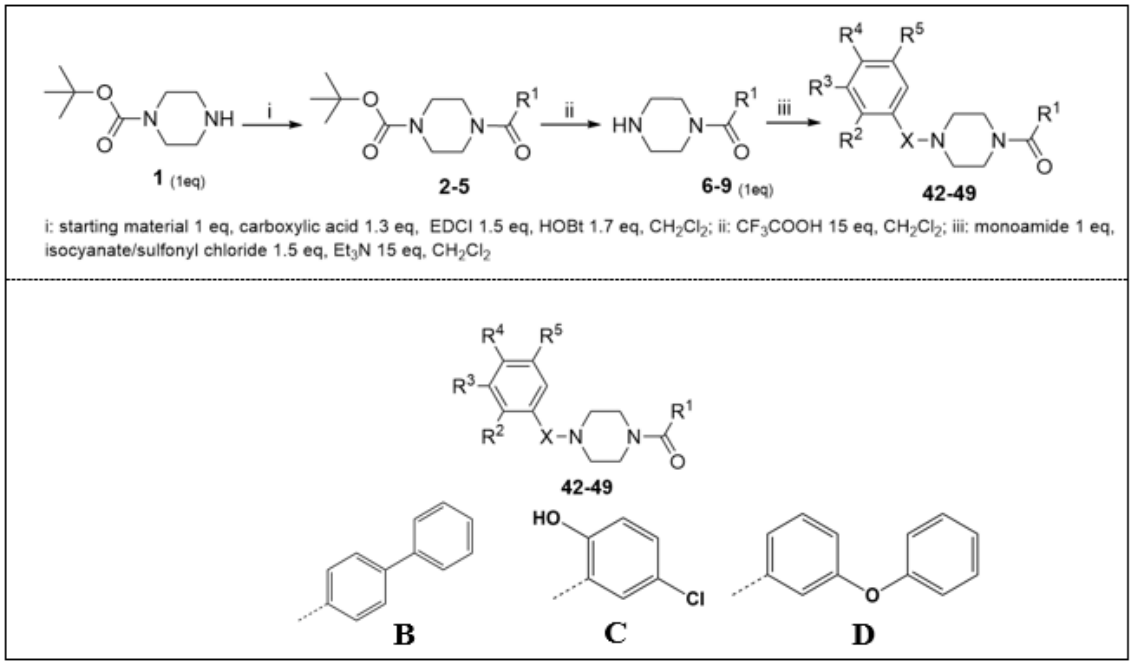

Scheme 3.5. Synthesis of compounds **42-49**

All reactions were performed at room temperature, and the resulting compounds were purified by column chromatography, achieving high yields and purity. The compounds were then characterized by nuclear magnetic resonance (NMR) spectroscopy and mass spectrometry (MS) to confirm their structures.

Table 3.8. Final compounds **42-49**

Comp.	R^1	R^2	R^3	R^4	R^5	X	Yield %
42	**B**	H	Cl	Cl	H	-NHCO-	80
43	**C**	OCH_3	H	OCH_3	H	-NHCO-	73
44	**C**	H	Cl	Cl	H	-NHCO-	86
45	**D**	OCH_3	H	OCH_3	H	-NHCO-	67
46	**D**	H	Cl	Cl	H	-NHCO-	65
47	**B**	H	H	OCH_3	H	$-SO_2-$	72
48	**D**	OCH_3	H	OCH_3	H	$-SO_2-$	62
49	**D**	H	H	OCH_3	H	$-SO_2-$	79

3.2.3 *In vitro* evaluation

The preliminary antiproliferative effects of the synthesized compounds were evaluated using the MTT assay on two breast cell lines: MCF7 (tumor breast cancer cells) and MCF10A (non-tumor, normal breast cells), to assess the cytotoxic and antiproliferative effects of the synthesized compounds. These tests were conducted at the Department of Pharmacy, Health and Nutritional Science at the University of Calabria under the supervision of Professor Catia Morelli and her research team.

The MTT assay is a rapid colorimetric method that uses the tetrazolium salt MTT (3-(4,5-dimethylthiazol-2-yl)-2,5-diphenyl tetrazolium bromide) to evaluate cell viability by targeting only living cells [78].

Cell viability was determined by the reduction of MTT to formazan by metabolically active cells. A significant decrease in viability in MCF7 cells would indicate effective cytotoxicity against breast cancer, while minimal impact on MCF10A cells would suggest selective toxicity, with the compounds targeting cancer cells while sparing normal ones.

We decided to evaluate both newly synthesized compounds and previously developed antiviral agents due to their promising molecular properties, which suggest a dual functionality encompassing both antiviral and anticancer activities.

In very preliminary *in vitro* experiments using the MTT assay, compounds **11**, **13**, **42** and **46** demonstrated the best compromise between efficacy and selectivity. These compounds exhibited a dose-dependent antiproliferative effect against MCF-7 breast cancer cells, reducing their viability, Compounds **11**, **13** and **42** were all highly effective at the concentration of 100 μM, while showing a much lower growth inhibition on MCF10A normal mammary epithelial cells (Figure 3.25). Notably, compound 46 exhibited a similar antiproliferative activity already at a concentration as low as 10 μM

in MCF-7 tumor cells, with minimal effect on MCF-10A normal cells. Compounds **11** and **13** also demonstrated antiviral properties, underscoring their potential for dual therapeutic applications.

Ongoing experiments will confirm the observed selectivity of these compounds toward tumor cells, an essential characteristic for safer anticancer therapies, highlighting their potential as candidates for further development.

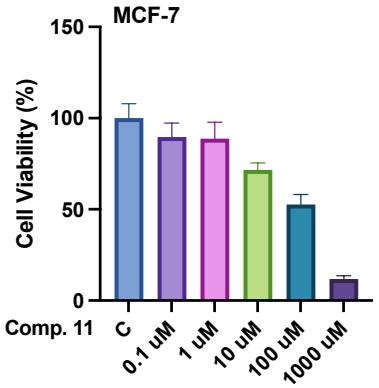
MCF-7
Cell Viability (%)
150
100
50
0
Comp. 11
C
0.1 uM
1 uM
10 uM
100 uM
1000 uM

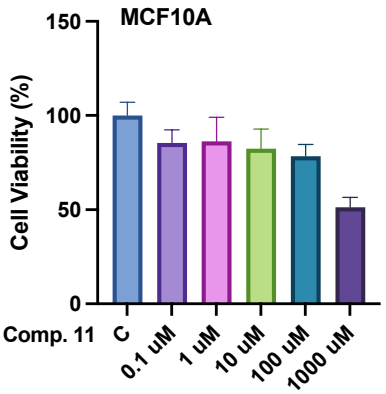
MCF10A
Cell Viability (%)
150
100
50
0
Comp. 11
C
0.1 uM
1 uM
10 uM
100 uM
1000 uM

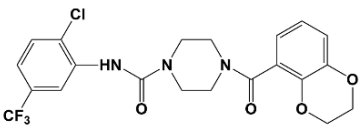
Cl
HN
N
N
O
O
O
CF3

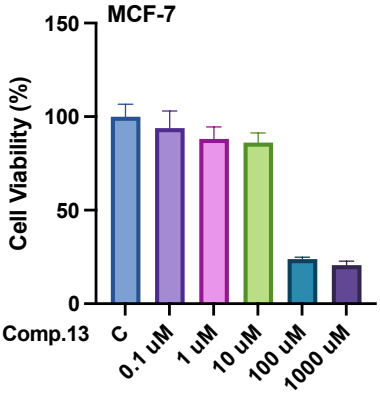
MCF-7
Cell Viability (%)
150
100
50
0
Comp.13
C
0.1 uM
1 uM
10 uM
100 uM
1000 uM

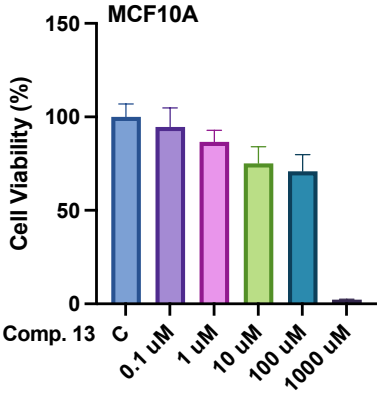
MCF10A
Cell Viability (%)
150
100
50
0
Comp. 13
C
0.1 uM
1 uM
10 uM
100 uM
1000 uM

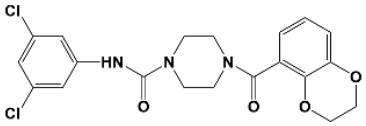
Cl
Cl
HN
N
N
O
O
O

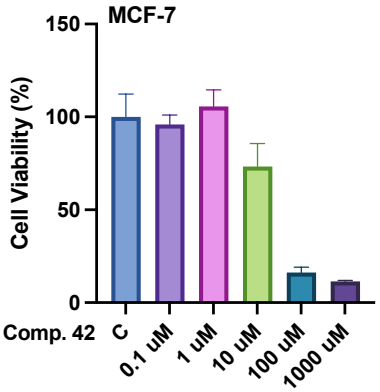
MCF-7
Cell Viability (%)
150
100
50
0
Comp. 42
C
0.1 uM
1 uM
10 uM
100 uM
1000 uM

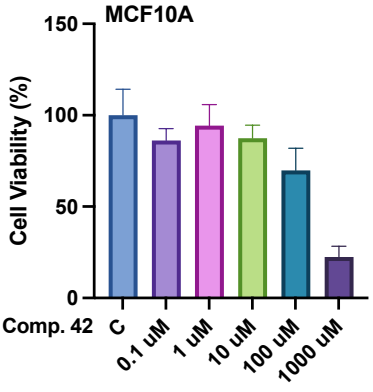
MCF10A
Cell Viability (%)
150
100
50
0
Comp. 42
C
0.1 uM
1 uM
10 uM
100 uM
1000 uM

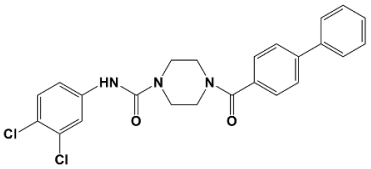
Cl
Cl
HN
N
N
O
O

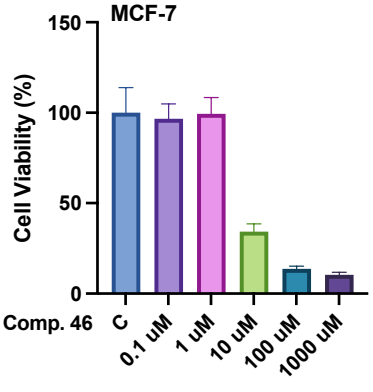
MCF-7
Cell Viability (%)
150
100
50
0
Comp. 46
C
0.1 uM
1 uM
10 uM
100 uM
1000 uM

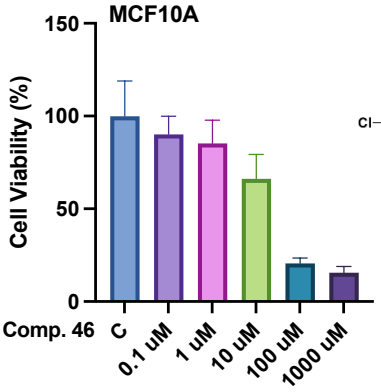
MCF10A
Cell Viability (%)
150
100
50
0
Comp. 46
C
0.1 uM
1 uM
10 uM
100 uM
1000 uM

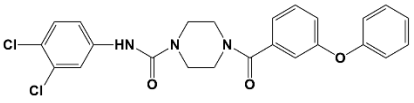
Cl
Cl
HN
N
N
O
O
O

Figure 3.25. Compounds **11**, **13**, **42**, **46** inhibit breast cancer cell growth without affecting significantly normal mammary epithelial cells. Cells were treated with increasing concentrations (0.1, 1, 10, 100, 1000 μM) of the indicated compounds or left untreated (C = control) for 72 hours. The results are expressed as % respect to control cells (C). The values represent the means ± SDs of three different experiments, performed in sestuplicate. ** $p < 0.05$, ** $p < 0.006$, *** $p < 0.001$, **** $p < 0.0001$.*

3.3 Experimental part

3.3.1 Chemistry

3.3.1.1 General Chemistry Methods

All reagents and starting materials were purchased from commercial suppliers and used without further purification. The solvents employed in the reactions were purified following standard procedures and distilled before use. The crude reaction mixtures were concentrated under reduced pressure by removing the organic solvents in a rotary evaporator. Reactions were monitored by thin layer chromatography (TLC) using Kieselgel 60 F254 plates and UV detector for visualization. Flash column chromatography was performed on Silica Gel 60. All reported yields refer to purified products. Melting points were obtained on a GALLENKAMP Melting Point Apparatus MPD350.BM2.5 with open capillaries (Kimax-51°, 1.5–1.8 × 90 mm) and are uncorrected. Mass spectra were recorded on a Orbitrap Elite (Thermo Scientific), a Hybrid Ion trap-orbitrap mass spectrometer capable of acquiring with a resolution higher than 240000, with ESI, HESI, APCI and nanoESI ionization sources.

NMR spectra were recorded at 25 ºC on a Bruker AV500 spectrometer at 500 MHz for ^{1}H and 125 MHz for ^{13}C. The chemical shifts (δ) reported are given in parts per million (ppm) relative to TMS, and the coupling constants (J) are in hertz (Hz). ^{1}H chemical shift values (δ) are referenced to the residual nondeuterated components of the NMR solvents (δ = 2.54 ppm for DMSO-d_6). The ^{13}C chemical shifts (δ) are referenced to deuterated solvent (central peak, δ = 39.5 ppm for DMSO-d_6) as the internal standard. The spin multiplicities are reported as s (singlet), d (doublet), dd (double doublet), t (triplet), q (quadruplet), m (multiplet), or bs (broad singlet).

3.3.1.2. General procedure 1. *N-acylation reaction of 1- tert-butyloxycarbonyl-piperazine (1-Boc-piperazine)* **(2-5)**

To a solution of the appropriate acid (3.9 mmol) in DCM (15 mL), EDCI (4.5 mmol) and HOBt (5.1 mmol) were added, and the mixture was stirred at room temperature for 45 minutes. Subsequently, a solution of 1-Boc-piperazine (3.0 mmol) in DCM was added. The reaction was stirred at room temperature for 72 hours, until TLC showed complete conversion of the starting material. The reaction mixture was sequentially washed with dilute hydrochloric acid, saturated aqueous sodium bicarbonate, and brine. It was then dried over anhydrous Na_2SO_4, filtered, and evaporated to dryness. The resulting compounds were purified by flash column chromatography on silica gel [46].

1-*tert*-butyloxycarbonyl-4-(1,4-benzodioxane-5-carbonyl)-piperazine (2)

The product was isolated as a solid (0.760 g, 99% yield) following purification through column chromatography, using dichloromethane-methanol (60:1) as the eluent; mp = 182-184 °C. ^{1}H NMR (500 MHz, DMSO-d_6) δ 6.97 (dd, J = 8.1, 1.7 Hz, 1H), 6.92 (t, J = 7.7 Hz, 1H), 6.81 (dd, J = 7.3, 1.7 Hz, 1H), 4.33 (s, 4H), 3.74 – 3.52 (m, 2H), 3.51 – 3.32 (m, 4H), 3.30 – 3.16 (m, 2H), 1.47 (s, 9H). ^{13}C NMR (125 MHz, DMSO-d_6) δ 166.23, 154.24, 143.81, 140.04, 125.94, 121.66, 120.08, 118.16, 79.67, 64.65, 64.43, 46.61, 41.45, 28.49. HRMS (m/z): calc. per $C_{18}H_{24}N_2O_5Na$ 371.1577 $[M+Na]^+$; found 371.1567.

1-*tert*-butyloxycarbonyl-4-(1,1'-biphenyl-4-carbonyl)piperazine (3)

The product was isolated as a solid (0.793 g, 99% yield) following purification through column chromatography, using dichloromethane-methanol (60:1) as the eluent; mp = 138-140°C. ^{1}H NMR (500 MHz, DMSO-d_6) δ 7.76 – 7.70 (m, 4H), 7.56 – 7.48 (m, 4H), 7.42 (m, 1H), 3.69-3.52 (m, 2H), 3.47-3.36 (m, 4H), 3.35-3.29 (m, 2H), 1.43 (s, 9H). ^{13}C NMR (125 MHz, DMSO-d_6) δ 169.46, 154.30, 141.82, 139.80, 135.08, 130.43, 129.52, 128.26, 127.28, 127.16, 79.68, 28.51. HRMS (m/z): calc. per $C_{22}H_{26}N_2O_3Na$ 389.1836 $[M+Na]^+$; found 389.1836. HRMS (m/z): calc. per $C_{22}H_{26}N_2O_3Na$ 389.1836 $[M+Na]^+$; found 389.1836.

1-*tert*-butyloxycarbonyl-4-(5-chloro-2-hydroxybenzoyl)piperazine (4)

The product was isolated as a solid (0.800 g, 99 % yield) following purification through column chromatography, using hexane-ethyl acetate (2:1) as the eluent; mp = 137-139 °C. ^{1}H NMR (500 MHz, DMSO-d_6) δ 10.18 (s, 1H), 7.30 (dd, J = 8.8, 2.7 Hz, 1H), 7.21 (d, J = 2.7 Hz, 1H), 6.92 (d, J = 8.8 Hz, 1H), 3.74-3.53 (m, 2H), 3.49-3.29 (m, 4H), 3.27-3.16 (m, 2H), 1.44 (s, 9H).^{13}C NMR (125 MHz, DMSO-d_6) δ 166.07, 154.28, 152.65, 130.36, 128.07, 125.96, 123.11, 117.92, 79.63, 46.56, 43.60, 41.48, 28.48. HRMS (m/z): calc. per $C_{16}H_{21}ClN_2O_4Na$ 363.1082 $[M+Na]^+$; found 363.1084.

1-*tert*-butyloxycarbonyl-4-(3-phenoxybenzoyl) piperazine (5)

The product was isolated as a solid (0.625 g, 84% yield) following purification through column chromatography, using hexane-ethyl acetate (2:1) as the eluent; mp = 97-98 °C. ^{1}H NMR (500 MHz, DMSO-d_6) δ 7.50 – 7.39 (m, 3H), 7.23 – 7.13 (m, 2H), 7.12 -7.05 (m, 3H), 3.66 - 3.48 (bs, 2H), 3.44-3.19 (m, 6H), 1.41 (s, 9H). ^{13}C NMR (125 MHz, DMSO-d_6) δ 168.78, 157.33, 156.54, 154.28, 138.02, 130.79, 130.66, 124.44, 122.16, 119.88, 119.58, 117.09, 79.67, 47.35, 42.05, 28.49. HRMS (m/z): calc. per $C_{22}H_{26}N_2O_4$ Na 405.1785 $[M+Na]^+$; found 405.1784.

3.3.1.3. General procedure 2. *Removal of Boc group* (**6-9** and **36-38**)

To a solution of the Boc derivatives (3.0 mmol) in dry dichloromethane (20 mL) was added the trifluoroacetic acid (45.0 mmol). The reaction mixture was stirred at room temperature until TLC showed that all the starting material had reacted. The reaction mixture was evaporated to dryness and co-evaporated with toluene. The products were detected by mass spectrometry and employed directly for the next synthetic step [46].

1-(1,4-benzodioxane-5-carbonyl)piperazine (6)

The product was obtained as a white solid (0.760 g, 99% yield). HRMS (m/z): calcd. for $C_{13}H_{16}N_2O_3$ 249.2821 $[M+H]^+$; found 249.1201

1-(1,1'-biphenyl-4-carbonyl)piperazine (7) The product was obtained as a white solid (0.790 g, 99% yield). HRMS (m/z): calcd. for $C_{17}H_{18}N_2O$ 267.1492 [M+H] +; found 267.1499.

1-(5-chloro-2-hydroxybenzoyl)piperazine (8)

The product was obtained as a white solid (0.795 g, 99%). HRMS (m/z): calcd. for $C_{11}H_{14}ClN_2O_2$ 241.0738 $[M+H]^+$; found 241.0743.

1-(3-phenoxybenzoyl)piperazine (9)

The product was obtained as a white solid (0,600 g, 96%). HRMS (m/z): calcd. for $C_{17}H_{19}N_2O_2$ 283.1441 $[M+H]^+$; found 283.1447.

1-L-Prolyl-4-(1,4-benzodioxane-5-carbonyl)piperazine (36)

The product was obtained as a white solid (0.245 g, 95%). HRMS (m/z): calcd. for $C_{18}H_{24}N_3O_4$ 346.1761 $[M+H]^+$; found 346.1761.

1-L-Prolyl-4-(5-chloro-2-hydroxybenzoyl)piperazine (37)

The product was obtained as a white solid (0.320 g, 93%). HRMS (m/z): calcd. for $C_{16}H_{21}O_3N_3Cl$ 338.1266 $[M+H]^+$; found 338.1259

1-L-Prolyl-4-(3-phenoxybenzoyl)piperazine (38)

The product was obtained as a white solid (0.255 g, 91%). HRMS (m/z): calcd. for $C_{22}H_{26}O_3N_3$ 380.1969 $[M+H]^+$; found 380.1968.

3.3.1.4. General procedure 3. *General procedure for the synthesis of the urea and sulfonamide derivatives* **10-28, 29-32**, **39-49**.

To a solution of the monoacyl derivative of piperazine (1 mmol) in dry dichloromethane (20 mL) was added triethylamine (15 mmol) and the appropriate isocyanate or sulphonyl chloride (1.5 mmol). The reaction mixture was stirred at room temperature until TLC showed that all the starting material had

reacted. The reaction mixture was then washed sequentially with diluted hydrochloric acid, brine, and dried over anhydrous Na_2SO_4. After filtration, the solvent was removed under reduced pressure. The resulting products were purified by flash chromatography using the appropriate eluent [46].

1-(2-chloro-4-nitrophenylcarbamoyl)-4-(1,4-benzodioxane-5-carbonyl)piperazine (10)

The product was isolated as a white solid (0.148 g, 68% yield) following purification through column chromatography, using dichloromethane-methanol (80:1) as the eluent; mp = 155-157 °C. ^{1}H NMR (500 MHz, DMSO-d_6) δ 8.63 (bs, 1H), 8.32 (d, J = 2.6 Hz, 1H), 8.17 (dd, J = 9.1, 2.6 Hz, 1H), 7.96 (d, J = 9.1 Hz, 1H), 6.94 – 6.85 (m, 2H), 6.79 (dd, J = 7.3, 1.9 Hz, 1H), 4.28 (bs, 4H), 3.77-3.65 (m, 2H), 3.64 -3.52 (m, 2H), 3.51-3.45 (m, 2H), 3.44 - 3.38 (m, 2H). ^{13}C NMR (126 MHz, DMSO) δ 166.30, 154.25, 143.84, 143.80, 142.83, 140.07, 125.90, 125.27, 125.09, 123.65, 123.53, 121.70, 120.13, 118.23, 64.69, 64.44, 46.50, 44.83, 44.89, 41.57. HRMS (m/z): calcd. for $C_{20}H_{19}ClN_4O_6Na$ 469.0885 $[M+Na]^+$; found 469.0875.

1-(2-chloro-5-(trifluoromethyl)phenylcarbamoyl)-4-(1,4-benzodioxane-5-carbonyl) piperazine (11)

The product was isolated as a white solid (0.285 g, 70% yield) following purification through column chromatography, using dichloromethane-methanol (60:1) as the eluent; mp = 211-214 °C. ^{1}H NMR (500 MHz, DMSO-d_6) δ 8.58 (s, 1H), 7.99 (d, J = 1.9 Hz, 1H), 7.76 (d, J = 8.3 Hz, 1H), 7.54 (dd, J = 8.4, 1.9 Hz, 1H), 7.01 – 6.92 (m, 2H), 6.84 (dd, J = 7.3, 1.8 Hz, 1H), 4.34 (s, 4H), 3.79 - 3.69 (m, 2H), 3.66 – 3.56 (m, 2H), 3.54 – 3.49 (m, 2H), 3.35 -3.27 (m, 2H). ^{13}C NMR (125 MHz, DMSO-d_6) δ 166.31, 155.04, 143.84, 140.07, 138.11, 131.99, 130.99, 128.25, 125.94, 122.93, 122.90, 122.11, 121.70, 120.12, 118.21, 64.68, 64.44, 46.55, 44.66, 44.24, 41.54. HRMS (m/z): calc. for $C_{21}H_{19}ClF_3N_3O_4Na$ 492.09084 $[M+Na]^+$; found 492.0901.

1-(2,4-dimethoxyphenylcarbamoyl)-4-(1,4-benzodioxane-5-carbonyl)piperazine (12)

The product was isolated as a white solid (0.147 g, 73% yield) following purification through column chromatography, using dichloromethane-methanol (60:1) as the eluent; mp = 174-176 °C. ^{1}H NMR

(500 MHz, DMSO-d_6) δ 8.38 (s, 1H), 7.79 (d, J = 8.8 Hz, 1H), 7.25 (d, J = 8.7 Hz, 1H), 6.87 – 6.77 (m, 1H), 6.70 (m, 1H), 6.51 (m, 1H), 6.38 (m, 1H), 4.21 (s, 4H), 3.69 (s, 3H), 3.66 (s, 3H), 3.60 – 3.54 (m, 2H), 3.45 – 3.38 (m, 2H), 3.33 – 3.25 (m, 2H) 3.21-3.09 (m, 2H). ^{13}C NMR (125 MHz, DMSO-d_6) δ 166.26, 157.28, 156.04, 155.35, 143.83, 140.05, 125.95, 122.57, 121.69, 121.67, 120.08, 118.16, 104.50, 99.21, 64.67, 64.45, 56.10, 55.73, 46.61, 44.50, 44.03, 41.58. HRMS (m/z): calc. for $C_{22}H_{25}N_3O_6$ Na 450.1636 $[M+Na]^+$; found 450.1638.

1-(3,5-dichlorophenylcarbamoyl)-4-(1,4-benzodioxane-5-carbonyl)piperazine (13)

The product was isolated as a white solid (0.130g, 88% yield) following purification through column chromatography, using dichloromethane-methanol (60:1) as the eluent; mp = 203-205 °C. ^{1}H NMR (500 MHz, DMSO-d_6) δ 9.01 (s, 1H), 7.64 (d, J = 1.7 Hz, 2H), 7.18 (t, J = 1.7 Hz, 1H), 6.98 (dd, J = 8.0, 1.5 Hz, 1H), 6.94 (t, J = 7.7 Hz, 1H), 6.83 (dd, J = 7.3, 1.5 Hz, 1H), 4.33 (s, 4H), 3.77 – 3.68 (m, 2H), 3.64 – 3.53 (m, 2H), 3.52 - 3.46 (m, 2H), 3.35 – 3.25 (m, 2H). ^{13}C NMR (125 MHz, DMSO-d_6) δ 166.27, 154.68, 143.83, 143.53, 140.07, 134.17, 125.90, 121.69, 121.19, 120.14, 118.23, 117.66, 64.68, 64.44, 46.55, 44.44, 44.13, 41.52. HRMS (m/z): calc. for $C_{20}H_{19}Cl_2N_3O_4$ Na 458.0645 $[M+Na]^+$; found 458.0651.

1-(2-chloro-4-nitrophenylcarbamoyl)-4-(1,1'biphenyl-4-carbonyl)piperazine (14)

The product was isolated as a solid (0.337 g, 65% yield) following purification through column chromatography, using hexane-ethyl acetate (1:1.2) as the eluent; mp = 159-161 °C.

^{1}H NMR (500 MHz, DMSO-d_6) δ 8.69 (s, 1H), 8.36 (d, J = 2.6 Hz, 1H), 8.23 (dd, J = 9.1, 2.6 Hz, 1H), 8.02 (d, J = 9.1 Hz, 1H), 7.81 (d, J = 8.3 Hz, 2H), 7.77 (d, J = 8.5 Hz, 1H), 7.60 (d, J = 8.3 Hz, 2H), 7.55 (m, 2H), 7.46 (t, J = 7.4 Hz, 1H), 3.88 – 3.47 (m, 8H). ^{13}C NMR (125 MHz, DMSO-d_6) δ 169.52, 154.29, 143.79, 142.85, 141.88, 139.78, 135.03, 130.43, 129.52, 128.40, 128.33, 127.28, 127.17, 125.31, 125.29, 123.54, 47.36, 44.52, 42.10. HRMS (m/z): calc. for $C_{24}H_{21}ClN_4O_4$ Na 487.1144 $[M+Na]^+$; found 487.1143.

1-(2-chloro-5-(trifluoromethyl)phenylcarbamoyl)-4-(1,1'biphenyl-4-carbonyl)piperazine (15)

The product was isolated as a solid (0.273 g, 74% yield) following purification through column chromatography, using hexane-ethyl acetate (1:1.2) as the eluent; mp = 148-150 °C.

^{1}H NMR (500 MHz, DMSO-d_6) δ 8.59 (s, 1H), 8.01 (d, J = 2.0 Hz, 1H), 7.82 (d, J = 8.1 Hz, 2H), 7.80 -7.73 (m, 3H), 7.60 (d, J = 8.2 Hz, 2H), 7.55 (t, J = 7.8 Hz, 3H), 7.46 (t, J = 7.4 Hz, 1H), 3.90 – 3.42 (m, 8H). ^{13}C NMR (125 MHz, DMSO-d_6) δ 169.53, 155.07, 141.85, 139.80, 138.11, 135.08, 132.01, 131.01, 129.52, 128.40, 128.32, 127.29, 127.17, 125.28, 123.12, 122.90, 122.15, 47.46, 44.33, 42.07. HRMS (m/z): calc. for $C_{25}H_{21}ClF_3N_3O_2$ Na 510.1167 $[M+Na]^+$; found 510.1166.

1-(2,4-dimethoxyphenylcarbamoyl)-4-(1,1'-biphenyl-4-carbonyl)piperazine (16)

The product was isolated as a solid (0.230 g, 66 % yield) following purification through column chromatography, using hexane-ethyl acetate (1:1.2) as the eluent; mp = 130-131 °C.

^{1}H NMR (500 MHz, DMSO-d_6) δ 7.81-7.70 (m, 4H), 7.67 (s, 1H), 7.58 – 7.47 (m, 4H), 7.41 (t, *J* = 7.4 Hz, 1H), 7.34 (d, *J* = 8.7 Hz, 1H), 6.59 (d, *J* = 2.7 Hz, 1H), 6.46 (dd, *J* = 8.7, 2.7 Hz, 1H), 3.78 (s, 3H), 3.74(s, 3H), 3.71- 3.59 (m, 2H), 3.48 - 3.36 (m, 6H). ^{13}C NMR (125 MHz, DMSO-d_6) δ 169.47, 157.28, 156.05, 153.29, 141.80, 139.80, 135.15, 129.52, 128.39, 128.29, 127.28, 127.16, 125.97, 121.69, 104.50, 99.22, 56.11, 55.74, 47.56, 44.11, 42.22. HRMS (m/z): calcd. for $C_{26}H_{27}O_4N_3Na$ 468.1894 $[M+Na]^+$; found 468.1881.

1-(2-chloro-4-nitrophenylcarbamoyl)-4-(5-chloro-2-hydroxybenzoyl)piperazine (17)

The product was isolated as a solid (0.280 g, 68 % yield) following purification through column chromatography, using hexane-ethyl acetate (1:1.2) as the eluent; mp = 201-203 °C.

^{1}H NMR (500 MHz, DMSO-d_6) δ 10.26 (s, 1H), 8.69 (s, 1H), 8.39 (d, *J* = 2.6 Hz, 1H), 8.24 (dd, *J* = 9.1, 2.6 Hz, 1H), 8.04 (d, *J* = 9.1 Hz, 1H), 7.36 (dd, *J* = 8.7, 2.7 Hz, 1H), 7.29 (d, *J* = 2.7 Hz, 1H), 6.98 (d, *J* = 8.7 Hz, 1H), 3.82 – 3.71 (m, 2H), 3.70 – 3.50 (m, 4H), 3.38 – 3.25 (m, 2H). ^{13}C NMR (125 MHz, DMSO-d_6) δ 166.13, 154.27, 152.69, 143.81, 142.84, 130.45, 128.16, 125.93, 125.29, 123.54, 123.14, 117.95, 46.49, 44.84, 44.30, 41.54. HRMS (m/z): calc. for $C_{18}H_{16}O_5N_4Cl_2Na$ 461.0390 $[M+Na]^+$; found 461.0384.

1-(2-chloro-5-(trifluoromethyl)phenylcarbamoyl)-4-(5-chloro-2-hydroxybenzoyl) piperazine (18)

The product was isolated as a solid (0.260 g, 58% yield) following purification through column chromatography, using hexane-ethyl acetate (1:1.2) as the eluent; mp = 121-123 °C.

^{1}H NMR (500 MHz, DMSO-d_6) δ 10.23 (s, 1H), 8.56 (s, 1H), 8.01 (d, J = 1.9 Hz, 1H), 7.76 (d, J = 8.4 Hz, 1H), 7.54 (dd, J = 8.4, 1.9 Hz, 1H), 7.34 (dd, J = 8.7, 2.7 Hz, 1H), 7.26 (d, J = 2.7 Hz, 1H), 6.96 (d, J = 8.7 Hz, 1H), 3.81 – 3.67 (m, 2H), 3.66 – 3.47 (m, 4H), 3.35 – 3.23 (m, 2H). ^{13}C NMR (125 MHz, DMSO-d_6) δ 166.13, 155.04, 152.68, 138.10, 131.99, 130.98, 130.43, 128.51, 128.25, 128.15, 125.97, 125.27, 123.13, 122.88, 122.13, 117.95, 46.53, 44.63, 44.21, 41.57. HRMS (m/z): calc. for $C_{19}H_{16}O_3N_3Cl_2F_3Na$ 484.0413 $[M+Na]^+$; found 484.0407.

1-(2-chloro-5-(trifluoromethyl)phenylcarbamoyl)-4-(3-phenoxybenzoyl)piperazine (19)

The product was isolated as a solid (0.230 g, 60% yield) following purification through column chromatography, using hexane-ethyl acetate (1:1) as the eluent; mp = 138-141 °C.

^{1}H NMR (500 MHz, DMSO-d_6) δ 8.52 (s, 1H), 7.94 (d, J = 1.9 Hz, 1H), 7.71 (d, J = 8.3 Hz, 1H), 7.51 – 7.41 (m, 4H), 7.23 – 7.18 (m, 2H), 7.13 – 7.07 (m, 3H), 7.03 (m, 1H), 3.74 – 3.34 (m, 8H). ^{13}C NMR (125 MHz, DMSO-d_6) δ 168.84, 157.33, 156.56, 155.04, 138.09, 138.03, 132.00, 130.99, 130.81, 130.67, 128.51, 128.25, 124.45, 122.91, 122.88, 122.23, 122.16, 122.13, 119.94, 119.58, 117.16, 47.33, 44.22, 41.97. HRMS (m/z): calc. for $C_{25}H_{21}ClF_3N_3O_3Na$ 526.1116 $[M+Na]^+$; found 526.1108.

1-(4-chloro-2-nitrophenylsulfonyl)-4-(1,4-benzodioxane-5-carbonyl)piperazine (20)

The product was isolated as a solid (0.275 g, 83% yield) following purification through column chromatography, using hexane-ethyl acetate (1:1) as the eluent; mp = 220-223 °C.

^{1}H NMR (500 MHz, DMSO-d_6) δ 8.35 (d, J = 2.0 Hz, 1H), 8.02 – 7.94 (m, 2H, ArH), 6.91 (dd, J = 8.1, 1.7 Hz, 1H), 6.88 – 6.84 (m, 1H), 6.75 (dd, J = 7.4, 1.7 Hz, 1H), 4.33 – 4.15 (m, 4H), 3.76 (m, 1H), 3.65 (m, 1H), 3.31– 3.29 (m, 2H), 3.28 – 3.24 (m, 2H), 3.22 – 3.13 (m, 2H). ^{13}C NMR (125 MHz, DMSO-d_6) δ 166.20, 148.83, 143.83, 140.05, 139.65, 132.88, 132.58, 128.11, 125.44, 124.84,

121.68, 120.19, 118.33, 64.62, 64.39, 46.38, 46.32, 45.98, 41.05. HRMS (m/z): calc. for $C_{19}H_{18}ClN_3O_7SNa$ 490.0446 $[M+Na]^+$; found 490.0451.

1-(4-chlorophenylsulfonyl)-4-(1,4-benzodioxane-5-carbonyl)piperazine (21)

The product was isolated as a solid (0.283 g, 74% yield) following purification through column chromatography, using hexane-ethyl acetate (1:1.2) as the eluent; mp = 153-155 °C.

^{1}H NMR (500 MHz, DMSO-d_6) δ 7.86 -7.77 (m, 4H), 6.94 (dd, J = 8.1, 1.6 Hz, 1H), 6.89 (t, J = 7.8 Hz, 1H), 6.76 (dd, J = 7.5, 1.6 Hz, 1H), 4.35-4.24 (m, 2H), 4.19 (t, J = 4.0 Hz, 2H), 3.80-3.64 (m, 2H), 3.35 – 3.27 (m, 2H), 3.05 (m, 1H), 3.01 – 2.91 (m, 3H). ^{13}C NMR (125 MHz, DMSO-d_6) δ 166.12, 143.77, 139.97, 138.91, 134.23, 130.15, 129.95, 125.46, 121.68, 120.09, 118.28, 64.55, 64.35, 46.51, 46.15, 46.09, 40.76. HRMS (m/z): calcd. for $C_{19}H_{19}ClN_2O_5SNa$ 445.0595 $[M+Na]^+$; found 445.0585.

1-(4-methoxyphenylsulfonyl)-4-(1,4-benzodioxane-5-carbonyl)piperazine (22)

The product was isolated as a solid (0.200 g, 83 % yield) following purification through column chromatography, using hexane-ethyl acetate (1:1.2) as the eluent; mp = 156-158 °C.

^{1}H NMR (500 MHz, DMSO-d_6) δ 7.73 (d, J = 8.9 Hz, 2H), 7.24 (d, J = 8.9 Hz, 2H), 6.94 (dd, J = 8.1, 1.5 Hz, 1H), 6.89 (t, J = 7.8 Hz, 1H), 6.74 (dd, J = 7.5, 1.5 Hz, 1H), 4.37-4.21 (m, 2H), 4.17 (t, J = 3.9 Hz, 2H), 3.92 (s, 3H), 3.84 – 3.74 (m, 1H), 3.73 -3.63 (m, 1H), 3.35 - 3.25 (m, 2H), 3.06-2.99 (m, 1H), 2.98 - 2.93 (m, 1H), 2.91 - 2.78 (m, 2H). ^{13}C NMR (125 MHz, DMSO-d_6) δ 166.10, 163.39, 143.77, 139.95, 130.31, 126.61, 125.50, 121.70, 120.03, 118.27, 115.09, 64.53, 64.35, 56.24, 46.61, 46.23, 46.07, 40.75. HRMS (m/z): calcd. for $C_{20}H_{22}N_2O_6SNa$ 441.1091 $[M+Na]^+$; found 441.1082.

1-(2,4-dimethoxyphenylsulfonyl)-4-(1,4-benzodioxane-5-carbonyl)piperazine (23)

The product was isolated as a solid (0.320 g, 65 % yield) following purification through column chromatography, using dichloromethane-methanol (50:1) as the eluent; mp = 188-190 °C. ^{1}H NMR (500 MHz, DMSO-d_6) δ 7.71 (d, J = 8.8 Hz, 1H), 6.95 (dd, J = 8.1, 1.6 Hz, 1H), 6.91 (t, J = 7.7 Hz, 1H), 6.82 – 6.76 (m, 2H), 6.72 (dd, J = 8.8, 2.3 Hz, 1H), 4.37- 4.21 (m, 4H), 3.94 (s, 3H), 3.91 (s,

3H), 3.80 - 3.71 (m, 1H), 3.67- 3.58 (m, 1H), 3.33 -3.30 (m, 1H), 3.28 -3.17 (m, 2H), 3.15 – 3.03 (m, 3H). ^{13}C NMR (125 MHz, DMSO-d_6) δ 166.20, 165.08, 158.84, 143.79, 140.00, 133.07, 125.71, 121.69, 120.10, 118.23, 117.67, 105.70, 100.00, 64.59, 64.39, 56.55, 56.31, 46.75, 46.44, 45.94, 41.42. HRMS (m/z): calcd. for $C_{21}H_{24}N_2O_7SNa$ 471.1196 $[M+Na]^+$; found 471.1188.

1-(4-chloro-2-nitrophenylsulfonyl)-4-(1,1'-biphenyl-4-carbonyl)piperazine (24)

The product was isolated as a solid (0.330 g, 72 % yield) following purification through column chromatography, using hexane-ethyl acetate (1:1) as the eluent; mp = 159-162 °C. ^{1}H NMR (500 MHz, DMSO-d_6) δ 8.39 (d, J = 2.0 Hz, 1H), 8.06 (d, J = 8.6 Hz, 1H), 8.01 (dd, J = 8.6, 2.1 Hz, 1H), 7.78 (d, J = 8.3 Hz, 2H), 7.76 – 7.71 (m, 2H), 7.58 -7.51 (m, 4H), 7.45 (t, J = 7.4 Hz, 1H), 3.85– 3.25 (m, 8H). ^{13}C NMR (125 MHz, DMSO-d_6) δ 169.54, 148.85, 141.94, 139.72, 139.64, 134.61, 132.87, 132.62, 129.52, 128.42, 128.32, 128.05, 127.26, 127.14, 124.77, 46.01. HRMS (m/z): calc. for $C_{23}H_{20}ClN_3O_5SNa$ 508.0704 $[M+Na]^+$; found 508.0705.

1-(4-chlorophenylsulfonyl)-4-(1,1'-biphenyl-4-carbonyl)piperazine (25)

The product was isolated as a solid (0.180 g, 77 % yield) following purification through column chromatography, using hexane-ethyl acetate (1:1.2) as the eluent; mp = 214-216 °C.

^{1}H NMR (500 MHz, DMSO-d_6) δ 7.84 – 7.79 (m, 4H), 7.78 - 7.72 (m, 4H), 7.57 – 7.49 (m, 4H), 7.48 – 7.43 (m, 1H), 3.86 – 3.53 (m, 4H), 3.21 - 2.96 (m, 4H). ^{13}C NMR (125 MHz, DMSO-d_6) δ 168.93, 141.38, 139.24, 138.35, 134.14, 133.95, 129.67, 129.44, 128.99, 127.88, 127.81, 126.75, 126.59, 45.64. HRMS (m/z): calcd. for $C_{23}H_{21}ClN_2O_3SNa$ 463.0854 $[M+Na]^+$; found 463.0855.

1-(2,4-dimethoxyphenylsulfonyl)-4-(1,1'-biphenyl-4-carbonyl)piperazine (26)

The product was isolated as a solid (0.227 g, 69% yield) following purification through column chromatography, using hexane-ethyl acetate (1:1.2) as the eluent; mp = 164-166 °C.

^{1}H NMR (500 MHz, DMSO-d_6) δ 7.82 – 7.67 (m, 5H), 7.57 - 7.50 (m, 4H), 7.49 – 7.43 (m, 1H), 6.79 (d, J = 2.3 Hz, 1H), 6.72 (dd, J = 8.8, 2.3 Hz, 1H), 3.93 (s, 3H), 3.91 (s, 3H), 3.85 - 3.63 (m, 4H), 3.28 - 3.07 (m, 4H). ^{13}C NMR (125 MHz, DMSO-d_6) δ 169.55, 165.08, 158.89, 141.87, 139.73, 134.77,

133.06, 129.53, 128.40, 128.33, 127.24, 127.13, 117.73, 105.70, 100.14, 56.58, 56.29, 46.07, 41.97. HRMS (m/z): calcd. for $C_{25}H_{26}O_5N_2NaS$ 489.1455 $[M+Na]^+$; found 489.1443.

1-(4-nitrophenylsulfonyl)-4-(1,1'-biphenyl-4-carbonyl)piperazine (27)

The product was isolated as a solid (0.230 g, 85% yield) following purification through column chromatography, using hexane-ethyl acetate (1:1) as the eluent; mp = 213-216 °C.

^{1}H NMR (500 MHz, DMSO-*d*$_6$) δ 8.47 (d, *J* = 8.6 Hz, 2H), 8.03 (d, *J* = 8.6 Hz, 2H), 7.85 (d, *J* = 8.5 Hz, 2H), 7.76 – 7.63 (m, 4H), 7.51 – 7.38 (m, 3H), 3.93-3.36 (m, 5H), 3.21-2.99 (m, 3H). ^{13}C NMR (125 MHz, DMSO-*d*$_6$) δ 169.41, 150.65, 141.93, 141.30, 139.72, 136.33, 134.60, 129.62, 129.50, 128.40, 127.26, 127.09, 125.29, 46.13. HRMS (m/z): calcd. for $C_{23}H_{21}O_5N_3NaS$ 474.1094 $[M+Na]^+$; found 474.1085

1-(4-chloro-2-nitrophenylsulfonyl)-4-(3-phenoxybenzoyl)piperazine (28)

The product was isolated as a solid (0.190 g, 78% yield) following purification through column chromatography, using hexane-ethyl acetate (1:1) as the eluent; mp = 113-115 °C. ^{1}H NMR (500 MHz, DMSO-*d*$_6$) δ 8.52 (s, 1H), 7.94 (d, *J* = 1.9 Hz, 1H), 7.71 (d, *J* = 8.3 Hz, 1H), 7.51 – 7.40 (m, 4H), 7.23- 7.17 (m, 2H), 7.14 – 7.05 (m, 2H), 7.04 – 7.01 (m, 1H), 3.75 – 3.34 (m, 8H).^{13}C NMR (125 MHz, DMSO-*d*$_6$) δ 168.79, 157.29, 156.49, 148.85, 139.60, 137.61, 132.83, 132.59, 130.80, 130.65, 128.03, 124.76, 124.42, 122.20, 119.99, 119.55, 117.13, 47.10, 45.90, 41.50. HRMS (m/z): calc. for $C_{23}H_{20}ClN_3O_6SNa$ 524.0654 $[M+Na]^+$; found 524.0638.

1-(adamantan-1-ylcarbamoyl)-4-(1,4-benzodioxane-5-carbonyl)piperazine (29)

The product was isolated as a solid (0.322 g, 75% yield) following purification through column chromatography, using dichloromethane-methanol (50:1) as the eluent; mp = 155-158 °C. ^{1}H NMR (500 MHz, DMSO-*d*$_6$) δ 6.96 (dd, J = 8.1, 1.7 Hz, 1H), 6.92 (t, J = 7.7 Hz, 1H), 6.80 (dd, J = 7.3, 1.7 Hz, 1H), 5.79 (s, 1H), 4.32 (s, 4H), 3.65 – 3.58 (m, 2H), 3.38 – 3.32 (m, 2H), 3.30-3.14 (m, 4H), 2.08-2.02 (m, 3H), 2.01 - 1.94 (m, 6H), 1.70 – 1.60 (m, 6H). ^{13}C NMR (125 MHz, DMSO-*d*$_6$) δ 166.16, 156.88, 143.80, 140.01, 126.09, 121.65, 120.05, 118.11, 64.65, 64.44, 50.94, 46.69, 44.93, 44.35,

44.10, 42.02, 41.60, 36.66, 29.46. HRMS (m/z): calcd. for $C_{24}H_{31}N_3O_4Na$ 448.2207 $[M+Na]^+$; found 448.2209.

1-(adamantan-1-ylcarbamoyl)-4-(1,1'-biphenyl-4-carbonyl)piperazine (30)

The product was isolated as a solid (0.176 g, 78% yield) following purification through column chromatography, using hexane-ethyl acetate (1:1.2) as the eluent; mp = 201-203 °C. ^{1}H NMR (300 MHz, DMSO-d_6) δ 7.78 – 7.68 (m, 4H), 7.57 – 7.46 (m, 4H), 7.45-7.36 (m, 1H), 5.74 (s, 1H), 3.72-3.32 (m, 8H), 2.06 – 1.97 (m, 3H), 1.96 – 1.88 (m, 5H), 1.87 – 1.79 (m, 1H), 1.68 -1.55 (m, 6H). ^{13}C NMR (125 MHz, DMSO-d_6) δ 166.61, 153.10, 142.77, 142.50, 141.32, 128.83, 128.16, 127.77, 126.77, 125.29, 79.97, 72.65, 57.85, 57.81, 28.55. HRMS (m/z): calcd. for $C_{28}H_{33}O_2N_3Na$ 466.2465 [M+Na]+; found 466.2463.

1-(adamantan-1-ylcarbamoyl)-4-(5-chloro-2 hydroxybenzoyl)piperazine (31)

The product was isolated as a solid (0.280 g, 83% yield) following purification through column chromatography, using hexane-ethyl acetate (1:1.5) as the eluent; mp = 240-242 °C.

^{1}H NMR (300 MHz, DMSO-d_6) δ 10.15 (s, 1H), 7.27 (dd, J = 8.7, 2.7 Hz, 1H), 7.17 (d, J = 2.7 Hz, 1H), 6.88 (d, J = 8.7 Hz, 1H), 5.74 (s, 1H), 3.60 – 3.45 (m, 2H), 3.35-3.03 (m, 6H), 2.02 – 1.95 (m, 3H), 1.94 - 1.88 (m, 6H), 1.68 – 1.53 (m, 6H). ^{13}C NMR (125 MHz, DMSO-d_6) δ 166.01, 156.92, 152.66, 130.32, 128.06, 126.11, 123.07, 117.89, 50.93, 46.62, 44.35, 44.08, 42.03, 41.59, 36.66, 29.46. HRMS (m/z): calcd. for $C_{22}H_{28}O_3N_3Cl$ Na 440.1711 $[M+Na]^+$; found 440.1705.

1-(adamantan-1-ylcarbamoyl)-4-(3-phenoxybenzoyl)piperazine (32)

The product was isolated as a solid (0.130 g, 69% yield) following purification through column chromatography, using hexane-ethyl acetate (1:2) as the eluent; mp = 139-142 °C.

^{1}H NMR (500 MHz, DMSO-d_6) δ 7.50 – 7.37 (m, 3H), 7.24 – 7.12 (m, 2H), 7.11 – 7.03 (m, 3H), 6.99 -6.97 (m, 1H), 5.73 (s, 1H), 3.60 -3.45 (m, 2H), 3.34 - 3.14 (m, 6H), 2.03 – 1.96 (m, 3H), 1.94 – 1.88 (m, 5H), 1.85 – 1.80 (m, 1H), 1.63 -1.55 (m, 6H). ^{13}C NMR (125 MHz, DMSO-d_6) δ 168.72, 157.31, 156.88, 156.54, 138.13, 130.76, 130.66, 124.44, 122.17, 119.83, 119.56, 117.09, 50.95, 49.73, 47.47,

44.16, 42.52, 42.31, 42.02, 36.65, 29.46, 29.42. HRMS (m/z): calcd. for $C_{28}H_{33}N_3O_3Na$ 482.2414 $[M+Na]^+$; found 482.2399.

1-(N-(2-chloro-5-trifluoromethylphenylcarbamoyl)-L-prolyl)-4-(1,4-benzodioxane-5-carbonyl)piperazine (39)

The product was isolated as a solid (0.080 g, 55% yield) following purification through column chromatography, using hexane-ethyl acetate (1:2) as the eluent; mp = 149-153 °C.

^{1}H NMR (500 MHz, DMSO-d_6) δ 8.25 (s, 1H), 7.88 (bs, 1H), 7.76 (d, J = 8.5 Hz, 1H), 7.48 (dd, J = 8.5, 1.7 Hz, 1H), 7.01 - 6.98 (m, 1H), 6.97 -6.95 (m, 2H), 5.14 -4.80 (m, 1H), 4.33 (m, 4H), 3.81 – 3.42 (m, 10H), 2.36 – 2.20 (m, 1H), 2.07 – 1.93 (m, 2H), 1.92 – 1.80 (m, 1H). ^{13}C NMR (125 MHz, DMSO-d_6) δ 170.61, 169.16, 153.22, 145.14, 143.53, 137.64, 130.78, 129.48, 128.93, 128.55, 128.24, 125.30, 123.17, 120.97, 117.39, 116.82, 64.68, 64.54, 57.20, 46.74, 45.04, 31.44, 29.61. HRMS (m/z): calcd. for $C_{26}H_{26}N_4O_5ClF_3Na$ 589.1436 $[M+Na]^+$; found 589.1429.

1-(N-(2-chloro-5-trifluoromethylphenylcarbamoyl)-L-prolyl)-4-(5-chloro-2-hydroxybenzoyl)piperazine (40)

The product was isolated as a solid (0.058 g, 58% yield) following purification through column chromatography, using ethyl acetate-methanol (12:1) as the eluent; mp = 119-122 °C.

^{1}H NMR (500 MHz, DMSO-d_6) δ 10.26 (s, 1H), 8.25 (s, 1H), 7.88 (bs, 1H), 7.76 (d, J = 8.3 Hz, 1H), 7.48 (d, J = 7.3 Hz, 1H), 7.34 (dd, J = 8.7, 2.5 Hz, 1H), 7.26 (s, 1H), 6.95 (d, J = 8.7 Hz, 1H), 5.10 – 4.80 (m, 1H), 3.81 – 3.46 (m, 8H), 3.35 – 3.19 (m, 2H), 2.38 – 2.14 (m, 1H), 2.05 – 1.93 (m, 2H), 1.92 – 1.80 (m, 1H). ^{13}C NMR (125 MHz, DMSO-d_6) δ 170.64, 166.16, 153.24, 152.66, 137.61, 131.05, 130.77, 130.45, 128.55, 128.29, 128.15, 125.87, 125.31, 123.15, 121.01, 117.93, 60.47, 57.19, 46.88, 44.88, 27.30. HRMS (m/z): calcd. for $C_{24}H_{23}O_4N_4Cl_2F_3Na$ 581.0941 $[M+Na]^+$; found 581.0931.

1-(N-(2-chloro-5-trifluoromethylphenylcarbamoyl)-L-prolyl)-4-(3-phenoxybenzoyl) piperazine (41)

The product was isolated as a solid (0.070 g, 52% yield) following purification through column chromatography, using ethyl acetate-methanol (10:1) as the eluent; mp = 163-166 °C.

^{1}H NMR (500 MHz, DMSO-*d*$_6$) δ 8.26 (s, 1H), 7.88 (bs, 1H), , 7.76 (d, J = 8.4 Hz, 1H), 7.60 – 7.38 (m, 4H), 7.28 – 7.22 (m, 2H), 7.18 – 7.11 (m, 3H), 7.08 (s, 1H), 5.11-4.79 (m, 1H), 3.90 – 3.39 (m, 10H), 2.39 – 2.17 (m, 1H), 2.07 - 1.94 (m, 2H), 1.91 – 1.79 (m, 1H). ^{13}C NMR (125 MHz, DMSO-*d*$_6$) δ 168.83, 157.34, 156.54, 153.23, 137.63, 130.80, 130.78, 130.67, 128.54, 128.28, 125.31, 124.45, 123.15, 122.20, 120.98, 119.93, 119.58, 117.14, 57.18, 46.74, 36.68, 29.47. HRMS (m/z): calcd. for $C_{30}H_{28}O_4N_4ClF_3Na$ 623.1643 $[M+Na]^+$; found 623.1631

1-(3,4 dichlorophenylcarbamoyl)-4-(1,1'-biphenyl-4-carbonyl)piperazine (42)

The product was isolated as a solid (0.230 g, 80% yield) following purification through column chromatography, using hexane-ethyl acetate (1:1.5) as the eluent; mp = 195-198 °C.

^{1}H NMR (500 MHz, DMSO-d$_6$) δ 8.95 (s, 1H), 8.08 (d, *J* = 8.4 Hz, 2H), 7.90 (d, *J* = 2.4 Hz, 1H), 7.85 (d, *J* = 8.4 Hz, 2H), 7.83-7.75 (m, 2H), 7.64 – 7.44 (m, 5H), 3.92 – 3.43 (m, 8H). ^{13}C NMR (125 MHz, DMSO-d$_6$) δ 169.48, 154.89, 141.85, 141.24, 139.77, 135.05, 131.07, 130.69, 130.10, 129.55, 128.76, 128.32, 127.16, 123.53, 120.89, 119.76, 44.19. HRMS (m/z): calc. for $C_{24}H_{21}O_2N_3Cl_2Na$ 476.0903 $[M+Na]^+$; found 476.0890.

1-(2,4-dimethoxyphenylcarbamoyl)-4-(5-chloro-2 hydroxybenzoyl)piperazine (43)

The product was isolated as a solid (0.184 g, 73% yield) following purification through column chromatography, using hexane-ethyl acetate (1:1.5) as the eluent; mp = 162-167 °C.

^{1}H NMR (500 MHz, DMSO-*d*$_6$) δ 10.23 (s, 1H), 7.69 (s, 1H), 7.37 (d, *J* = 8.7 Hz, 1H), 7.33 (dd, *J* = 8.7, 2.7 Hz, 1H), 7.25 (d, *J* = 2.7 Hz, 1H), 6.95 (d, *J* = 8.8 Hz, 1H), 6.62 (d, *J* = 2.7 Hz, 1H), 6.50 (dd, *J* = 8.7, 2.7 Hz, 1H), 3.81 (s, 3H), 3.78 (s, 3H), 3.73 – 3.63 (m, 2H), 3.57 - 3.43 (m, 4H), 3.34 – 3.22 (m, 2H). ^{13}C NMR (125 MHz, DMSO-*d*$_6$) δ 166.09, 157.29, 156.06, 153.30, 152.67, 130.38, 128.12, 126.05, 125.99, 123.12, 121.67, 117.93, 104.48, 99.21, 56.10, 55.73, 46.58, 44.48, 43.96, 41.63. HRMS (m/z): calc. for $C_{20}H_{22}O_5N_3ClNa$ 442.1151 $[M+Na]^+$; found 442.1135.

1-(3,4-dichlorophenylcarbamoyl)-4-(5-chloro-2-hydroxybenzoyl)piperazine (44)

The product was isolated as a solid (0.284 g, 86% yield) following purification through column chromatography, using hexane-ethyl acetate (1:2) as the eluent; mp = 250-252 °C.

^{1}H NMR (500 MHz, DMSO-d_6) δ 10.23 (s, 1H), 8.92 (s, 1H), 7.88 (d, J = 2.4 Hz, 1H), 7.54 (d, J = 8.9 Hz, 1H), 7.49 (dd, J = 8.9, 2.4 Hz, 1H), 7.34 (dd, J = 8.7, 2.7 Hz, 1H), 7.25 (d, J = 2.7 Hz, 1H), 6.95 (d, J = 8.7 Hz, 1H), 3.77 -3.65 (m, 2H), 3.64 -3.44 (m, 4H), 3.36 – 3.24 (m, 2H). ^{13}C NMR (125 MHz, DMSO-d_6) δ 166.11, 154.85, 152.68, 141.23, 131.06, 130.68, 130.44, 128.15, 125.94, 123.50, 123.13, 120.88, 119.74, 117.94, 46.55, 44.35, 44.06, 41.60. HRMS (m/z): calc. for $C_{18}H_{16}O_3N_3Cl_3Na$ 450.0160 $[M+Na]^+$; found 450.0146.

1-(2,4-dimethoxyphenylcarbamoyl)-4-(3-phenoxybenzoyl)piperazine (45)

The product was isolated as a solid (0.145 g, 67% yield) following purification through column chromatography, using hexane-ethyl acetate (1:1.5) as the eluent; mp = 143-144 °C.

^{1}H NMR (500 MHz, DMSO-d_6) δ 7.65 (s, 1H), 7.51 – 7.40 (m, 3H), 7.34 (d, J = 8.6 Hz, 1H), 7.22 – 7.17 (m, 2H), 7.13 – 7.06 (m, 3H), 7.05 – 6.99 (m, 1H), 6.59 (d, J = 2.7 Hz, 1H), 6.46 (dd, J = 8.7, 2.7 Hz, 1H), 3.77 (s, 3H), 3.74 (s, 3H), 3.70 – 3.55 (m, 2H), 3.52 -3.36 (M, 6H). ^{13}C NMR (125 MHz, DMSO-d_6) δ 168.79, 157.34, 157.28, 156.56, 156.02, 153.27, 138.10, 130.79, 130.67, 125.95, 124.44, 122.21, 121.68, 119.88, 119.58, 117.15, 104.49, 99.21, 56.10, 55.73, 49.20, 44.22, 43.91, 42.02. HRMS (m/z): calc. for $C_{26}H_{27}O_5N_3Na$ 484.1854 $[M+Na]^+$; found 484.1838.

1-(3,4-dichlorophenylcarbamoyl)-4-(3-phenoxybenzoyl)piperazine (46)

The product was isolated as a solid (0.165 g, 65% yield) following purification through column chromatography, using hexane-ethyl acetate (1:2) as the eluent; mp = 139-140 °C. ^{1}H NMR (500 MHz, DMSO-d_6) δ 8.93 (s, 1H), 7.88 (d, J = 2.4 Hz, 1H), 7.56 – 7.43 (m, 5H), 7.26 – 7.21 (m, 2H), 7.18 – 7.11 (m, 3H), 7.09 – 7.05 (m, 1H), 3.80 – 3.40 (m, 8H). ^{13}C NMR (125 MHz, DMSO-d_6) δ 168.80, 157.33, 156.56, 154.85, 141.22, 140.01, 138.01, 131.07, 130.80, 130.67, 124.44, 123.52, 122.23,

120.88, 119.95, 119.74, 119.57, 117.16, 47.36, 44.08, 41.98. HRMS (m/z): calc. for $C_{24}H_{21}O_3N_3Cl_2Na$ 492.0863 $[M+Na]^+$; found 492.0847.

1-(4-methoxyphenylsulfonyl)-4-(1,1'-biphenyl-4-carbonyl)piperazine (47)

The product was isolated as a solid (0.193g, 72% yield) following purification through column chromatography, using hexane-ethyl acetate (1:1.5) as the eluent; mp = 224-228 °C.

^{1}H NMR (500 MHz, DMSO-d_6) δ 7.78– 7.70 (m, 6H), 7.60 – 7.41 (m, 5H), 7.26 – 7.22 (m, 2H), 3.93 (s, 3H), 3.86 – 3.44 (m, 4H), 3.17 – 2.84 (m, 4H). ^{13}C NMR (125 MHz, DMSO-d_6) δ 169.45, 163.36, 141.91, 139.75, 134.63, 130.42, 130.28, 129.51, 128.33, 127.26, 127.12, 126.91, 115.16, 56.22, 46.26. HRMS (m/z): calc. for $C_{24}H_{24}O_4N_2SNa$ 459.1349 $[M+Na]^+$; found 459.1338.

1-(2,4-dimethoxyphenylsulphonyl)-4-(3-phenoxybenzoyl)piperazine (48)

The product was isolated as a solid (0.155 g, 62% yield) following purification through column chromatography, using hexane-ethyl acetate (1:1.5) as the eluent; mp = 162-167 °C.

^{1}H NMR **(**500 MHz, DMSO-d_6) δ 7.50 – 7.43 (m, 3H), 7.36 (dd, J = 8.5, 2.2 Hz, 1H), 7.27 – 7.20 (m, 2H), 7.18 (d, J = 2.2 Hz, 1H), 7.17 – 7.07 (m, 4H), 6.99 – 6.96 (m, 1H), 3.91 (s, 3H), 3.89 (s, 3H), 3.81 – 3.59 (m, 2H), 3.57 -3.39 (m, 2H), 3.12 -2.87 (m, 4H). ^{13}C NMR (125 MHz, DMSO-d_6) δ 168.73, 157.27, 156.45, 153.10, 149.23, 137.59, 130.76, 130.64, 126.85, 124.44, 122.23, 121.88, 119.95, 119.58, 117.10, 111.94, 110.51, 56.35, 56.31, 46.18. HRMS (m/z): calc. for $C_{25}H_{26}O_6N_2SNa$ 505.1415 $[M+Na]^+$; found 505.1401.

1-(4-methoxyphenylsulfonyl)-4-(3-phenoxybenzoyl)piperazine (49)

The product was isolated as a solid (0.274 g, 79% yield) following purification through column chromatography, using hexane-ethyl acetate (1:1) as the eluent; mp = 151-145 °C.

^{1}H NMR (500 MHz, DMSO-d_6) δ 7.75 – 7.69 (m, 2H), 7.50 – 7.44 (m, 3H), 7.26 – 7.19 (m, 3H), 7.16 – 7.07 (m, 4H), 6.97 – 6.94 (m, 1H), 3.92 (s, 3H), 3.78 – 3.58 (m, 2H), 3.57 – 3.41 (m, 2H 3.08-2.84 (m, 4H). ^{13}C NMR (125 MHz, DMSO-d_6) δ 168.75, 163.34, 157.29, 156.44, 137.54, 130.78, 130.65,

130.24, 126.89, 124.46, 122.21, 119.94, 119.61, 117.03, 115.13, 56.21, 46.15. HRMS (m/z): calc. per $C_{24}H_{24}O_5N_2SNa$ 475.1309 $[M+Na]^+$; found 475.1295.

3.3.1.5. General procedure 4. Synthesis of proline derivatives (**33-35**).

To a solution of N-Boc-L-proline (1.5 mmol) in dry DCM (20 mL), EDCI (1.7 mmol) and HOBt (1.9 mmol) were added, and the mixture was stirred at room temperature for 45 minutes. Subsequently, a solution of the monoacyl derivative of piperazine **6**, **8**, **9** (1 mmol) in dry DCM, along with 1 mmol of triethylamine, was added [46].

The reaction was stirred at room temperature until TLC showed complete conversion of the starting material. At the end of the reaction, the mixture was sequentially washed with dilute hydrochloric acid, brine, and dried over anhydrous sodium sulfate (Na_2SO_4). After filtration, the solvent was removed under reduced pressure. The resulting compounds (**33-35**) were purified by flash column chromatography on silica gel.

1-(N-Boc-L-Prolyl)-4-(1,4-benzodioxane-5-carbonyl)piperazine (33)

The product was isolated with a 82% yield (0.260 g) following purification through column chromatography, using hexane-ethyl acetate (1:5) as the eluent. ^{1}H NMR (500 MHz, DMSO-d_6) δ 7.03 - 6.98 (m, 1H), 6.97 – 6.93 (m, 2H), 4.66 (m, 1H), 4.40 – 4.28 (m, 4H), 3.76 – 3.44 (m, 8H), 3.42 – 3.32 (m, 2H), 2.21 (m, 1H) 1.97 – 1.73 (m, 3H), 1.44 (s, 3H), 1.39 (s, 6H).^{13}C NMR (125 MHz, DMSO-d_6) δ 171.08, 169.21, 153.54, 145.16, 143.53, 128.87, 120.97, 117.39, 116.80, 78.68, 64.69, 64.54, 56.88, 46.96, 46.79, 44.81, 41.85, 30.36, 28.66, 28.54, 23.48. HRMS (m/z): calc. for $C_{23}H_{31}O_6N_3Na$ 468.2105 $[M+Na]^+$; found 468.2105.

1-(N-Boc-L-Prolyl)-4-(5-chloro-2-hydroxybenzoyl)piperazine (34)

The product was isolated with a 75% yield (0.345 g) following purification through column chromatography, using chloroform: methanol (9.5:0.5) as the eluent. ^{1}H NMR (500 MHz, DMSO-d_6) δ 10.24 (s, 1H), 7.34 (dd, J = 8.7, 2.7 Hz, 1H), 7.26 (d, J = 2.7 Hz, 1H), 6.95 (dd, J = 8.7, 2.3 Hz, 1H), 4.67 (m, 1H), 3.81 – 3.44 (m, 8H), 3.35 – 3.17 (m, 2H), 2.19 (m, 1H) 1.91 – 1.73 (m, 3H), 1.44 (s,

3H), 1.37 (s, 6H).^{13}C NMR (125 MHz, DMSO-d_6) δ 171.08, 170.78, 153.78, 152.66, 130.46, 128.16, 125.85, 123.14, 117.92, 78.67, 56.89, 46.96, 46.80, 41.64, 30.37, 28.66, 28.54, 23.48. HRMS (m/z): calc. for $C_{21}H_{28}O_5N_3ClNa$ 460.1610 $[M+Na]^+$; found 460.1613.

1-(N-Boc-L-Prolyl)-4-(3-phenoxybenzoyl)piperazine (35)

The product was isolated with a 70% yield (0.281 g) following purification through column chromatography, using ethyl acetate: methanol (10:1) as the eluent.

^{1}H NMR (500 MHz, DMSO-d_6) δ 7.56 – 7.36 (m, 3H), 7.22 – 7.17 (m, 2H), 7.14 – 7.05 (m, 3H), 7.04 – 6.99 (m, 1H), 4.59 (m, 1H), 3.74 – 3.38 (m, 6H), 3.39 – 3.28 (m, 4H), 2.13 (m, 1H) 1.95 – 1.61 (m, 3H), 1.39 (s, 3H), 1.31 (s, 6H). ^{13}C NMR (125 MHz, DMSO-d_6) δ 171.10, 168.93, 157.34, 156.52, 153.57, 130.83, 130.67, 124.46, 122.21, 119.96, 119.90, 119.59, 117.14, 117.09, 78.67, 56.88, 56.67, 46.96, 46.79, 30.35, 28.66, 28.55, 23.48. HRMS (m/z): calc. for $C_{27}H_{33}O_5N_3Na$ 502.2312 $[M+Na]^+$; found 502.2313.

3.3.2 Biology

3.3.2.1 *In vitro* antiviral activity against Zika and Dengue Viruses, cells and reference compound

The H/PF/2013 ZIKV strain, belonging to the Asian lineage, and the New Guinea C DENV serotype 2 strain were kindly provided by "Istituto Toscano Tumori, Core Research Laboratory", Siena, Italy. Once expanded, viral stocks were stored at 80 ◦C and titrated by plaque assay, as previously described [79].

Vero E6 (African green monkey kidney cell line; ATCC, Manassas, VA, USA, CRL-1586) and C6/36 (Aedes albopictus mosquito; ATCC CRL- 1660) cell lines were used to expand ZIKV and DENV, respectively. The *in vitro* cytotoxicity and antiviral activity of candidate compounds was determined in Huh7 cell line (human hepatoma cell line; kindly provided by Instituto Toscano Tumori, Core Research Laboratory, Siena, Italy). Dulbecco's modified Eagle's medium high glucose with sodium pyruvate, and L-glutamine (DMEM High Glucose, Euroclone, Milan, Italy)

supplemented with 10% fetal bovine serum (FBS; Euroclone) and 1% of Streptomycin/Penicillin (Euroclone) was used as propagation medium. The propagation medium was supplemented with 2 mM of L- glutamine and HEPES (25 mM) to propagate the C6/36 medium cell line. The propagation medium with a lower concentration of FBS (1%) was used in infection experiments. The mammalian cells were incubated at 37 ◦C in a humidified incubator supplemented with 5% CO_2, whereas the mosquito cell line was maintained at 28 ◦C. Sofosbuvir (MedChem Express cat. HY-15005), used as reference compound, was supplied as a powder, and dissolved in 100% dimethyl sulfoxide (DMSO).

3.3.2.2. Cytotoxicity assay

Cytotoxicity of compounds was determined by CellTiter-Glo 2.0 M. 106408 Luminescent Cell Viability Assay (Promega) in the Huh7 cell line, according to the manufacturer's protocol. The luminescent signal obtained from cells treated with 5-fold dilution of the test compound, or DMSO as a control, was measured through the GloMax® Discover Microplate Reader (Promega). Raw data were elaborated with the GraphPad PRISM software version 6.01 (La Jolla) to calculate the half-maximal cytotoxic concentration ($_{CC50}$). The putative inhibitory activity of compounds was tested starting from the concentration causing the 20% of cellular toxicity (CC_{20})

3.3.2.3 Antiviral assay

Immunodetection assay (IA) using a pan-flavivirus monoclonal antibody recognizing a conserved domain of the envelope protein was the read out to determine the antiviral activity of candidate compounds on the whole viral replication cycle as previously published [80, 81].

Briefly, 6,000 Huh7 cells per well were infected using 50 TCID tissue culture infectious dose TCID 50 50 (50%) of DENV or ZIKV viral stocks, as defined by previous titration according to Reed & Muench [82]. Viral adsorption was performed in 96-well plates for 1 h at 37 ◦ C with 5% CO 2 and after virus removal, serial dilutions of each compound tested were added to the cells and incubated at 37 ◦ C with 5% CO_2. After 72 h, culture supernatants were collected, properly diluted, and used to re-infect in triplicate uninfected Huh7 cells in absence of the compounds (infectious virus yield) for 72

h at 37 ◦ C with 5% CO_2. After incubation, cells were fixed for 30 min with 10% formaldehyde (Carlo Erba), rinsed with 1% PBS and permeabilized for 10 min with 1% Triton X-100 (Carlo Erba). After washing, cells monolayer was incubated with monoclonal anti-flavivirus mouse antibody (clone D1-4G2-4–15; Novus Bio) and then with a polyclonal Horseradish Peroxidase (HRP)-coupled anti-mouse IgG secondary antibody (Novus Bio NB7570). Absorbance values were measured after 10 min incubations with the 3,3 ′ ,5,5 ′-tetramethylbenzidine substrate (TMB, Sigma Aldrich) and signals were acquired at 450 nm optical density (OD450) using the absorbance module of the GloMax® Discover Multimode Microplate Reader (Promega). Each IA run was validated by the OD450 value above 1 in the virus control culture. All drug concentrations were tested in triplicate in two independent experiments. In each test, sofosbuvir was used as reference compounds and infected and uninfected cells without drugs were used to calculate the 100% and 0% of viral replication, respectively. The half-maximal inhibitory concentration (IC_{50}) was calculated through a non-linear regression analysis of the dose–response curves generated with GraphPad PRISM software version 6.01. Selectivity Index (SI) of compounds was calculated as ratio between CC_{50}.

3.3.2.4 Anticancer activity

Chemicals and Reagents

Dulbecco's Modified Eagle Medium/Nutrient Mixture F-12 (DMEM/F-12), Horse Serum (HS) and Fetal Bovine Serum (FBS) were from Gibco™ (Life Technologies, Monza MB, Italy). Trypsin-EDTA solution 10×, L-Glutamine, penicillin/streptomycin (pen/strep) and phosphate-buffered saline (PBS) were from Sigma Aldrich (Merck Spa, Milano MI, Italy).

Cell Cultures and Treatments

Human breast cancer MCF-7 and human normal mammary epithelial MCF10A cell lines were purchased from ATCC, where they were authenticated. Cells were stored according to supplier’s instructions and used within 6 months after frozen aliquot resuscitations. MCF-7 were cultured in

DMEM/F-12 containing 5% FBS and MCF10A were grown in DMEM/F12 supplemented 5% HS, 20ng/ml EGF, 10 ug/ml human insulin, 0.5 mg/ml hydrocortisone, 100 ng/ml cholera toxin. Mycoplasma negativity was tested monthly (PlasmoTest, Invivogen, Aurogene, Rome, Italy). For cell treatments, compounds were dissolved in DMSO at the stock concentration of 100mM. Serial dilutions were prepared, and the following concentrations were tested: 0.1 μM, 1 μM, 10 μM, 100 μM, and 1000 μM [83].

Cell proliferation assay

Cell proliferation was determined by using 3-(4,5- dimethylthiazol-2-yl)-2,5-diphenylformazan (MTT) assay. Cells (5.000 cells/well) were seeded in 96-well plates and treated or not with piperazine derivatives, as indicated, for 72 hours. MTT (2mg/ml) was added to each well, and the plates were incubated for 2 h at 37°C. The medium was then removed, and formazan crystals dissolved in 100 μl DMSO (Sigma Aldrich). Absorbance was measured at 570 nm.

3.3.3. Docking studies

3.3.3.1 Methods

Dataset

Zika and Dengue NS3/2B protease structures were generated from the PDB database using the proteins with the codes 5LC0 [34] and 2FOM [84] for each organism, respectively. Subsequently, the chain A for each without water and ions was extracted to PDB format. The proteins in PDB format were converted to PDBQT using AutoDockTools [85] and to MOL2 using Maestro software (Schrödinger Release 2022-1: Desmond Molecular Dynamics System, D. E. Shaw Research, New York, NY, 2021). The compounds' SMILES were obtained from their CDX files using OpenBabel tools [86]. The Chemaxon tool molconvert transformed these SMILES to mol2 files with 3D

coordinates. Regarding PDBQT files, AutoDockTools converted the SMILES to PDBQT files with the corresponding charges and 3D coordinates.

Molecular Modelling and Docking calculations

Once the molecules and proteins models were generated, docking calculations were performed using the AutoDock and LeadFinder docking algorithms. In both cases, the docking was targeting the 5CL0 and 2FOM proteases active site. Calculations in both cases were launched using the in-house software MetaScreener [87].

Calculations were executed in parallel using the same compounds as queries on the Leftraru supercomputer at NLHPC. When the calculations finished, ESSENCE-Dock [88] was running to check the consensus between both docking software. Also, the interactions with each residue were registered to check possible contacts with key residues using PLIP software [89].

3.4 Conclusions

1) A library of piperazine-derived small molecules was designed using a privileged structure-based approach, with an unsubstituted piperazine ring as the core scaffold. These compounds exhibit dual potential as antiviral agents targeting Flaviviridae viruses and as anticancer agents against breast cancer cells.

2) Cell-based assay revealed that six compounds (**13**, **14**, **15**, **24**, **26** and **31)** showed activity against ZIKV with IC_{50} < 5 μM (1.6-5.1 μM), similar to that of reference, Sofosbuvir (SOF), (IC_{50} 3.7 μM) and good security profile. Among them, **14**, **15** and **31** also displayed high anti DENV activity and good selectivity index, with compound **15 (**IC_{50} ZIKV 1.6 μM, SI > 125; IC_{50} DENV 3.8 μM, SI 52.7) emerging as the most promising, displaying higher activity and selectivity index than SOF for both viruses.

3) The molecular docking analyses on compounds **14**, **15** and **31** showed compound residues interacting with both ZIKV and DENV NS3/2B protease active sites, supporting their expected mechanism of action as protease inhibitors. Further studies will be performed to explore the proposed mechanism of action in greater depth.

This positions the piperazine scaffold as a strong candidate for developing broad-spectrum antiviral agents targeting flaviviruses. Future research will focus on further chemical optimization to enhance potency and spectrum.

4) In terms of anticancer activity, select piperazine-based compounds were tested on breast cancer cell lines, exploring their potential as anticancer agents in addition to their antiviral properties. Preliminary *in vitro* results revealed that compounds **11**, **13**, **42** and **46** showed the most promising results, showing a dose-dependent antiproliferative effect on tumor cells (MCF-7), indicating a good balance between efficacy and selectivity.

5) These findings suggest that these compounds hold potential as dual-action therapeutic agents, effective against both viruses and cancer cells. Further works will focus on optimizing these molecules through novel functionalization to enhance their antiviral efficacy and to improve their anticancer activity and selectivity through targeted therapeutic strategies.

3.5 References

1. Young, P. R., Ng, L. F., Hall, R. A., Smith, D. W., & Johansen, C. A. Arbovirus infections. *Manson's tropical infectious diseases* **2014**, 129-161.
2. Boruah, A. P., & Thakur, K. T. Arthropod-borne encephalitis: an overview for the clinician and emerging considerations. *Postgraduate medical journal* **2023**, *99*(1174), 826-833.
3. Wilder-Smith, A., Ooi, E. E., Horstick, O., & Wills, B. Dengue. *The Lancet* **2019**, *393*(10169), 350-363.
4. Young, P. R. Arboviruses: a family on the move. *Dengue and Zika: control and antiviral treatment strategies* **2018**, 1-10.
5. Gerold, G., Bruening, J., Weigel, B., & Pietschmann, T. Protein interactions during the flavivirus and hepacivirus life cycle. *Molecular & Cellular Proteomics* **2017**, *16*(4), S75-S91.
6. Gubler D.J., Kuno G., Markoff L. Flaviviruses. In: Knipe D.M., Howley P.M., editors. *Fields Virology.* 5th ed. Lippincott Williams and Wilkins; Philadelphia, PA, USA, **2007**. pp. 1153–1252.
7. Capeding, M. R., Tran, N. H., Hadinegoro, S. R. S., Ismail, H. I. H. M., Chotpitayasunondh, T., Chua, M. N. et al. Clinical efficacy and safety of a novel tetravalent dengue vaccine in healthy children in Asia: a phase 3, randomised, observer-masked, placebo-controlled trial. *The Lancet* **2014**, *384*(9951), 1358-1365.
8. Ishak, R., Tovey, D. G., Howard, C. R. Morphogenesis of yellow fever virus 17D in infected cell cultures. *Journal of general virology* **1988**, *69*(2), 325-335.
9. Ng, M. L., Lau, L. C. Possible involvement of receptors in the entry of Kunjin virus into Vero cells. *Archives of virology* **1988**, *100*, 199-211.
10. Chao, L. H., Klein, D. E., Schmidt, A. G., Peña, J. M., & Harrison, S. C. Sequential conformational rearrangements in flavivirus membrane fusion. *Elife* **2014**, *3*, e04389.
11. Bressanelli, S., Stiasny, K., Allison, S. L., Stura, E. A., Duquerroy, S., Lescar, J. et al. Structure of a flavivirus envelope glycoprotein in its low-pH-induced membrane fusion conformation. *The EMBO journal* **2004**, *23*(4), 728-738.
12. Corver, J., Ortiz, A., Allison, S. L., Schalich, J., Heinz, F. X., & Wilschut, J. Membrane fusion activity of tick-borne encephalitis virus and recombinant subviral particles in a liposomal model system. *Virology* **2000**, *269*(1), 37-46.
13. Mukhopadhyay, S., Kuhn, R. J., & Rossmann, M. G. A structural perspective of the flavivirus life cycle. *Nature Reviews Microbiology* **2005**, *3*(1), 13-22.
14. Upstream Processing. Available online: https://www.mpi-magdeburg.mpg.de/25643/upstream_processing
15. Lowe,R.; Barcellos, C.; Brasil, P.; Cruz, O.G.; Honório, N.A.; Kuper, H.; Carvalho, M.S. The Zika Virus Epidemic in Brazil: From Discovery to Future Implications. *Int. J. Environ. Res. Public Health* **2018**, *15*, 96.
16. Musso, D.; Ko, A.I.; Baud, D. Zika Virus Infection—After the Pandemic. *N. Engl. J. Med.* **2019**, *381*, 1444–1457.
17. World Health Organization. *Vector-borne diseases* (No. SEA-CD-300) **2014**. WHO Regional Office for South-East Asia. Available online: http://www.who.int/news-room/factsheets/detail/vector-borne-diseases.

18. da Silva-Júnior, E. F., & de Araújo-Júnior, J. X. Peptide derivatives as inhibitors of NS2B-NS3 protease from Dengue, West Nile, and Zika flaviviruses. *Bioorganic & Medicinal Chemistry* **2019**, *27*(18), 3963-3978.
19. Voss, S., Nitsche, C. Inhibitors of the Zika virus protease NS2B-NS3. *Bioorganic & medicinal chemistry letters* **2020**, *30*(5), 126965.
20. Yao, Y., Huo, T., Lin, Y. L., Nie, S., Wu, F., Hua, Y. et al. Discovery, X-ray crystallography and antiviral activity of allosteric inhibitors of flavivirus NS2B-NS3 protease. *Journal of the American Chemical Society* **2019**, *141*(17), 6832-6836.
21. Meewan, I., Shiryaev, S. A., Kattoula, J., Huang, C. T., Lin, V., Chuang, C. H. et al. Allosteric inhibitors of Zika virus NS2B-NS3 protease targeting protease in "super-open" conformation. *Viruses* **2023**, *15*(5), 1106).
22. Gangopadhyay, A., Saha, A. Exploring allosteric hits of the NS2B-NS3 protease of DENV2 by structure-guided screening. *Computational Biology and Chemistry* **2023**, *104*, 107876.
23. Wahaab, A., Mustafa, B. E., Hameed, M., Stevenson, N. J., Anwar, M. N., Liu, K. et al. Potential role of flavivirus NS2B-NS3 proteases in viral pathogenesis and anti-flavivirus drug discovery employing animal cells and models: a review. *Viruses* **2021**, *14*(1), 44.
24. Noble, C. G., Seh, C. C., Chao, A. T., Shi, P. Y. Ligand-bound structures of the dengue virus protease reveal the active conformation. *Journal of virology* **2012**, *86*(1), 438-446).
25. Coluccia, A., Puxeddu, M., Nalli, M., Wei, C. K., Wu, Y. H. et al. Discovery of Zika virus NS2B/NS3 inhibitors that prevent mice from life-threatening infection and brain damage. *ACS Medicinal Chemistry Letters* **2020**, *11*(10), 1869-1874.
26. E. Clapham, H., & A. Wills, B. Implementing a dengue vaccination programme—who, where and how?. *Transactions of the Royal Society of Tropical Medicine and Hygiene* **2018**, *112*(8), 367-368.
27. Chan, J. F. W., Chik, K. K. H., Yuan, S., Yip, C. C. Y., Zhu, Z. et al. Novel antiviral activity and mechanism of bromocriptine as a Zika virus NS2B-NS3 protease inhibitor. *Antiviral research* **2017**, *141*, 29-37.
28. Kumar, A., Liang, B., Aarthy, M., Singh, S. K., Garg, N. et al. Hydroxychloroquine inhibits Zika virus NS2B-NS3 protease. *ACS omega* **2018**, *3*(12), 18132-18141.
29. Ho, Y. J., Lu, J. W., Huang, Y. L., Lai, Z. Z. Palmatine inhibits Zika virus infection by disrupting virus binding, entry, and stability. *Biochemical and Biophysical Research Communications* **2019**, *518*(4), 732-738.
30. Lai, Z. Z., Ho, Y. J., Lu, J. W. Harringtonine inhibits Zika virus infection through multiple mechanisms. *Molecules* **2020**, *25*(18), 4082.
31. Nguyen, C. Q., Nguyen, T. H. M., Nguyen, T. T. T., Bui, T. B. H., Nguyen, T. T., Huynh, N. T. et al. Designs, synthesis, docking studies, and biological evaluation of novel berberine derivatives targeting zika virus. *Journal of Chemistry* **2021**, *2021*(1), 5567111.
32. Byler, K. G., Ogungbe, I. V., Setzer, W. N. In-silico screening for anti-Zika virus phytochemicals. *Journal of Molecular Graphics and Modelling* **2016**, *69*, 78-91.
33. Yadav, R., Selvaraj, C., Aarthy, M., Kumar, P., Kumar, A., Singh, S. K., Giri, R. Investigating into the molecular interactions of flavonoids targeting NS2B-NS3 protease from ZIKA virus through in-silico approaches. *Journal of Biomolecular Structure and Dynamics* **2021**, *39*(1), 272-284.

34. Lei, J., Hansen, G., Nitsche, C., Klein, C. D., Zhang, L., Hilgenfeld, R. Crystal structure of Zika virus NS2B-NS3 protease in complex with a boronate inhibitor. *Science* **2016**, *353*(6298), 503-505.
35. Sánchez-Céspedes, J., Martínez-Aguado, P., Vega-Holm, M., Serna-Gallego, A., Candela, J. I., Marrugal-Lorenzo, J. A. et al. New 4-acyl-1-phenylaminocarbonyl-2-phenylpiperazine derivatives as potential inhibitors of adenovirus infection. synthesis, biological evaluation, and structure–activity relationships. *Journal of Medicinal Chemistry* **2016**, *59*(11), 5432-5448.
36. Mazzotta, S., Marrugal-Lorenzo, J. A., Vega-Holm, M., Serna-Gallego, A., Alvarez-Vidal, J., Berastegui-Cabrera, J. Et al. Optimization of piperazine-derived ureas privileged structures for effective antiadenovirus agents. *European Journal of Medicinal Chemistry* **2020**, *185*, 111840).
37. Gettys, K. E., Ye, Z., Dai, M. Recent advances in piperazine synthesis. *Synthesis* **2017**, *49*(12), 2589-2604.
38. Walker, M. A. Novel tactics for designing water-soluble molecules in drug discovery. *Expert opinion on drug discovery* **2014**, *9*(12), 1421-1433).
39. Sharma, A., Wakode, S., Fayaz, F., Khasimbi, S., Pottoo, F. H., Kaur, A. An overview of piperazine scaffold as promising nucleus for different therapeutic targets. *Current pharmaceutical design* **2020**, *26*(35), 4373-4385.
40. Kumar, R. R., Sahu, B., Pathania, S., Singh, P. K., Akhtar, M. J. et al. Piperazine, a Key Substructure for Antidepressants: Its Role in Developments and Structure-Activity Relationships. *Chem Med Chem* **2021**, *16*(12), 1878-1901.
41. Bari, D. G., Saravanan, K., Ahmad, R. Antipsychotic evaluation of novel series of aryl Piperazine congeners. *International Journal of Pharmaceutical Research* **2021**, *13*(2), 1687–1695.
42. Al-Ghorbani, M., Gouda, M. A., Baashen, M., Alharbi, O., Almalki, F. A., Ranganatha, L. V. Piperazine heterocycles as potential anticancer agents: A review. *Pharmaceutical Chemistry Journal* **2022**, *56*(1), 29–37.
43. Sanad, S. M., Mekky, A. E. Synthesis, in vitro antibacterial and anticancer screening of novel nicotinonitrile-coumarin hybrids utilizing piperazine citrate. *Synthetic Communications* **2020**, *50*(10), 1468–1485.
44. Jain, A., Chaudhary, J., Khaira, H., Chopra, B., & Dhingra, A. Piperazine: A promising scaffold with analgesic and anti-inflammatory potential. *Drug Research* **2021**, *71*(2), 62–72.
45. Shaquiquzzaman, M., Verma, G., Marella, A., Akhter, M., Akhtar, W. et al. Piperazine scaffold: A remarkable tool in generation of diverse pharmacological agents. *European journal of medicinal chemistry* **2015**, *102*, 487-529.
46. García-Lozano, M. Del Rosario, Dragoni, F., Gallego, P., Mazzotta, S., López-Gómez, A., Boccuto. et al. Piperazine-derived small molecules as potential Flaviviridae NS3 protease inhibitors. In vitro antiviral activity evaluation against Zika and Dengue viruses. *Bioorganic Chemistry* **2023**, *133*, 106408.
47. Xu, J., Shi, P. Y., Li, H., Zhou, J. Broad spectrum antiviral agent niclosamide and its therapeutic potential. *ACS infectious diseases* **2020**, *6*(5), 909-915.

48. Gerzon, K., Krumkalns, E. V., Brindle, R. L., Marshall, F. J., Root, M. A. The adamantyl group in medicinal agents. I. Hypoglycemic N-arylsulfonyl-N'-adamantylureas. *Journal of medicinal chemistry* **1963**, *6*(6), 760-763.
49. Rapala, R. T., Kraay, R. J., Gerzon, K. The adamantyl group in medicinal agents. II. Anabolic steroid 17β-adamantoates. *Journal of Medicinal Chemistry* **1965**, *8*(5), 580-583.
50. Gerzon, K., Kau, D. The adamantyl group in medicinal agents. III. Nucleoside 5′-adamantoates. The adamantoyl function as a protecting group. *Journal of Medicinal Chemistry* **1967**, *10*(2), 189-199.
51. Wanka, L., Iqbal, K., Schreiner, P. R. The lipophilic bullet hits the targets: medicinal chemistry of adamantane derivatives. *Chemical reviews* **2013**, *113*(5), 3516-3604.
52. De, S. K. Novel Proline Derivatives for Treating COVID-19. *Current Medicinal Chemistry* **2023**, *30*(12), 1458-1461.
53. Kallam, S. R., Eda, V. R., Sen, S., Datrika, R., Rapolu, R. K., Khobare, S. et al. A diastereoselective synthesis of boceprevir's gem-dimethyl bicyclic [3.1. 0] proline intermediate from an insecticide ingredient cis-cypermethric acid. *Tetrahedron* **2017**, *73*(30), 4285-4294.
54. Millies, B., von Hammerstein, F., Gellert, A., Hammerschmidt, S., Barthels, F., Göppel, U. et al. Proline-based allosteric inhibitors of Zika and Dengue virus NS2B/NS3 proteases. *Journal of medicinal chemistry* **2019**, *62*(24), 11359-11382.
55. Zhou, G. C., Weng, Z., Shao, X., Liu, F., Nie, X., Liu, J.. et al. Discovery and SAR studies of methionine–proline anilides as dengue virus NS2B-NS3 protease inhibitors. *Bioorganic & medicinal chemistry letters* **2013**, *23*(24), 6549-6554.
56. Trott, O.,Olson, A. J. AutoDock Vina: improving the speed and accuracy of docking with a new scoring function, efficient optimization, and multithreading. *Journal of computational chemistry* **2010**, *31*(2), 455-461.
57. Stroganov, O. V., Novikov, F. N., Stroylov, V. S., Kulkov, V., Chilov, G. G. Lead finder: An approach to improve accuracy of protein− ligand docking, binding energy estimation, and virtual screening. *Journal of Chemical Information and Modeling* **2008**, *48*(12), 2371-2385.
58. Salaemae, W., Junaid, M., Angsuthanasombat, C., Katzenmeier, G. Structure-guided mutagenesis of active site residues in the dengue virus two-component protease NS2B-NS3. *Journal of biomedical science* **2010**, *17*, 1-8.
59. Gomtsyan, A. Heterocycles in drugs and drug discovery. *Chemistry of heterocyclic compounds* **2012**, *48*, 7-10.
60. Sharma, V., Das, R., Mehta, D. K., Sharma, D., Sahu, R. K. Exploring quinolone scaffold: Unravelling the chemistry of anticancer drug design. *Mini Reviews in Medicinal Chemistry* **2022**, *22*(1), 69-88.
61. Das, R., Mehta, D. K., Dhanawat, M. Bestowal of quinazoline scaffold in anticancer drug discovery. *Anti-Cancer Agents in Medicinal Chemistry (Formerly Current Medicinal Chemistry-Anti-Cancer Agents)* **2021**, *21*(11), 1350-1368.
62. Sharma, V., Kumar Mehta, D., Das, R. Synthetic methods of quinoline derivatives as potent anticancer agents. *Mini Reviews in Medicinal Chemistry* **2017**, *17*(16), 1557-1572).
63. Cabrele, C., Reiser, O. The modern face of synthetic heterocyclic chemistry. *The Journal of Organic Chemistry* **2016**, *81*(21), 10109-10125.

64. Vitaku, E., Smith, D. T., Njardarson, J. T. Analysis of the structural diversity, substitution patterns, and frequency of nitrogen heterocycles among US FDA approved pharmaceuticals: miniperspective. *Journal of medicinal chemistry* **2014**, *57*(24), 10257-10274.
65. Taylor, R. D., MacCoss, M., & Lawson, A. D. Rings in drugs: Miniperspective. *Journal of medicinal chemistry* **2014**, *57*(14), 5845-5859.
66. Verma, S., & Kumar, S. Review exploring biological potentials of piperazines. *Med. Chem.(Los Angeles)* **2017**, *7*, 750-757.
67. Solomon, V. R., Hu, C., Lee, H. Design and synthesis of anti-breast cancer agents from 4-piperazinylquinoline: a hybrid pharmacophore approach. *Bioorganic & medicinal chemistry* **2010**, *18*(4), 1563-1572.
68. Deveshegowda, S. N., Metri, P. K., Shivakumar, R., Yang, J. R., Rangappa, S. et al. Development of 1-(4-(Substituted) piperazin-1-yl)-2-((2-((4-methoxybenzyl) thio) pyrimidin-4-yl) oxy) ethanones That Target Poly (ADP-Ribose) Polymerase in Human Breast Cancer Cells. *Molecules* **2022**, *27*(9), 2848.
69. Yarim, M., Koksal, M., Durmaz, I., Atalay, R. Cancer cell cytotoxicities of 1-(4-substitutedbenzoyl)-4-(4-chlorobenzhydryl) piperazine derivatives. *International journal of molecular sciences* **2012**, *13*(7), 8071-8085.
70. Elmeligie, S., Aboul-Magd, A. M., Lasheen, D. S., Ibrahim, T. M., Abdelghany, T. M.. et al. Design and synthesis of phthalazine-based compounds as potent anticancer agents with potential antiangiogenic activity via VEGFR-2 inhibition. *Journal of Enzyme Inhibition and Medicinal Chemistry* **2019**, *34*(1), 1347-1367.
71. Yang, J., Chen, K., Zhang, G., Yang, Q. Y., Li, Y. S. et al. Structural optimization and structure-activity relationship studies of N-phenyl-7, 8-dihydro-6H-pyrimido [5, 4-b][1, 4] oxazin-4-amine derivatives as a new class of inhibitors of RET and its drug resistance mutants. *European Journal of Medicinal Chemistry* **2018**, *143*, 1148-1164.
72. Walayat, K., MOHSIN, N. U. A., Aslam, S., Ahmad, M. An insight into the therapeutic potential of piperazine-based anticancer agents. *Turkish Journal of Chemistry* **2019**, *43*(1), 1-23.
73. Brown, J. R., DuBois, R. N. (2005). COX-2: a molecular target for colorectal cancer prevention. *Journal of Clinical Oncology* **2005**, *23*(12), 2840-2855.
74. Grösch, S., Maier, T. J., Schiffmann, S., Geisslinger, G. Cyclooxygenase-2 (COX-2)–independent anticarcinogenic effects of selective COX-2 inhibitors. *Journal of the National Cancer Institute* **2006**, *98*(11), 736-747.
75. Green, D. R., Walczak, H. Apoptosis therapy: driving cancers down the road to ruin. *Nature medicine* **2013**, *19*(2), 131-133).
76. Walayat, K., MOHSIN, N. U. A., Aslam, S., & Ahmad, M. An insight into the therapeutic potential of piperazine-based anticancer agents. *Turkish Journal of Chemistry* **2019**, *43*(1), 1-23.
77. Zhang, Y., Huang, Y. J., Xiang, H. M., Wang, P. Y., Hu, D. Y., Xue, W., et al.Synthesis and anticancer activities of 4-(4-substituted piperazin)-5, 6, 7-trialkoxy quinazoline derivatives. *European Journal of Medicinal Chemistry* **2014**, 78, 23-34.
78. Mosmann, T. Rapid colorimetric assay for cellular growth and survival: application to proliferation and cytotoxicity assays. *Journal of immunological methods* **1983,** *65*(1-2), 55-63.

79. Vicenti, I., Boccuto, A., Giannini, A., Dragoni, F., Saladini, F., Zazzi, M. Comparative analysis of different cell systems for Zika virus (ZIKV) propagation and evaluation of anti-ZIKV compounds in vitro. *Virus research* **2018**, *244*, 64-70).
80. Vicenti, I., Dragoni, F., Giannini, A., Giammarino, F., Spinicci, M., Saladini, F. et al. Development of a cell-based immunodetection assay for simultaneous screening of antiviral compounds inhibiting Zika and dengue virus replication. *SLAS DISCOVERY: Advancing the Science of Drug Discovery* **2020**, *25*(5), 506-514.
81. Brai, A., Boccuto, A., Monti, M., Marchi, S., Vicenti, I. et al. Exploring the implication of DDX3X in DENV infection: discovery of the first-in-class DDX3X fluorescent inhibitor. *ACS Medicinal Chemistry Letters* **2020**, *11*(5), 956-962).
82. H.M.L.J. Reed, A simple method of estimating fifty per cent endpoints, *Am. J. Hyg.* **1938**, *27*, 546–558.
83. Pellegrino, M., Rizza, P., Nigro, A., Ceraldi, R., Ricci, E., Perrotta, I. et al. FoxO3a mediates the inhibitory effects of the antiepileptic drug lamotrigine on breast cancer growth. *Molecular Cancer Research* **2018**, *16*(6), 923-934.
84. Erbel, P., Schiering, N., D'Arcy, A., Renatus, M., Kroemer, M., Lim, S. P. et al. Structural basis for the activation of flaviviral NS3 proteases from dengue and West Nile virus. *Nature structural & molecular biology* **2006**, *13*(4), 372-373.
85. Morris, G. M., Huey, R., Lindstrom, W., Sanner, M. F., Belew, R. K., Goodsell, D. S. et al. AutoDock4 and AutoDockTools4: Automated docking with selective receptor flexibility. *Journal of computational chemistry* **2009,** *30*(16), 2785-2791.
86. Banck, M., James, C. A., Morley, C., Vandermeersch, T., Hutchison, G. R. Open Babel: An open chemical toolbox. *J. Cheminf* **2011**, *3*(1), 33.
87. Available online: (https://github.com/bio-hpc/metascreener/).
88. Nelen, J., Carmena-Bargueño, M., Martínez-Cortés, C., Rodríguez-Martínez, A., Villalgordo-Soto, J. M., Pérez-Sánchez, H. ESSENCE-Dock: A Consensus-Based Approach to Enhance Virtual Screening Enrichment in Drug Discovery. *Journal of Chemical Information and Modeling* **2024**, *64*(5), 1605-1614.
89. Adasme, M. F., Linnemann, K. L., Bolz, S. N., Kaiser, F., Salentin, S., Haupt, V. J., Schroeder, M. PLIP 2021: Expanding the scope of the protein–ligand interaction profiler to DNA and RNA. *Nucleic acids research* **2021** , *49*(W1), W530-W534.

Chapter 4

Engineered Mesoporous Silica-Based Nanoparticles: Characterization of Surface Properties

Antonio Grisolia, Marzia De Santo, Manuela Curcio, Palmira Alessia Cavallaro, Catia Morelli, Antonella Leggio, Luigi Pasqua

Published on: *Materials,* **2024**, 17(13), 3352

DOI:10.3390/ma17133352

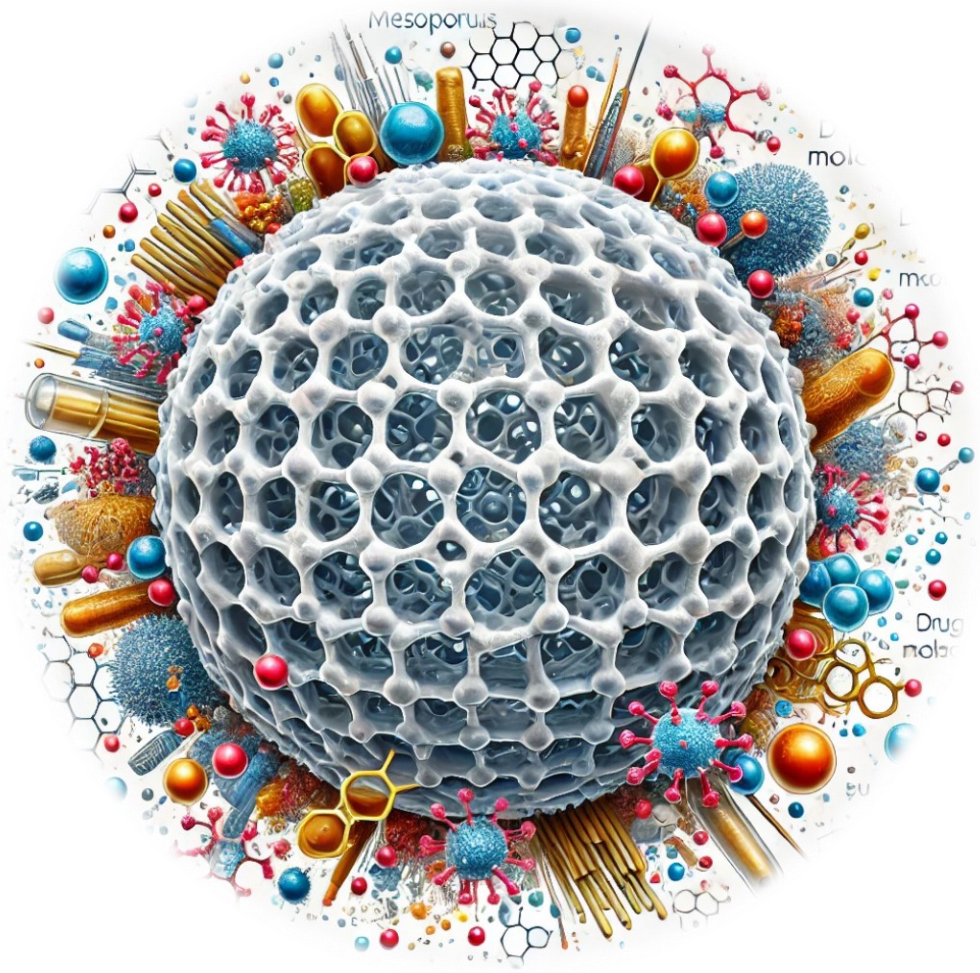

4.1 Introduction

Small molecules are pivotal in numerous biological processes and form the basis of most pharmaceutical drugs. However, delivering these molecules effectively to specific target sites within the body remains a major challenge in drug development. This challenge underscores the importance of advanced drug delivery systems (DDS) in optimizing therapeutic efficacy and patient outcomes. A significant obstacle to successful drug delivery is the poor solubility of many organic molecules in aqueous environments, which contributes to incomplete drug absorption and is responsible for over 40% of drug development failures [1].

To address the issue of low bioavailability, several strategies have been developed to enhance drug solubility, often through the modulation of the local microenvironment. For instance, pH modifiers can be utilized to increase the solubility of compounds that exhibit pH-dependent solubility profiles. Additionally, advanced drug delivery systems based on nanoparticles and microparticles have shown significant promise in addressing solubility and bioavailability challenges. These particulate systems not only improve the solubility and absorption of small molecules but also enable targeted drug delivery, directing therapeutic agents to specific sites within the body. This targeted approach reduces off-target effects, increases therapeutic efficacy, and ultimately leads to improved clinical outcomes [2]. Over the past few decades, DDS have evolved into powerful tools that significantly enhance the therapeutic potential of conventional drugs, particularly, providing innovative solutions to complex medical challenges.

A drug delivery system is an advanced formulation or device meticulously engineered through a multidisciplinary approach, to ensure the safe, efficient, and precise delivery of pharmaceutical compounds. An ideal DDS not only improves bioavailability but also optimizes the pharmacokinetic and pharmacodynamic profiles of the active agent, ensuring a rapid therapeutic response and maintaining prolonged efficacy. Furthermore, depending on the chosen administration route, a DDS may incorporate advanced controlled-release mechanisms, enabling prolonged drug release,

minimizing dosing frequency, and improving patient adherence, key factors in achieving superior clinical outcomes [3,4]. DDS utilizing small-scale carriers, such as nanoparticles (NPs), offer the ability to modulate critical pharmacological parameters like pharmacokinetics, biodistribution, and tissue-specific targeting. Nanotechnology has become central to advancing DDS, enabling the incorporation of therapeutic agents into nanoparticles or nanocomposites through methods such as physical encapsulation, adsorption, or chemical conjugation. These approaches can markedly enhance drug stability, improve bioavailability, and optimize biodistribution, leading to superior therapeutic outcomes compared to conventional drug formulations [5].

An optimal drug administration strategy should focus on selectively targeting diseased tissues while minimizing exposure to healthy cells. This precise targeting ensures that the drug's therapeutic effects are concentrated at the site of the disease, reducing off-target effects and preventing damage to normal cells. Achieving this level of specificity can significantly enhance treatment efficacy, reduce side effects, and improve patient safety. To accomplish this, the drug can be modified, encapsulated, and delivered within nanostructured carriers that are biomimetic and, in many cases, responsive to specific physiological stimuli, allowing for controlled release and ensuring sustained therapeutic action [6].

Stimuli-responsive nanostructures are designed to respond to specific environmental triggers such as pH changes, temperature fluctuations, or enzymatic activity, ensuring that the drug is released precisely at the target site [7].

The design of a drug-targeting system relies on optimizing factors such as drug concentration, therapeutic potency, and circulation time, taking into account the pathophysiological changes that occur during disease progression. By exploiting these disease-specific characteristics, targeted delivery systems can direct drugs to the intended areas, improving both the precision and effectiveness of treatment. Nanotechnology has been particularly impactful in the development of NPs, which are widely utilized in cancer therapy [8].

Various types of nanoparticles have been developed, each offering distinct advantages and limitations in terms of drug loading capacity, targeted delivery, and patient compliance. Nanomaterials has been extensively investigated to boost chemotherapy efficacy, and these can be classified into two main groups: organic and inorganic nanoparticles. Organic nanoparticles are valued for their biocompatibility and flexibility in drug conjugation, making them suitable for a variety of therapeutic applications. In contrast, inorganic nanoparticles are known for their stability, precise targeting capabilities, and potential for multifunctional therapeutic applications. Together, these nanomaterials provide a versatile platform to optimize chemotherapy treatment (Figure 4.1).

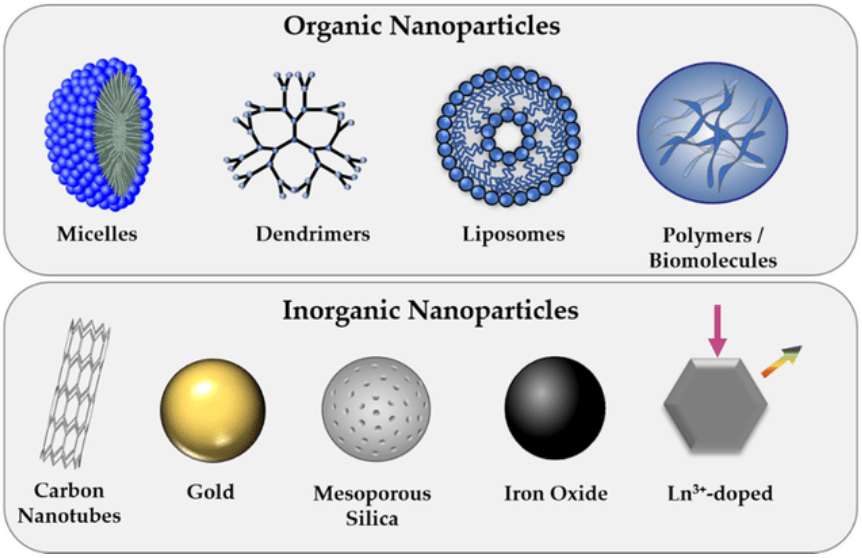

Figure 4.1. Schematic representations of different types of Nanoparticles [9]

Organic nanomaterials, such as liposomes, polymeric micelles, dendrimers, and carbon nanotubes, have shown strong potential in drug delivery. Some, like liposomes and polymeric micelles, have successfully reached the market and received FDA approval for clinical use, marking key progress in cancer therapy [10].

Inorganic nanomaterials, especially mesoporous silica nanoparticles, are gaining attention in nanomedicine for their versatility, safety, and ability to control drug release and improve targeting. These advancements are making cancer treatments more effective and patient-friendly [11].

4.1.1 Mesoporous silica nanoparticles (MSNs)

Mesoporous silica nanoparticles (MSNs) have emerged as highly promising candidates for drug delivery systems due to their unique intrinsic properties. With a large surface area and high pore volume, MSNs offer excellent drug loading capacity, while their biocompatibility, biodegradability, and chemical stability make them well-suited for therapeutic applications. One of the key advantages of MSNs is their highly tunable surface properties, which allow for precise control over pore size, surface chemistry, and particle morphology, critical factors for optimizing drug delivery efficiency and improving targeting capabilities [12].

Extensive *in vitro* and *in vivo* studies have demonstrated the excellent performance of MSNs in drug release, targeting, and safety profiles. Their versatility, coupled with the ability to be engineered for specific therapeutic needs, makes them a powerful platform in nanomedicine, with the potential to significantly enhance treatment outcomes while minimizing adverse effects. Thus, MSNs represent a cutting-edge solution in drug delivery field [13, 14].

Mesoporous silica nanoparticles are a class of porous materials characterized by an ordered pore structure, with pore diameters typically ranging from 2 to 50 nm. MSNs were first synthesized in the early 1990s by Kresge et al. at the Mobile Research and Development Corporation [15].

The synthesis process involves using an amphiphilic surfactant as a structure-directing agent, combined with a silica precursor, leading to the formation of an ordered hexagonal mesophase. Since their discovery, various MSN prototypes with different physicochemical properties have been developed by modifying factors such as the silica source, surfactant templates, and reaction conditions. MSNs can be classified into several types, including Santa Barbara (SBA, with key examples like SBA-15 and SBA-16) [16], Mobile Corporation of Matter (MCM, such as (MCM-41, MCM-48 and MCM-50) [17-19], Michigan State University (MSU) [20] and Hexagonal Mesoporous Silica (HMS) [21].

The synthesis of the ordered mesoporous silica materials primarily relies on templating method that employs a silica source, such as tetraethoxysilane (TEOS) and an amphiphilic surfactant like cetyltrimethylammonium bromide (CTAB) acting as structure-directing agent. This strategy, known as Ströber method or sol-gel method [22], involves the initial dissolution of surfactant molecules in an alkaline medium, where they self-assemble into micelles once the critical micelle concentration (CMC) is exceeded.

Afterward, the silica precursor interacts with the micelles via electrostatic interactions between the inorganic silica and organic surfactants, leading to the formation of an ordered mesoarchitecture. Silica condenses around the polar heads of the surfactant micelles, generating a layered structure. Mesopores become accessible by removing the surfactant via calcination or solvent extraction processes (Figure 4.2).

The precise control of the interfacial tensions during the micelle self-assembly and silica condensation is crucial to achieve the desired particle size and shape, as well as tunable pore dimensions [23].

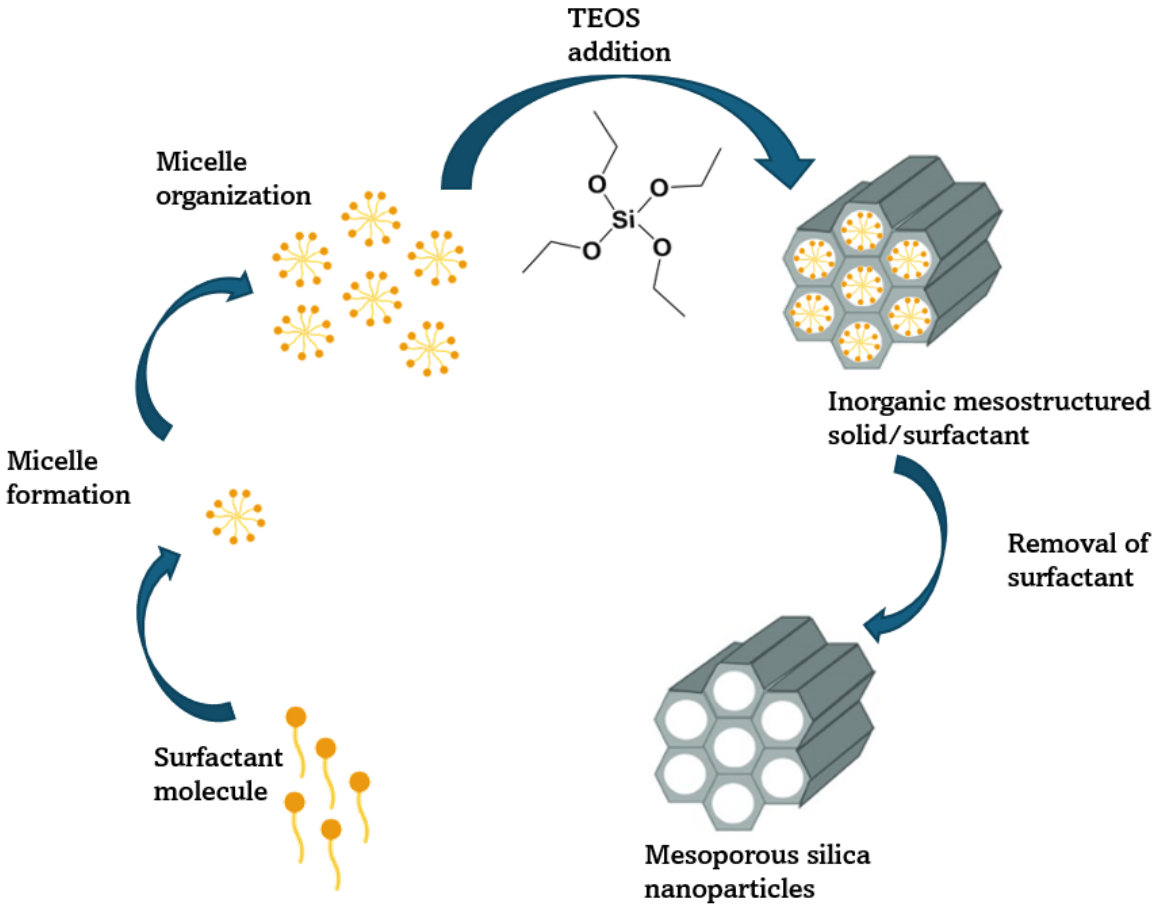

Figure 4.2. Schematic representation of sequential steps of the fabrication process of MSN materials

MSNs properties, such as shape and size, can be well-modulated by changing synthesis conditions, including the choice of surfactant, silica source and solvent, and/or modifying operative parameters like pH, temperature and stirring speed [24-26].

The sol-gel method consists of two key stages: the hydrolysis of the precursor in the reaction medium and the subsequent condensation of the hydrolysed product. The particle size of MSNs is mostly controlled by the pH of the reaction medium; lower pH values lead to smaller particle sizes. For instance, Fang *et al.* reported that decreasing the pH to 11.38, 11.32, and 11.00, resulted in average particle sizes of 170 nm, 110 nm, and 50 nm, respectively [27]. In addition to pH, other parameters such as silica precursor concentration, reaction time, temperature, catalyst type, co-solvent, and water content also affect particle size [28, 29].

The choice of surfactant molecules can influence pore dimensions: surfactants with longer chain lengths produce MSNs with larger pores, whereas shorter chain surfactants yield smaller pores [30]. Moreover, increasing the concentration of CTAB surfactant results in highly disordered mesostructure [31] , a similar effect is observed with an increase in TEOS concentration [32].

The shape of MSNs can be modulated by varying the molar concentrations of TEOS, surfactant, and base catalyst. Cai et al. demonstrated that by varying concentrations of CTAB, TEOS, and NH_4OH/NaOH, they could synthesize MSNs in different shapes, such as nanorods, oblate particles, and spheres [33].

4.1.2 Design of Mesoporous silica nanoparticles for drug delivery applications

The surfaces of MSNs are covered with a large amount of silanol groups (Si-OH), making them highly susceptible to both internal and external surface modifications [34]. These modifications can confer new physical and chemical properties, broadening the applicability of mesoporous materials across various fields.

In drug delivery, surface functionalization of mesoporous silica nanoparticles (MSNs) is a widely used approach to achieve selectivity to targeted tissue, increase the specificity of therapeutic treatments, reduce adverse effects, and potentially overcome multi-drug resistance.

Two main techniques for modifying MSNs are co-condensation and grafting. Co-condensation is a direct modification method that utilizes sol-gel chemistry between to combine tetralkoxysilanes with one or more organoalkoxysilane [35]. This approach results in a more uniform distribution of functional groups on the nanoparticle surface [36], but it may lead to a less ordered final structure [37].

In contrast, grafting is a post-synthesis method where functional groups are attached to the pre-formed silica network. This technique preserves the original mesostructure of the silica nanoparticles [38], offering greater control over particle size, morphology, and pore diameter [39].

Targeted drug delivery systems can involve passive or active targeting. Passive targeting refers to the accumulation of drug-loaded nanoparticles at the desired site due to pharmacological or physicochemical factors. In this case, drug delivery is guided by the inherent properties of nanoparticles, such as size, surface charge, and lipophilicity. These properties allow nanoparticles to preferentially accumulate in specific tissues or organs [40]. In contrast, active targeting exploits the overexpression of specific receptors on the surface of cancer cells, compared to normal cells [41]. The conjugation of targeting molecules to the external surfaces of nanoparticles enhances cellular uptake via specific molecular recognition between the ligands and overexpressed receptors on tumor cells [42].

A wide range of targeting ligands have been explored for the development of tumor-targeted drug delivery systems, including, small molecules (i.e. folic acid) [43], proteins [44], small peptides [45], antibodies [46] and aptamers [47] (Figure 4.3).

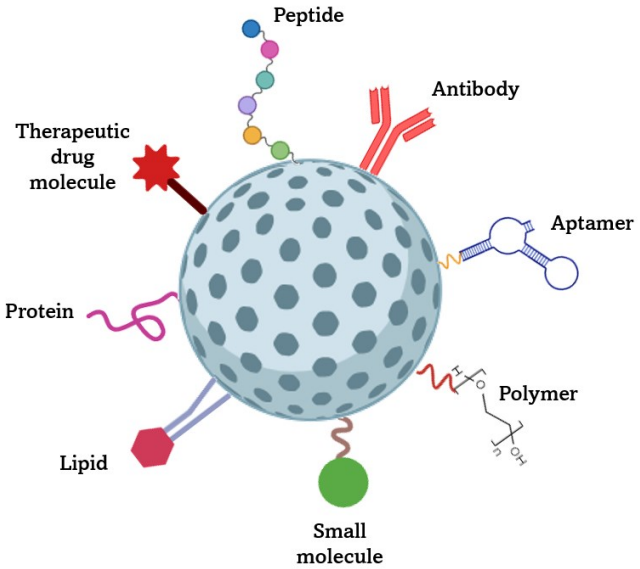

Figure 4.3. Illustration of various ligands that can be attached to mesoporous silica nanoparticles (MSNs) to optimize their performance in cancer therapy

4.1.3 Stimuli-responsive strategies for drug delivery

Even though targeting improves the efficiency of the drug delivery systems, it does not prevent the premature drug release from DDSs or ensure optimal release of the drug once the target site is reached [48]. An ideal DDS should effectively inhibit premature drug release and ensure the controlled, precise, and complete release of the therapeutic payload at the target site [49].

To address these challenges, stimuli-responsive DDSs have been developed to enhance the efficacy of targeted delivery strategies. These systems are specifically designed to exploit the unique characteristics of the tumor microenvironment (TME) compared to normal tissues.

Stimuli-responsive nanocarriers can be activated by external triggers such as magnetic fields, temperature, ultrasound, and light, as well as internal stimuli, including pH, ATP, enzymes, redox potential, and hypoxia. These stimuli may originate from within cancer cells or the surrounding TME, enabling precise and controlled drug release [50].

Recent advancements have introduced dual- or multi-stimuli approaches, which showed enhanced performance in drug delivery and release. Unlike single-stimulus systems, multi-stimuli DDSs integrate multiple activation strategies within a single nanocarrier, enabling them to respond to various stimuli either individually or simultaneously [51] (Figure 4.4).

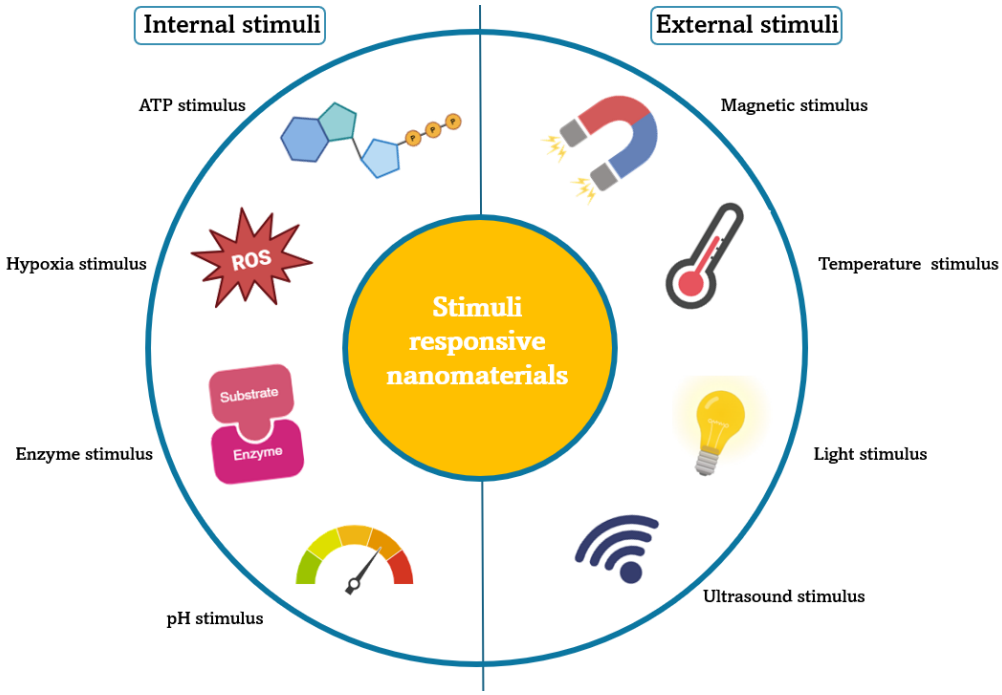

Figure 4.4. External and internal stimuli responsive strategies in drug delivery systems

Stimuli responsive MSN-based nanosystems incorporate therapeutic agents conjugated to the pore walls via stimuli-sensitive bonds, linkers, or substrates. These systems are engineered to selectively release the therapeutic agents at the target site in response to specific stimuli [52].

Due to the pH differences between normal and tumor tissues, as well as between intracellular and extracellular environments, pH responsive nanoplatforms are widely utilized as effective tools to prevent unspecific and uncontrolled drug release. These nanoplatforms retain drugs under normal pH conditions and release them exclusively in the acidic tumor microenvironment.

To achieve this, different pH-sensitive chemical bonds such as hydrazone [53], imine [54], oxime [55], amide [56], acetal [57] and orthoester [58] are incorporated within the internal surfaces of the nanocarrier. In addition to the cleavage of acid-labile chemical bonds, another approach for developing pH-sensitive nanosystems involves the protonation. This method uses polymers with ionizable pendant groups, which can accept or donate protons in response to pH changes, thereby triggering drug release [59, 60].

4.1.4 Pharmacokinetics, biocompatibility, and toxicity of MSNs

The rational design of MSN-based drug delivery systems should carefully consider key physicochemical parameters, such as morphology, size, shape, surface area, and surface charge, as these strongly impact the system's *in vivo* performance, biodistribution, and biocompatibility [61]. The degradation of MSNs in the body is primarily governed by factors such as their morphology, surface area, surface modifications, and the nature of the encapsulated drug. Spherical MSN degrade faster than rod-shaped ones due to their larger surface area in contact with the physiological environment [62]. The degradation rate can be further accelerated by incorporating cations like Ca^{2+} and Fe^{3+}, which disrupt the silica network [63, 64].

To optimize MSN degradation, they can be coated with macromolecules or polymers, such as polyethylene glycol (PEG).

The extent of PEGylation, influenced by both the polymer chain length and the density of the coating, can significantly reduce the dissolution rate, thus promoting disintegration of the MSNs [65]. Additionally, recent studies suggest that drug loading within the MSN pores can enhance their *in vitro* degradability [66]. The biocompatibility and biodistribution of MSNs can be fine-tuned by modifying their surface properties.

MSNs are widely recognized for their high biocompatibility, as they degrade into silicic acid, a safe compound naturally present in the body [67]. The biocompatibility and biodistribution of MSNs can be fine-tuned by modifying their surface properties. He and coworkers investigated the effects of PEGylation and particle size on the *in vivo* biodistribution and urinary excretion of MSNs.

Results revealed that MSNs of various sizes primarily accumulated in the liver and spleen. PEGylation was particularly effective in reducing uptake by the liver, spleen, and lungs, especially for larger particles, resulting in longer blood-circulation lifetime, slower biodegradation, and lower

excretion rate of the degradation products [68]. Additionally, cytotoxicity can be significantly reduced by modifying the surface chemistry and lowering the overall surface charge of MSNs [69].

In a mouse model, Liu *et al.* demonstrated that MSNs exhibit good biocompatibility, even at high doses. The lethal dose for 110 nm MSNs exceeded 1000 mg/kg, and no adverse effects or mortality were observed in mice after repeated administrations over a 14-day observation period [70].

Nanoparticles size plays a pivotal role in determining their biodistribution. Nanoparticles larger than 200 nm are typically removed from the bloodstream and sequestered in the liver and spleen, while particles smaller than 10 nm are rapidly cleared by the kidneys [71].

Larger MSNs, due to their slower clearance rates and prolonged retention in the body, are more likely to induce adverse effects in organs and tissues, such as inflammation, oxidative stress, and tissue [72]. The cytotoxicity of MSNs is mainly linked to the silanol groups on their surface. These negatively charged groups can interact with red blood cells, increasing the risk of haemolysis, and may also trigger immune responses by promoting protein opsonization *in vivo* [73].

The formation of a protein corona, which occurs when plasma proteins adsorb onto the surface of nanoparticles, plays a crucial role in determining their biological behaviour. This phenomenon influences several key aspects, including circulation time, tissue distribution, cellular uptake, and ultimately, the therapeutic efficacy of the nanoparticles [74, 75].

A materials engineering approach offers versatile strategies for creating mesoporous silica-based nanodevices, which are highly promising for applications in bionanotechnology and nanomedicine [6, 76-78].

The aim of this research was to examine the surface properties of a series of MSU-type mesoporous silica nanoparticles that have undergone various post-synthesis modifications, and to explore how these properties change in response to the different treatments.

Using a variety of characterization techniques, such as FTIR, Zeta potential, and nitrogen adsorption porosimetry, insights into the surface modifications of mesoporous silica nanoparticles were provided. These findings contribute to a deeper understanding of the nanostructure and the potential interactions of these nanoparticles, highlighting the potential for new applications.

We specifically examined how the surface properties of these nanoparticles vary following both single and multi-step modification procedures, as well as surfactant extraction protocols used during the synthesis of MSN precursor materials. Evaluating these modifications is essential for determining the suitability of the nanoparticles for various applications, particularly in drug delivery. The accessibility of nanoparticle pores and surfaces, along with potential electrostatic interactions to which the hybrid material may be subjected, will significantly influence the behaviour of the nanomaterial, determining its effectiveness for the intended application.

4.2 Results and Discussion

Mesoporous silica nanoparticles have been specifically designed for targeted therapy applications, incorporating features that enhance both selectivity and efficacy. Different MSN-based prototypes were developed using proprietary MSN technology of NanoSiliCal Devices, an innovative SME and spin-off from the University of Calabria, where I undertook a 10-month internship during my doctoral studies. These nanodevices were engineered with a dual-functionalized architecture: targeting molecules are conjugated to their external surface, enabling precise tissue recognition and efficient cellular internalization, while the internal pores are equipped with linkers suitable for subsequent drug conjugation through covalent pH-sensitive bonds, as well as non-covalent interactions, such as Van der Waals forces, hydrogen bonding, and electrostatic interactions. This design allows therapeutic drugs to be loaded into the pores and released in a controlled manner, specifically within the microenvironment of pathological tissues. Such targeted release ensures maximum therapeutic efficacy while minimizing off-target effects.

In this study, we developed MSN-based nanosystems with folic acid (FOL) as the targeting ligand on the external surface (FOL-MSN). Folic acid provides high specificity for folate receptors, which are commonly overexpressed in many types of cancer cells. Furthermore, the pores of the MSNs were functionalized with linkers specifically designed to conjugate therapeutic agents via covalent pH-sensitive bonds or non-covalent interactions (FOL-MSN-DIOL, FOL-MSN-COOH, FOL-MSN-HYD). Figure 4.5 illustrates the schematic synthesis of MSNs, highlighting the key steps: synthesis, external surface functionalization, surfactant removal from inner pores, and internal surface functionalization.

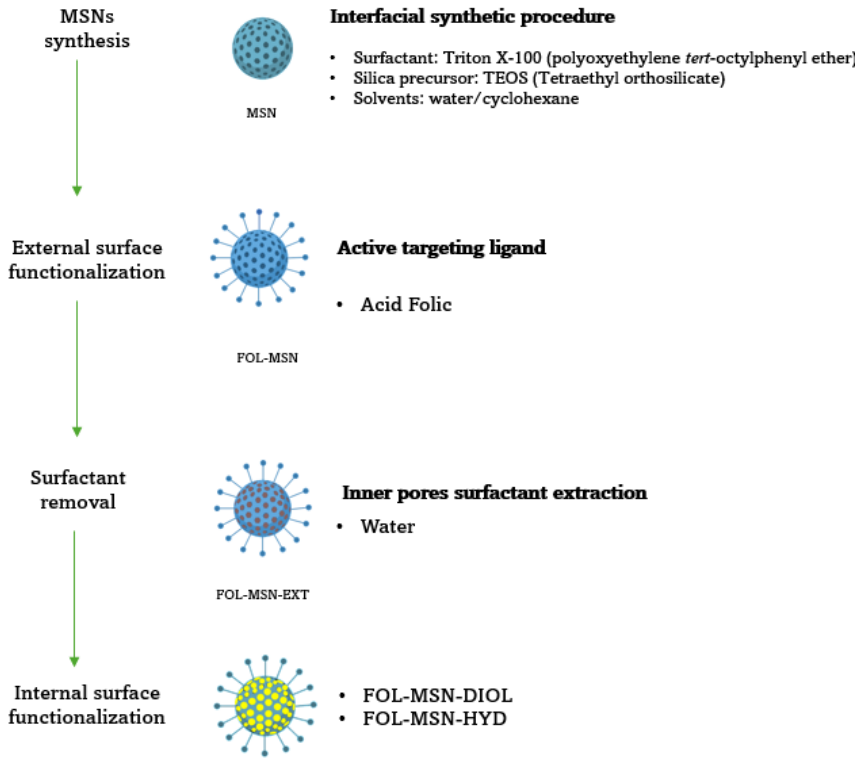

Figure 4.5. Schematic illustration of the synthesis process for the developed MSN prototype

MSU-type mesoporous silica nanoparticles were synthesized using a non-catalyzed biphasic synthetic method [79], following a modified protocol claimed in an international patent [80].

The synthesis was carried out at room temperature, with cyclohexane serving as the organic phase in which the silica precursor, tetraethyl orthosilicate (TEOS), was dissolved. Hydrolysis of TEOS occurred in the presence of a neutral, low-cost, non-toxic, and biodegradable surfactant, Triton X-

100, which acted as a structure-directing agent. As a result, silica condensed around the surfactant micelles, forming an inorganic oxide framework.

The as-synthesized MSNs (MSN_{AS}) were characterized using both scanning electron microscopy (SEM, Figure 4.6) and transmission electron microscopy (TEM, Figure 4.7). The nanoparticles exhibited a mesoporous structure typical of the MSU family, with primary particle sizes ranging from 80 to 120 nm, displaying an irregular, spheroidal morphology.

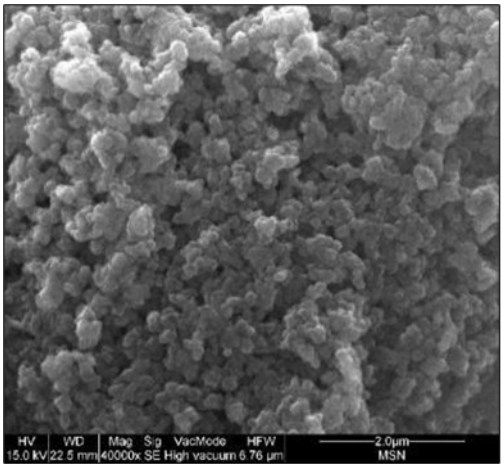

Figure 4.6. SEM micrograph image of MSN_{AS}

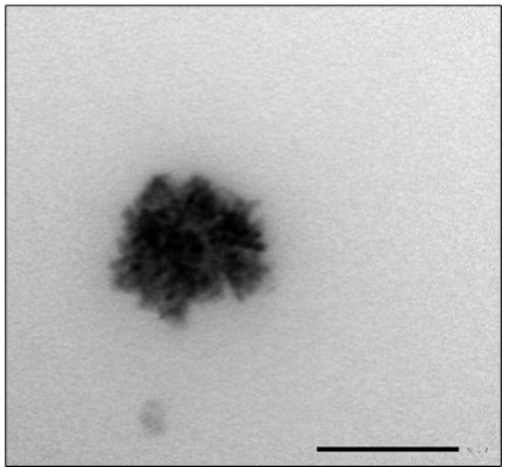

Figure 4.7. TEM micrograph image of MSN_{AS}

The small-angle XRD pattern (Figure 4.8) of the as-synthesized sample, MSN_{AS}, demonstrated a single d100 diffraction peak at the range of 0-1°, typical of the family of the MSU-type materials [81].

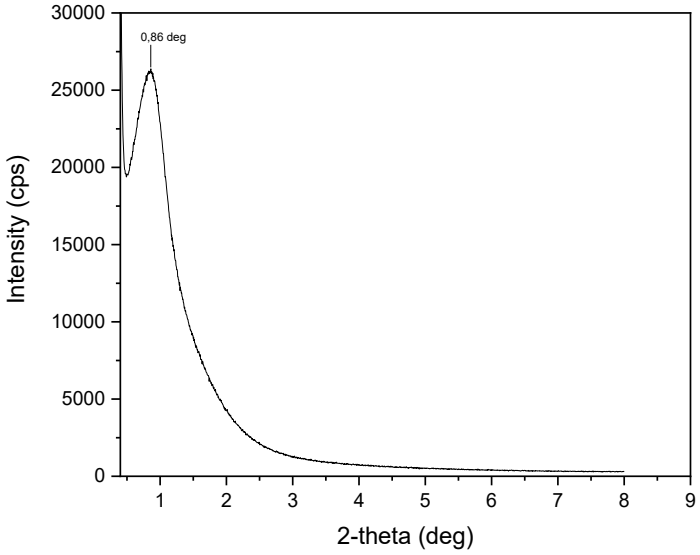

Figure 4.8. XRD pattern of MSN_{AS} sample

The zeta potential of the MSN_{AS} samples was also evaluated, revealing values of approximately -18.00 mV, primarily attributed to the presence of -OH groups on the nanomaterial surface [82]. This measurement is essential for characterizing the suspension behaviour of nanomaterials, as it is directly correlated with suspension stability, as well as the size and morphology of the particles [83].

The FT-IR spectrum (Figure 4.9) revealed characteristic vibrational modes of mesoporous silica structures. At approximately 3400 cm^{-1}, a broad absorption band was observed primarily due to the stretching of the different kinds of OH groups and related interacting water, along with a sharp peak at 1635 cm^{-1}. Vibrations at 2946 and 2882 cm^{-1} were attributed to the C-H stretching of methylene and methyl groups of the template (Triton X-100). The bands at 1463 cm^{-1} and 1511 cm^{-1} corresponded to methyl asymmetric bending, overlapped with scissoring of the methylene groups, while the symmetrical bending vibration of the methyl groups was observed at 1355 cm^{-1}. The most intense band at 1094 cm^{-1}, with a shoulder at 1210 cm^{-1}, was attributed to the symmetric and antisymmetric stretching of the Si-O-Si structure, along with a less intense signal at 803 cm^{-1}. Finally, silanol peaks arising from vibrational bending modes were observed at 972 cm^{-1} [84, 85].

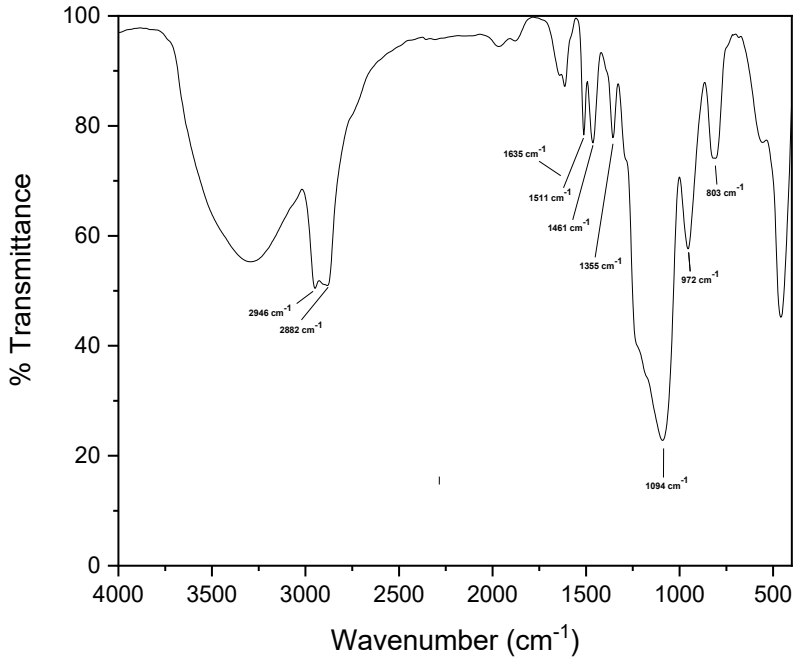

Figure 4.9. FT-IR pattern of MSN_{AS} sample.

MSN_{AS} were then converted into aminopropyl-functionalized nanoparticles (AP-MSN) by covalent grafting of (3-aminopropyl)triethoxysilane (APTES) onto the MSN surface. Subsequently, folic acid-functionalized nanoparticles (FOL-MSN) were synthesized by forming an amide bond between the amino group of AP-MSN and the carboxylic function of folic acid (FOL) (Figure 4.10).

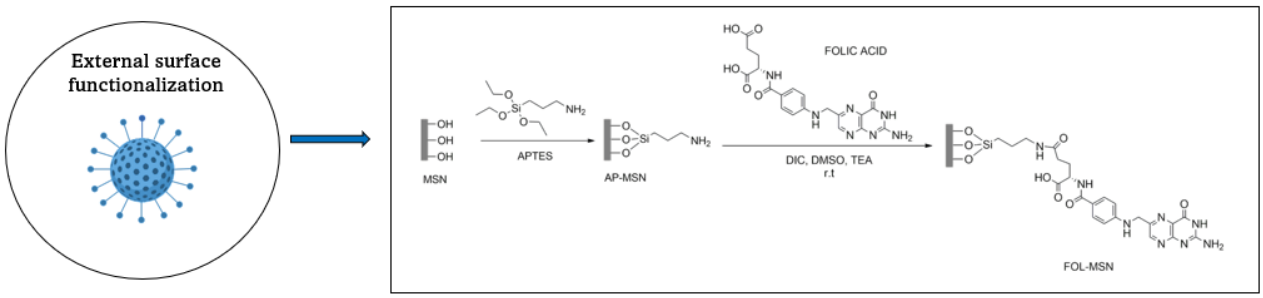

Figure 4.10. Graphical representation of external MSN surface functionalization

After surface grafting with 3-aminopropyltriethoxysilane, the zeta potential shifted to a positive value of approximately +27 mV (Fig. a, black curve).

This shift is due to the amino groups introduced onto the nanomaterial surface, which become positively charged at pH 7—the condition under which the zeta potential measurements were conducted—resulting in an overall positive surface charge.

Following functionalization with folic acid, the surface charge of the nanoparticles decreased significantly to +10 mV (Figure 4.11a, red curve). This reduction is attributed to the consumption of amino groups that were previously present on the surface [86].

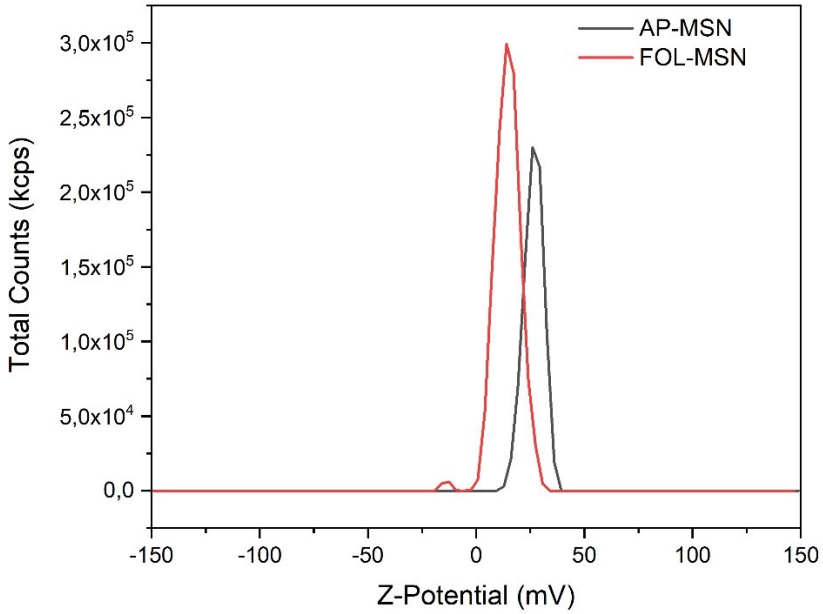

Figure 4.11. Comparison of zeta potential graphs for AP-MSN (black) and FOL-MSN (red) samples

Importantly, to prevent a substantial reduction in pore volume, MSNs were externally functionalized prior to surfactant extraction. This approach ensured that a significant pore volume was maintained after surfactant removal, with the folic acid targeting molecule predominantly anchored on the external surface, thus enhancing drug loading efficiency.

Finally, the surfactant within the pores of FOL-MSN was then efficiently removed by solvent extraction using ultrapure water, resulting in FOL-MSN-EXT.

As displayed in Figure 4.12, the removal of the surfactant from the inner pores of FOL-MSN sample did not substantially affect the zeta potential value.

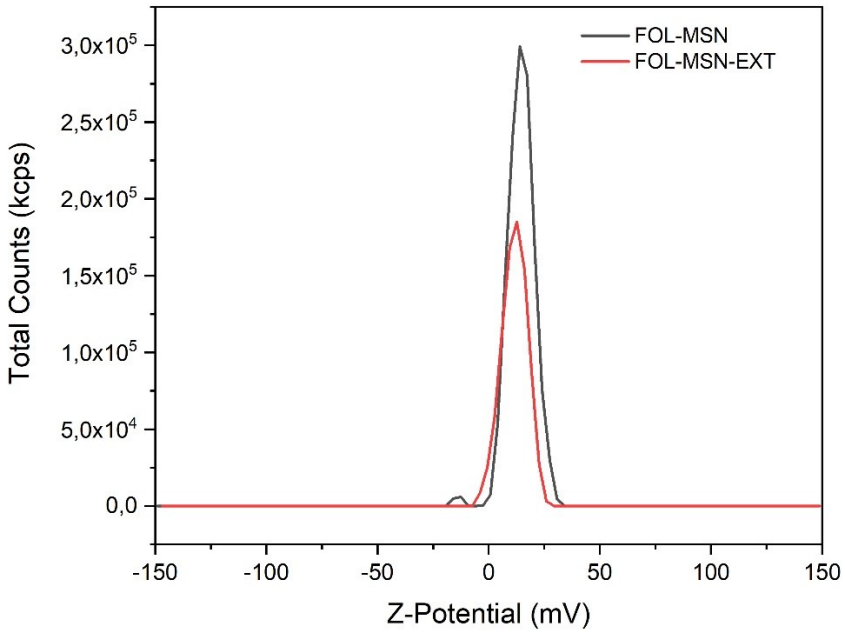

Figure 4.12. Comparison of zeta potential graphs for FOL-MSN (black) and FOL-MSN-EXT (red) samples

The FTIR spectra of the AP-MSN, FOL-MSN, and FOL-MSN-EXT samples provided insights into the functional groups present, enabling a comparison of the modifications in each sample. Variations in the characteristic peaks indicated specific interactions and changes resulting from the functionalization process.

The FT-IR spectrum of the AP-MSN sample (Figure 4.13) reveals additional peaks compared to the MSN_{AS} spectrum (Figure 9). Two peaks, in the range of 3400-3300 cm^{-1} and 3330-3250 cm^{-1}, correspond to the stretching vibrations of the NH_2 group. A peak at 1576 cm^{-1}, characteristic of N-H bending vibrations, further supports the presence of amine groups introduced during the functionalization process [87]. Additionally, the stretching vibrations of C-H bonds from the propyl groups of organosilanes molecules and surfactants are observed. The Si-OH symmetric stretching peak at 949 cm^{-1} shows reduced intensity in the AP-MSN sample, indicating successful grafting of the aminopropyl groups.

The FT-IR spectrum of the FOL-MSN sample shows absorptions in the regions 1600-1585 cm^{-1} and 1500-1400 cm^{-1} corresponding to carbon-carbon stretching vibrations in the aromatic ring of folic acid. The N–H stretching band around 3400 -3300 cm^{-1}, attributed to amide functions, overlaps with the O–H stretching band (ν O–H). In the FOL-MSN spectrum, bands in the 1608-1450 cm^{1} range are assigned to C–N stretching, N–H bending, and O–H bending vibrations, with considerable overlap with the aromatic ring bands [88]. Additionally, the characteristic peaks at 1402 cm^{-1} and 1327 cm^{-1}, associated with the asymmetric and symmetric bending of the methyl group from the surfactant Triton X-100, are no longer visible in the FOL-MSN-EXT sample, suggesting successful removal of the surfactant during the extraction process.

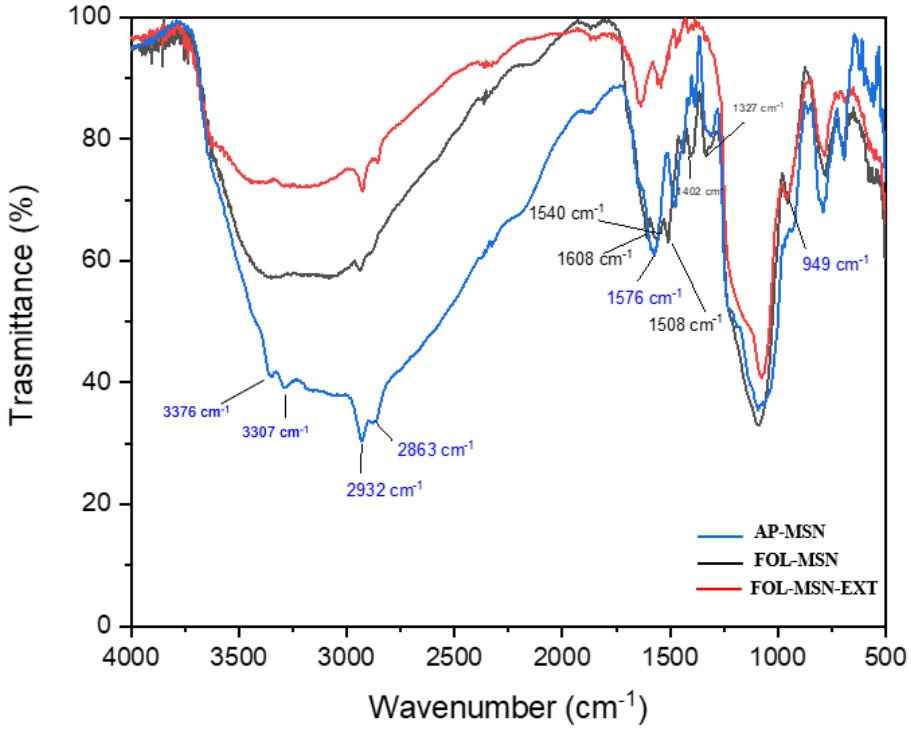

Figure 4.13. FT-IR spectra overlap of AP-MSN (blue), FOL-MSN (black) and FOL-MSN-EXT (red) samples

Nitrogen adsorption characterization is a technique used to determine specific surface properties of porous materials, such as surface area, pore volume, and pore size distribution, by analyzing the adsorption and desorption of nitrogen at low temperatures. The N_2 adsorption-desorption isotherms for all synthesized MSN systems exhibited type IV behaviour as shown in Figure 4.14.

According to IUPAC classification, this confirms the mesoporous feature of the materials.

The BET (Brunauer-Emmett-Teller) surface area and pore volume values are determined using the BJH (Barrett-Joyner-Halenda) method. BET and pore volume values are summarized in Table 4.1. The removal of surfactant from the inner pores of FOL-MSN led to an increase in the BET surface area, from 207.45 m^2/g before extraction to 423.38 m^2/g for FOL-MSN-EXT. Similarly, the pore volume increased to 1.512 cm^3/g in the extracted FOL-MSN.

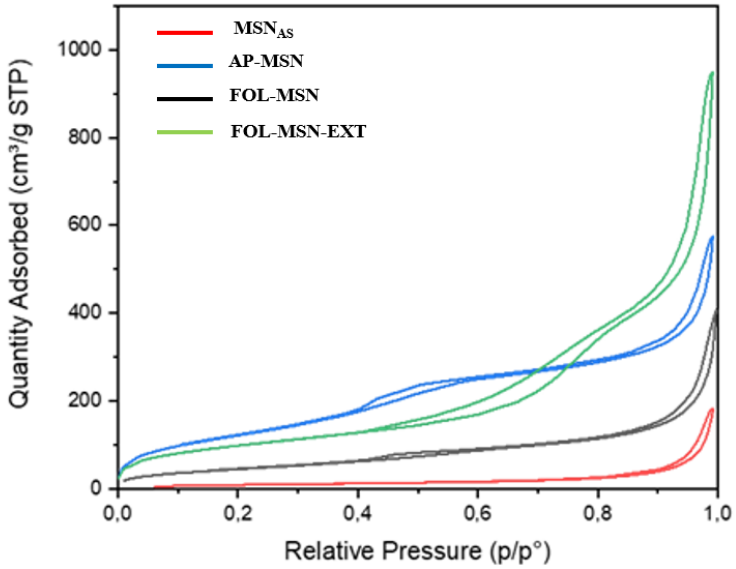

Figure 4.14. Adsorption Isotherm overlap of MSN_{AS} (red), AP-MSN (blue), FOL-MSN (black) and FOL-MSN-EXT (green) samples

Table 4.1. N_2 adsorption data

Sample	**BET surface area ($m^2 \cdot g^{-1}$)**	**Pore Volume ($cm^3 \cdot g^1$) at $P/P^0 = 0.96$**
AP-MSN	250.45	0.615
FOL-MSN	207.45	0.361
FOL-MSN-EXT	423.38	1.512

After surfactant removal using ultrapure water at room temperature, the inner pores of the extracted FOL-MSN (FOL-MSN-EXT) were functionalized with different organosilanes to introduce specific functional groups on the MSN surface, enabling the formation of stimuli responsive bonds.

The FOL-MSN-EXT sample was first functionalized with 3-glycidoxypropyltrimethoxysilane (GLY), followed by hydrolysis to obtain FOL-MSN-DIOL (Figure 4.15). It was also functionalized with (3-aminopropyl)triethoxysilane (APTES), resulting in FOL-MSN-APint. Starting from FOL-MSN-APint sample, treatment with succinic anhydride led to the formation of FOL-MSN-COOH, which was then reacted with hydrazine monohydrate to yield FOL-MSN-HYD (Figure 4.15).

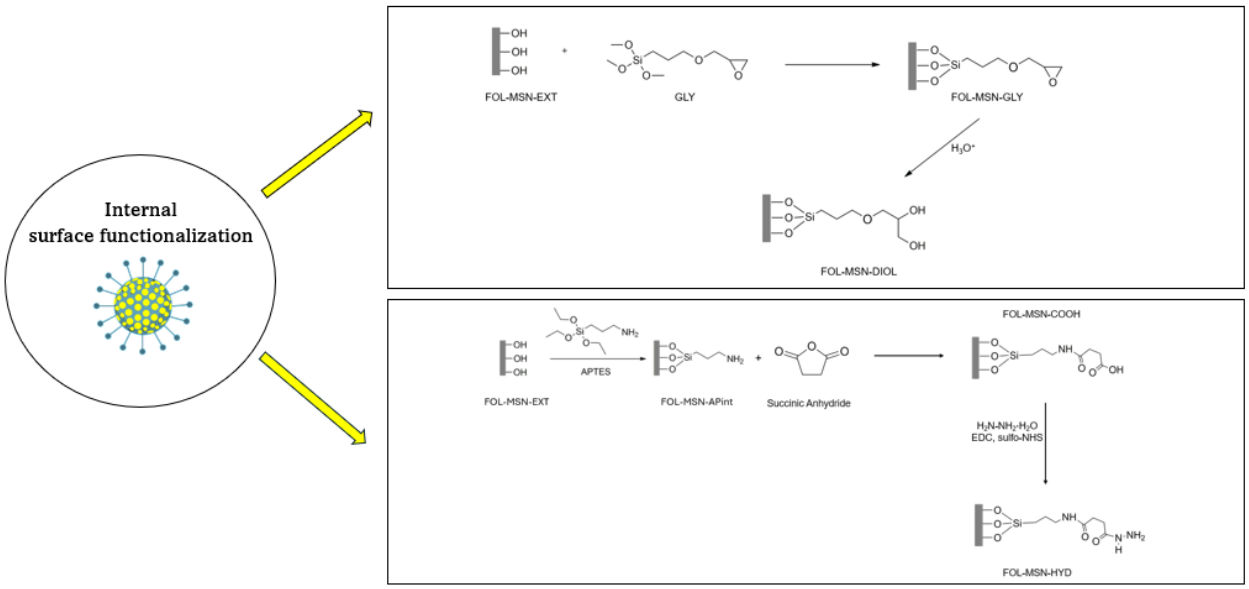

Figure 4.15. Graphical representation of internal MSN surface functionalization processes

Figure 4.16 shows the FT-IR spectra of FOL-MSN-EXT, FOL-MSN-GLY, and its hydroxylated derivative FOL-MSN-DIOL. Compared with the FT-IR spectra of FOL-MSN-EXT (green curve) the spectrum of FOL-MSN-GLY (black curve) shows increased peak intensities around 2928–2861 cm^{-1}, attributed to the symmetric and antisymmetric vibrations of CH and CH_2 groups of the glycidoxypropyl group, These peaks are more prominent in the FOL-MSN-GLY sample, while are reduced in intensity in FOL-MSN-DIOL spectrum. The peak at 801 cm^{-1}, associated with the asymmetric stretching of the C-O-C bond in the epoxide ring, overlaps with the bending vibrations

of Si-O bonds [89]. This peak is more intense in the FOL-MSN-GLY sample, confirming the presence of the epoxide group, while its reduction in FOL-MSN-DIOL is consistent with the epoxide ring opening during hydrolysis. Additionally, an intense peak at 1460 cm^{-1} is observed in both the FOL-MSN-GLY and FOL-MSN-DIOL samples compared to FOL-MSN-EXT. This peak could be assigned to the bending vibrations of methylene groups (CH_2) in the alkyl chain of the 3-glycidoxypropyl substituent.

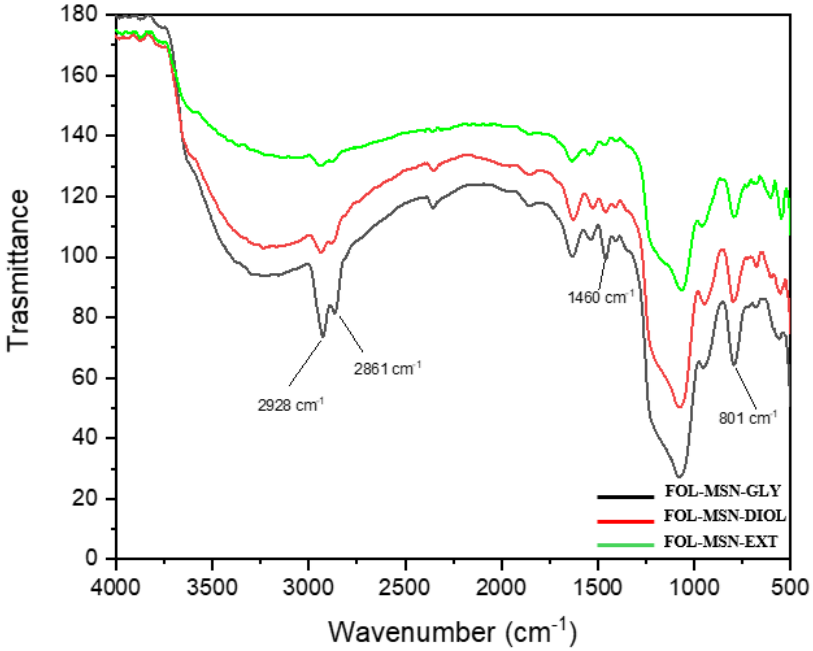

Figure 4.16. FT-IR spectra overlap of FOL-MSN-GLY (black) and FOL-MSN-DIOL (red) and FOL-MSN-EXT (green) samples

Figure 4.17 illustrates the FT-IR spectral overlap between the FOL-MSN-EXT sample and the sample further functionalized with 3-aminopropyltriethoxysilane (FOL-MSN-APint). The grafting process occurs after the surfactant is removed from the internal pores through successive extractions with ultrapure water. As a result, APTES primarily reacts with the free -OH groups within the pores of the FOL-MSN-EXT nanomaterial.

The FT-IR spectrum of the FOL-MSN-APint sample (red curve) displays some additional bands compared to the FOL-MSN-EXT spectrum (black curve) (Figure 4.17).

Two weak peaks, in the ranges of 3400-3300 cm^{-1} and 3330-3250 cm^{-1}, are attributed to the stretching vibrations of the NH_2 group, while the band at approximately 1550 cm^{-1} is characteristic of N-H bending vibrations.

The FT-IR spectrum of FOL-MSN-COOH sample (blue curve, Figure 4.17) exhibits a very broad band centered around 3000 cm^{-1}, corresponding to the O-H stretching vibration of the carboxylic group together with bands at 2938 and 2878 cm^{-1} due to -CH stretching frequencies.

The C=O stretching bands for the amide and carboxylic groups in the FOL-MSN-COOH sample appear at approximately 1650 cm^{-1} and 1719 cm^{-1}, respectively. Furthermore, the -NH bending vibration appears at 1446 cm^{-1}, and the -CH bending vibrations are observed near 1411 cm^{-1}. These bands confirm the presence of an amidic succinic acid moiety on the FOL-MSN-COOH sample [90].

In the FT-IR spectrum of the FOL-MSN-HYD sample (green curve, Figure 4.17), the broad band centered around 3000 cm^{-1}, attributed to the O-H stretching vibration of the carboxylic group, is no longer present, confirming the conversion of the carboxylic group into a hydrazide.

Furthermore, the band at 1719 cm^{-1}, corresponding to the C=O stretching vibration of the carboxylic group observed in the spectrum of the FOL-MSN-COOH sample (blue curve, Figure 4.17), is absent.

This is because the carbonyl vibration of the hydrazide shifts to a lower frequency, around 1620 cm^{-1}, due to electron delocalization from the nitrogen atom. This shifted band overlaps with the amide bond vibration at approximately 1650 cm^{-1}, which correspond to the covalent linkage of the succinic acid hydrazide linker to the MSN pores.

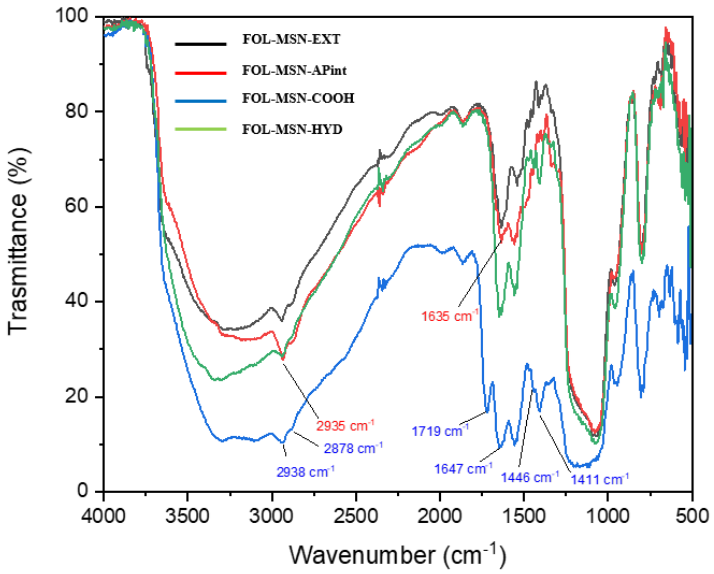

Figure 4.17. FTIR spectra overlap of FOL-MSN-EXT (black), FOL-MSN-APint (red), FOL-MSN-COOH (blue) and FOL-MSN-HYD (green) samples

The BET surface area and pore volume values, as shown in Table 4.2, provide clear evidence for the successful introduction of DIOL and HYD functional groups into FOL-MSN-EXT.

Table 4.2. BET surface area and pore volume values of FOL-MSN-EXT, FOL-MSN-DIOL and FOL-MSN-HYD samples

Sample	BET surface area ($m^2 \cdot g^{-1}$)	Pore Volume ($cm^3 \cdot g^1$) at $P/P^0 = 0.96$
FOL-MSN-EXT	423.38	1.512
FOL-MSN-DIOL	349.02	0.820
FOL-MSN-HYD	226.52	0.572

As shown, the pore surface modifications resulted in a reduction in both BET surface area and pore volume. Specifically, the BET surface area dropped from 423.38 m^2/g in FOL-MSN-EXT to 349.02 m^2/g in FOL-MSN-DIOL, and to 226.52 m^2/g in FOL-MSN-HYD. Similarly, the pore volume was reduced from 1.512 cm^3/g in FOL-MSN-EXT to 0.820 cm^3/g in FOL-MSN-DIOL and to 0.572 cm^3/g in FOL-MSN-HYD. These reductions reflect the successful functionalization of the MSN surface in

both cases, with each modification decreasing the accessible surface area and pore volume in distinct ways. The results revealed significant variations in the surface characteristics of MSNs following each post-synthesis operation.

Inner functionalization of nanoparticles also induces changes in zeta potential. Further modification of FOL-MSN-EXT with APTES to obtain FOL-MSN-APint sample (Fig. 4.18, b) restored the zeta potential to positive value, as expected. In contrast, the introduction of -COOH groups in the FOL-MSN-COOH sample, following the treatment of FOL-MSN-APint with succinic anhydride, resulted in a more negative zeta potential (Fig. 4.18, c). In the case of the FOL-MSN-HYD sample (Fig. 4.18, d), the synthesis involved the formation of an amide bond between hydrazine and the free carboxylic groups in FOL-MSN-COOH sample. The resulting zeta potential reflects the influence of positively charged free amino groups, which increase the surface charge of the hybrid nanomaterial, shifting the value back to positive.

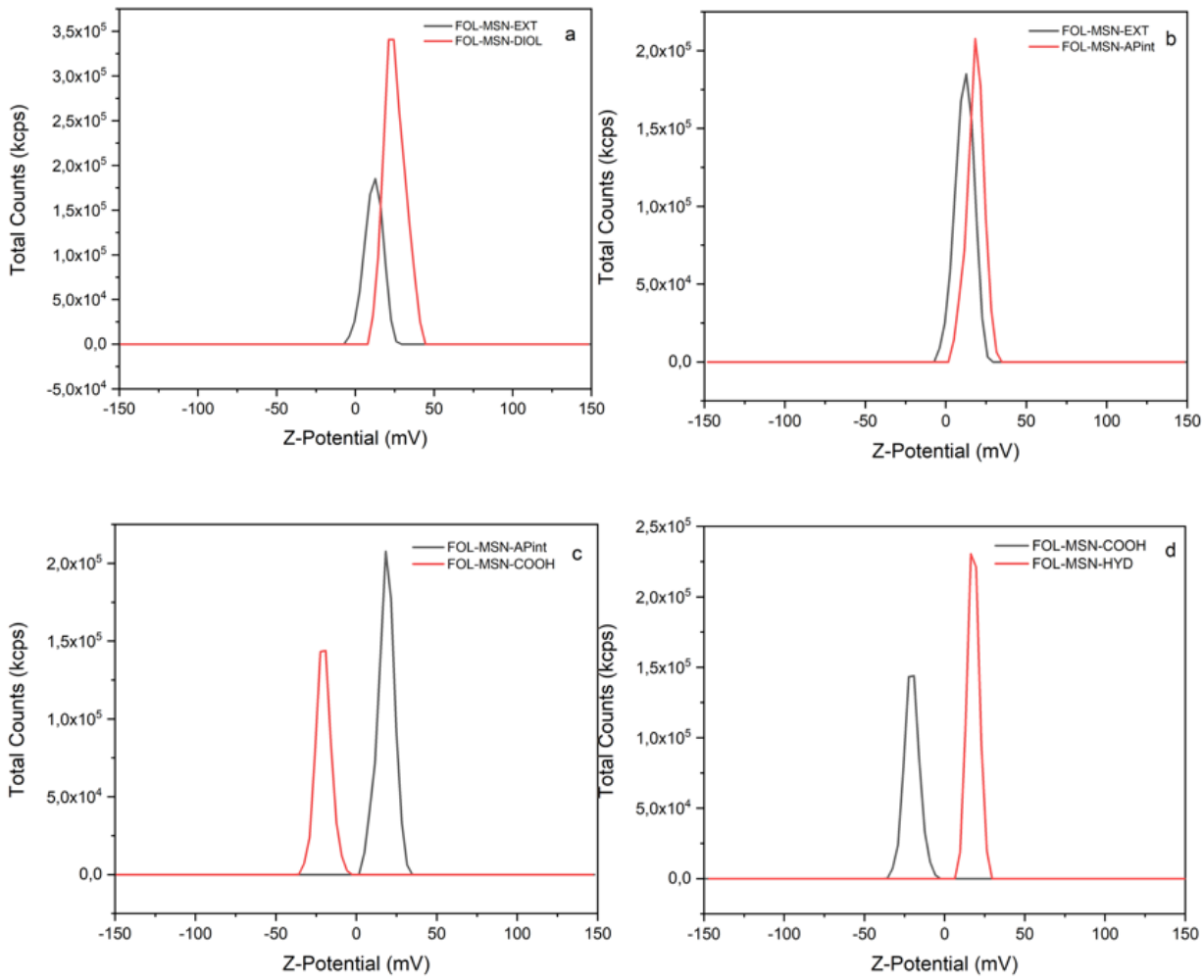

Figure 4.18. Comparison of zeta potential graphs for samples a) FOL-MSN-EXT vs FOL-MSN-DIOL; b) FOL-MSN-EXT vs FOL-MSN-APint; c) FOL-MSN-APint vs FOL-MSN-COOH; d) FOL-MSN-COOH vs FOL-MSN-HYD

4.3 Experimental part

4.3.1 Chemicals and reagents

Reagents were commercially available with analytical grade and used as purchased without further purification. Solvents were purified according to well-known laboratory methods and freshly distilled prior to use. Triton X-100, neutral polyoxyethylene(10) octylphenyl ether, tetraethylorthosilicate (TEOS), (3-aminopropyl)-triethoxysilane (APTES), Folic acid (FOL), Diisopropylcarbodiimide (DIC), water (HPLC grade), Acetone (HPLC grade) were purchased by MERCK/Sigma-Aldrich (Milan, Italy). Bortezomib was purchased from LC Laboratories, Woburn, MA. Ethanol, Diethyl ether, 1,4-Dioxan, Dimethylformamide (DMF), Tetrahydrofuran (THF), trifluoroacetic acid (TFA), Acetic Acid from VWR. Dimethyl sulfoxide (DMSO) and Cyclohexane from Merck and Triethylamine from Carlo Erba. Ultrapure water was distilled with the MilliQ® water, Millipore.

4.3.2 Instrumental characterizations

Thermogravimetric analysis (TGA) was conducted using a Netzsch STA 409 instrument in the temperature range of 293.15 K to 1123.15 K, with a heating rate of 10 K min^{-1} under ambient air conditions with a flow rate of 10 mL min^{-1}. Zeta potential values were determined using the Zeta-sizer ZS (Malvern Instruments Ltd, Malvern, U.K.) at 298.15 ± 0.1 K. Measurements were conducted in ultrapure water, with a viscosity of 0.8872 cp and a refractive index of 1.330 at 298 K. The thermostatting time was 120 s, the dielectric constant of the dispersing medium was 78.5, and 3 replicate measurements were taken for each sample. Approximately 10 mg of each sample were dispersed in 10 ml of pre-filtered MilliQ water using 0.2 μm filters. The dispersion was vortexed for 1 minute and then sonicated in an ultrasonic bath (45 kHz, 80 W) for 10 minutes to completely disaggregate any present aggregates. TEM Transmission Electron Microscopy and the images were obtained with a Jeol 1400 Plus electron microscope, operating at an acceleration voltage of 80kV.

Fourier transform infrared (FT-IR) spectra were performed with Infrared Spectrometer (FT/IR-4600 FT-8IR, Jasco; Germany). The specific surface area and the average pore width of all samples were evaluated according to Brunauer-Emmett-Teller (BET) method, by physical adsorption measurements of nitrogen, using a Micromeritics Tristar II plus with pre-treatment degassing system Micromeritics FlowPrep 060. Samples were pretreated at 120 °C in the degassing system for 150 min before analysis. XRD measurements were performed with a MiniFlex Rigaku, scan interval 0.3 <2theta <10, with a scan speed of 0.005 °/sec.

The negative potential was measured at a temperature of 298.15 K in ultrapure water with a viscosity of 0.8872 cp and a refractive index of 1.330 at 298 K. The thermostatting time was 120 s, the dielectric constant of the dispersing medium was 78.5, and 3 replicate measurements were taken for each sample. To ensure better dispersion, the solution was vortexed for 1 minute and then sonicated in an ultrasonic bath (45 kHz, 80 W) for 10 minutes to completely disaggregate any present aggregates.

4.3.3 General procedures

MSN_{AS} Synthesis

MSU-type MSNs were synthesized through an assembly mechanism at neutral pH of non-ionic poly(ethylene oxide)-based surfactants and silica sources [79].

The surfactant Triton X-100 (21 g) was dissolved in ultrapure water (230 g) in about 4 h at room temperature. In order to create two phases, along the vessel it was slowly added a solution of TEOS (22 g) in cyclohexane (9.8 g) (molar composition TEOS: Cyclohexane: Triton X-100: H_2O 1: 1.08: 0.32: 120, respectively). The synthesis was carried out at room temperature. The upper phase was removed, and the resulting precipitate was collected by filtration and washed three times with ultrapure water. Finally, the sample was dried in the oven at 70 °C for 24 h, thus a white powder was obtained.

Synthesis of AP-MSN

The nanoparticles' surface was coated with aminopropyl groups using (3-aminopropyl)triethoxysilane (APTES). A solution of APTES in ethanol (33 mL, 0.85 g/mL) was added to a suspension of MSNs (8 g) in ethanol (27.85 mL). The mixture was stirred at room temperature for 48 h. Afterward, the suspension was filtered and washed once with ethanol and twice with ultrapure water. The resulting sample (AP-MSN) was dried in an oven at 70° C for 24 h.

Synthesis of FOL-MSN

Folic acid (1.11 g, 2.51 mmol) was dissolved in DMSO (19.30 mL). Triethylamine (0.554 mL, 3.9 mmol), DIC (1.11 mL, 7 mmol), and AP-MSN (5.50 g) were added to the solution. The obtained suspension was stirred at room temperature for 40 h. Afterward, the mixture was filtered and washed sequentially with dimethylformamide, dioxane, diethyl ether, and ultrapure water. The resulting yellow powder (6.98 g) was dried and stored in sealed, light-protected containers.

Template extraction protocol: synthesis of FOL-MSN-EXT

To remove the surfactant within the pores of FOL-MSN sample, 1 g of the material was suspended in 0.33 L of ultrapure water at room temperature. The number of extractions required for complete surfactant removal was determined by monitoring the total mass loss of little amounts of samples via thermogravimetric analysis (TGA) after each extraction step until a constant value was reached. Finally, the solution from the last extraction was filtered, and the obtained nanoparticles (FOL-MSN-EXT) were washed with 1,4-dioxane and dried at 45 °C overnight.

Synthesis of FOL-MSN-DIOL

The inner pores of FOL-MSN-EXT were functionalized with 3-glycidoxypropyltrimethoxysilane. To a suspension of FOL-MSN-EXT (1 g) in 1,4-dioxane (30 mL), 3-glycidoxypropyltrimethoxysilane (2 mL) was added.

The reaction mixture was kept stirring at room temperature for 18 h.

Then, the mixture was washed with dioxane and THF and filtered through nylon filters, the resulting powder was dried at 318.15 K. The recovered product (FOL-MSN-GLY) was subsequently treated with a 0.001 N HCl solution (pH 2–3). The mixture was stirred at room temperature for 10 h. After this time, the reaction mixture was washed with ultrapure water and THF, filtered, and dried at 318.15 K to afford FOL-MSN-DIOL.

Synthesis of FOL-MSN-APint

FOL-MSN-EXT was dissolved in 1,4-dioxan (0.05 g/mL) and then APTES (2.2 g/g_{MSNs}) was added. After 18 hours of stirring the suspension was filtered and the solid washed with 1,4-dioxan and THF. The nanoparticles (FOL-MSN-APint) were dried at 318.15 K overnight.

Synthesis of FOL-MSN-COOH

Succinic Anhydride (0.005 g/ml) was solubilized in dry dioxane, then FOL-MSN-APint was added. The mixture was stirred at room temperature for 24 h, next filtration and washing with dry dioxan and dry dichloromethane occurred. The so-synthesized sample, FOL-MSN-COOH, was dried at 318.15 K overnight.

Synthesis of FOL-MSN-HYD

The recovered FOL-MSN-COOH ($2.19 \cdot 10^{-4}$ mol_{COOH}) powder was suspended in DMSO (0.02 g/mL), the EDC (2· mol_{COOH}) and Sulfo-NHS (2·mol_{COOH}) were added and the mixture was stirred for 1 h. After that, hydrazine monohydrate (21.3 mL) was added to the reaction mixture that was left stirring at room temperature for 24 h. The final FOL-MSN-HYD sample was recovered after filtration and washing with DMSO, dioxane and dichloromethane.

4.4 Conclusions

Different MSN-based nanodevices were successfully designed, developed, and characterized in this study, with a focus on the surface properties of mesoporous silica nanoparticles (MSNs) and the impact of tailored functionalization.

Starting from precursor materials, a systematic approach was used to apply specific surface modifications. Through detailed characterization, the research provided a clear understanding of how these modifications affect the chemical and physical properties of MSNs.

This study highlighted how post-synthesis treatments can improve MSNs for specific applications, particularly as advanced drug delivery systems. These nanodevices were engineered to deliver biologically active compounds, such as peptides and small molecules, in a targeted manner.

Folic acid (FOL) was conjugated to the surface of MSNs (FOL-MSN) to target folate receptors, which are overexpressed in tumor cells but not in normal cells. Following surfactant removal, the internal pores of the MSNs were further modified with organosilanes and organic linkers leading to the development of the FOL-MSN-DIOL, FOL-MSN-COOH, and FOL-MSN-HYD systems. The functional groups introduced in the pores of these systems provide a versatile platform for the attachment of therapeutic agents, enabling both covalent and non-covalent, stimulus-responsive binding. This approach facilitates the controlled release of drugs to specific tissues or cells.

Future research will focus on binding the newly synthesized antiviral and anticancer molecules to the internal surfaces of MSNs, utilizing pH-sensitive linkages or exploiting weak and electrostatic interactions for targeted, controlled drug delivery.

4.5 References

1. Smith, R. C., Riollano, M., Leung, A., Hammond, P. T. Layer-by-Layer Platform Technology for Small Molecule Delivery. *Angewandte Chemie (International ed. in English)* **2009**, *48*(47).
2. Anselmo, A. C., Mitragotri, S. Nanoparticles in the clinic. *Bioengineering & translational medicine, 1*(1), 10-29; Anselmo, A. C., Mitragotri, S. (2019). Nanoparticles in the clinic: An update. *Bioengineering & translational medicine* **2019**, *4*(3), e10143.
3. Li, C., Wang, J., Wang, Y., Gao, H., Wei, G., Huang, Y. et al. Recent progress in drug delivery. *Acta pharmaceutica sinica B* **2019**, *9*(6), 1145-1162.
4. Laffleur, F., Keckeis, V. Advances in drug delivery systems: Work in progress still needed?. *International journal of pharmaceutics* **2020**, *590*, 1199129.
5. Zhang, L., Pornpattananangkul, D., Hu, C. M., Huang, C. M. Development of nanoparticles for antimicrobial drug delivery. *Current medicinal chemistry* **2010**, *17*(6), 585-594
6. Mazzotta, E., De Santo, M., Lombardo, D., Leggio, A., Pasqua, L. Mesoporous silicas in materials engineering: Nanodevices for bionanotechnologies. *Materials Today Bio* **2022**, *17*, 100472.
7. Torchilin, V. P. Multifunctional, stimuli-sensitive nanoparticulate systems for drug delivery. *Nature reviews Drug discovery* **2014,** *13*(11), 813-827.
8. Devulapally, R., Paulmurugan, R. Polymer nanoparticles for drug and small silencing RNA delivery to treat cancers of different phenotypes. *Wiley Interdisciplinary Reviews: Nanomedicine and Nanobiotechnology* **2014**, *6*(1), 40-60).
9. Gessner, I., Neundorf, I. Nanoparticles modified with cell-penetrating peptides: Conjugation mechanisms, physicochemical properties, and application in cancer diagnosis and therapy. *International journal of molecular sciences* **2020**, *21*(7), 2536.
10. Dristant, U., Mukherjee, K., Saha, S., Maity, D. An overview of polymeric nanoparticles-based drug delivery system in cancer treatment. *Technology in cancer research & treatment* **2023**, *22*.
11. Kazemzadeh, P., Sayadi, K., Toolabi, A., Sayadi, J., Zeraati, M.. et al. Structure-property relationship for different mesoporous silica nanoparticles and its drug delivery applications: A review. *Frontiers in Chemistry* **2022**, *10*, 823785.
12. Stephen, S., Gorain, B., Choudhury, H., Chatterjee, B. Exploring the role of mesoporous silica nanoparticle in the development of novel drug delivery systems. *Drug delivery and translational research* **2022**, 1-19.
13. Lin, C. Y., Yang, C. M., Lindén, M. Dissolution and morphology evolution of mesoporous silica nanoparticles under biologically relevant conditions. *Journal of Colloid and Interface Science* **2022**, *608*, 995-1004.
14. Lindén, M. Biodistribution and excretion of intravenously injected mesoporous silica nanoparticles: implications for drug delivery efficiency and safety. *the enzymes* **2018**, *43*, 155-180.
15. Kresge, A. C., Leonowicz, M. E., Roth, W. J., Vartuli, J. C., Beck, J. S. Ordered mesoporous molecular sieves synthesized by a liquid-crystal template mechanism. *Nature* **1992**, *359*(6397), 710-712), who named them Mobil Corporation of Matter (MCM-41.

16. Van Speybroeck, M., Barillaro, V., Do Thi, T., Mellaerts, R., Martens, J. Ordered mesoporous silica material SBA-15: a broad-spectrum formulation platform for poorly soluble drugs. *Journal of pharmaceutical sciences* **2009**, *98*(8), 2648-2658.
17. Chen, C. Y., Li, H. X., & Davis, M. E. Studies on mesoporous materials: I. Synthesis and characterization of MCM-41. *Microporous materials* **1993**, *2*(1), 17-26.
18. Kim, T. W., Chung, P. W., & Lin, V. S. Y. Facile synthesis of monodisperse spherical MCM-48 mesoporous silica nanoparticles with controlled particle size. *Chemistry of Materials* **2010**, *22*(17), 5093-5104.
19. Øye, G., Sjöblom, J., & Stöcker, M. Synthesis, characterization and potential applications of new materials in the mesoporous range. *Advances in colloid and interface science* **2001**, *89*, 439-466.
20. Bagshaw, S. A., Prouzet, E., & Pinnavaia, T. J. Templating of mesoporous molecular sieves by nonionic polyethylene oxide surfactants. *Science* **1995**, *269*(5228), 1242-1244.
21. Lin, H. Y., & Chen, Y. W. Preparation of spherical hexagonal mesoporous silica. *Journal of Porous Materials* **2005**, *12*, 95-105). Each category offers specific structural features and properties, making MSNs highly versatile for a wide range of applications.
22. Stöber, W., Fink, A., & Bohn, E. Controlled growth of monodisperse silica spheres in the micron size range. *Journal of colloid and interface science* **1968**, *26*(1), 62-69.
23. Duan, L., Wang, C., Zhang, W., Ma, B., Deng, Y., Li, W., Zhao, D. Interfacial assembly and applications of functional mesoporous materials. *Chemical reviews* **2021**, *121*(23), 14349-14429.
24. Wu, S. H., Mou, C. Y., Lin, H. P. Synthesis of mesoporous silica nanoparticles. *Chemical Society Reviews* **2013**, *42*(9), 3862-3875.
25. Lee, C. H., Lin, T. S., & Mou, C. Y. Mesoporous materials for encapsulating enzymes. *Nano today* **2009**, *4*(2), 165-179.
26. Lang, N., & Tuel, A. A fast and efficient ion-exchange procedure to remove surfactant molecules from MCM-41 materials. *Chemistry of materials* **2004**, *16*(10), 1961-1966.
27. Lu, F., Wu, S. H., Hung, Y., Mou, C. Y. Size effect on cell uptake in well-suspended, uniform mesoporous silica nanoparticles. *Small* **2009**, *5*(12), 1408-1413.
28. Dabbaghian, M. A., Babalou, A. A., Hadi, P., Jannatdoust, E. A parametric study of the synthesis of silica nanoparticles via sol-gel precipitation method. *International Journal of Nanoscience and Nanotechnology* **2010**, *6*(2), 104-113.
29. Chiang, Y. D., Lian, H. Y., Leo, S. Y., Wang, S. G., Yamauchi, Y., Wu, K. C. W. Controlling particle size and structural properties of mesoporous silica nanoparticles using the Taguchi method. *The Journal of Physical Chemistry C* **2011**, *115*(27), 13158-13165.
30. Vallet-Regi, M., Rámila, A., Del Real, R. P., Pérez-Pariente, J. A new property of MCM-41: drug delivery system. *Chemistry of Materials* **2001**, *13*(2), 308-311.
31. Beck, J. S., Vartuli, J. C., Roth, W. J., Leonowicz, M. E., Kresge, C. T., Schmitt, K. D. et al. A new family of mesoporous molecular sieves prepared with liquid crystal templates. *Journal of the American Chemical Society* **1992**, *114*(27), 10834-10843.
32. Chiang, Y. D., Lian, H. Y., Leo, S. Y., Wang, S. G., Yamauchi, Y., Wu, K. C. W. Controlling particle size and structural properties of mesoporous silica nanoparticles using the Taguchi method. *The Journal of Physical Chemistry C* **2011**, *115*(27), 13158-13165.

33. Cai, Q., Luo, Z. S., Pang, W. Q., Fan, Y. W., Chen, X. H., Cui, F. Z. Dilute solution routes to various controllable morphologies of MCM-41 silica with a basic medium. *Chemistry of materials* **2001**, *13*(2), 258-263.
34. Huang, R., Shen, Y. W., Guan, Y. Y., Jiang, Y. X., Wu, Y., Rahman, K. et al. Mesoporous silica nanoparticles: Facile surface functionalization and versatile biomedical applications in oncology. *Acta Biomaterialia* **2020**, *116*, 1-15.
35. Gao, P., Liang, Z., Zhao, Z., Wang, W., Yang, C., Hu, B., Cui, F. Enhanced adsorption of steroid estrogens by one-pot synthesized phenyl-modified mesoporous silica: Dependence on phenyl-organosilane precursors and pH condition. *Chemosphere* **2019**, *234*, 438-449.
36. Putz, A. M., Almásy, L., Len, A., Ianăşi, C. Functionalized silica materials synthesized via co-condensation and post-grafting methods. *Fullerenes, Nanotubes and Carbon Nanostructures* **2019**, *27*(4), 323-332.
37. Wang, G., Otuonye, A. N., Blair, E. A., Denton, K., Tao, Z., Asefa, T. Functionalized mesoporous materials for adsorption and release of different drug molecules: A comparative study. *Journal of Solid State Chemistry* **2009**, *182*(7), 1649-1660.
38. Zhang, W., Zheng, N., Chen, L., Xie, L., Cui, M., Li, S., Xu, L. Effect of shape on mesoporous silica nanoparticles for oral delivery of indomethacin. *Pharmaceutics* **2018**, *11*(1), 4.
39. Ritter, H., Nieminen, M., Karppinen, M., Brühwiler, D. A comparative study of the functionalization of mesoporous silica MCM-41 by deposition of 3-aminopropyltrimethoxysilane from toluene and from the vapor phase. *Microporous and mesoporous materials* **2009**, *121*(1-3), 79-83.
40. Narum, S. M., Le, T., Le, D. P., Lee, J. C., Donahue, N. D., Yang, W., Wilhelm, S. Passive targeting in nanomedicine: fundamental concepts, body interactions, and clinical potential. In *Nanoparticles for biomedical applications* **2020***,* (pp. 37-53). Elsevier.
41. Bertrand, N., Wu, J., Xu, X., Kamaly, N., Farokhzad, O. C. Cancer nanotechnology: the impact of passive and active targeting in the era of modern cancer biology. *Advanced drug delivery reviews* **2014**, *66*, 2-25.
42. Lin, Y. S., Lee, M. Y., Yang, C. H., Huang, K. S. Active targeted drug delivery for microbes using nano-carriers. *Current topics in medicinal chemistry* **2015**, *15*(15), 1525-1531.
43. Tripathi, A. D., Labh, Y., Katiyar, S., Singh, A. K., Chaturvedi, V. K., Mishra, A. Folate-Mediated Targeting and Controlled Release: PLGA-Encapsulated Mesoporous Silica Nanoparticles Delivering Capecitabine to Pancreatic Tumor. *ACS Applied Bio Materials* **2024**.
44. Díaz-García, D., Fischer-Fodor, E., Vlad, C. I., Méndez-Arriaga, J. M., Prashar, S., Gómez-Ruiz, S. Study of cancer cell cytotoxicity, internalization and modulation of growth factors induced by transferrin-conjugated formulations of metallodrug-functionalized mesoporous silica nanoparticles. *Microporous and Mesoporous Materials* **2021**, *323*, 111238.
45. Hou, L., Hou, Y., Liang, Y., Chen, B., Zhang, X., Wang, Y., ... & Meng, X. Anti-tumor effects of P-LPK-CPT, a peptide-camptothecin conjugate, in colorectal cancer. *Communications Biology* **2022**, *5*(1), 1248.
46. Lee, S. H., Park, O. K., Kim, J., Shin, K., Pack, C. G., Kim, K. et al. Deep tumor penetration of drug-loaded nanoparticles by click reaction-assisted immune cell targeting strategy. *Journal of the American Chemical Society* **2019**, *141*(35), 13829-13840.

47. Zhang, J., Shang, J., Tang, X., Xu, X. TfR Aptamer-functionalized MSNs for enhancing targeted cellular uptake and therapy of cancer cells. *ACS omega* **2023**, *8*(51), 48975-48983.
48. Zhu, S., Gao, H., Li, W., He, X., Jiang, P., Xu, F. Stimuli-Responsive Aptamer-Drug Conjugates for Targeted Drug Delivery and Controlled Drug Release. *Advanced Healthcare Materials* **2024**, 2401020.
49. Ulbrich, K., Hola, K., Subr, V., Bakandritsos, A., Tucek, J. Targeted drug delivery with polymers and magnetic nanoparticles: covalent and noncovalent approaches, release control, and clinical studies. *Chemical reviews* **2016**, *116*(9), 5338-5431.
50. Mi, P. Stimuli-responsive nanocarriers for drug delivery, tumor imaging, therapy and theranostics. *Theranostics* **2020**, *10*(10), 4557.
51. Jia, R., Teng, L., Gao, L., Su, T., Fu, L., Qiu, Z., Bi, Y. Advances in multiple stimuli-responsive drug-delivery systems for cancer therapy. *International journal of nanomedicine **2021***, 1525-1551.
52. Mura, S., Nicolas, J., Couvreur, P. Stimuli-responsive nanocarriers for drug delivery. *Nature materials* **2013**, *12*(11), 991-1003.
53. Fu, D., Wang, Y., Xu, J., Wu, H. Hydrazone modified nanoscale metal-organic frameworks as pH responsive nanoplatforms for cancer therapy. *Journal of Solid State Chemistry* **2022**, *310*, 123029.
54. Liao, S. C., Ting, C. W., Chiang, W. H. Functionalized polymeric nanogels with pH-sensitive benzoic-imine cross-linkages designed as vehicles for indocyanine green delivery. *Journal of colloid and interface science* **2020**, *561*, 11-22.
55. Jin, Y., Song, L., Su, Y., Zhu, L., Pang, Y., Qiu, F. et al. Oxime linkage: a robust tool for the design of pH-sensitive polymeric drug carriers. *Biomacromolecules* **2011**, *12*(10), 3460-3468.
56. Luo, F., Fan, Z., Yin, W., Yang, L., Li, T., Zhong, L. et al. Q. pH-responsive stearic acid-O-carboxymethyl chitosan assemblies as carriers delivering small molecular drug for chemotherapy. *Materials Science and Engineering: C* **2019**, *105*, 110107.
57. Gannimani, R., Walvekar, P., Naidu, V. R., Aminabhavi, T. M., Govender, T. Acetal containing polymers as pH-responsive nano-drug delivery systems. *Journal of controlled release* **2020**, *328*, 736-761.
58. Bruyère, H., Westwell, A. D., Jones, A. T. Tuning the pH sensitivities of orthoester based compounds for drug delivery applications by simple chemical modification. *Bioorganic & Medicinal Chemistry Letters* **2010**, *20*(7), 2200-2203.
59. Li, Y., Wang, S., Song, F. X., Zhang, L., Yang, W., Wang, H. X., Chen, Q. et al. A pH-sensitive drug delivery system based on folic acid-targeted HBP-modified mesoporous silica nanoparticles for cancer therapy. *Colloids and Surfaces A: Physicochemical and Engineering Aspects* **2020**, *590*, 124470.
60. Kong, J., Park, S. S., & Ha, C. S. pH-sensitive polyacrylic acid-gated mesoporous silica nanocarrier incorporated with calcium ions for controlled drug release. *Materials* **2022**, *15*(17), 5926.
61. Zhang, C., Xie, H., Zhang, Z., Wen, B., Cao, H., Bai, Y. et al. Applications and biocompatibility of mesoporous silica nanocarriers in the field of medicine. *Frontiers in pharmacology* **2022**, *13*, 829796.

62. Hao, N., Liu, H., Li, L., Chen, D., Li, L., Tang, F. In vitro degradation behavior of silica nanoparticles under physiological conditions. *Journal of nanoscience and nanotechnology* **2012**, *12*(8), 6346-6354.
63. Li, X., Zhang, L., Dong, X., Liang, J., Shi, J. Preparation of mesoporous calcium doped silica spheres with narrow size dispersion and their drug loading and degradation behavior. *Microporous and Mesoporous Materials* **2007**, *102*(1-3), 151-158.
64. Pohaku Mitchell, K. K., Liberman, A., Kummel, A. C., Trogler, W. C. Iron (III)-doped, silica nanoshells: a biodegradable form of silica. *Journal of the American Chemical Society* **2012**, *134*(34), 13997-14003.
65. Cauda, V., Argyo, C., Bein, T. Impact of different PEGylation patterns on the long-term bio-stability of colloidal mesoporous silica nanoparticles. *Journal of Materials Chemistry* **2010**, *20*(39), 8693-8699.
66. Choi, E., Kim, S. How can doxorubicin loading orchestrate in vitro degradation behaviors of mesoporous silica nanoparticles under a physiological condition?. *Langmuir* **2017**, *33*(20), 4974-4980.
67. Hong, X., Zhong, X., Du, G., Hou, Y., Zhang, Y., Zhang, Z. et al. The pore size of mesoporous silica nanoparticles regulates their antigen delivery efficiency. *Science advances* **2020**, *6*(25), eaaz4462.
68. He, Q., Zhang, Z., Gao, F., Li, Y., Shi, J. In vivo biodistribution and urinary excretion of mesoporous silica nanoparticles: effects of particle size and PEGylation. *Small* **2011**, *7*(2), 271-280.
69. Nabeshi, H., Yoshikawa, T., Arimori, A., Yoshida, T., Tochigi, S., Hirai, T. et al. Effect of surface properties of silica nanoparticles on their cytotoxicity and cellular distribution in murine macrophages. *Nanoscale research letters* **2011**, *6*, 1-6.
70. Liu, T., Li, L., Teng, X., Huang, X., Liu, H., Chen, D. et al. Single and repeated dose toxicity of mesoporous hollow silica nanoparticles in intravenously exposed mice. *Biomaterials* **2011**, *32*(6), 1657-1668.
71. Longmire, M., Choyke, P. L., Kobayashi, H. Clearance properties of nano-sized particles and molecules as imaging agents: considerations and caveats. *Nanomedicine* **2008**, *3*(5), 703-717.
72. Niroumand, U., Firouzabadi, N., Goshtasbi, G., Hassani, B., Ghasemiyeh, P., Mohammadi-Samani, S. The effect of size, morphology and surface properties of mesoporous silica nanoparticles on pharmacokinetic aspects and potential toxicity concerns. *Frontiers in Materials* **2023**, *10*, 1189463.
73. Frickenstein, A. N., Hagood, J. M., Britten, C. N., Abbott, B. S., McNally, M. W., Vopat, C. A. et al. Mesoporous silica nanoparticles: Properties and strategies for enhancing clinical effect. *Pharmaceutics* **2021**, *13*(4), 570.
74. Zhao, Z., Ukidve, A., Krishnan, V., Mitragotri, S. Effect of physicochemical and surface properties on in vivo fate of drug nanocarriers. *Advanced drug delivery reviews* **2019**, *143*, 3-21.
75. Al-Ahmady, Z. S., Hadjidemetriou, M., Gubbins, J., Kostarelos, K. Formation of protein corona in vivo affects drug release from temperature-sensitive liposomes. *Journal of Controlled Release* **2018**, *276*, 157-167.
76. Manzano, M., Vallet-Regí, M. Mesoporous silica nanoparticles for drug delivery. *Advanced functional materials* **2020**, *30*(2), 1902634.

77. Nigro, A., Frattaruolo, L., Fava, M., De Napoli, I., Greco, M., Comandè, A. et al. Bortezomib-loaded mesoporous silica nanoparticles selectively alter metabolism and induce death in multiple myeloma cells. *Cancers* **2020**, *12*(9), 2709.
78. De Santo, M., Giovinazzo, A., Fava, M., Mazzotta, E., De Napoli, I. E., Greco, M. et al. Engineered mesoporous silica-based nanoparticles as smart chemotherapy nanodevice for bortezomib administration. *Materials Chemistry Frontiers* **2023**, *7*(2), 216-229.
79. Garofalo, N., Comandé, A., Perrotta, I., Davoli, M., Niceforo, G., Pasqua, L. Synthesis and Characterization of Large Pore MSU-Type Mesoporous Silica. *Advanced Science Letters* **2017**, *23*(6), 6026-6028.
80. EP2001514B1 Pasqua, L., Rosario, A., & Umberto, M. (**2006**). Preparation of micro or nano systems based on inorganic oxides with controlled porosity for carrying biologically active or activable substances.
81. Boissiere, C., Larbot, A., van Der Lee, A., Kooyman, P. J., Prouzet, E. A new synthesis of mesoporous MSU-X silica controlled by a two-step pathway. *Chemistry of materials* **2000**, *12*(10), 2902-2913.
82. Talavera-Pech, W. A., Esparza-Ruiz, A., Quintana-Owen, P., Vilchis-Nestor, A. R., Carrera-Figueiras, C., Ávila-Ortega, A. Effects of different amounts of APTES on physicochemical and structural properties of amino-functionalized MCM-41-MSNs. *Journal of Sol-Gel Science and Technology* **2016**, *80*, 697-708.
83. Delgado, Á. V., González-Caballero, F., Hunter, R. J., Koopal, L. K., Lyklema, J. Measurement and interpretation of electrokinetic phenomena. *Journal of colloid and interface science* **2007**, *309*(2), 194-224.
84. Pérez-Quintanilla, D., Sánchez, A., del Hierro, I., Fajardo, M., Sierra, I. Synthesis and characterization of novel mesoporous silicas of the MSU-X family for environmental applications. *J. Nanosci. Nanotechnol*. **2009**, *9*(8), 4901-4909.
85. Rami, M.D., Taghizadeh, M., Akhoundzadeh, H. Synthesis and characterization of nano-sized hierarchical porous AuSAPO-34 catalyst for MTO reaction: Special insight on the influence of TX 100 as a cheap and green surfactant. *Microporous Mesoporous Mater*. **2019**, *285*, 259-270.
86. López, V., Villegas, M. R., Rodríguez, V., Villaverde, G., Lozano, D., Baeza, A.,Vallet-Regí, M. Janus mesoporous silica nanoparticles for dual targeting of tumor cells and mitochondria. *ACS applied materials & interfaces* **2017**, *9*(32), 26697-26706.
87. Joseph, T., Kumar, K.V., Ramaswamy, A.V., Halligudi, S.B. Au–Pt nanoparticles in amine functionalized MCM-41: Catalytic evaluation in hydrogenation reactions. *Catal. Commun.* **2007**, *8*(3), 629-634.
88. Freitas, L.B.O., Bravo, I.J.G., Macedo, W.A.D.A., de Sousa, E.M.B. Mesoporous silica materials functionalized with folic acid: preparation, characterization and release profile study with methotrexate. *J. Sol-Gel Sci. Technol*. **2016**, 77, 186-204.
89. Smith, B. (**2022**). The Infrared Spectra of Polymers V: Epoxies.
90. Selvakumar, R., Geib, S. J., Premkumar, T., Govindarajan, S. Hydrolysis of hydrazido-oxalic acid leading to the formation of hydrazinium cadmium hydrazido-oxalate/uranium oxalate species with a polymeric structure. *Polyhedron* **2015**, *87*, 321-328.

LIST OF PUBLICATIONS

1. A way to broad spectrum antiviral agents: small molecules based on piperazine core as potential Flaviviridae NS3 protease. ACS Infection Disease. *Article in submission*.
   Cavallaro, P.A., Bartolini, N., Varasi, I., Vega-Pèrez, J.M., Iglesias-Guerra, F., Vicenti, I., Leggio, A., Vega-Holm, M.
2. Efficient Solution-Phase Dipeptide Synthesis Using Titanium Tetrachloride and Microwave Heating. International Journal of Molecular Sciences **2024**, 25(17).
   Cavallaro, P. A., De Santo, M., Marinaro, R., Belsito, E. L., Liguori, A., and Leggio.
3. Engineered Mesoporous Silica-Based Nanoparticles: Characterization of Surface Properties. Materials **2024**, 17(13), 3352.
   Grisolia, A., De Santo, M., Curcio, M., **Cavallaro, P. A**., Morelli, C., Leggio, A. and Pasqua, L.
4. Titanium Tetrachloride-Assisted Direct Esterification of Carboxylic Acids. Molecules **2024**, 29, 777.
   Cavallaro P.A., De Santo M., Greco M., Marinaro R., Belsito E.L., Liguori A., Leggio A.
5. Peptides Targeting HER2-Positive Breast Cancer Cells and Applications in Tumor Imaging and Delivery of Chemotherapeutics. Nanomaterials **2023**,13, 2476.
   Cavallaro P.A., De Santo M., Belsito E.L., Longobucco C., Curcio M., Morelli C., Pasqua L., Leggio A.

CONGRESSES

1. 7th Innovative Approaches for Antiviral Agents Summer School (IAAASS). Pula (CA). 23-27/09/2024
   Evaluation of broad-spectrum piperazine-based compounds able to inhibit flavivirus and/or SARSCoV-2 replication in a live virus assay.
   Varasi, I. Biba, C., **Cavallaro, P. A**., Giammarino, F., Bartolini, N., Vega-Perez, J. M, Iglesias-Guerra, F., Leggio, A., Vega-Holm, M., Vicenti, I.
2. NanoInnovation-Conference and Exhibition. Rome, 9-13 September 2024.
   Oral presentation: "Novel Piperazine-Based Small Molecules in Antiviral and Anticancer Research".
   Cavallaro, P.A.; Longobucco, C.; Varasi, I.; Bartolini, N.; Giammarino F.; De Santo, M.; Marinaro, R.; Belsito, E.L.; Vega-Perez, J. M.; Iglesias-Guerra, F.; Vicenti, I.; Leggio, A.; Vega-Holm, M.
3. NanoInnovation-Conference and Exhibition. Rome, 9-13 September 2024.
   "Targeted Mesoporous Silica Nanoparticles as Smart Vehicles for Highly Selective Drug Delivery."
   Morelli, C., M. De Santo, Longobucco, C., Fava, M., Sisci, D., **Cavallaro, P.A.**, Marinaro, R., Leggio, A., Pasqua, L.
4. 52° National Congress of the Italian Society of Microbiology SIM. Pavia - 8-11 September 2024.
   Poster presentation: "Evaluation of broad-spectrum piperazine-based compounds able to inhibit flavivirus and/or SARSCoV-2 replication in a live virus assay."
   Varasi, I. Biba, C., **Cavallaro, P. A**., Giammarino, F., Bartolini, N., Vega-Perez, J. M, Iglesias-Guerra, F., Leggio, A., Vega-Holm, M., Vicenti, I.
5. 8° National Congress of the Italian Society for Virology, One Virology One Health – Bologna – 7-9 July 2024.
   Poster presentation: "Evaluation of broad-spectrum piperazine-based compounds able to inhibit flavivirus and/or SARSCoV-2 replication in a live virus assay."
   Varasi, I. Biba, C., **Cavallaro, P. A**., Giammarino, F., Bartolini, N., Vega-Perez, J. M, Iglesias-Guerra, F., Leggio, A., Vega-Holm, M., Vicenti, I.
6. EFMC-ASMC- IX International Symposium on Advances in Synthetic and Medicinal Chemistry-Zagreb, Croatia, 3-7 Sep 2023

Poster presentation: “A way to broad spectrum antiviral agents: small molecules based on piperazine core as potential Flaviviridae NS3 protease inhibitors."
Cavallaro, P.A.; Giammarino, F.; Bartolini, N.; De Santo, M.; Belsito, E.L.; . Vega-Pèrez, J. M.; Iglesias-Guerra, F.; Vicenti,I.; Leggio, A.; Vega-Holm, M.

7. EFMC-ASMC- IX International Symposium on Advances in Synthetic and Medicinal Chemistry, Zagreb, Croatia, 3-7 Sept 2023.
   Poster presentation: “Mesoporous silica-based nanodevice for targeted therapy.”
   De Santo, M., **Cavallaro, P.A.**, Longobucco, C., Fava, M., Morelli, C., Pasqua, L., Leggio, A.
8. PhD day 2023. PhD@unical: a future to research 4. Unical- 30 Maggio **2023**.
   Poster presentation: **“**Solution and Solid Phase $TiCl_4$-mediated Synthesis of Dipeptides using Microwave Irradiation”. **P. A. Cavallaro**, M. De Santo , E. L. Belsito, A. Liguori, A. Leggio.
9. SCICaSi- Joint Conference 2022 of the Calabria and Sicily Sections of the Italian Chemical Society- Reggio Calabria, Italy, 1-2 Dec 2022
   Poster presentation: “Design and synthesis of a novel Somatostatin analogue cyclic peptide as a potential anticancer agent”.
   Cavallaro, P.A., De Santo, M., Prejanò, M., Belsito, E.L., Liguori, A., Marino, T., Leggio, A.
10. MYCS 2022 – Merck Young Chemists’- Symposium **2022**, 21-23 November, Rimini, Italia. “Engineered mesoporous silica-based nanodevice for targeted cancer therapy”. De Santo, M., **Cavallaro**, P.A., Fava, M., Longobucco, C., Morelli, C., Pasqua, L., Leggio, A.
11. SISOC XIII EDITION, Spanish-Italian Symposium on Organic Chemistry, Tarragona, Spain, 4-6 SEP 2022.
    Poster presentation: “Efficient TiCl4-assisted synthesis of dipeptides using microwave irradiation”.
    Cavallaro, P.A., De Santo, M., Belsito, E.L., Liguori, A., Leggio, A.

COURSES

• Advanced scientific English- CLA- **3** CFU
• Research and innovation-Liason Office- **3** CFU
• Preclinical and clinical evidence for drug development-Prof Giacinto Bagetta- **1** CFU
• Nanomaterials for medicine-Prof. Gerardo F Goya- **1** CFU
• Nanotechnologies and drug delivery: · Physicochemical properties of nanomaterials: implication and drug delivery · Innovative technologies for drug delivery- Prof. Fiore Nicoletta, Prof. Giuseppe Cirillo- **4** CFU
• Extracellular vesicles in translational medicine-Dr. Cinzia Giordano- **1**CFU
• Molecular Cell Biology:
-Steroid hormones in cancer progression-Prof. Francesca De Amicis- **1** CFU
-Targeting cholesterol for anti-cancer therapy-Prof. Rosa Sirianni- **1** CFU
-Serine and one carbon metabolism in cancer-Dr. Ivan Casaburi- **1** CFU
-Cancer cell metabolism: the role of nutrients-Prof. Vincenzo Pezzi- **1** CFU
• Advanced mass spectrometry for food safety and quality-Prof. Leonardo Di Donna- **2** CFU
• The role of proteomics in cancer-Dr. Luca Gelsomino-**1** CFU
• Natural bioactive compounds: extraction and characterization by advanced methodologies-Dr. Lucia Bartella- **2** CFU
• Flow cytometry and ‘*in vivo*’ imaging-Dr. Rosamaria Lappano-**1** CFU
• Next Generation Sequencing for the diagnosis of rare diseases-Prof. Francesca Luisa Conforti- **1** CFU
• Translational cancer research-Prof. Regine Schneider-Stock-**1** CFU

SEMINARS and SCHOOLS

1. LC-MS/MS Fundamentals: The Overview (webinar), 8 December 2022
2. DIGITALIZZAZIONE E UMANIZZAZIONE DELLE CURE IN SANITA', 17 May 2022, Edificio Polifunzionale, Università della Calabria, Rende (CS)
3. ISPROCHEM 2022 - International School of Process Chemistry, Advanced Edition: New Trend in Process Chemistry, 29 May - 1 June, Gargnano, Italy.
4. "PhD3.0 La Terza Missione dell'Università nel Terzo Livello della Formazione: EUROPROGETTAZIONE, PROPRIETA' INDUSTRIALE E DIRITTI D'AUTORE", 22 November 2021, 1 Dicember 2021, 16 Dicember 2021, 14 January 2022, 7 February 2022.
5. AGILENT LC/MSD iQ: "la spettrometria di massa alla portata di Chiunque" (webinar), January 2022.

La borsa è stata cofinanziata con risorse del Programma Operativo Nazionale Ricerca e Innovazione 2014-2020 (CCI 2014IT16M2OP005), risorse FSE REACT-EU, Azione IV.4 "Dottorati e contratti di ricerca su tematiche dell'innovazione" e Azione IV.5 "Dottorati su tematiche Green"